JYU DISSERTATIONS 753

Sailee Shroff

Virus Persistence on Surfaces

Studies on Nature-Based Solutions

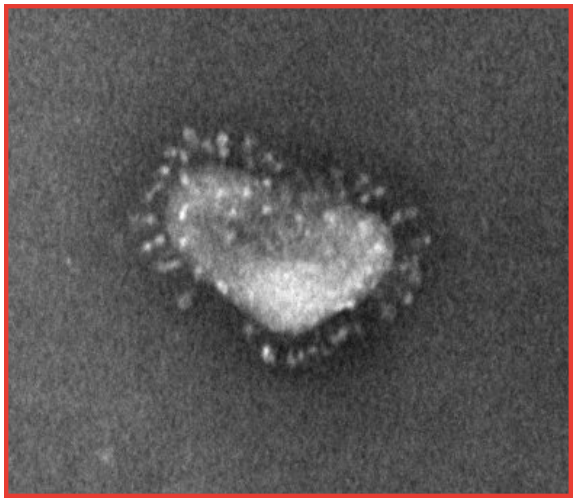

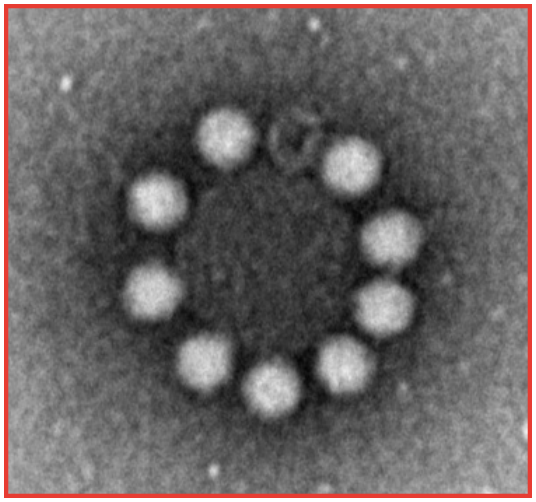

UNIVERSITY OF JYVÄSKYLÄ
FACULTY OF MATHEMATICS
AND SCIENCE

JYU DISSERTATIONS 753

Sailee Shroff

Virus Persistence on Surfaces

Studies on Nature-Based Solutions

Esitetään Jyväskylän yliopiston matemaattis-luonnontieteellisen tiedekunnan suostumuksella
julkisesti tarkastettavaksi Ylistönrinteen auditoriossa Kem4
maaliskuun 8. päivänä 2024 kello 12.

Academic dissertation to be publicly discussed, by permission of
the Faculty of Mathematics and Science of the University of Jyväskylä,
in Ylistönrinne, auditorium Kem4, on March 8, 2024, at 12 o'clock.

JYVÄSKYLÄN YLIOPISTO
UNIVERSITY OF JYVÄSKYLÄ

JYVÄSKYLÄ 2024

Editors
Matti Jalasvuori
Department of Biological and Environmental Science, University of Jyväskylä
Päivi Vuorio
Open Science Centre, University of Jyväskylä

ISBN 978-951-39-9945-2 (PDF)
URN:ISBN:978-951-39-9945-2
ISSN 2489-9003

Permanent link to this publication: http://urn.fi/URN:ISBN:978-951-39-9945-2

ABSTRACT

Shroff, Sailee
Virus persistence on surfaces: studies on nature-based solutions
Jyväskylä: University of Jyväskylä, 2024, 74 p.+ original papers
(JYU Dissertations
ISSN 2489-9003; 753)
ISBN 978-951-39-9945-2 (PDF)
Yhteenveto: Virus persistence on surfaces: studies on nature-based solutions
Diss.

The emergence of new viruses is always a global health threat, as they have the potential to cause widespread outbreaks. Viruses can spread through direct transmission but also via contaminated surfaces. The recent COVID-19 pandemic, in particular, highlighted the importance of maintaining clean public spaces to minimize the transmission risk through surfaces. While surface disinfection remains a practical solution, it can be laborious, time-consuming, costly, and environmentally harmful. This dissertation has examined nature-derived antiviral surface solutions to complement traditional strategies. Six wood species were investigated for their antiviral properties in the first study. Most of the wood species displayed broad-spectrum antiviral activity, with varying capacities to inactivate both enveloped and non-enveloped viruses. The antiviral efficacy of wood was hypothesized to be attributed to its porous nature and the presence of wood extractives. The second study evaluated the efficacy of a tall oil rosin-functionalized plastic surface against coronaviruses. The active component rosin rapidly reduced the infectivity of both seasonal human coronavirus OC43 and SARS-CoV-2 without apparent changes in the virion structure, as evidenced by different imaging techniques. The third study demonstrated that polyphenols have potent antiviral activity against different serotypes of enteroviruses. The efficacy of these polyphenols significantly increased when functionalized on the surface of gold nanoparticles. The antiviral activity is hypothesized to be associated with their ability to bind to multiple sites on the capsid. This interaction may result in the super stabilization of the virion, preventing the virus's binding to its host cells.

Keywords: antiviral solutions; coronavirus; enterovirus; gold nanoparticles; polyphenols; rosin; plastic; wood.

Sailee Shroff, University of Jyväskylä, Department of Biological and Environmental Science, P.O. Box 35, FI-40014 University of Jyväskylä, Finland

TIIVISTELMÄ

Shroff, Sailee
Virusten säilyminen infektiokykyisinä pinnoilla: tutkimuksia luontoperäisillä ratkaisuilla
Jyväskylä: Jyväskylän yliopisto, 2024, 74 s. + alkuperäiset artikkelit
(JYU Dissertations
ISSN 2489-9003; 753)
ISBN 978-951-39-9945-2 (PDF)
Diss.

Viime vuosina virukset ovat aiheuttaneet merkittäviä maailmanlaajuisia terveysuhkia, koska ne voivat aiheuttaa laajoja epidemioita. Tuorein SARS-CoV-2:n aiheuttama COVID-19-pandemia on korostanut julkisten tilojen puhtauden ylläpitämisen tärkeyttä pintojen kautta leviämisen riskin minimoimiseksi. Vaikka pintojen desinfiointi on edelleen tehokas ratkaisu, se voi olla työvoimavaltaista, aikaa vievää, kallista ja ympäristölle haitallista. Tässä väitöskirjatyössä tutkittiin kolmea luonnosta peräisin olevaa antiviraalista pintaratkaisua, jotka voisivat täydentää perinteisiä desinfiointistrategioita. Ensimmäisessä osatyössä tutkimme eri puulajien antiviraalisia ominaisuuksia. Suurin osa puulajeista osoitti laajakirjoista antiviraalista aktiivisuutta, mutta eri puulajeilla oli vaihteleva kyky inaktivoida vaipallisia ja vaipattomia viruksia. Puun antiviraalinen teho johtui ensisijaisesti sen huokoisuudesta ja puun uuteaineiden läsnäolosta. Toisessa osatyössä tutkittiin mäntyöljyhartsia sisältävän muovin tehoa koronaviruksia vastaan. Aktiivista ainesosaa, hartsia, uuttui muovipinnasta ja se kykeni vähentämään sekä kausiluonteisen ihmisen koronaviruksen (HCoV-OC43) että SARS-CoV-2:n infektiokykyä nopeasti ilman näkyviä muutoksia virionin rakenteessa, mikä varmistettiin eri kuvantamistekniikoilla. Käsitellyt virukset kykenivät kulkeutumaan solujen sisään, mutta ne eivät näyttäneet etenevän endosomivaiheesta eteenpäin. Tämä viittaa siihen, että estomekanismi voisi liittyä viruksen ja endosomaalisten kalvojen vähentyneeseen fuusioon, mikä estää viruksen genomin vapautumisen sytoplasmaan. Viimeisessä osatyössä polyfenolit osoittivat voimakasta antiviraalista aktiivisuutta erilaisia enteroviruksia vastaan. Tehokkuus monikertaistui, mikäli käytettiin polyfenoleilla päällystettyjä kultapartikkeleita. Polyfenolien antiviraalinen teho perustui siihen, että ne sitoutuivat useaan kohtaan viruksen pinnassa, mikä voimakkaasti stabiloi viruspartikkeleita ja vähensi niiden sitoutumista solujen pintaan.

Avainsanat: Antiviraali; koronavirus; enterovirus; muovi; polyfenolit; hartsi; puu.

Sailee Shroff, Jyväskylän yliopisto, Bio- ja ympäristötieteiden laitos PL 35, 40014 Jyväskylän yliopisto

Author's address Sailee Shroff
Department of Biological and Environmental Science
P.O. Box 35
FI-40014 University of Jyväskylä
Finland
sailee.s.shroff@jyu.fi

Supervisors Prof. Varpu Marjomäki
Department of Biological and Environmental Science
P.O. Box 35
FI-40014 University of Jyväskylä
Finland

Reviewers Assoc. Prof. Docent Jussi Hepojoki
University of Helsinki
Department of Virology
PL 21 (Haartmanin katu 3)
00014
Finland

Dr. Ilona Rissanen
University of Helsinki
Institute of Biotechnology
PL 65 (Viikinkaari 1)
00014
Finland

Opponent Assoc. Prof. Tarja Sironen
University of Helsinki
Department of Virology
PL 21 (Haartmanin katu 3)
00014
Finland

CONTENTS

LIST OF ORIGINAL PUBLICATIONS

The thesis is based on the following original papers, which will be referred to in the text by their Roman numerals I–III

I Shroff S.*, Peramäki A.*, Väisänen A., Pasanen P., Grönlund K., Nissinen V., Jänis J., Haapala A. & Marjomäki V. 2023. Tree species-dependent inactivation of coronaviruses and enteroviruses on solid wood surfaces. Manuscript. *Equal contribution.

II Shroff S., Haapakoski M., Tapio K., Laajala M., Leppänen M., Plavec Z., Haapala A., Butcher S.J., Ihalainen J.A., Toppari J.J., & Marjomäki V. 2024. Antiviral action of a functionalized plastic surface against human coronaviruses. *Microbiology Spectrum*, e03008-23.

III Reshamwala D.*, Shroff S.*, Sheik Amamuddy O., Laquintana V., Denora N., Zacheo A., Lampinen V., Hytonen V.P., Tastan Bishop Ö., Krol S. & Marjomäki V. 2021. Polyphenols Epigallocatechin Gallate and Resveratrol, and Polyphenol-Functionalized Nanoparticles Prevent Enterovirus Infection through Clustering and Stabilization of the Viruses. *Pharmaceutics* 13: 1182. *Equal contribution

RESPONSIBILITIES

Article I: This project was headed by Varpu Marjomäki (VM) and Antti Haapala (AH). The antiviral studies and confocal experiments were planned by Sailee Shroff (SS) and executed by both SS and master's student Anni Perämäki (AP). Collaborators were responsible for the isolation and chemical characterization of volatile compounds from various wood species. SS and AP drafted the manuscript, and the final editing was done by VM and AH.

Article II: This project involved collaboration with the Finnish company Premix Oy and multiple research groups in Finland. The conception of the original idea can be credited to VM. Both VM and SS contributed to the experimental design. SS played a key role in conducting virus persistence and antiviral studies, and performing TEM, binding assay, sedimentation assay, and confocal imaging. Atomic Force Microscopy (AFM), Helium Ion Microscopy (HIM), UV-Visible (UV-Vis) Spectroscopy, contact angle measurements, and Cryo Electron Microscopy (Cryo-EM) were carried out by our collaborators. The writing of the manuscript was undertaken by SS and edited by VM.

Article III: The original idea for this project was conceived by VM and Silke Krol (SK). The planning and execution of the experimental work was a joint effort by Dhanik Reshawmala (DR) and SS. DR was responsible for producing the purified and radioactively labelled virus, and conducting the initial antiviral screening assays, time of addition assay, and gradient separation assay. SS performed transmission electron microscopy (TEM) and conducted the time and temperature assay, thermal assay, real-time fluorescence uncoating assay, and binding assay. Certain aspects of the project, such as the characterization of the polyphenols functionalized nanoparticles and docking studies, were carried out by our collaborators. Data analysis was a collaborative effort by SS, DR and VM. All the authors contributed to writing their respective sections for the article. DR and SS have equally contributed towards curating this article.

ABBREVIATIONS

A549	adenocarcinoma human alveolar basal epithelial cells
ABS	acrylonitrile butadiene styrene
ACE2	angiotensin-converting enzyme 2
CDC	Centers for Disease Control and Prevention
COVID-19	Coronavirus Disease 2019
CPE	cytopathic effect
CTO	crude tall oil
CVA	coxsackie virus A
CVB	coxsackie virus B
ddH20	double distilled water
EGCG	epigallocatechin gallate
ER	endoplasmic reticulum
FDA	Food and Drug Administration
HCoV-OC43	human coronavirus OC43
ISO	International Organization for Standardization
LDPE	low-density polyethylene
MERS	Middle East respiratory syndrome coronavirus
MOI	multiplicity of infection
MRC-5	human lung fibroblast cell line
nm	nanometer
nsps	non-structural proteins
ORF	open reading frame
PE	polyethylene
PFU	particle forming unit
qPCR	quantitative polymerase chain reaction
RES	resveratrol
RH	relative humidity
RNA	ribonucleic acid
S-protein	spike protein
SARS-CoV-2	severe acute respiratory syndrome coronavirus 2
SGII	sybr green II
S.D.	standard deviation
SVOCs	semi-volatile organic compounds
TEM	transmission electron microscopy
TOR	tall oil rosin
TVOCs	total volatile organic compounds
VOCs	volatile organic compounds
WHO	World Health Organization

1 INTRODUCTION

Every few years, the world has witnessed an alarming number of viral outbreaks in various regions. The most recent example of the pandemic caused by the severe acute respiratory syndrome coronavirus 2 (SARS-CoV-2) has led to a death toll of approximately 6.9 million and counting (WHO, 2023). Early into the pandemic, the scientific community realized that contaminated surfaces could play a significant role in the transmission of viruses. While conventional methods like surface disinfection can help prevent fomite-based transmission, they have their own set of limitations (Gebel *et al.* 2013). To strengthen and complement the existing strategies, it is essential to explore additional antiviral solutions. One approach is to use natural surfaces with antiviral properties, while another is to develop antiviral surfaces by coating or embedding nature-based compounds into everyday surfaces.

This thesis explores the antiviral capabilities of nature-derived compounds and surfaces and elucidates the underlying antiviral mechanisms. Our study found that, of the six wood species tested, most of them could inactivate both enveloped and non-enveloped viruses. We also found that the distinct chemical compositions of wood species, besides their absorption properties, might govern their antiviral functionality. A rosin-functionalized plastic surface demonstrated remarkable ability to rapidly inactivate coronaviruses in a relatively short time frame compared to regular plastic surfaces. While this surface treatment did not induce apparent changes in virion structure, it effectively hindered the viruses from progressing beyond the entry and internalization stages in their infection cycle.

Furthermore, our investigations into polyphenols revealed their potent antiviral activity against enteroviruses. Notably, their efficacy was significantly enhanced when they were functionalized onto the surface of gold nanoparticles. These compounds functioned by super stabilizing the viruses, preventing their attachment to host cell receptors, and preventing the release of their genetic material. Together, these innovative approaches provide a comprehensive defense against enveloped and non-enveloped viruses.

2 REVIEW OF THE LITERATURE

2.1 Enteroviruses

2.1.1 Overview and health implications

The *Enterovirus* genus is part of the *Picornaviridae* family, found within the *Picornavirales* order. There are 15 species of Enteroviruses, namely enterovirus A-L and rhinovirus A-C, with 7 of these species (enterovirus A-D and rhinovirus A-C) associated with human diseases (B'Krong *et al.* 2018). Our study focuses on coxsackievirus A9 (CVA9), coxsackievirus B1 (CVB1), and B3 (CVB3), which belong to the enterovirus B species. Enteroviruses primarily infect through the faecal-oral route and replicate within gastrointestinal tract cells, aligning with the Greek origin of their name "enteros" meaning "intestine". However, enterovirus D68 is an exception, as it replicates in the respiratory tract (Jacobs *et al.* 2013). From these primary sites of infection, these viruses can spread to and affect other organs, including the nervous system (CNS) (Lee 2016, B'Krong *et al.* 2018).

Enteroviruses can cause various human diseases, ranging from mild flu-like symptoms to severe cases of meningitis, encephalitis, acute flaccid paralysis, to name a few (Nikonov *et al.* 2017, Simons-Linares *et al.* 2021). Additionally, enteroviruses have been linked to type I diabetes (Nekoua *et al.* 2022) and myocarditis (Bouin *et al.* 2019). Enteroviruses became popular in the last century mainly due to the deadly outbreaks of the poliovirus. In the 21st century, non-polio enteroviruses have also emerged as global health concerns, like EV-A71, which caused hand-foot-and-mouth disease outbreaks in children in Southeast Asia and EV-D68, which caused severe lower respiratory tract disease in children in North America (Lee 2016, Baggen *et al.* 2018).

Recurrent outbreaks of these virus infections impose a significant burden on society. There are currently no vaccines against enteroviruses, except poliovirus vaccines and an EV71 vaccine that was approved only in China. There

are also no antivirals against enteroviruses. Therefore, effective prevention strategies with timely, accurate surveillance are needed to mitigate future viral outbreaks.

2.1.2 Structure and genome

Enteroviruses are small, non-enveloped viruses, measuring roughly 30 nm in size (Muckelbauer *et al.* 1995). They have a single-stranded RNA genome with positive polarity, measuring around 7.9 kilobase in length, flanked by untranslated regions (UTRs) at both ends. At the 5' end of the genome, there is a virion protein, genome linked (VPg), that acts as a primer during RNA replication, and at the 3' end, there is a poly(A) tail. The genome is translated as a single large polyprotein, which is then proteolytically processed by viral proteinases to yield structural and non-structural proteins.

The viral genome is enclosed within an icosahedral capsid made up of four structural viral proteins (VP1-VP4), with VP1, VP2, and VP3 forming the outer part of the capsid and VP4 located on the inside (Rossmann *et al.* 1985, Hogle *et al.* 1985). Most enteroviruses have a deep, circular depression surrounding each of the fivefold axes of symmetry, called the "canyon", which is a critical site for virus receptor binding (Rossmann *et al.* 2002). The floor of this canyon houses a small hydrophobic pocket filled with a lipid moiety, often referred to as the "pocket factor," which has been associated with virus stability (Smyth *et al.* 2003).

2.1.3 Lifecycle

Enteroviruses usually replicate in the mucosal cells of the gastrointestinal tract, although for some types, like rhinoviruses and EV-D68, the primary replication occurs in the respiratory tract (Wells and Coyne 2019). The lifecycle of a virus, sometimes also addressed as the infection cycle, refers to the process in which the virus reproduces inside the host cell to create new viruses. Fig. 1 illustrates a schematic of the enterovirus lifecycle.

(1) Attachment: The enterovirus life cycle is initiated by the binding of the virus to its host cell receptor. Depending on the serotype of the virus and the host cell type, a plethora of enterovirus receptors have been identified (Vuorinen *et al.* 1999). These receptors facilitate cell attachment and entry, and some of them also contribute to the virus uncoating step by inducing conformational changes in the capsid (Yamauchi and Greber 2016). Most enterovirus receptors are proteins and belong to the immunoglobulin-like or integrin receptor family. For example, cluster of differentiation 155 (CD155) protein, also known as poliovirus receptor (PVR), is used by poliovirus. Coxsackie adenovirus receptor (CAR), is used for the entry and uncoating of coxsackie B group viruses (Laajala and Marjomäki 2019).

(2) Endocytosis: Following receptor binding, the virus is engulfed inside vesicles and enters the cell via receptor-mediated endocytosis (Wells and Coyne 2019). The widely known endocytic mechanisms recognized

for picornaviruses involve clathrin-(CME-) and caveolin-1 (CAV1)-mediated pathways (Marjomäki *et al.* 2002, Kim and Bergelson 2012). However, some studies have explored endocytic mechanisms that operate independently of CME and CAV1 (Brandenburg *et al.* 2007, Khan *et al.* 2010).

(3) Uncoating: Receptor binding, heat, acidic pH, ion concentrations inside the endosome, or exposure to albumin are some of the cues for the virus to uncoat and release its genome into the cytoplasm (Ruokolainen *et al.* 2019). The externalized N-terminus of VP1 in conjugation with myristoyl-VP4 facilitate pore formation in the endosomal membrane through which the RNA genome can be released into the cytoplasm (Tuthill *et al.* 2006, Brandenburg *et al.* 2007).

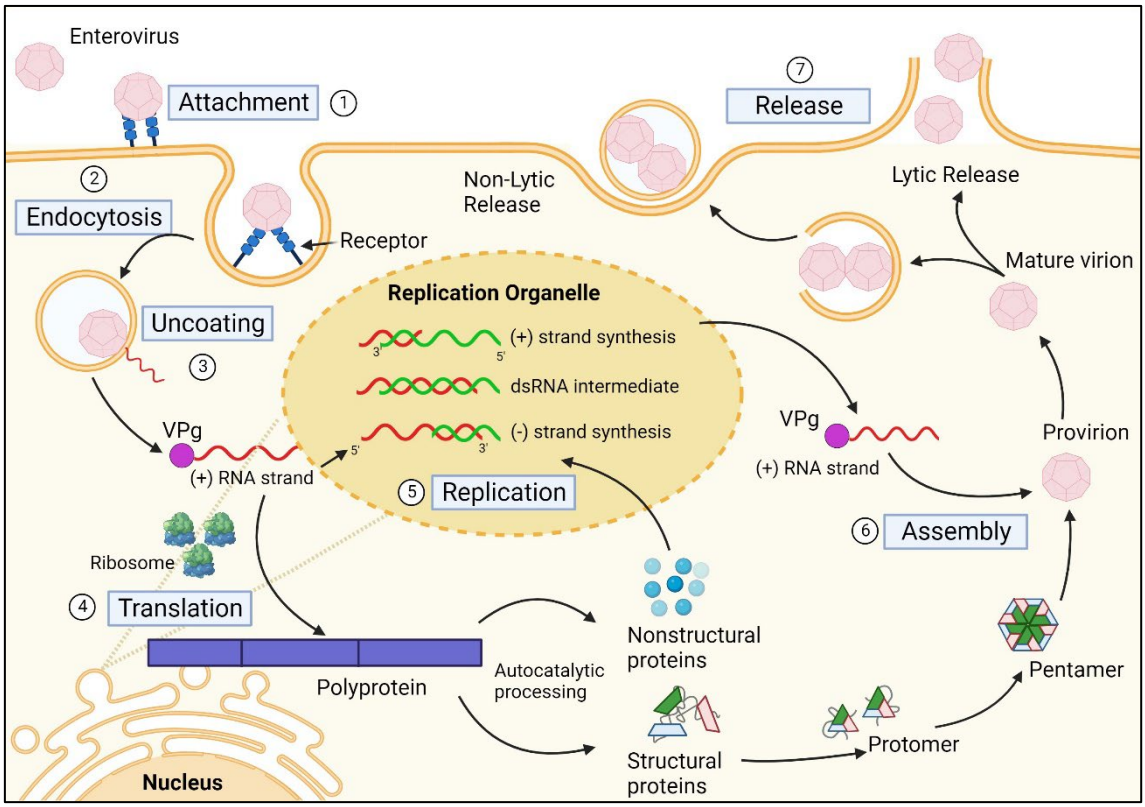

FIGURE 1 Enterovirus lifecycle. The image is adapted and modified from Baggen et al. 2018. The main stages of viral infection can be summarised in 7 steps, which include: 1. Attachment of the virus to its host cell receptor. 2. Internalisation of the virus through endocytosis. 3. Viral uncoating inside the endosome and release of the RNA genome through the endosomal membrane into the cytoplasm. 4. Translation of the (+) ssRNA using the host ribosome into a single long polyprotein. Proteolytic processing of the polyprotein generates some viral structural and non-structural proteins. 5. Replication of the (+) ssRNA inside replication organelles (RO). 6. Packaging the structural proteins and the newly synthesised (+) ssRNA to form provirions. Additional RNA-regulated processing of the structural proteins matures the provirion into a fully infectious virion. 7. Finally, the fully matured virions exit through lytic or non-lytic release from the cell. This image was created using BioRender.com.

(4) Translation: The (+) ssRNA viral genome is translated into one continuous long polyprotein in the cytoplasm. The polyprotein is cleaved by three viral proteinases, namely $2A^{pro}$, $3C^{pro}$, and $3CD^{pro}$, into three precursor proteins, P1, P2 and P3, which are further processed into smaller polypeptides. P1 encodes for the structural proteins, while P2 and P3 encode the non-structural proteins that participate in the viral RNA translation and replication and also interfere with some cellular processes to optimize viral replication (Teterina *et al.* 2011, Baggen *et al.* 2018). P1 is cleaved into viral capsid proteins VP1, VP3, and VP0. Despite the proteolytic cleavage, VP1, VP3, and VP0 do not physically separate from each other; rather stay together as a protomer unit (Fernandez-Tomas and Baltimore 1973, Palmenberg 1982).

(5) Replication: RNA replication occurs inside replication organelles (ROs) that are generated by the remodeling of host cell membranes (mostly endoplasmic reticulum or Golgi membranes) by the viral non-structural proteins such as 3A and 2BC (Dales *et al.* 1965, van der Schaar *et al.* 2016). The RNA-dependent RNA polymerase ($3D^{pol}$) initiates replication inside these ROs, generating a complementary negative strand (Yin-Murphy and Almond 1996). The negative strand serves as a template for synthesizing more positive strands (Novak and Kirkegaard 1991). The newly synthesized positive strands can have multiple fates; these can (a) act as a template for more genome replication, (b) be used for translating polyproteins, or (c) combine with the structural proteins to assemble into a progeny virion (Chase and Semler 2012).

(6) Assembly: The assembly of the virus takes place in the cytoplasm, where protomers collate into pentamers, and 12 pentamers assemble around the newly synthesized (+) ssRNA to form a provirion (Fernandez-Tomas and Baltimore 1973). The packaging of the RNA inside the "provirion" occurs by a mechanism that is not well understood. The packed RNA is thought to trigger an autocatalytic cleavage, splitting VP0 into VP2 and VP4, resulting in mature virions (Basavappa *et al.* 1994). Sometimes, the capsids can assemble without the genome, which results in a dead end for particle assembly (Verlinden *et al.* 2000).

(7) Release: Traditionally, it has been believed that the enteroviruses egressed through the lytic pathway only; however, recent evidence shows that some enteroviruses like the Hepatitis A virus (HAV) can also egress through a non-lytic pathway using exosomes during early infection. They primarily do this to evade the immune system and infect neighboring cells by inducing autophagy (Lai *et al.* 2016).

2.2 Coronaviruses

2.2.1 Overview and health implications

According to the most recent classification by the International Committee on Taxonomy of Viruses (ICTV), coronaviruses fall under the family *Coronaviridae* and subfamily *Orthocoronavirinae* (Woo *et al.* 2023). The subfamily is further divided into four genera: *Alpha-*, *Beta-*, *Gamma-*, and *Delta Coronavirus*. While *Alpha Coronaviruses* and *Beta Coronaviruses* primarily infect mammalian species, *Gamma* and *Delta Coronaviruses* have a broader host range that includes avian species too (V'kovski *et al.* 2021). Amongst the *Alpha* and *Beta Coronaviruses*, seven coronaviruses are associated with human diseases: HCoV-NL63, HCoV-229E, MERS-CoV, HCoV-HKU1, SARS-CoV, HCoV-OC43, and the latest SARS-CoV-2 (Liu *et al.* 2021). HCoV-NL63 and HCoV-229E belong to *Alpha Coronaviruses*, while the remaining five belong to the *Beta Coronaviruses*.

Coronaviruses transmit mainly through direct contact or respiratory aerosols, but recently their transmission through faecal-oral route and from contaminated surfaces was also highlighted (Guo *et al.* 2021). When surfaces get contaminated by bodily secretions of infected people, they are known as fomites (Geng and Wang 2023). Among coronaviruses, HCoV-HKU1, HCoV-OC43, HCoV-NL63, and HCoV-229E are well-documented to circulate in the population and tend to resurge seasonally, with the highest prevalence during the winter months (Aldridge *et al.* 2020). These viruses typically cause mild upper respiratory tract symptoms that resolve on their own (Liu *et al.* 2021). However, in some cases, they can lead to severe complications, particularly in vulnerable groups such as infants, individuals with underlying health conditions, or those with compromised immune systems, affecting the lower respiratory tract and central nervous system (Dominguez *et al.* 2009, Zhang *et al.* 2018, Almqvist *et al.* 2020).

On the other hand, the three other coronaviruses that have emerged over the past two decades, namely SARS-CoV, MERS, and SARS-CoV-2, are highly pathogenic and have been associated with severe outbreaks, including epidemics and a pandemic. Patients infected with these coronaviruses typically exhibit symptoms resembling the flu, but some cases reported severe illness like pneumonia, acute respiratory distress syndrome (ARDS), liver damage, acute renal failure, gastroenteritis, cardiac failure to name a few (Gulati *et al.* 2020).

2.2.2 Structure and genome

Human coronaviruses are quasi-spherical to pleomorphic, with an average diameter of 80-120 nm (Prasad *et al*. 2020). They possess a positive-sense, single-stranded RNA genome ranging from 27 to 32 kb, which is one of the largest genomes among RNA viruses (Denison *et al*. 2011). The first two-thirds of the genome has two open reading frames (ORFs), a and b (ORF1a and ORF1b), which encode 16 non-structural proteins (nsps) required for viral replication, and the

remaining third of the genome encodes the structural proteins. The RNA is bound to multiple copies of the nucleocapsid (N) protein in a beads-on-a-string arrangement to form a helical ribonucleoprotein (RNP) within the lipid envelope (Fields 2013). The envelope of coronaviruses house three proteins that include the membrane protein (M), the envelope protein (E), and the spike protein (S), and in certain beta coronaviruses such as HCoV-OC43 and HCoV-HKU1, a haemagglutinin-esterase (HE) glycoprotein is also present (Woo *et al*. 2023).

The S protein is a type I transmembrane fusion protein primarily responsible for recognizing and binding to host-cell receptors and facilitating membrane fusion during viral infection. The S protein assembles into homotrimers, creating bulb-like structures protruding from the lipid envelope called spikes or peplomers, which gives the virus its name (Masters 2006). During assembly, the S protein of the spike is synthesized as a single polypeptide chain, which is then cleaved by host furin-like proteases into an amino (N)-terminal S1 subunit and a carboxyl (C)-terminal S2 subunit, which remains non-covalently associated (Jackson *et al.* 2022). The S1 subunit harbors the receptor-binding domain (RBD) responsible for engaging with the host cell receptor. The RBD of the S1 subunit undergoes hinge-like conformational changes, alternately hiding or exposing the determinants of the binding site. The "down" conformation represents the receptor-inaccessible state, while the "up" conformation signifies the receptor-accessible state, which is a highly unstable state (Wrapp *et al.* 2020).

The S2 subunit anchors the S protein to the viral membrane. Within the S2 subunit, the fusion peptide and heptad repeats are crucial in mediating membrane fusion between the viral and cellular membranes (Song *et al.* 2023). The M and E proteins are involved in virus assembly (Fields 2013). Additionally, the HE protein has also been identified to support the S protein's activity in receptor binding and the egress of newly synthesized progeny virions (Vlasak *et al.* 1988, Liu *et al.* 2021).

2.2.3 Lifecycle

The coronavirus life cycle includes several key stages, such as host receptor binding, cell entry, virion uncoating, protein translation, RNA replication and transcription, virion assembly, and the release of mature virions outside the cell. Although the various coronaviruses that infect humans follow a similar life cycle, differences can be observed in their entry routes and the production of specific structural and accessory proteins (V'kovski *et al.* 2021). Fig. 2 illustrates the lifecycle of the coronavirus.

(1) Virus attachment: The coronavirus life cycle starts with the engagement of the virus spike protein with the host cell receptors. Scientists have identified several molecules that serve as primary receptors for virus attachment. For instance, HCoV-OC43 uses 9-acetyl-9-O-acetyl neuraminic acid, HCoV-HKU1 uses O-acetylated sialic acid, HCoV-229E uses amino peptidase N, and HCoV-NL63, SARS-CoV and SARS-CoV-2 have a common receptor, which is the angiotensin-converting enzyme 2 (ACE2) (Vlasak *et al.* 1988, Yeager *et*

al. 1992, Li *et al.* 2003, Raj *et al.* 2013, Hulswit *et al.* 2019, Hoffmann *et al.* 2020). In addition to these primary receptors, other molecules such as neuropilin 1 (NRP1), phosphatidylserine receptors, heparan sulphate, and extracellular vimentin are also involved in the attachment process (Clausen *et al.* 2020, Cantuti-Castelvetri *et al.* 2020, Wang *et al.* 2020, Suprewicz *et al.* 2021, Bohan *et al.* 2021).

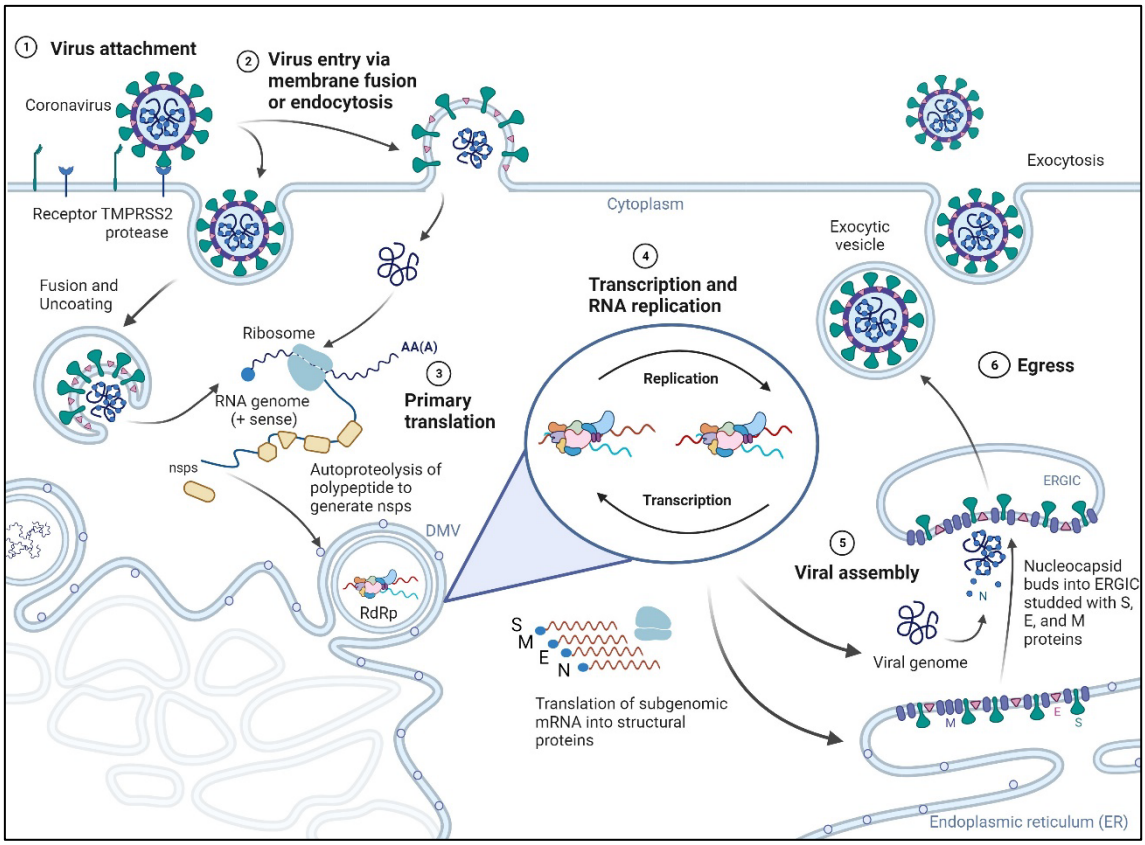

FIGURE 2 Coronavirus life cycle. This image was adapted and modified from a review by V'kovski *et al.* 2021. The general lifecycle of coronaviruses can be classified into primarily six steps. 1. The first step is the engagement of the virus to its host receptor. 2. The second step is the entry; SARS-CoV-2 uses either endocytosis or membrane fusion and HCoV-OC43 uses mainly caveolin-mediated endocytosis. 3. The host cell ribosomes in the cytoplasm translate the viral genome into non-structural proteins (nsps). The nsps serve to build the replication-transcription complex inside double-membrane vesicles (DMVs) derived from the ER. 4. The RNA replication and transcription of subgenomic mRNAs occur simultaneously inside the DMVs. 5. Newly synthesized viral RNA bound to N-protein is condensed and encapsulated within the ERGIG membrane, expressing the viral structural proteins to assemble into mature virions. 6. Virions egress from the host cell through exocytosis. This image was created using BioRender.com.

(2) Virus entry: After the binding of the S-protein to the ACE2 receptor, the internal S2' site within the S2 subunit is exposed in the case of SARS-CoV-2 (Jackson *et al.* 2022). The virus can enter the host cell at this stage through endocytosis or plasma membrane fusion (Simmons *et al.* 2005, Inoue *et al.* 2007). Plasma membrane fusion is contingent

upon the presence of the transmembrane serine protease 2 (TMPRSS2) on the cell surface (Simmons *et al.* 2005, Shulla *et al.* 2011). TMPRSS2 cleaves at the S2′ site, inducing conformational changes in S2, dissociation of S1, and the insertion of the fusion peptide into the host cell membrane (Thunders and Delahunt, 2020). Alternatively, in cases where cell surface proteases are absent or insufficient, most coronaviruses have demonstrated the ability to internalize into cells via receptor-mediated endocytosis involving clathrin-dependent, caveolae-dependent, or clathrin- and caveolae-independent pathways (Nomura *et al.* 2004, Inoue *et al.* 2007, Wang *et al.* 2008, Milewska *et al.* 2018, Owczarek *et al.* 2018). Once virions are internalized into endosomes, the acidic pH activates the cysteine protease cathepsin L (CatL), leading to the cleavage of the spike protein within the S2 subunit. This is followed by the insertion of the fusion peptide into the endosomal membrane (Bosch *et al.* 2008). Once the fusion peptide is inserted into the (plasma/endosomal) membrane, conformational changes in the S2 subunit push the S protein into a more stable post-fusion conformation (Walls *et al.* 2017). The α-helical heptad repeats (HR1 and HR2) in the S2 subunit fold back, forming a six-helix bundle, which pulls both membranes together, facilitating fusion and creating a fusion pore for the release of the viral RNA to the cytoplasm (White and Whittaker 2016, Jackson *et al.* 2022).

(3) Primary translation: The coronavirus RNA encodes both structural and non-structural proteins. Once the viral RNA is released into the cytoplasm, host ribosomes translate the viral RNA genes ORF1a and ORF1b, forming two polyproteins, pp1a and pp1ab, respectively (V'kovski *et al.* 2021). These polyproteins undergo cleavage by viral proteases, including the Papain-like protease (PLpro, Nsp3) and the 3C-like protease or chymotrypsin-like protease (3CLpro or Mpro, Nsp5) (Thiel *et al.* 2003). This cleavage results in the generation of sixteen nsps that are required for the viral replication and along with other host factors collectively form the viral replication and transcription complex (RTC) (Pizzato *et al.* 2022). Some notable functions of the nsps include: nsp1 shuts down the host cell translation machinery (Kamitani *et al.* 2006). Nsp 12 is the RNA-dependent RNA polymerase (RdRP) whose role is to synthesize viral RNA, and nsp7 and nsp8 act as cofactors for polymerase activity (Snijder *et al.* 2016). Nsp 13 has helicase activity. Nsp14 possesses a 3′–5′ exonuclease activity, functioning as a proofreading mechanism to correct errors that may occur during the replication of the viral RNA genome (Eckerle *et al.* 2007). Thus, coronaviruses are less mutation-prone than most RNA viruses, although they are still more prone to mutation than most DNA viruses.

(4) Replication and Transcription: To protect viral replication products from the host defense system, nsps generated during primary translation remodel host cell membranes, forming a specialized

replication organelle (RO) (Hagemeijer *et al.* 2014). SARS-CoV-2 has been exhibited to induce the formation of ROs called double-membrane vesicles (DMVs) on the host cell endoplasmic reticulum (ER) membrane (Cortese *et al.* 2020). Within these DMVs, viral RNA replication and transcription of subgenomic mRNAs (sgRNA) occur. Inside the DMVs, the RdRp (nsp12) initiates the synthesis of a full-length negative-sense RNA copy of the viral mRNA (Snijder *et al.* 2016). This negative-sense RNA then serves as a template for generating positive-sense genomic RNA. The newly synthesized genomes can have multiple fates. They can be utilized either for the translation of additional viral nsps or directed for packaging into new virions (V'kovski *et al.* 2021). Concurrently, within the DMVs, the negative strand can undergo discontinuous transcription to form sgRNA that encodes for viral structural and accessory proteins. Nsp3 has been demonstrated to create pores facilitating the import of metabolites essential for replication and transcription. Additionally, these pores serve as exit points for the viral RNA from which viral RNA leaves the DMVs for virion assembly (Wolff *et al.* 2020). The host ribosomes in the ER translate the sgRNAs into viral structural proteins such as S, E, M, and HE, while free ribosomes translate the N protein.

(5) Virus assembly: These structural proteins are then expressed on the ER-Golgi intermediate compartment (ERGIG) (Stertz *et al.* 2007). An exception is made for the N protein, which is directed to the cytoplasm to package viral genomic RNA into a helical structure, forming the ribonucleoprotein complex (Lu *et al.* 2021). Among all structural proteins, the M protein plays a pivotal role in orchestrating virion assembly (Neuman *et al.* 2011). Interactions amongst the M proteins form the fundamental framework of the viral envelope. Together with the E protein, M proteins induce membrane curving and budding. Alongside the N protein and viral genome, they encapsulate the ribonucleoprotein complex, completing the formation of the virion (Lu *et al.* 2021).

(6) Egress: The virus buds off from the lumen of the ERGIC compartment and is secreted from the infected cell by exocytosis in two ways: by using vesicles of the biosynthetic secretory pathway or through the incorporation in deacidified lysosomes that fuse with the plasma membrane and release the virions into the extracellular space (Ghosh *et al.* 2020, Liu *et al.* 2021). The structural protein HE in HCoV-OC43 has been identified to have acetyl esterase activity, which aids in releasing viral progeny from infected cells (Vlasak *et al.* 1988).

2.3 Virus transmission and persistence

When individuals infected with a virus release bodily secretions into the immediate environment, some of the smaller virus-laden aerosols remain suspended in the air, while the heavier droplets settle on surfaces and objects (Morawska and Cao 2020, Leung 2021). Transmission that occurs by directly inhaling these aerosols is called as airborne transmission, while viruses that spread through contaminated surfaces are associated with fomite transmission (Castaño *et al.* 2021). Although viruses cannot replicate outside their host cells, they can remain infectious on surfaces for varying durations (Kramer *et al.* 2006, Taylor 2014). Understanding how long viruses persist on surfaces and their potential for transmission via fomites is crucial when devising strategies to prevent the indirect spread of viruses. The persistence of viruses on surfaces and their potential for transmission via fomites relies on many factors, including the virus itself, fomite properties, and extrinsic environmental factors such as temperature or relative humidity (RH). These factors will be discussed in detail in the following chapters.

Researching pathogenic viruses is always accompanied by a risk to human health. Therefore, surrogate viruses are commonly used as models for such studies (Schirtzinger *et al.* 2022). Previous studies related to SARS-CoV-2 have utilized surrogate viruses, such as HCoV-HKU1, HCoV-OC43, and porcine respiratory coronavirus (PCRV), as well as murine hepatitis virus (MHV), transmissible gastroenteritis virus (TGEV), and bacteriophage Φ6 (Owen *et al.* 2021). For our research, we have chosen HCoV-OC43 as a study model as it belongs to the same genus as SARS-CoV-2 and shares a maximum genetic similarity of 68.93% (Lu *et al.* 2020, Kaur *et al.* 2021). Also, the American Society for Testing and Materials (ASTM) has identified HCoV-OC43 as a preferred surrogate for SARS-CoV-2 due to their shared characteristics (Schirtzinger *et al.* 2022).

2.4 Factors affecting virus persistence

2.4.1 Environmental factors: temperature and relative humidity

Recent studies have shown that temperature and relative humidity (RH) are important environmental factors affecting virus persistence (Kumar *et al.* 2021). In particular, their impact on aerosolized viruses has been well explored, but their influence on larger droplets settling on surfaces remains limited (Wang *et al.* 2021). Researchers have employed two primary methods to investigate the persistence of virus in these larger droplets on surfaces. The first involves applying a virus droplet to a surface and incubating it under selected conditions (Riddell *et al.* 2020), while the second allows natural drying of the virus droplet on the surface before subjecting it to specific conditions (Casanova *et al.* 2010a,

Chan *et al.* 2011, Biryukov *et al.* 2020). It's important to understand how viruses behave in desiccated conditions, as surfaces may not always remain wet or moist, and desiccation can significantly impact virus survival (Abad *et al.* 2001). Table 1 summarizes studies on coronavirus persistence under varying temperature and humidity conditions, indicating whether viruses were dried on surfaces or in suspension before incubation.

TABLE 1 The effect of temperature and humidity on coronavirus persistence

Surface(s)	virus(es)	method	Temp (°C)	RH (%)	observed effect	Reference
Stainless steel, paper note, polymer note, cotton, glass, vinyl	SARS-CoV-2	virus in ASTM E2197 dried on the surface 1h before testing	20, 30, 40	50	decrease in persistence with increase in temp	Riddell *et al.* 2020
Stainless steel, ABS plastic, nitrile glove	SARS-CoV-2	virus in simu-lated saliva	24, 28, 35	20, 40, 60 80	decrease in persistence with increase in temp and RH	Biryukov *et al.* 2020
Plastic	SARS CoV-2	virus dried on the surface before testing	28, 33 38	80~89, >95	decrease in persistence with increase in temp and RH	Chan *et al.* 2011
Stainless steel	TGEV MHV	virus dried on the surface before testing	4, 20, 40	20, 50, 80	decrease in persistence with increase in temp RH: U shaped relation	Casanova *et al.* 2010

SARS-CoV-2-severe acute respiratory syndrome coronavirus 2, TGEV-transmissible gastroenteritis coronavirus, MHV-murine hepatitis virus

Table 1 reveals distinct trends in how environmental conditions affect the persistence of coronaviruses on various surfaces. Regarding temperature, the studies indicate that higher temperatures tend to inactivate the viruses faster than lower temperatures (Casanova *et al.* 2010, Chan *et al.* 2011, Biryukov *et al.* 2020, Riddell *et al.* 2020). In contrast, the impact of RH on virus persistence lacks a unanimous consensus. Chan *et al.* and Biryulov *et al.* reported a linear decrease in virus persistence with increasing RH levels, whereas Casanova *et al.* proposed a U-shaped model (Casanova *et al.* 2010, Chan *et al.* 2011, Biryukov *et al.* 2020). According to the U-shaped model, the virus persists longer at extreme humidities than at moderate levels. This variability in findings suggests that the relationship between RH and virus persistence is complex and needs more detailed investigation. Non-enveloped viruses have not received as much research focus

regarding the influence of environmental conditions on their survival on various surfaces. Table 2 summarizes studies that have explored the persistence of different non-enveloped viruses under different temperature and humidity conditions.

TABLE 2 The effect of temperature and humidity on non-enveloped virus persistence

Surface (s)	virus(es)	method	Temp (°C)	RH (%)	observed effect	Reference
stainless steel disk	HAV & PV-1 in faecal suspe-nsion	virus droplet added on the surface and kept for incubation	5, 20 35	25, 55 80, 95	HAV: decrease in persistence with increase in temp and RH PV-1: persistence increases at high RH	Mbithi *et al.* 1991
glass, stainless steel, smooth & rough plastic, cloth, postcard, currency note, 4 types of paper	HRV in faecal suspe-nsion	virus dried on the surface before testing	4, 22	25, 50, 85	decrease in persistence with increase in temp and RH	Sattar *et al.* 1986
lacquer coated rubber tree wood, stainless steel	NoV, HAV	virus droplet added on the surface and kept for incubation	15, 25 32, 40	30, 50, 70	NoV & HAV: decrease in persistence with increase in temp NoV: higher persistence at higher RH HAV: higher persistence at medium RH	Kim *et al.* 2012

HAV-hepatitis A virus, PV-1- poliovirus 1, HRV-human rhinovirus, NoV-norovirus

All the studies summarized in Table 2 consistently indicate that higher temperatures reduce the persistence of non-enveloped viruses, aligning with the trends observed in previous studies on coronaviruses (Sattar *et al.* 1986, Mbithi *et al.* 1991, Casanova *et al.* 2010, Chan *et al.* 2011, Kim *et al.* 2012, Biryukov *et al.* 2020, Riddell *et al.* 2020). However, the influence of RH on non-enveloped viruses exhibits a more diverse pattern. For instance, norovirus (NoV) and poliovirus (PV) exhibit enhanced persistence at higher humidity levels, whereas human

rhinovirus (HRV) shows the same at lower humidity. Results concerning hepatitis A virus (HAV) were more varied, with Mbithi et al. (1991) observing that lower humidity favored HAV survival on stainless steel surfaces, while Kim et al. (2012) showed that HAV survived best at moderate humidity on the same surface (Mbithi *et al.* 1991, Kim *et al.* 2012).

It is worth noting that studies have shown that virus persistence on surfaces, regardless of whether they are enveloped or non-enveloped, generally decreases with higher temperatures (Sattar *et al.* 1986, Mbithi *et al.* 1991, Casanova *et al.* 2010, Chan *et al.* 2011, Kim *et al.* 2012, Biryukov *et al.* 2020, Riddell *et al.* 2020). However, when it comes to RH, no consistent patterns were identified. Additionally, virus persistence is a complex process that can be influenced by a variety of factors at the same time, such as virus concentration, surface composition, the presence of organic materials, and the type of solution in which the virus is suspended (e.g., saliva, serum buffer) (Oswin *et al.* 2022). It is essential to recognize that all these factors collectively exert a significant influence on the overall duration that a virus remains viable on a surface, rather than any single factor in isolation. Therefore, future studies should aim to replicate real-world conditions more closely to provide a more comprehensive perspective on virus persistence and transmission.

2.4.2 Persistence of enveloped versus non-enveloped viruses

The stability of viruses is influenced by several factors, with one of the key factors being the presence or absence of an envelope. According to a review by Kramer et al. (2006), non-enveloped viruses are generally more stable than their enveloped counterparts (Kramer *et al.* 2006). The lipid membrane in enveloped viruses is fragile and makes them more vulnerable to inactivation compared to non-enveloped viruses, which have a strong protein capsid (van Engelenburg *et al.* 2002, Watts *et al.* 2021). Further supporting this distinction, a study by Firquet et al. (2015) investigating the stability of various viruses on plastic surfaces found that enveloped viruses such as influenza A (H1N1) and herpes simplex virus type 1 (HSV-1) retained infectivity for less than 5 days, while non-enveloped viruses like minute virus of mice (MVM) and coxsackievirus B4 (CVB4) persisted for 5 weeks (Firquet *et al.* 2015). The fragility of the lipid membrane even made them vulnerable to destruction by disinfectants. For example, Lin and colleagues showed that numerous alcohol-based disinfecting agents and surfactants could inactivate enveloped viruses more easily than non-enveloped viruses (Lin *et al.* 2020). Enveloped viruses can also be easily inactivated with lower UV-C radiation doses, while non-enveloped viruses exhibit partial inactivation even with higher doses (Blázquez *et al.* 2019). In summary, these studies suggest that non-enveloped viruses are generally more stable and are comparatively more difficult to inactivate.

2.4.3 Surface composition

Surface composition is another well-documented factor influencing virus persistence on surfaces. (Hall *et al.* 1980, Tiwari *et al.* 2006, Watanabe *et al.* 2022). Surfaces can be classified as either porous or non-porous based on their ability to absorb liquids (Chatterjee *et al.* 2021). Porous surfaces can be attributed to small holes, pits, crevices, or interconnected spaces inside a material. Examples of commonly used porous surfaces include paper, cardboard, and cotton textiles. Examples of non-porous surface include plastic, stainless steel, glass, copper, latex gloves, and surgical gloves. Table 3 is a compilation of studies that assessed the persistence of coronaviruses on different porous and non-porous surfaces.

TABLE 3 Persistence of coronaviruses on porous and non-porous surfaces

Surface	Virus	Persistence	Reference
Non-Porous			
Plastic	SARS-CoV-2	3 days	van Doremalen *et al.* 2020
	SARS-CoV-2	4 days	Chin *et al.* 2020
	SARS-CoV-1	28 days	Chan *et al.* 2011
	SARS-CoV-1	4 days	Duan *et al.* 2003
	SARS-CoV-1	6 days	Rabenau *et al.* 2005
	SARS-CoV-1	3 days	van Doremalen *et al.* 2020
	HCoV-229E	2 days	Rabenau *et al.* 2005
	MERS	1 day	van Doremalen *et al.* 2013
Glass	SARS-CoV-2	2 days	Chin *et al.* 2020
stainless steel	SARS-CoV-2	3 days	van Doremalen *et al.* 2020
copper	SARS-CoV-2	4 h	van Doremalen *et al.* 2020
surgical gloves	HCoV-OC43	<1 h	Sizun *et al.* 2000
	TGV	4 h	Casanova et al. 2010
Porous			
Surgical mask	SARS-CoV-2	7 days	Chin *et al.* 2020
paper	SARS-CoV-2	30 min	Chin *et al.* 2020
Cardboard	SARS-CoV-2	1 day	van Doremalen *et al.* 2020
Wood	SARS-CoV-2	1 day	Chin *et al.* 2020
Cloth	SARS-CoV-2	1 day	Chin *et al.* 2020

SARS-CoV-2/-1-severe acute respiratory syndrome coronavirus 2/1, HCoV-229E–human coronavirus 229E, MERS-Middle East respiratory syndrome, HCoV-OC43-human coronavirus OC43, TGV-transmissible gastroenteritis virus

These studies highlight the fact that different surfaces vary in their capacity to retain and transmit coronaviruses (Sizun *et al.* 2000, Duan *et al.* 2003, Rabenau *et al.* 2005, Casanova *et al.* 2010, Chan *et al.* 2011, van Doremalen *et al.* 2020, Chin *et al.* 2020). Generally, non-porous surfaces exhibited extended persistence of coronaviruses, often exceeding 24 h, except for copper and surgical gloves. Copper, known for its antimicrobial properties (Grass *et al.* 2011), demonstrated a 4-log reduction in Influenza A (H1N1) virus titer after 6 h of contact (Noyce *et al.* 2007). In contrast, porous surfaces led to quicker virus inactivation, typically

within 24 h or less. The absorption of the virus into the material, coupled with rapid evaporation and drying of the liquid containing the virus on porous surfaces, contributed to their faster inactivation (Owen *et al.* 2021). Fewer studies have investigated the persistence of non-enveloped viruses on various surfaces compared to enveloped viruses, and some examples are provided in Table 4.

TABLE 4 Persistence of non-enveloped viruses on porous and non-porous surfaces

Surface	Virus	Persistence	Reference
Non-Porous			
plastic	CVB4	6 weeks	(Firquet *et al.* 2015)
	MVM	>6 weeks	
	CVA16	3 h	(Sittikul *et al.* 2023)
	EV-A71	4 h	
	HRV	>10 days	(Sattar *et al.* 1986)
stainless steel	CVA16	6 h	(Sittikul *et al.* 2023)
	EV-A71	3 h	
	HRV	>10 days	(Sattar *et al.* 1986)
toilet china	human AsV-4	7 days	(Abad *et al.* 2001)
glass	HRV	>10 days	(Sattar *et al.* 1986)
Porous			
cellulose paper	human AsV-4	60 days at RT	(Abad *et al.* 2001)
wood	CVA16	6 h	(Sittikul *et al.* 2023)
	EV-A71	>7 h	
postcard	HRV	<3 h	(Sattar *et al.* 1986)
cloth	HRV	2 days	

CVB4-coxsackievirus B4, MVM-minute virus of mouse, CVA16-coxsackievirus A16, EV-A71–enterovirus A71, AsV-Astrovirus, HRV- human rotavirus

From the data presented in Table 4, there is no clear trends emerging from the persistence of non-enveloped viruses on porous and non-porous surfaces. HRV seems to follow a patter similar to that reported earlier for enveloped viruses where it persists for over 10 days on non-porous surfaces such as plastic and stainless steel but only 2 days on porous cloth (Sattar *et al.* 1986). Consistent with the resilience commonly associated with non-enveloped viruses, MVM and CVB4 exhibited prolonged persistence on non-porous plastic for at least 6 weeks (Firquet *et al.* 2015). However, CVA16, EV-A71, and human AsV-4 demonstrated more variable responses compared to other non-enveloped viruses (Abad *et al.* 2001, Sittikul *et al.* 2023). It is difficult to corelate the finding between all these studies due to several reasons such as differences in the specific type of non-enveloped virus, variations in type of material (especially in the case of plastic, polymer type was not specified), diverse environmental conditions, and differences in testing methodologies among studies. These challenges of data comparison highlight the need for researchers to adopt more standardized testing conditions to enhance the comparability of data across studies.

2.5 Antiviral solutions

Managing viral diseases presents considerable challenges, mainly because of limited availability of vaccines and antivirals approved for treating them. Developing vaccines for all known viruses is not economically feasible and the constant mutation in viruses leads to the emergence of new variants that may render existing vaccines ineffective (Hayawi *et al.* 2021). As of today, there are no approved antivirals for enteroviruses. In the case of coronaviruses, a handful of drugs received emergency use authorization during the pandemic (Malin *et al.* 2020). It is worth noting that a typical timeline for a drug to transition from laboratory development to reaching the consumer market spans approximately 10 to 12 years (Cassidy *et al.* 2020). This just shows how time-consuming and challenging antiviral drug discovery could be. Given these challenges, implementing community-level strategies would be key in enhancing the overall management of viral diseases and preparation for future viral outbreaks.

2.5.1 Existing strategies

At the community level, there are several key strategies for managing viral diseases, including the use of face masks, hand sanitization, surface disinfection, isolation, travel restrictions, and vaccination (WHO 2020). Among these strategies, surface disinfection plays a vital role in preventing transmission through fomites. Traditional disinfection methods include chemical agents, heat, and UV radiation (Choi *et al.* 2021). However, traditional disinfection methods do have limitations, such as the need for repeated applications, potential health and environmental risks associated with prolonged use of chemical disinfectants, and adverse effects of UV exposure (Rai *et al.* 2020, Mahmood *et al.* 2020). Therefore, innovative solutions to complement the existing strategies are always needed. One such solution is the implementation of antiviral surfaces that can reduce the persistence of viruses on fomites. These surfaces can be particularly useful in high-risk environments, such as healthcare facilities and enclosed public spaces. Nature provides inspiring examples of unique antimicrobial surfaces, such as lotus leaves and frog skin, which can serve as role model for building such surfaces artificially (Conlon *et al.* 2007, Li and Xu 2008).

Previous research has primarily focused on developing surfaces that can inactivate bacteria. In a recent review by Mahanta and colleagues, they explored various strategies, including physical and chemical modifications, to develop antimicrobial surfaces that can inhibit microbial adhesion, growth, and proliferation (Mahanta *et al.* 2021). Physical modifications involve changing the roughness of the surface, which can either prevent microbes from coming into contact with it due to steric hindrance or destroy the microbe by penetrating it with the surface feature. For instance, Hasan and colleagues designed a nanopatterned aluminum alloy surface, which was successful in eliminating both gram-positive and gram-negative bacteria within 3 h of contact and significantly reducing rhinovirus titers after 24 h (Hasan *et al.* 2020). Chemical modification

involve coating or integrating biocidal compounds into surfaces (Borkow and Gabbay 2004). Biocidal compounds commonly used include N-halamine (Chen and Sun 2006), quaternary ammonium compounds (QACs) (Tuladhar *et al.* 2012), chitosan (Ciejka *et al.* 2017), halogenated phenols (Dhiman and Chakraborty 2015), L-cysteine (Caldeira *et al.* 2013), and metals such as silver and copper (Borkow and Gabbay 2004, Bajpai 2013).

Surfaces that have been incorporated with biocidal compounds can either be classified as leaching or non-leaching, depending on how they interact with the pathogen (Bruenke *et al.* 2016). In the leaching method, the biocidal compound is embedded inside the surface and slowly releases out into the environment. For example, Delgado and colleagues created an antibacterial surface by incorporating copper metal and copper oxide nanoparticles into a polypropylene matrix (Delgado *et al.* 2011). The surface released copper ions (Cu^{2+}) upon exposure to oxygen and water, killing *Escherichia coli* bacteria. Non-leaching surfaces, on the other hand, physically anchor biocidal compounds through strong covalent or ionic interactions and prevent their release. Haldar and coworkers demonstrated the antimicrobial effect of a non-leaching glass surface functionalized with N-dodecyl methyl-polyethyleneimines (PEIs), that effectively inactivated *E. coli*, *Staphylococcus aureus,* and influenza virus (H1N1) upon contact (Haldar *et al.* 2006).

While current antimicrobial strategies do show promise, they do come with their own set of limitations. For example, the scalability of nanopatterning for large commercial applications remains a challenge, and harsh weather conditions can lead to a degradation of nanopattern durability (Mahanta *et al.* 2021). Additionally, biocidal compounds that leach into the environment can pose risks not only to target organisms but also non-target ones and contribute to overall environmental toxicity. In light of these challenges, exploring alternative strategies which are nature-based could provide a more sustainable and safer means of mitigating the spread of infectious pathogens via surfaces.

2.5.2 Secondary metabolites as nature-based antiviral solutions

Plants possess a remarkable ability to produce a wide variety of structurally diverse chemical compounds that orchestrate different functions for them. Those that are required for the fundamental process such as growth and development are called as primary metabolites. In contrast, those that serve specialized functions of defense from predators and parasites, attracting pollinators and protect the plant from harsh environmental conditions, are called as secondary metabolites (Rodrigues *et al.* 2016, Nawrot-Chorabik *et al.* 2022). Plants can produce a diverse set of these compounds in response to different stressors, and this adaptability makes them interesting for different human applications. Even in the field of medicine, many modern-age drugs owe their existence to chemical compounds initially discovered in plants (Veeresham 2012). Notable examples include aspirin for pain relief, quinine for malaria treatment, and paclitaxel and camptothecin for cancer (Bourgaud *et al.* 2001). Interestingly, even traditional medicine practices in cultures such as Indian Ayurveda and Chinese medicine

have long recognized the healing properties of herbs and plants (Atanasov *et al.* 2021). For instance, the Ashwagandha (*Withania somnifera)* in Indian Ayurveda demonstrates a versatile range of applications from anti-cancer properties to aid in the management of memory loss associated with Alzheimer's disease, and reducing cortisol levels induced by stress (Bhattacharya *et al.* 1987, Sumantran *et al.* 2007, Pandey *et al.* 2018, Lopresti *et al.* 2019).

Plant secondary metabolites can be broadly categorized into three major groups of chemical compounds: alkaloids, phenolic compounds, and terpenes and each of these groups have a range of individual compounds (Ebenezer *et al.* 2019). Secondary metabolites can be obtained as plant extracts or isolated from these extracts as individual compounds. While numerous prior studies have illuminated the efficacy of both extracts and isolated secondary metabolites against bacteria, their potential in combating viruses has received comparatively little attention (Kumar and Pandey 2013). In one such study, for example, Silva and colleagues reported the antiviral activity of six plant extracts against Herpes simplex virus type 1 (HSV-1) and African swine fever virus (ASFV). However, one challenge in studying plant extracts lies in the absence of chemical characterization, hindering the identification of the specific bioactive compounds responsible for the antimicrobial activity. Once the structures of these bioactive compounds are elucidated, they can be further modified to enhance their bioactivity through *in silico* and synthetic chemistry approaches. Therefore, a comprehensive process should include the initial screening of plant extracts to assess their pharmacological activity, followed by fractionation and chemical characterization to isolate the bioactive compound (Atanasov *et al.* 2021). Alternatively, an *in silico* approach can be employed to screen natural product libraries for potential compounds, followed by in vitro testing (Romano and Tatonetti 2019).

Most researchers only report the antiviral efficacy of screened natural compounds but fail to elaborate on the mechanism of antiviral action. A study by Flechas and coworkers showed that β-Caryophyllene, a secondary metabolite found in essential oils from medicinal plants exhibited very good antiviral activity against four serotypes of dengue virus (Flechas *et al.* 2017). Investigating the antiviral mechanism of action provides insights into whether the bioactive compound has viral or cellular targets. This information proves invaluable in anticipating potential resistance that the virus may develop against the bioactive compound. Additionally, it is also useful in the context of designing antiviral materials (e.g., functionalization of surfaces to make them antiviral would only work if the target was viral and not cellular). Furthermore, understanding how the bioactive agent interacts enables researchers to refine and optimize the compound's design, potentially making it more effective and safer.

2.5.2.1 Polyphenols

Phenolic compounds constitute the most prominent family of plant secondary metabolites, encompassing over 8,000 structurally distinct variants across diverse plant species (Ćavar Zeljković *et al.* 2021). Polyphenols range from simple

structures with one or more aromatic rings to more complex polymeric structures with carboxyl or methoxy group modifications (Hussein *et al.* 2018). Based on the number of aromatic rings and the elements that anchor to the rings, polyphenols can broadly be classified into three groups: phenolic acids, flavonoids, and non-flavonoids (Singla *et al.* 2019). Fig. 3 shows a classification scheme for different polyphenol groups with representative examples. Polyphenols are naturally present in fruits, vegetables, coffee, tea, wine, dry fruits, and cacao (Singla *et al.* 2019). Numerous reports highlight their therapeutic potential. For instance, laboratory studies have demonstrated that polyphenols can lower blood glucose levels, LDL cholesterol, blood pressure, and platelet aggregation (Liu *et al.* 2010, Choi *et al.* 2015). They also can inhibit the growth of tumor cells, enhance HDL cholesterol, and improve overall brain function due to their antioxidant and anti-inflammatory properties (Yang *et al.* 1998, Zhuang *et al.* 2003, Grassi *et al.* 2016).

Apart from these health benefits, polyphenols have been recognized as potent compounds with antiviral activity (Chojnacka *et al.* 2021). For example, in a study by Ciesek and colleagues, Epigallocatechin gallate (EGCG) from green tea strongly reduced hepatitis C virus (HCV) infectivity by inhibiting virus attachment to a host cell (Ciesek *et al.* 2011). Another exciting aspect of polyphenols is that due to their structural diversity, they not only target various stages of viral infection but also impact host cell processes. For example, Mastromarino and colleagues showed that resveratrol was not only able to inhibit the production of human rhinovirus 16 (HRV16) protein (VP2), but also reduce the levels of HRV infection induced cytokines (IL-6 and IL-8) (Mastromarino *et al.* 2015). Despite their wide-ranging therapeutic potential, the practical use of polyphenols is restricted due to their limited bioavailability and poor water solubility (Chen *et al.* 2018, Di Lorenzo *et al.* 2021). Several strategies have been proposed to address this challenge. These include slightly modifying the chemical structure to improve solubility. Another approach includes encapsulating polyphenols within nanoparticles, enhancing their water solubility, and thereby increasing their absorption by the gastrointestinal tract (Peñalva *et al.* 2018, Layas *et al.* 2022).

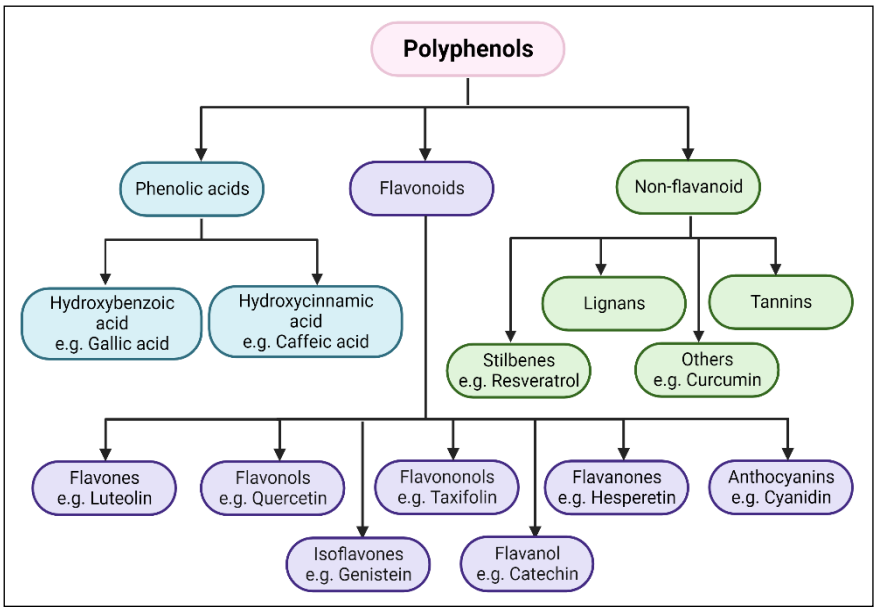

FIGURE 3 Classification of naturally occurring polyphenols. This image has been adapted and modified from Beconcini *et al.* 2020.

2.5.2.2 Rosin

Rosin is another natural product obtained mainly from coniferous trees and is a mixture of different secondary metabolites (Sipponen and Laitinen 2011). Rosin products have a rich history of being used in diverse applications due to their unique properties and versatility (Kugler *et al.* 2019). For example, rosin is commonly used by musicians to enhance the friction between bow hair and string instruments and by athletes in sports like baseball and weightlifting to improve grip (Guettler 2011). Rosin has found application even as antibacterial, in soaps and as binding agent in drugs and cosmetics (Söderberg *et al.* 1990, Bell *et al.* 2021). While the conventional method of rosin extraction involved tapping live pine trees for sap (gum rosin), technological advances have unveiled two more eco-friendly and sustainable sources: tree stumps (wood rosin) and pulpwood (tall oil rosin) (Paul 2002). Fig. 4 schematically illustrates different sources of rosin from coniferous trees.

Tall oil rosin (TOR), considered a more sustainable source than gum rosin, is a by-product of paper production, making it environmentally favorable due to its association with existing industrial processes (Kugler *et al.* 2019). Paper manufacturing involves several steps, with pulping being the first and most crucial for rosin production (Höfer 2015a). During pulping, softwood undergoes alkaline digestion to yield pulp. Simultaneously, a secondary product called black liquor is generated on a large scale, which in former times was discarded as waste. Using black liquor as a source for tall oil rosin production is a step towards circular economy. Lignin is separated by subjecting black liquor to acidification with sulphates, and the resulting liquid is called crude tall oil (CTO). CTO comprises 15–55% rosin acids, 5–50% fatty acids, and 5–35% unsaponifiable and neutral materials (Bajpai 2018). The exact composition can vary based on tree species, age, and the extraction process. Fractional distillation of CTO yields a

mixture of five distinct components, each separable based on their boiling points: TOR, distilled tall oil (DTO), tall oil fatty acids (TOFAs), pitch and tall oil heads. TOR is made up of 9 resin acids or rosin isomers, namely isopimaric, levopimaric, neoabietic, dehydroabietic, abietic, pimaric, sandaracopimaric, and palustric acids, all of which belong to the class of phenolic compounds (Höfer 2015).

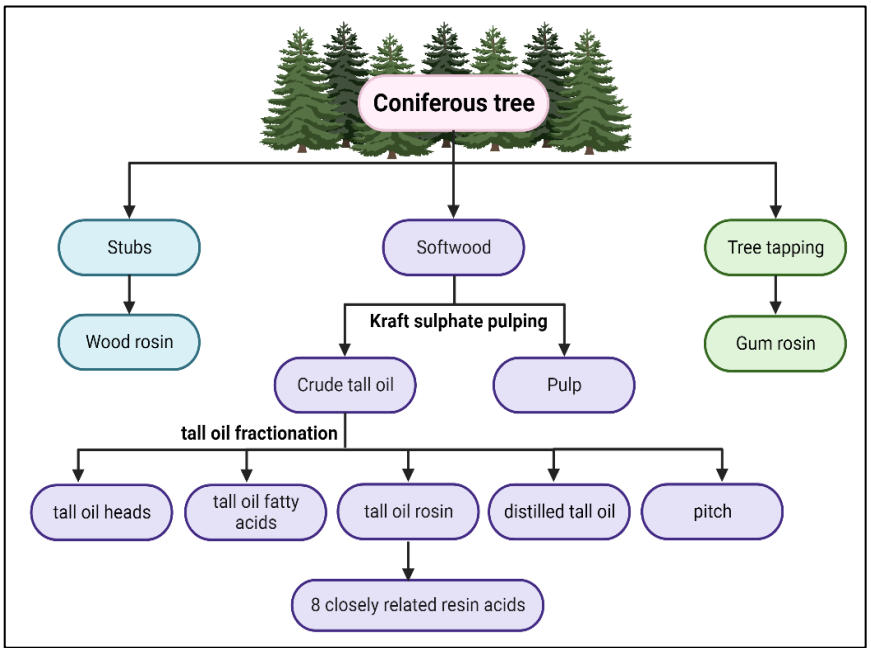

FIGURE 4 Schematic of different sources of rosin (wood, gum and tall oil) from coniferous trees.

For centuries, rosin derived from coniferous trees has been widely used in traditional medicine to treat a variety of ailments. (Barnett 2004). However, recently, there has been a resurgence of interest in their antimicrobial properties. For example, Sipponen and coworkers were able to show that a minimum of 10% coniferous rosin salve mixture could demonstrate a bactericidal effect against both gram-positive and gram-negative bacteria, as well as antifungal effects against *Trichophyton* species (Sipponen and Laitinen 2011). While the literature mainly focusses on the antibacterial attributes of rosin, its antiviral and antifungal properties have received limited attention. One study highlighted the activity of commercial resin acids and their analogues against Herpes Simplex Virus types 1 and 2 (HSV-1 and HSV-2 (Agudelo Gómez *et al.* 2012). However, in these studies, the mechanism of antiviral action was not investigated. Interestingly, rosin has been functionalized onto materials to impart antimicrobials properties. For example, Kanerva and colleagues incorporated industrially refined rosin into different thermoplastics to produce functional fibers. Amongst the different fibers tested, only polyethylene fibers doped with 10 wt% rosin demonstrated an antibacterial effect against both *S. aureus* and *E. coli* (Kanerva *et al.* 2019). Hence, rosin-based functionalization of materials might be another promising strategy to achieve antimicrobial surfaces.

2.5.3 Wood as a natural antiviral surface

Wood is one of the earliest known materials utilized by humanity. Its versatility has seamlessly integrated it into our everyday lives. While the 20th century saw a shift towards materials like glass, metals, and plastic, wood has regained popularity due to its renewable nature and low carbon footprint that contribute to sustainability (Franzini *et al.* 2018). Due to the organic and porous nature of wood, its use in sanitary environments places has been questionable, however, plenty of studies have debunked this myth and highlighted the antimicrobial properties of wood (Munir *et al.* 2019). Fundamentally wood is made up of cellulose, hemicellulose, lignin, and extractives (Nhuchhen *et al.* 2014). Cellulose and hemicellulose, while essential structural components, do not exhibit antimicrobial properties. In contrast, both lignin and extractives have been found to possess significant antimicrobial activity (Dong *et al.* 2011, Laireiter *et al.* 2013). Solvent extraction studies conducted on various wood species reveal that the extractives consist of a blend of plant secondary metabolites, including alkaloids, waxes, di- and triglycerides, proteins, phenolics, gums, pectins, resin acid, terpenes, and essential oils (Kadir and Hassan 2020). Given that the primary role of these extractives is to defend trees against pathogens and physical damage, it is reasonable to anticipate that these secondary metabolites might be contributing to the antimicrobial properties of wood.

Understanding how viruses behave on wood is important in today's urbanizing world characterized by a rising trend in the emergence of pathogens. However, a knowledge gap exists about how different wood species influence viruses. To the best of our knowledge, only two studies have highlighted the antiviral aspects of wood. In the first study, no infectious influenza A virus was detected after 4 h of contact with pine wood surface. (Greatorex *et al.* 2011), whereas the other study conducted by Chin *et al*. (2020), found that there were no detectable infectious SARS-CoV-2 on a treated wood surface after 48 h (Chin *et al.* 2020). Further exploration is needed to identify the antiviral capabilities of different wood species. This investigation would highlight wood's utility and offer a greener and safer nature-based surface solution in our ongoing battle against viral infections.

3 AIMS OF THE STUDY

Exploring the use of nature-derived compounds to design antiviral surfaces paves the way toward a healthier and environmentally conscious tomorrow. Our study involved screening various natural compounds and surfaces for their antiviral potential. Additionally, we aimed to shed light on the mechanism of action of these antiviral surfaces and compounds, contributing towards a comprehensive understanding of their potential applications. To address these, we aimed:

I To study the persistence of enveloped and non-enveloped viruses on six wood species, and to identify the secondary metabolite profile specific to each wood species.

II To determine whether a rosin-functionalized plastic surface has antiviral activity against HCoV-OC43 and SARS-CoV-2 and to reveal the effect of the antiviral surface on the virion structure and life cycle.

III To explore the antiviral efficacy of two polyphenols (EGCG and RES) and polyphenol functionalized nanoparticles against enteroviruses and find the antiviral mechanism of action.

4 SUMMARY OF THE METHODS

The methods used in all the articles related to this thesis are summarized in Table 5. A more detailed description of these methods can be found in the original publications, depicted by Roman numerals.

TABLE 5 Summary of methods used in the original publications I-III of this thesis.

Methods	Publications
Cell culture, virus production and purification	I, II, III
Statistical analysis	I, II, III
Antiviral assays for enterovirus	III
Time and temperature assay	III
Particle stability thermal release assay	III
Transmission electron microscopy	II, III
Gradient centrifugation	III
Real-time fluorescence uncoating assay	III
Binding assay with radioactive enterovirus	III
Dynamic light scattering	III
Nanoparticle synthesis	III
Time of addition assay	III
Dilution and temperature assay	III
Ellman's assay	III
Molecular docking	III
Virus persistence studies on surfaces	I, II
RT-qPCR	I, II
Atomic force microscopy	II
Helium ion microscopy	II
Contact angle measurements	II
Cryogenic electron microscopy	II
Sedimentation assay	II
Binding assay for coronavirus	II
Immunofluorescence and confocal microscopy	I, II
UV-Visible spectroscopy	II
Thermal desorption-gas chromatography-mass spectrometry	I
timTOF	I

5 RESULTS AND DISCUSSION

For a long time, the scientific community believed that viruses majorly spread through direct person-to-person contact. However, fomite-based transmission gained significant attention during the recent pandemic, especially when the Centers for Disease Control and Prevention (CDC) highlighted the potential risk of coronavirus spread through contaminated surfaces (CDC, 2020). Although disinfection methods are in place, there are limitations to their effectiveness. Therefore, there is a need to develop sustainable antiviral solutions that can complement existing strategies. One promising approach is to functionalize surfaces with nature-based compounds that exhibit antiviral properties. Another approach is to identify surfaces of natural origin that have inherent antiviral properties. This thesis explores three independent investigations that examine the potential of such compounds and surfaces with antiviral properties. Through a combination of in vitro experiments and imaging techniques, we demonstrate the ability of wood, tall oil rosin-functionalized plastic, and polyphenolic compounds to exhibit antiviral efficacy against enveloped and non-enveloped viruses while shedding some light on their mechanism of action.

5.1 Antiviral efficacy studies

5.1.1 Six wood species

At first, we conducted investigations to examine the persistence of enveloped (HCoV-OC43) and non-enveloped (CVA9) viruses on six different types of wood commonly used in everyday life and commercial settings. The wood species we tested included Scots pine (*Pinus sylvestris*), silver birch (*Betula pendula*), grey alder (*Alnus incana*), eucalyptus (*Eucalyptus globulus*), spruce (*Picea abies*), and pedunculate oak (*Quercus robur*). To conduct our persistence studies, we incubated the viruses on the surface of each wood species for varying periods under different temperature and humidity conditions. We used room

temperature and high RH (>90%), which are the conditions used in standardized testing protocols (ISO 21702:2019 2020). Standardized methodology helped ensure uniform testing conditions and reproducibility and provided a comparative baseline for subsequent studies with antiviral surfaces. After incubation, we flushed the viruses from the surfaces and added them to host cells. We then evaluated the infectivity of the viruses using the cytopathic effect (CPE) inhibition assay.

Our findings revealed notable differences in the persistence of enveloped and non-enveloped viruses on various wood species (I, Fig. 1 and Fig. 4). Specifically, HCoV-OC43 infectivity on pine and spruce surfaces declined almost immediately, within 5 and 10 minof incubation on the surface (I, Fig. 1A). Birch and alder showed a gradual reduction in virus infectivity over a 15-min period, but we did not see complete inactivation. Oak and eucalyptus, on the other hand, did not exhibit any inactivation within the 15-min time period. Interestingly, when we extended the incubation period of the virus to a minimum of 1 h, all the wood species were able to completely inactivate HCoV-OC43 except for eucalyptus, which required at least 2 h to achieve comparable inactivation (I, Fig. 1B).

Our study results revealed a significant difference in the persistence time of coronavirus on various wood species compared to previous research studies conducted by other researchers (Duan *et al.* 2003, Chin *et al.* 2020). Duan and colleagues reported a 75% decrease in SARS-CoV infectivity after 12 h, with complete inactivation only after 3 days. Similarly, Chin and colleagues found that infectious SARS-CoV-2 persisted for at least 2 days. However, it is essential to note that comparing these studies is challenging for several reasons. Firstly, Chin and colleagues used a treated wood surface, and the type of treatment used was not disclosed. Secondly, both studies evaluated viral persistence at different time intervals from ours, with initial measurements taken only after 12 and 24 h.

Our persistence studies with CVA9 on six different wood species yielded contrasting results compared to HCoV-OC43. Among the tested wood species, only oak exhibited remarkable CVA9 inactivation within a notably short span of 7.5 min (I, Fig. 4A). On the other hand, pine, spruce, birch, and eucalyptus required extended exposure times of at least 1 or 2 h to achieve comparable CVA9 inactivation (I, Fig. 4B). Interestingly, alder was the only wood species where CVA9 persisted even after 4 h of incubation. Comparing our results with previous studies was challenging due to the limited number of studies with enteroviruses and wood. However, we came across one study by Sittikul and colleagues who reported a reduction of 50% and 75% in EVA-71 and CVA16 infectivity on a painted wood surface after 7 h of incubation (Sittikul *et al.* 2023). Compared to ours, the prolonged persistence observed in their study may be attributed to the use of a painted wood surface, which could alter the wood's natural properties and influence the virus interaction with the surface.

In summary, different wood species displayed selective abilities towards inactivating enveloped and non-enveloped viruses on their surface. While some surfaces like pine and spruce were very efficient at inactivating enveloped coronaviruses, oak displayed its potential at inactivating the non-enveloped

enterovirus. Alder was one surface that could not inactivate the enteroviruses even after 4 h, suggesting that it could act as a potential fomite for virus transmission during this duration.

Wood products can undergo different modifications and treatments, such as polishing, high-temperature treatment, or incorporation of other materials like plastic (as seen in composite woods), to enhance their appearance and durability depending on their intended use. We conducted a study to determine the persistence of HCoV-OC43 on modified surfaces, including pine wood with different coarseness, thermally treated S- and D-wood, spruce wood, and wood-plastic composite (WPC). Our findings revealed that pine wood's impressive antiviral properties against coronaviruses were unaffected by variations in wood coarseness (I, Supplementary Fig. 5). However, the antiviral properties of some wood species were affected by thermal treatment and the incorporation of plastic materials into the wood (I, Supplementary Fig. 6A and Fig. 9).

Two thermal treatments were tested: Thermo-S, which involves heat treatment at 190 °C for indoor wood products to enhance stability, and Thermo-D, which involves treatment at 212 °C for outdoor wood products to ensure durability. Our results demonstrated that the antiviral activity of pine was still maintained on both S- and D-treated surfaces, comparable to an untreated pine surface. However, there was a marginal delay in the inactivation of HCoV-OC43 on the S-treated spruce surface (I, Supplementary Fig. 6A and 6B). Surprisingly, D-treated spruce surfaces did not show any antiviral activity during the tested timeframe (I, Supplementary Fig. 6B).

Furthermore, WPC surfaces did not exhibit any antiviral effects, indicating that the incorporation of plastic had negated the wood's antiviral properties. This could be due to the significant alteration of the wood's architecture caused by the integration of plastic, rendering the wood completely non-porous and making the antiviral compounds within the wood inaccessible for virus inactivation. Further details regarding the explanation for the loss in antiviral activity observed on the thermally treated D-spruce surface are discussed in Section 5.3.3.

5.1.2 Rosin-functionalized plastic surface

We also investigated the persistence of seasonal coronavirus (HCoV-OC43) and pathogenic SARS-CoV-2 on a plastic surface that was functionalized with tall oil rosin provided by a company called Premix Oy. Previous research has yielded varying results on coronavirus persistence on plastic surfaces, making it difficult to establish a baseline for comparison (Rabenau *et al.* 2005, Warnes *et al.* 2015, Terio *et al.* 2021). Therefore, we first examined the persistence of HCoV-OC43 on six industrial-grade plastic surfaces before studying the functionalized surface. Our findings showed that infectious HCoV-OC43 could be recovered from all six plastic surfaces up to 48 h (II, Fig. 1A). Our results closely aligned with those reported by Rabenau et al. (2005) and van Doremalen et al. (2020), who reported the persistence of HCoV-229E for 2 days and SARS-CoV-1 and SARS-CoV-2 for 3 days, respectively (Rabenau *et al.* 2005, van Doremalen *et al.* 2020).

Next, we evaluated the persistence of HCoV-OC43 on a rosin-functionalized plastic surface under standardized testing conditions. As a reference, we always included a non-functionalized plastic (LDPE) and an untreated virus as controls. The findings demonstrated a significant contrast between the functionalized and non-functionalized surfaces. The virus infectivity declined as early as after 15 min of interaction with the rosin-functionalized surface, and complete inactivation was observed at 30 min (II, Fig. 1B). The antiviral effect was sustained even after 24 h of incubation, while the non-functionalized LDPE did not decrease the viral infectivity during the 24 h incubation period. Furthermore, the functionalized surface had no toxic effects on MRC-5 cells. The rosin-functionalized plastic surface also showed excellent efficacy against the pathogenic SARS-CoV-2, reducing the initial viral titer by 2.59 logs within 5 min of contact. After 4 h, the virus infectivity further reduced to 3.67 logs. According to the ISO standard, compounds that produce a 3-log reduction in viral titer are considered good, while compounds producing a 4-log reduction are considered excellent antiviral agents, indicating that our rosin-functionalized plastic surface had very good antiviral efficacy.

5.1.3 Polyphenols and polyphenol functionalized on the surface of gold nanoparticles

Finally, we opted to test two of the most widely recognized polyphenols, namely resveratrol (RES) and epigallocatechin gallate (EGCG), against three different enteroviruses (CVB1, CVB3, CVA9). In addition to free polyphenols, we tested their efficacy when functionalized on the surface of gold nanoparticles (AuNPs).

In our study, we utilized a green chemistry approach to functionalize polyphenols on the surface of AuNPs. We then thoroughly characterized the resulting particles, including their size, stability, and ligand concentration (III, Fig. 1C and 1D). The hydrodynamic radius and core diameter of the functionalized AuNPs were determined using dynamic light scattering and transmission electron microscopy, and their stability was confirmed using a zeta potential. We also estimated the Au concentration of the particles using inductively coupled plasma mass spectroscopy (ICP-MS). Ligand concentration on the surface of AuNPs was determined both theoretically and using a biochemistry assay. Using the information from the TEM data (diameter of NPs) and ICP-MS (Au concentration), the ligand concentration was determined theoretically to be 5.61 μM for EGCG and 34.4 μM for RES (III, Supplementary calculation). Using the titration-based biochemistry assay it was found to be 5.5±0.1 μM for EGCG and 42.9±1.1 μM for RES. From here onwards, free polyphenols and polyphenol functionalized nanoparticles will be collectively addressed as polyphenolic compounds.

The results of the antiviral tests showed that all the polyphenolic compounds were very effective in inhibiting the infectivity of all the enterovirus (III, Fig. 2 A, 2B and 2C). Except for free RES, all the polyphenolic compounds had very low 50 % effective concentration (EC50) values (III, Table 2). Only free EGCG showed slight toxicity at high concentrations, while none of the other

compounds exhibited toxicity (III, Table 2 and Fig. 2D). Regarding the antiviral efficacy, EGCG outperformed RES, likely due to its higher availability of hydroxyl groups for interactions with viruses. A prior study by Li and colleagues established a direct correlation between the quantity of hydroxyl groups and the antiviral effectiveness of phenolic compounds (Li *et al.* 2018). Furthermore, EGCG's molecular structure comprises two planar aromatic ring systems with a third ring oriented perpendicular to them. This configuration would enable EGCG to crosslink with multiple viruses.

We also found that polyphenol-functionalized nanoparticles exhibited greater efficacy than free polyphenols, particularly with RES (III, Table 2). This may be due to the enhanced solubility of RES when bound to the nanoparticle surface, as well as the high surface-to-volume ratio of nanoparticles. Significantly, immobilization on the surface of gold nanoparticles greatly reduced the cytotoxicity observed with soluble EGCG at high concentrations. We also demonstrated that a short incubation period of just 5 min was enough for the polyphenolic compounds to show their antiviral effect (III, Fig. 3D). We also wanted to identify whether the antiviral activity originated from the functionalized nanoparticles or from the free ligands in the supernatant. To study this, we pelleted the nanoparticles using ultracentrifugation, resuspended them in ddH20, and immediately evaluated their antiviral activity. The results showed that the freshly resuspended nanoparticles still displayed antiviral activity, confirming that the antiviral activity originated from the functionalized nanoparticles (III, Supplementary Fig. 1).

5.2 Factors affecting antiviral efficacy

It is worth noting that several factors can impact the efficacy of the antiviral compounds and surfaces. These factors include environmental conditions, surface characteristics, and the structural features and concentration of the virus. For example, antiviral products may not work as well under certain conditions, such as when the antiviral is diluted by body fluids (McCormack *et al.* 2010). This dilution effect can decrease the ability of the antiviral molecule to bind with and neutralize the virus, which can increase the risk of some viruses not being inactivated by the antiviral or the infectious viruses being released after the detachment of the antiviral. In our research, we have investigated the impact of environmental factors and the effect of dilution (in the case of polyphenolic compounds) on the performance of our antiviral surfaces and compounds.

5.2.1 Impact of environmental condition and porosity on wood

The preliminary persistence studies with the six different wood species and HCoV-OC43 were performed at room temperature and high RH conditions, as per the ISO standard requirements. To understand if different environmental conditions impact the different wood species' antiviral capabilities, we conducted

further testing at lower and moderate humidity levels of 20%, 40%, and 60% at both room temperature and 37 °C. We chose these humidity levels to simulate the range of conditions from the dry, low humidity of winter (20%) to the higher humidity of summer (50-70%). Similarly, we selected temperatures to mimic the typical indoor temperature extremes experienced in Europe throughout the year. Our findings showed that HCoV-OC43 survived longer on different wood species at lower temperatures (21 °C) compared to higher temperatures (37 °C) (I, Fig. 2 and Fig. 3). For instance, the eucalyptus surface demonstrated little or no antiviral activity in the first hour of contact with the surface at 21 °C. In contrast, the virus was inactivated within the same duration at 37 °C. There has been a significant amount of research conducted by various researchers in the past to study the impact of temperature on virus persistence on different surfaces (Aboubakr *et al.* 2021). The general consensus among these researchers is that the virus tends to survive longer at lower temperatures than higher temperatures.

We hypothesized that humidity levels would have an impact on virus persistence by affecting the wood's absorption properties. However, our findings suggested otherwise. We observed that humidity had a negligible effect on virus persistence on wood at room temperature (I, Fig. 2). However, at 37 °C, the virus persisted longer on the wood surface at very low (20%) and moderately high (60%) humidity levels, compared to moderate humidity (40%) (I, Fig. 3). This U-shaped relationship between RH and virus persistence had also been previously reported by Casanova *et al*. for coronaviruses on non-porous surfaces (Casanova *et al.* 2010). Given the fact that the virus is inactivated on wood within a relatively short period of time, RH appears to play a minor role, likely because it takes more time for humidity to manifest its effects.

As the persistence of viruses could be influenced by porosity, we hypothesized that there might be a relationship between the virus persistence and the porosity of the wood (Geng and Wang 2023). A prominent result that supports the role of porosity in virus inactivation on wood is from the wood plastic composite (WPC). Comprising 50% wood flour and 50% polypropylene, WPC had lost its natural wood porosity due to a significant amount of plastic infusion. Consequently, WPC could not inactivate viruses on its surface, and the virus persisted for a similar time on the surface as it did on a regular plastic (LDPE) surface (I, Fig. 9). The degree of porosity is connected to the wood's capacity to absorb moisture, which varies among wood species (Plötze and Niemz 2011). For instance, Norway spruce has a porosity of 73.68%, Scots pine 69.7%, birch 60.45%, and oak 53.8%. Interestingly, wood species with higher porosity, such as pine and spruce, demonstrated quicker coronavirus inactivation compared to less porous woods like oak (I, Fig. 1). This suggested that there might be a direct correlation between the porosity of wood and its efficiency in inactivating enveloped viruses. However, our studies with non-enveloped enteroviruses suggested otherwise: enteroviruses were inactivated more efficiently on less porous oak in comparison to pine and spruce (I, Fig. 4). Therefore, porosity alone cannot be responsible for virus inactivation on various wood surfaces and other factors might be contributing towards complete inactivation, some of which are discussed in the upcoming chapters.

5.2.2 Impact of environmental conditions on the rosin-functionalized plastic

We investigated the impact of environmental conditions on the effectiveness of the rosin-functionalized plastic surface by assessing the antiviral efficacy under reduced humidity conditions of 20% and 40% at room temperature (II, Fig. 2A and 2B). We found that humidity did not affect the effectiveness of the rosin-functionalized surface, even though previous research has suggested that lower humidity levels can promote longer virus persistence (Biryukov *et al.* 2020). Casanova et al. and Biryukov et al. examined the influence of humidity on virus persistence over various time intervals, ranging from a few hours to several days (Casanova *et al.* 2010, Biryukov *et al.* 2020). Their findings indicated that a noticeable difference in virus persistence due to humidity was only observed after a minimum of 24 h of incubation. However, we observed that our rosin-functionalized plastic inactivated the virus within just 15 min, and the maximum time-point studied was only 1 h of incubation. Therefore, humidity did not have enough time to show its effect in our case.

5.2.3 Impact of dilution and temperature on polyphenolic compounds

As the antiviral properties of polyphenolic compounds may have a wide range of applications in the future such as oral antivirals, or in antiviral creams, or as surface coatings. Hence, it was crucial to ensure that the observed antiviral effect of these compounds remains unchanged by variables like time, temperature, and dilutions. To accomplish this, we first evaluated the antiviral efficacy of these compounds at different temperatures (8 °C, 21 °C, and 37 °C) up to 72 h. We chose these temperatures as they are relevant to applications like coatings and antiviral creams and to account for the stability of enteroviruses at lower temperatures. After pretreating the polyphenolic compounds with the viruses and incubating them at the respective temperatures for 6, 24, 48, or 72 h, we found that the compounds were able to inactivate the virus at all time points and temperatures tested (III, Fig. 3A and 3B). These findings demonstrate that the effectiveness of the polyphenolic compounds remains constant despite temperature changes, which is a significant finding for their potential use in various applications.

To examine the impact of dilution, the virus was treated with polyphenolic compounds for 1 h at 37 °C before being diluted by a factor of 50 and left to incubate for 72 h. This experiment aimed to determine whether a significant dilution would eventually disrupt the interaction between the virus and the polyphenolic compounds, resulting in the virus infectivity to be re-established. The assay results demonstrated that despite the dilution of the virus-compound mixture, the polyphenolic compounds maintained their antiviral efficacy, with no reduction in effect over time (III, Fig. 3C). A similar study was conducted by Zacheo et al. (2020), in which six different multi-sulfonated ligands coated on the surface of gold nanoparticles were tested against the dengue virus (Zacheo *et al.* 2020). While all of the ligands effectively inhibited virus infection, only two of the compounds retained their efficacy when subjected to dilution, highlighting the importance of testing dilution in antiviral research.

5.3 Mechanism of antiviral action

5.3.1 Wood and rosin-functionalized plastic have different abilities to absorb viruses

To decipher the mechanism of antiviral action of wood and rosin-functionalized plastic surfaces, we initially proposed a hypothesis that the observed reduction in infectivity on the wood and rosin-functionalized plastic surface could be due to the binding and absorption of viruses by the surfaces. To test this hypothesis, HCoV-OC43 and CVA9 were added on pine wood and oak wood, followed by incubation of the virus for 15 min on these surfaces. In the case of the plastic surfaces, HCoV-OC43 was added to the rosin-functionalized and non-functionalized LDPE plastic and incubated for up to 4 h. After the specific incubation periods, the surfaces were gently flushed with cell culture media, and the amount of viral RNA in the flush was quantified using qPCR. In the case of wood surfaces, the results showed that there was a difference in the amount of viral RNA recovered from pine and oak wood compared to non-surface treated HCoV-OC43, which supported the hypothesis of viral absorption contributing to antiviral activity (I, Fig. 5). However, no absorption was seen for CVA9. Altogether, these results suggest that viral absorption inside the surface is only a partial reason for the loss in viral infectivity on wood surfaces.

As for the plastic surfaces, the results showed similar amounts of viral RNA recovered from both rosin-functionalized and non-functionalized surfaces and the amounts were comparable to the virus control (II, Fig. 3). These results indicated that the rosin-functionalized plastic still retains the non-porous, non-absorbing nature of plastics and viral absorption is not the reason behind the antiviral action of the rosin-functionalized surface. If there is any interaction between the virus and the rosin-functionalized plastic surface, it can be considered weak based on these results.

5.3.2 Rosin leaching from the surface contributes towards the antiviral activity

Once we confirmed that the rosin-functionalized plastic did not absorb the virus, we proceeded to investigate whether the rosin was functioning solely at the surface or if it was leaching into the surrounding environment and inactivating the virus. To study this, we flushed the antiviral surface with ddH20 for 1 h and overnight and then used UV-Vis Spectroscopy to measure the absorption spectra of these samples. The absorption spectrum of only rosin (elemental conifer pitch) dissolved in 94% v/v ethanol served as a reference. The 1 h and overnight flushed samples showed similar spectra, but they deviated slightly from the reference spectrum (II, Fig. 7A). The deviations could be due to the different solvents used in the reference compound and flushing media or the additives or fillers incorporated by the company producing the functionalized plastic surface.

Nevertheless, the absorption spectra indicated that the rosin leached into the surrounding liquid environment over time.

To determine if the leached rosin was responsible for the antiviral activity of the rosin-functionalized plastic, we conducted an experiment where the plastic was flushed with ddH20 for an hour, and the resulting flush was incubated with HCoV-OC43 for another hour. Post incubation the infectivity of the virus was tested using the CPE assay. The test results indicated that the virus was completely inactivated by the leached solution containing the active ingredient. This suggests that the antiviral activity of the rosin-functionalized plastic was due to the rosin leaching from the surface (II, Fig. 7B).

5.3.3 Difference in virus persistence likely linked to the bioactive compounds present in wood

After discovering that porosity alone cannot explain the loss in virus infectivity on different wood surfaces, we shifted our focus to analyze the chemical compounds present in different wood species. Previous research has highlighted the antiviral properties of certain wood extractives, which provided us with a clear direction to explore (Granato *et al.* 2022). We focused on isolating the wood-specific volatile organic compounds (VOCs) using two techniques. The first technique was gas chromatography coupled with mass spectrometry (GC-MS), which detected the total volatile organic compounds (TVOCs). The second technique was Direct-Inlet Probe Atmospheric Pressure Chemical Ionization Quadrupole Time-of-Flight Mass Spectrometry (DIP-APCI-QTOF MS), which detected the semi-volatile organic compounds (SVOCs).

Our analysis using GC-MS showed differences in the type and quantity of total volatile organic compounds (TVOCs) emitted from dry and wet wood at 25 and 40 °C (I, Fig. 7 and Supplementary Table 1 and 2). Notably, the wet wood sample emitted more TVOCs than the dry wood samples, and the higher temperature of 40 °C emitted more TVOCs than the lower temperature of 25 °C. Pine wood emitted the largest number of chemical compounds in both cases. Our research places particular significance on the wet wood analysis, as it closely resembles wood that virus droplets have moistened during our prior persistence studies (I, Fig. 1).

Our study using DIP-APCI-QTOF MS generated Van Krevelen diagrams of the semi-volatile organic compounds (SVOCs) emitted from different wood species surfaces at three distinct temperatures ranging from 200 to 300 °C (I, Fig. 8 and Supplementary Fig. 4). This technique primarily detected the broader class of chemical components. The results from both DIP-APCI-QTOF MS and GC-MS analysis complemented each other, leading to a more comprehensive understanding of the wood-specific VOCs and their potential role in the antiviral properties of wood. The analysis showed little difference between wood species in the SVOCs desorbed at 200 °C. At 250 °C, pine and oak began to desorb some resin acids and phenolics, respectively. The most significant differences were observed at 300 °C, where some SVOCs, such as phenolics, were commonly desorbed by all wood species, while others were unique to a particular wood

species. For example, resin acids were desorbed by pine and spruce, carbohydrates were desorbed only by oak, and triterpenoids were desorbed by birch. Interestingly, pine and spruce showed a very similar profile of SVOCs.

Previous research has established a link between resin acids and antiviral activity against enveloped viruses, such as herpes simplex virus (González *et al.* 2010, Agudelo Gómez *et al.* 2012). Even our study with the rosin-functionalized plastic, in which rosin is a mixture of resin acids, demonstrated antiviral activity against HCoV-OC43. Based on these studies, resin acids in pine and spruce wood surfaces likely could be linked to the rapid inactivation of enveloped viruses. Furthermore, since all wood species commonly emitted phenolics, they could contribute to the antiviral action against both enveloped and non-enveloped viruses. Polyphenols, to which phenolics belong, are known for their antiviral potential against both enveloped and non-enveloped viruses. Some polyphenols exhibit broad-spectrum antiviral activity, while others are more specific to certain viruses (Chojnacka *et al.* 2021). For example, EGCG displayed broad-spectrum antiviral activity (Wang *et al.* 2021). In our study also, polyphenols have demonstrated antiviral activity against the non-enveloped enteroviruses (III, Fig. 2). We hypothesize that the antiviral activity of different wood species against enteroviruses could arise from the presence of different phenolics. Oak surfaces were mainly enriched with phenolics, which correlated well with the higher antiviral efficacy of oak against enteroviruses when compared to other wood surfaces. It is likely that the antiviral properties of pine and spruce against both enveloped and non-enveloped viruses are due to the significant amounts of resin acids and phenolics, both present in both wood species. Further studies involving isolated fractions should be evaluated for their specific efficacy against both kinds of viruses to prove this hypothesis.

Given that thermal treatments improve wood's stability and durability, it has become a common practice nowadays to subject wood to such treatments. Our research on thermally treated wood surfaces revealed a significant decrease in antiviral activity in Thermo-D treated spruce compared to Pine-D, Pine-S, and Spruce-S (I, Supplementary Fig. 6). Using DIP-APCI-QTOF-MS analysis, we found that thermally treated pine and Spruce-S still maintained high levels of resin acids and phenolic compounds compared to Spruce-D (I, Supplementary Fig. 7). Additionally, we observed an increase in carbohydrate levels in Spruce-D, possibly due to the decomposition of hemicellulose into sugar monomers. However, the interaction between carbohydrates and viruses is not yet fully understood. Based on our findings, we propose that the reduction in SVOCs like resin acids and phenolics, along with the increase in carbohydrate content, could be the reason for the loss of antiviral activity on the Spruce-D surface. Further investigation is needed to confirm this hypothesis.

5.3.4 Polyphenols stabilize the virus and prevent genome release

To understand how polyphenols work against enteroviruses, we first wanted to understand the stage of the virus lifecycle, at which the polyphenols exert their antiviral effect. To test this hypothesis, we conducted a time of addition assay.

Polyphenolic compounds were added to the cells 1 h post-infection (p.i.). Results of the time of addition assay showed that these polyphenolic compounds could not rescue the cells from the virus infection when they were added post infection (III, Fig. 4A). However, when the virus was treated with the compounds for 1 h, the virus was unable to complete its infection cycle (III, Fig. 2). This suggested that the polyphenolic compounds were targeting early stages of viral infection such as virus attachment or internalization.

Having established the direct effect of the polyphenolic compounds on the virus, we proposed the following possible mechanisms: (i) the polyphenolic compounds inactivate the virus by causing premature release of the viral genome from the capsid or (ii) the polyphenolic compounds stabilize the virus, preventing its opening and genome release, thus rendering it incapable of infecting host cells. To explore these mechanisms, we used two fluorescence-based assays - Particle Stability Thermal Release Assay (PaSTRy) and an in-house developed uncoating assay, which uses SYBR Green II (SGII) to detect genomic RNA. This nucleic acid dye fluoresces brightly when bound to the RNA and offers several advantages over traditional RNA dyes: lower cytotoxicity, high specificity for RNA and is cost-effective (Kiltie and Ryan 1997, Kirsanov *et al.* 2010).

The PaSTRy/Thermal assay was conducted using a PCR machine to investigate the release of RNA at increasing temperatures. The interaction between the released RNA and SGII was recorded and plotted as a function of temperature, resulting in a bell-shaped melt curve. The first derivative plot of this data was useful in determining the melting temperature (Tm), which was altered if there was any difference in virus stability due to the interaction of the antiviral compound with the capsid (Martikainen *et al.* 2015). To serve as a positive control during the study, untreated virus in storage buffer (PBS with 2mM $MgCl_2$) was used. The virus control in storage buffer showed a typical bell-shaped curve with a Tm of 42 °C (III, Fig. 4B), which was calculated from the melt peak data (data not shown). However, polyphenol-treated viruses generated very low fluorescence, with no significant change in the Tm. This is unusual because normally, stabilization results in an increase in Tm. It is possible that a strong stabilization in this case may have blocked the expansion and opening of the virus. It was confirmed in a separate control assay that polyphenols did not directly affect the fluorescence emitted by SGII binding to nucleic acids, indicating that the reduced fluorescence was due to the low accessibility to viral RNA (data not shown).

The effect of the polyphenols on virus stability was also tested under a special condition using an opening buffer. This buffer is a mixture of low sodium/high potassium ions and albumin (20 mM NaCl, 6 mM KH_2PO_4, 12 mM K_2HPO_4, and 0.01% fatty acid-free bovine serum albumin [faf-BSA]), which promotes the opening of the virus by releasing the pocket factor (Ruokolainen *et al.* 2019). When the virus was present in the opening buffer, it immediately showed very high fluorescence as compared to the virus in storage buffer, indicating that the viral RNA was readily accessible to SGII for binding. However, when the polyphenols were present with the virus in opening

conditions, lower fluorescence was recorded, with no significant variation in the Tm. Interestingly, the polyphenols seemed to prevent the opening up of the virus even under these strong ionic conditions, as the opening buffer was added after the polyphenols treatment to the virus. This suggested that the polyphenolic compounds effectively prevented majority of the virus from opening and releasing its genome, even in the presence of the ionic conditions.

To gain additional confirmation that polyphenolic compounds stabilize the virus and prevent genome release, we used an spectroscopy based, in-house developed real-time uncoating assay (Ruokolainen *et al.* 2020). Enteroviruses exhibit three distinct virion forms: intact, intermediate (or primed), and broken (Myllynen *et al.* 2016). Intact particles contain the RNA within the protein capsid. Intermediate particles still contain the RNA, but the capsid undergoes structural changes and expands. Broken particles no longer contain the viral genome. Our hypothesis was that the presence of antiviral polyphenolic compounds could influence the virus's structural state and its transition into an expanded or empty state. To test this hypothesis, we utilized two reporter molecules. The first, SGII, which binds to viral RNA and emits fluorescence upon contact. The second is RNase, which degrades viral RNA if it is released outside the capsid. Intact capsids would not emit fluorescence. In expanded capsids, SGII can penetrate the capsid and emit fluorescence, while RNase being a large molecule cannot access the expanded capsids to digest the RNA. For empty capsids, a high level of fluorescence is recorded with SGII, but the addition of RNase degrades the RNA, thus significantly reducing the fluorescence.

In our experiment, we studied the viruses in three different conditions: virus control in storage buffer, virus in uncoating buffer, and virus treated with polyphenols in storage buffer. For each condition, fluorescence was recorded from a sample with and without the addition of RNase [see the protocol in more detail in (Ruokolainen *et al.* 2020)]. We subtracted the fluorescence results of the samples with RNase from the ones without RNase to measure the amount of net RNA released from the virions. Our findings showed that in the virus control, the fluorescence level was very low and remained constant throughout the 1-h assay (III, Fig. 4C). Also, we observed minimal difference in fluorescence between the samples with and without RNAase, indicating that the virus control mainly contained intact capsids with some expanded capsids. On the other hand, in viruses subjected to uncoating conditions, we observed very high fluorescence without the RNase and there was a significant lowering of the fluorescence after the addition of RNase. This suggests that the ionic conditions of the opening buffer compelled most of the viruses to either open or expand. In the third condition when viruses were treated with polyphenolic compounds, the fluorescence signal without RNase was low, and there was not much difference in the fluorescence after RNase addition. This indicated that the viruses remained mostly intact, just like the virus control and the treatment with the polyphenolic compounds did not induce genome release. Thus, aligning with the results from the thermal assay.

5.4 The effect of antiviral treatment on virion structure

5.4.1 Coronaviruses

To study the impact of antiviral surfaces and polyphenolic compounds on the native virion structure, we utilized several imaging techniques. Our initial focus was on the structure of coronaviruses that had been flushed from the rosin functionalized plastic surface. To do this, we employed Atomic Force Microscopy (AFM) and Transmission Electron Microscopy (TEM). Surprisingly, no apparent changes were observed in the virion structure of the viruses flushed from the rosin-functionalized surface compared to the control virus that had not undergone any treatment or viruses flushed from the LDPE surface (II, Fig. 4A and 4B). The spikes and envelope membrane appeared to remain intact. AFM revealed the presence of small virus clusters and some donut-shaped viruses that had flattened out on the surface. It is worth noting that a previous study examining the impact of purified spruce resin on bacteria observed that bacterial cells underwent aggregation, displayed thicker-than-normal cell walls, and ultimately degraded when exposed to the resin (Jokinen and Sipponen 2016). However, unlike bacterial cells, we did not observe a similar thickening of the viral envelope or aggregation of viruses on rosin treatment.

The AFM and TEM studies on viral structure were limited to imaging viruses flushed from surfaces. However, helium ion microscopy (HIM) allowed the direct visualization of the viruses while on the surface. HIM imaging revealed that viruses on the antiviral surface appeared flatter than those on the LDPE surface (II, Fig. 5A). To quantify this difference, we measured the aspect ratio (width/height) of the viruses on each surface. The aspect ratio for viruses on LDPE was 1.6±0.3 (S.D.), while those on the antiviral surface were 2.5±0.5 (S.D.). The appearance of flatter viruses on the antiviral surface could be related to the surface's wettability that was assessed by measuring the droplet contact angle on the surface (II, Fig. 5B). The contact angle measurement provides information about surface properties like hydrophilicity or hydrophobicity. The contact angle of the droplet on LDPE was 95°, while the rosin-functionalized plastic surface had a contact angle of 55°, indicating that the antiviral surface was more hydrophilic than the LDPE surface (Law 2014). Hydrophilic surfaces promote liquid spreading, which could have caused the viruses within the droplet to appear flatter due to the surface's affinity.

Next, Cryo-EM was used to resolve the ultra-structure of the viruses flushed from the rosin-functionalized plastic and LDPE surfaces and to determine whether the virus genome was still present inside the virus. The viruses flushed from both surfaces appeared similar to the virus control, retaining spikes on the surface of the envelope and appearing intact with no apparent changes in the virion (II, Fig. 6A). Also, there was no visible thickening or alteration in the viral envelope, as observed previously by Jokinen and Sipponen (2016) in bacterial cells (Jokinen and Sipponen 2016). Additionally, an *in vitro* sedimentation assay confirmed the presence of viral RNA inside the

virion, with quantities of viral RNA recovered from the LDPE surface, virus control, and the antiviral surface all being similar (II, Fig. 6B). Both the Cryo-EM findings and the *in vitro* sedimentation assay complemented each other findings and confirmed the presence of the viral RNA inside the virion.

5.4.2 Enteroviruses

To investigate the impact of polyphenolic compounds on enterovirus structure, transmission electron microscopy (TEM) studies were conducted. The negative-stained control virus images revealed uniformly distributed, intact viruses on the grid that appeared bright against a dark background. A few broken virions that lacked a genome were also observed (III, Fig. 5B). In contrast, the viruses treated with polyphenolic compounds were mostly intact but formed large aggregates. The Dynamic Light Scattering (DLS) data supported the TEM findings, revealing that polyphenolic compound-treated viruses formed aggregates of about 1 µm in diameter (III, Fig. 5C). On the other hand, untreated viruses had a peak closer to 30 nm, which is the average diameter of intact enterovirus virions (Hogle *et al.* 1985). Taken together, these results suggested that the interaction between the virus and the polyphenolic compounds caused the viruses to aggregate, while keeping the virion intact. To support our findings, we found previous research by Ueda et al that demonstrated antiviral activity of a persimmon extract against non-enveloped virus (Ueda *et al.* 2013). The authors proposed that the antiviral action of the extract is associated with the aggregation of viral proteins.

To explore the potential interactions between the polyphenols and the enterovirus capsid, docking studies were conducted using an in house developed algorithm. Due to the computational complexity of docking the entire capsid surface, we targeted larger areas around the 2-fold and 3-fold axes of symmetry of CVB3 and CVA9. The analysis identified 159 docking poses based on favourable binding energies, hydrogen bonds, and hydrophobic interactions (III, Fig. 9). Overall, six distinct binding sites were observed, of which four were novel (S1, S2, S3, and 3-fold axis pore), and two had been reported earlier (hydrophobic pocket and the Butcher-Neyts pocket) (Abdelnabi *et al.* 2019). Interestingly, EGCG and RES shared some docking poses on CVB3 and CVA9, while others were specific to each virus. EGCG showed a higher propensity to bind to multiple sites across both viruses. Both polyphenols interacted favorably with the hydrophobic pocket, a well-known target for previously studied capsid binders (Oberste *et al.* 2009, Matz 2013, Makarov *et al.* 2015). Furthermore, CVB3 exhibited fewer docking poses in the hydrophobic pocket than CVA9, likely due to the collapsed hydrophobic pocket in the Nancy strain of CVB3 used in our study (Abdelnabi *et al.* 2019). RES displayed a higher affinity for binding within the hydrophobic pocket due to its small size and linear molecular structure. Overall, our docking studies provide insights into the possible binding sites for polyphenols on the enterovirus surface that contribute to the strong stabilization effect.

5.5 Effect of antiviral treatment on virus life cycle

Confocal microscopy was used to determine the specific stage of the HCoV-OC43 life cycle that was affected because of their interaction with the antiviral wood and rosin-functionalized plastic surfaces. We immunolabeled the virus's spike protein and the cell's nuclei and tubulin to follow the infection cycle. Two set of experiments were conducted, one where the viruses flushed from the surfaces (wood and rosin-functionalized plastic) were allowed to infect the cells for only 2 h, while the other for 15 h. The 2 h time point was used to study binding and entry, while the longer time point allowed to study virus replication and protein translation. In all the confocal studies, a virus without any surface treatment and a virus flushed from the LDPE surface were used as controls.

In the 2 h time point study with the pine wood surface, no S protein signal (red dots) was detected in cells incubated with the virus flushed from the wood surface (I, Fig. 6A). In contrast, in the case of the untreated virus control and virus flushed from the LDPE surface, a very strong S protein signal (red dots) was observed around the cell boundaries, suggesting successful viral attachment and/or internalization. In the 15 h time point study, in the case of both the untreated virus control and virus flushed from the LDPE surface, a significantly high amount of S protein signal was detected, suggesting that protein translation had occurred to produce more S proteins for new virions (I, Fig. 6B). However, no signal was detected in cells incubated with the virus flushed from the pine wood surface. Results from the confocal studies suggests that either the coronaviruses flushed from the pine wood surface were too few to infect and show up in the confocal studies or then the interaction of the coronavirus with the pine surface hindered the initial stage of viral attachment.

A similar study was performed with HCoV-OC43 viruses flushed from the rosin-functionalized plastic surface. In the 2 h time point study, a very strong S protein signal (red dots) was observed around the cell boundaries for cells infected with virus flushed from the rosin-functionalized plastic surface, LDPE surface and virus control (II, Fig. 8B). This suggested that the virus was successful in binding to its host cell. An in vitro binding assay was also conducted, wherein the viral infection was carried out at a low temperature of 4 °C to synchronize its entry into the cells. After removing the unbound viruses, the cells were lysed, and the amount of viral RNA was quantified using RT-qPCR to determine the amount of virus bound to the cells. Viruses flushed from the LDPE surface and untreated virus served as controls in this experiment. The results suggested that the virus flushed from the rosin-functionalized plastic surface bound to its host cell similarly to the untreated virus control and the virus flushed from the LDPE surface (II, Fig. 8A). This observation indicated that the virus flushed from the rosin-functionalized surface does not affect the virus's binding ability, thus supporting the results obtained from the confocal studies.

In the 15 h time point study, a significantly high amount of S protein signal was detected from cells infected with virus flushed from the LDPE surface and

the untreated virus control (II, Fig. 9A). Interestingly, the viruses flushed from the rosin-functionalized plastic surface still appeared to be present bound to the surface or inside vesicles. The infection % of the samples was quantified by using the software Cell Profiler 4.2.1. Results showed that the amount of infection in the wells with the virus flushed from the LDPE surface was comparable to the virus control (II, Fig. 9B), while the infection in the wells with the virus flushed from the rosin-functionalized plastic surface was significantly lower. These results corelated well with the persistence studies of HCoV-OC43 on LDPE and the rosin-functionalized surface (II, Fig. 1B). As protein translation and RNA replication occur simultaneously, we also immunolabeled dsRNA intermediates to check if replication was initiated. Analysis of the confocal images showed no signal in cells infected with the virus flushed from the antiviral surface as opposed to abundant dsRNA signal in cells inoculated with the untreated virus and virus flushed from the LDPE plastic surface (II, Fig. 9C). These findings suggested that the virus collected from the rosin-functionalized surface was unable to progress in the life cycle after virus attachment and vesicle-entry. Thus, it seems probable that the antiviral treatment affected the uncoating/fusion ability of the virus. However, further experiments would be required to confirm this.

In case of enteroviruses treated with the polyphenolic compounds, the first stage of infection i.e., virus attachment to its host cell was studied using a binding assay with metabolically radiolabeled CVA9. The virus treated with polyphenolic compounds were allowed to infect the cells at low temperature to synchronize their entry inside the host. After cell lysis, the radioactivity from the viruses was detected using a scintillation analyzer. Results from the binding assay demonstrated that the interaction with the polyphenolic compounds significantly prevented the virus from binding to its host cells, just like in the case of viruses treated on the wood surface (I, Fig. 4D).

6 CONCLUDING REMARKS

In summary, this thesis sheds light on three antiviral approaches aimed at reducing indirect transmission of viruses through surfaces. Two of the approaches were surface based, while the third focused on compounds in solution that could be applied as a coating to impart antiviral properties to a surface.

In the first study, we explored the antiviral properties of different wood species. While most woods displayed antiviral traits, there were significant variations between species. We found that pine and spruce wood displayed extraordinary inactivation capabilities against coronaviruses within a contact time of 15 min, while the hardwood oak displayed similar effectiveness against the non-enveloped enteroviruses. Wood modification like different coarseness did not impact the antiviral properties of wood, however, thermal treatments or integration of plastic materials influenced the antiviral efficacy of wood. Both pine and oak wood showed the ability to absorb enveloped coronaviruses, but not the non-enveloped enteroviruses. This suggested that virus absorption is not the only reason for loss in antiviral activity. Through the profiling of VOCs from various wood species, certain differences and similarities between the species were discovered. These VOCs signatures may help explain the differences in virus persistence observed across different wood species. Thus, we hypothesized that the antiviral properties of wood species could be tied to the absorption of viruses and the presence of different VOCs. However, future studies would determine whether the antiviral activity of certain wood species is linked to a specific compound or if the result is a synergistic effect of multiple compounds.

In the second study, we demonstrated that a regular plastic surface functionalized with tall oil rosin could inactivate both seasonal HCoV-OC43 and SARS-CoV-2 within a very short time, while virus on regular plastic stayed infective for about 2 days. The efficacy of the antiviral surface was not compromised under different humidity levels. We also found that the active component, rosin, leached out into the surroundings to mediate the antiviral effect. Interestingly, rosin seemingly did not alter the virion structure, as visualized by different imaging techniques and the virus retained its ability to

bind and enter the cells, suggesting that the mechanism of inhibition relies on the prevention of fusion with the cellular membranes or direct effect on S protein or even viral RNA. Future studies focusing on each of the infection cycle events post internalization would help reveal the real targets and the molecular mechanism of action.

Lastly, polyphenols also showcased remarkable antiviral efficacy against non-enveloped enteroviruses within a few min of contact at room temperature. The efficacy enhanced many folds when the polyphenols were functionalized on the surface of gold nanoparticles. Investigations into the mechanism of action revealed that both the polyphenols and polyphenol-functionalized nanoparticles acted directly on the viruses, stabilized them, and prevented their genome release. The interaction between the compounds and viruses resulted also in aggregation of intact virions. Further, docking studies predicted six binding sites on the enterovirus surface, amongst which two were previously identified targets, namely the hydrophobic pocket and Butcher-Neyts pocket, while four were new target sites.

This dissertation provides evidence that nature can provide us with highly effective antiviral surfaces in the form of wood, and one should consider using more wooden products to increase the hygiene standards in the surroundings. In situations where plastics, glass or metals are required, the introduction of natural products such as rosin or polyphenols, either by embedding or surface-functionalization, offers a viable approach to introduce antiviral functionality. Together, these strategies contribute to the arsenal of possible countermeasures against both enveloped and non-enveloped viruses. As a future prospect, wood and rosin-functionalized plastic could be used as antiviral surfaces. Moreover, antiviral polyphenolic compounds hold great potential as antiviral coatings for surfaces, potential oral antiviral agents, and could be valuable in wastewater treatment, surface disinfection, and vaccine development too.

This work was carried out at the University of Jyväskylä, at the Department of Biological and Environmental Science and Nanoscience Center, Division of Cell and Molecular Biology. This thesis was funded by the Jane & Aatos Erkko Foundation, Business Finland and the Academy of Finland. I would like to express my gratitude towards the people, the institute and funding agencies involved in my PhD journey.

Firstly, I would like to extend my heartfelt gratitude to my supervisor, Prof. Varpu Marjomäki. Despite the challenges I faced during my master's thesis, you allowed me to pursue my PhD studies under your guidance. Your mentorship and confidence in my abilities have been immensely valuable. I am grateful for your willingness to discuss even the most minor research problems and for allowing me to present my research at international conferences and boost my confidence. I also want to acknowledge the reviewers, Assoc. Prof. Jussi Hepojoki and Dr. Ilona Rissanen, for their invaluable feedback and critical comments, which greatly enhanced the quality of this thesis. I am equally grateful to Prof. Tarja Sironen for accepting the invitation to serve as my opponent. I want to thank my thesis advisory board, Dr. Giuseppe Balistreri, Prof. Lotta-Riina Sundberg, and Dr. Silke Krol, for all the scientific discussions and suggestions that helped guide my thesis work. I also want to sincerely thank all my thesis collaborators for their invaluable contributions to different projects.

I want to give special mention to Prof. Antti Happala, who has worked closely with me on several projects and always answered my emails, even during the oddest of hours. I am grateful for two other people during my PhD journey: Prof. Jussi Toppari and Dr. Tanja Lahtinen. I have had the longest association with Jussi during my academic career, and I am glad you have guided me professionally and personally through these years. Even after moving out of your group following my master's studies, you still included me in all your closed celebrations and parties. With Tanja, even though we did not work so closely on projects, I always felt like there was somebody who cared about how I was doing. Your cheerful nature made me smile every time we met, and there was an instant connection.

Next, I would like to express my gratitude to all the current and former members of the Marjomäki group, including Paula, Mira, Visa, Helena, Dhanik, Ville S, Tino, Sara, Kerttu, Kati, Elina L, Abhishek, Marjo, Jun, Laura, Anni P, Suvi, Jenni, and Anni W. You all made my transition into this group smooth, and the working environment so positive to work in. I would especially like to thank Mira and Visa with whom I've had the longest association during my PhD journey. Thank you for guiding me through the early days of my doctoral studies. You both have been incredibly supportive and kind. Kati, although you weren't in the same research group, you have always been an incredible colleague, constantly checking in with your colleagues and making sure everything was okay with them. Your willingness to assist not only with work-related matters but also personal ones is genuinely appreciated. I am grateful for your efforts in

maintaining the dynamics between the B- and C-corridor people, which allowed me to make connections beyond the Marjomäki group. Finding colleagues like you three is a rare privilege, and I couldn't have wished for anything better! I also want to thank my workmates, Ardra, Chandan, Lina, Ankita, Alka, and Amit, who always listened to me when I needed them and advised me when I was stuck with a problem in the lab or life. I also want to acknowledge Anni P., who did her master's thesis on my PhD project. While guiding you, there was so much I learned as a researcher, that I am grateful to you and Varpu for letting me have this experience. There are genuinely no words adequate to convey my gratitude for the technical support provided by Petri, Laura, and Alli. Your technical assistance and lab management have been the cornerstone of my research. You three have always patiently addressed all my queries and lab problems. Petri, I have always enjoyed your company and quirky sense of humor. You always knew when things were a bit off and always checked on me during those times. Thank you so much!

Next, I'd like to thank my friends, who are like family here in Finland, Bhavesh, Kunal, Vaibhav, Leeni, Ardra, Elan, Praveen, Afra, Jaako, Disheet, Souvik, Subrato, Vaishnavi, Praful, Shriya, Anmol, Nisha, Shashank, Barani, Asha, Vijay, Shweta, Rahul, Yash, Nidhi, Ankit, Sarika, Subhash, Aswini, Manoj, Sachin, Priya, Anju, Divya, Akshay, Ajay, Suvarna, Ankita, Disha, and all the kids. I have created so many beautiful memories with all of you that this book may fall short of pages to express how grateful I am. I also want to thank my friends who have lived far away but have always remained close in my heart: Charmi, Prerna, Ruchita, Deepa, Saquib, Prasad, Nandita, Ronak, and Abhay. I want to give a special mention to Nisha and Aswini, who have helped me a lot in the thesis writing process.

I am extremely grateful to Dhanik and my family for their unwavering support and encouragement throughout my PhD journey. I want to especially thank my family - Dada, Dadi, Dad, Mom, Shreya, Swapna foe, and Shilpa foe who have always pushed me to work hard and dream big in life, making me capable of achieving so much. This accomplishment would not have been possible without your sacrifices and belief in me. So what if you don't have a doctor, you have a doctorate in the family.

Finally, I would like to express my heartfelt gratitude to my husband, Dhanik Reshamwala, who has been my life partner and my valued colleague for so many years. It was only because of your motivation and constant support that I embarked on this journey of doing a PhD and sailed through it smoothly. You have always understood my challenges, and your support has been like my pillar of strength. Also, sorry for constantly pushing you under the bus.

REFERENCES

Abad F.X., Villena C., Guix S., Caballero S., Pintó R.M. & Bosch A. 2001. Potential Role of Fomites in the Vehicular Transmission of Human Astroviruses. *Applied and Environmental Microbiology* 67: 3904–3907.

Abdelnabi R., Geraets J.A., Ma Y., Mirabelli C., Flatt J.W., Domanska A., Delang L., Jochmans D., Kumar T.A., Jayaprakash V., Sinha B.N., Leyssen P., Butcher S.J. & Neyts J. 2019. A novel druggable interprotomer pocket in the capsid of rhino- and enteroviruses. *PLOS Biology* 17: e3000281.

Aboubakr H.A., Sharafeldin T.A. & Goyal S.M. 2021. Stability of SARS-CoV-2 and other coronaviruses in the environment and on common touch surfaces and the influence of climatic conditions: A review. *Transboundary and Emerging Diseases* 68: 296–312.

Agudelo Gómez L., Betancur L. & González-Cardenete M. 2012. Anti HHV-1 and HHV-2 activity in vitro of abietic and dehydroabietic acid derivatives. *Pharmacologyonline* 1: 36.

Aldridge R.W., Lewer D., Beale S., Johnson A.M., Zambon M., Hayward A.C. & Fragaszy E.B. 2020. Seasonality and immunity to laboratory-confirmed seasonal coronaviruses (HCoV-NL63, HCoV-OC43, and HCoV-229E): results from the Flu Watch cohort study. *Wellcome Open Res*: 52–52.

Almqvist J., Granberg T., Tzortzakakis A., Klironomos S., Kollia E., Öhberg C., Martin R., Piehl F., Ouellette R. & Ineichen B.V. 2020. Neurological manifestations of coronavirus infections - a systematic review. *Annals of Clinical and Translational Neurology* 7: 2057–2071.

Atanasov A.G., Zotchev S.B., Dirsch V.M. & Supuran C.T. 2021. Natural products in drug discovery: advances and opportunities. *Nature Reviews. Drug Discovery* 20: 200–216.

Baggen J., Thibaut H.J., Strating J.R.P.M. & Kuppeveld F.J.M. van. 2018. The life cycle of non-polio enteroviruses and how to target it. *Nature Reviews. Microbiology* 16: 368–381.

Bajpai S.K. 2013. Silver nanoparticles loaded thermosensitive cotton fabric for antibacterial application - Sunil Kumar Bajpai, Manjula Bajpai, Leena Sharma, Murali Mohan Yallapu, 2014.

Bajpai P. 2018. Chapter 12 - Pulping Fundamentals. In: Bajpai P. (ed.), *Biermann's Handbook of Pulp and Paper (Third Edition)*, Elsevier, pp. 295–351.

Barnett J.R. 2004. Langenheim, J.H. Plant resins: chemistry, evolution, ecology and ethnobotany. *Annals of Botany* 93: 784–785.

Basavappa R., Syed R., Flore O., Icenogle J.P., Filman D.J. & Hogle J.M. 1994. Role and mechanism of the maturation cleavage of VP0 in poliovirus assembly: structure of the empty capsid assembly intermediate at 2.9 A resolution. *Protein Science : A Publication of the Protein Society* 3: 1651–1669.

Beconcini D., Felice F., Fabiano A., Sarmento B., Zambito Y. & Di Stefano R. 2020. Antioxidant and Anti-Inflammatory Properties of Cherry Extract:

Nanosystems-Based Strategies to Improve Endothelial Function and Intestinal Absorption. *Foods* 9: 207.

Bell S.H., Fairley D.J., Kettunen H., Vuorenmaa J., Orte J., Bamford C.G.G. & McGrath J.W. 2021. Rosin Soap Exhibits Virucidal Activity. *Microbiology Spectrum* 9: e0109121.

Bhattacharya S.K., Goel R.K., Kaur R. & Ghosal S. 1987. Anti-stress activity of sitoindosides VII and VIII, new acylsterylglucosides from Withania somnifera. *Phytotherapy Research* 1: 32–37.

Biryukov J., Boydston J.A., Dunning R.A., Yeager J.J., Wood S., Reese A.L., Ferris A., Miller D., Weaver W., Zeitouni N.E., Phillips A., Freeburger D., Hooper I., Ratnesar-Shumate S., Yolitz J., Krause M., Williams G., Dawson D.G., Herzog A., Dabisch P., Wahl V., Hevey M.C. & Altamura L.A. 2020. Increasing Temperature and Relative Humidity Accelerates Inactivation of SARS-CoV-2 on Surfaces. *mSphere* 5: e00441-20.

B'Krong N.T.T.C., Minh N.N.Q., Qui P.T., Chau T.T.H., Nghia H.D.T., Do L.A.H., Nhung N.N., Van Vinh Chau N., Thwaites G., Van Tan L., Doorn H.R. van & Thanh T.T. 2018. Enterovirus serotypes in patients with central nervous system and respiratory infections in Viet Nam 1997–2010. *Virology Journal* 15: 69.

Blázquez E., Rodríguez C., Ródenas J., Navarro N., Riquelme C., Rosell R., Campbell J., Crenshaw J., Segalés J., Pujols J. & Polo J. 2019. Evaluation of the effectiveness of the SurePure Turbulator ultraviolet-C irradiation equipment on inactivation of different enveloped and non-enveloped viruses inoculated in commercially collected liquid animal plasma. *PloS One* 14: e0212332.

Bohan D., Van Ert H., Ruggio N., Rogers K.J., Badreddine M., Aguilar Briseño J.A., Elliff J.M., Rojas Chavez R.A., Gao B., Stokowy T., Christakou E., Kursula P., Micklem D., Gausdal G., Haim H., Minna J., Lorens J.B. & Maury W. 2021. Phosphatidylserine receptors enhance SARS-CoV-2 infection. *PLoS pathogens* 17: e1009743.

Borkow G. & Gabbay J. 2004. Putting copper into action: copper-impregnated products with potent biocidal activities. *FASEB journal: official publication of the Federation of American Societies for Experimental Biology* 18: 1728–1730.

Bosch B.J., Bartelink W. & Rottier P.J.M. 2008. Cathepsin L Functionally Cleaves the Severe Acute Respiratory Syndrome Coronavirus Class I Fusion Protein Upstream of Rather than Adjacent to the Fusion Peptide. *Journal of Virology* 82: 8887–8890.

Bouin A., Gretteau P.-A., Wehbe M., Renois F., N'Guyen Y., Lévêque N., Vu M.N., Tracy S., Chapman N.M., Bruneval P., Fornes P., Semler B.L. & Andreoletti L. 2019. Enterovirus Persistence in Cardiac Cells of Patients With Idiopathic Dilated Cardiomyopathy Is Linked to 5′ Terminal Genomic RNA-Deleted Viral Populations With Viral-Encoded Proteinase Activities. *Circulation* 139: 2326–2338.

Bourgaud F., Gravot A., Milesi S. & Gontier E. 2001. Production of plant secondary metabolites: a historical perspective. *Plant Science* 161: 839–851.

Brandenburg B., Lee L.Y., Lakadamyali M., Rust M.J., Zhuang X. & Hogle J.M. 2007. Imaging Poliovirus Entry in Live Cells. *PLoS Biology* 5: e183.
Bruenke J., Roschke I., Agarwal S., Riemann T. & Greiner A. 2016. Quantitative Comparison of the Antimicrobial Efficiency of Leaching versus Nonleaching Polymer Materials. *Macromolecular Bioscience* 16: 647–654.
Caldeira E., Piskin E., Granadeiro L., Silva F. & Gouveia I.C. 2013. Biofunctionalization of cellulosic fibres with L-cysteine: assessment of antibacterial properties and mechanism of action against Staphylococcus aureus and Klebsiella pneumoniae. *Journal of Biotechnology* 168: 426–435.
Cantuti-Castelvetri L., Ojha R., Pedro L.D., Djannatian M., Franz J., Kuivanen S., Meer F. van der, Kallio K., Kaya T., Anastasina M., Smura T., Levanov L., Szirovicza L., Tobi A., Kallio-Kokko H., Österlund P., Joensuu M., Meunier F.A., Butcher S.J., Winkler M.S., Mollenhauer B., Helenius A., Gokce O., Teesalu T., Hepojoki J., Vapalahti O., Stadelmann C., Balistreri G. & Simons M. 2020. Neuropilin-1 facilitates SARS-CoV-2 cell entry and infectivity. *Science (New York, N.y.)* 370: 856–860.
Casanova L.M., Jeon S., Rutala W.A., Weber D.J. & Sobsey M.D. 2010a. Effects of Air Temperature and Relative Humidity on Coronavirus Survival on Surfaces. *Applied and Environmental Microbiology* 76: 2712–2717.
Casanova L.M., Jeon S., Rutala W.A., Weber D.J. & Sobsey M.D. 2010b. Effects of Air Temperature and Relative Humidity on Coronavirus Survival on Surfaces. *Applied and Environmental Microbiology* 76: 2712–2717.
Cassidy C., Dever D., Stanbery L., Edelman G., Dworkin L. & Nemunaitis J. 2020. FDA efficiency for approval process of COVID-19 therapeutics. *Infectious Agents and Cancer* 15.
Castaño N., Cordts S.C., Kurosu Jalil M., Zhang K.S., Koppaka S., Bick A.D., Paul R. & Tang S.K.Y. 2021. Fomite Transmission, Physicochemical Origin of Virus–Surface Interactions, and Disinfection Strategies for Enveloped Viruses with Applications to SARS-CoV-2. *ACS Omega* 6: 6509–6527.
Ćavar Zeljković S., Šišková J., Komzáková K., De Diego N., Kaffková K. & Tarkowski P. 2021. Phenolic Compounds and Biological Activity of Selected Mentha Species. *Plants* 10: 550.
Chan K.H., Peiris J.S.M., Lam S.Y., Poon L.L.M., Yuen K.Y. & Seto W.H. 2011. The Effects of Temperature and Relative Humidity on the Viability of the SARS Coronavirus. *Advances in Virology* 2011: 1–7.
Chase A.J. & Semler B.L. 2012. Viral subversion of host functions for picornavirus translation and RNA replication. *Future virology* 7: 179–191.
Chatterjee S., Murallidharan J.S., Agrawal A. & Bhardwaj R. 2021. Why coronavirus survives longer on impermeable than porous surfaces. *Physics of Fluids* 33: 021701.
Chen L., Cao H. & Xiao J. 2018. 2 - Polyphenols: Absorption, bioavailability, and metabolomics. In: Galanakis C.M. (ed.), *Polyphenols: Properties, Recovery, and Applications*, Woodhead Publishing, pp. 45–67.
Chen Z. & Sun Y. 2006. N-Halamine-Based Antimicrobial Additives for Polymers. *Industrial & engineering chemistry research* 45: 2634–2640.

Chin A.W.H., Chu J.T.S., Perera M.R.A., Hui K.P.Y., Yen H.-L., Chan M.C.W., Peiris M. & Poon L.L.M. 2020. Stability of SARS-CoV-2 in different environmental conditions. *The Lancet Microbe* 1: e10.

Choi H., Chatterjee P., Lichtfouse E., Martel J.A., Hwang M., Jinadatha C. & Sharma V.K. 2021. Classical and alternative disinfection strategies to control the COVID-19 virus in healthcare facilities: a review. *Environmental Chemistry Letters* 19: 1945–1951.

Choi H.-N., Jeong S.-M., Huh G.H. & Kim J.-I. 2015. Quercetin ameliorates insulin sensitivity and liver steatosis partly by increasing adiponectin expression in ob/ob mice. *Food Science and Biotechnology* 24: 273–279.

Chojnacka K., Skrzypczak D., Izydorczyk G., Mikula K., Szopa D. & Witek-Krowiak A. 2021. Antiviral Properties of Polyphenols from Plants. *Foods* 10.

Ciejka J., Wolski K., Nowakowska M., Pyrc K. & Szczubiałka K. 2017. Biopolymeric nano/microspheres for selective and reversible adsorption of coronaviruses. *Materials Science & Engineering. C, Materials for Biological Applications* 76: 735–742.

Ciesek S., Hahn T. von, Colpitts C.C., Schang L.M., Friesland M., Steinmann J., Manns M.P., Ott M., Wedemeyer H., Meuleman P., Pietschmann T. & Steinmann E. 2011. The green tea polyphenol, epigallocatechin-3-gallate, inhibits hepatitis C virus entry. *Hepatology* 54: 1947–1955.

Clausen T.M., Sandoval D.R., Spliid C.B., Pihl J., Perrett H.R., Painter C.D., Narayanan A., Majowicz S.A., Kwong E.M., McVicar R.N., Thacker B.E., Glass C.A., Yang Z., Torres J.L., Golden G.J., Bartels P.L., Porell R.N., Garretson A.F., Laubach L., Feldman J., Yin X., Pu Y., Hauser B.M., Caradonna T.M., Kellman B.P., Martino C., Gordts P.L.S.M., Chanda S.K., Schmidt A.G., Godula K., Leibel S.L., Jose J., Corbett K.D., Ward A.B., Carlin A.F. & Esko J.D. 2020. SARS-CoV-2 Infection Depends on Cellular Heparan Sulfate and ACE2. *Cell* 183: 1043-1057.e15.

Conlon J.M., Al-Ghaferi N., Abraham B. & Leprince J. 2007. Strategies for transformation of naturally-occurring amphibian antimicrobial peptides into therapeutically valuable anti-infective agents. *Methods* 42: 349–357.

Coronavirus Disease 2019. 2020. *Centers for Disease Control and Prevention*.

Cortese M., Lee J.-Y., Cerikan B., Neufeldt C.J., Oorschot V.M.J., Köhrer S., Hennies J., Schieber N.L., Ronchi P., Mizzon G., Romero-Brey I., Santarella-Mellwig R., Schorb M., Boermel M., Mocaer K., Beckwith M.S., Templin R.M., Gross V., Pape C., Tischer C., Frankish J., Horvat N.K., Laketa V., Stanifer M., Boulant S., Ruggieri A., Chatel-Chaix L., Schwab Y. & Bartenschlager R. 2020. Integrative Imaging Reveals SARS-CoV-2-Induced Reshaping of Subcellular Morphologies. *Cell Host & Microbe* 28: 853-866.e5.

Dales S., Eggers H.J., Tamm I. & Palade G.E. 1965. Electron microscopic study of the formation of poliovirus. *Virology* 26: 379–389.

Delgado K., Quijada R., Palma R. & Palza H. 2011. Polypropylene with embedded copper metal or copper oxide nanoparticles as a novel plastic antimicrobial agent. *Letters in Applied Microbiology* 53: 50–54.

Denison M.R., Graham R.L., Donaldson E.F., Eckerle L.D. & Baric R.S. 2011. Coronaviruses. *RNA Biology* 8: 270–279.
Dhiman G. & Chakraborty J.N. 2015. Antimicrobial performance of cotton finished with triclosan, silver and chitosan. *Fashion and Textiles* 2: 13.
Di Lorenzo C., Colombo F., Biella S., Stockley C. & Restani P. 2021. Polyphenols and Human Health: The Role of Bioavailability. *Nutrients* 13: 273.
Dominguez S.R., Robinson C.C. & Holmes K.V. 2009. Detection of four human coronaviruses in respiratory infections in children: A one-year study in Colorado. *Journal of Medical Virology* 81: 1597–1604.
Dong X., Dong M., Lu Y., Turley A., Jin T. & Wu C. 2011. Antimicrobial and antioxidant activities of lignin from residue of corn stover to ethanol production. *Industrial Crops and Products* 34: 1629–1634.
Doremalen N. van, Bushmaker T., Morris D.H., Holbrook M.G., Gamble A., Williamson B.N., Tamin A., Harcourt J.L., Thornburg N.J., Gerber S.I., Lloyd-Smith J.O., Wit E. de & Munster V.J. 2020a. Aerosol and Surface Stability of SARS-CoV-2 as Compared with SARS-CoV-1. *The New England Journal of Medicine*: NEJMc2004973.
Doremalen N. van, Bushmaker T., Morris D.H., Holbrook M.G., Gamble A., Williamson B.N., Tamin A., Harcourt J.L., Thornburg N.J., Gerber S.I., Lloyd-Smith J.O., Wit E. de & Munster V.J. 2020b. Aerosol and Surface Stability of SARS-CoV-2 as Compared with SARS-CoV-1. *New England Journal of Medicine* 382: 1564–1567.
Doremalen N. van, Bushmaker T. & Munster V.J. 2013. Stability of Middle East respiratory syndrome coronavirus (MERS-CoV) under different environmental conditions. *Euro Surveillance: Bulletin Europeen Sur Les Maladies Transmissibles = European Communicable Disease Bulletin* 18: 20590.
Duan S.-M., Zhao X., Wen R.-F., Huang J.-J., Pi G.-H., Zhang S.-X., Han J., Bi S.-L., Ruan L., Dong X.-P. & Team S.R. 2003. Stability of SARS Coronavirus in Human Specimens and Environment and Its Sensitivity to Heating and UV Irradiation. *Biomedical and Environmental Sciences* 16: 246–255.
Ebenezer K.S., Manivannan R., Punniyamoorthy A. & Tamilselvan C. 2019. Plant Secondary Metabolites of Antiviral Properties a Rich Medicinal Source for Drug Discovery: A Mini Review. *Journal of Drug Delivery and Therapeutics* 9: 161–167.
Eckerle L.D., Lu X., Sperry S.M., Choi L. & Denison M.R. 2007. High fidelity of murine hepatitis virus replication is decreased in nsp14 exoribonuclease mutants. *Journal of Virology* 81: 12135–12144.
Engelenburg F.A.C. van, Terpstra F.G., Schuitemaker H. & Moorer W.R. 2002. The virucidal spectrum of a high concentration alcohol mixture. *Journal of Hospital Infection* 51: 121–125.
Fernandez-Tomas C.B. & Baltimore D. 1973. Morphogenesis of Poliovirus II. Demonstration of a New Intermediate, the Proviron. *Journal of Virology* 12: 1122–1130.
Fields B.N. 2013. *Fields virology* Knipe D.M. & Howley P.M. (eds.). Wolters Kluwer Health/Lippincott Williams & Wilkins, Philadelphia.

Firquet S., Beaujard S., Lobert P.-E., Sané F., Caloone D., Izard D. & Hober D. 2015. Survival of Enveloped and Non-Enveloped Viruses on Inanimate Surfaces. *Microbes and Environments* 30: 140–144.

Flechas M.C., Ocazionez R.E. & Stashenko E.E. 2017. Evaluation of in vitro Antiviral Activity of Essential Oil Compounds Against Dengue Virus. *Pharmacognosy Journal* 10: 55–59.

Franzini F., Toivonen R. & Toppinen A. 2018. Why Not Wood? Benefits and Barriers of Wood as a Multistory Construction Material: Perceptions of Municipal Civil Servants from Finland. *Buildings* 8: 159.

Gebel J., Exner M., French G., Chartier Y., Christiansen B., Gemein S., Goroncy-Bermes P., Hartemann P., Heudorf U., Kramer A., Maillard J.-Y., Oltmanns P., Rotter M. & Sonntag H.-G. 2013. The role of surface disinfection in infection prevention. *GMS hygiene and infection control* 8: Doc10.

Geng Y. & Wang Y. 2023. Stability and transmissibility of SARS-CoV-2 in the environment. *Journal of Medical Virology* 95: e28103.

Ghosh S., Dellibovi-Ragheb T.A., Kerviel A., Pak E., Qiu Q., Fisher M., Takvorian P.M., Bleck C., Hsu V.W., Fehr A.R., Perlman S., Achar S.R., Straus M.R., Whittaker G.R., Haan C.A.M. de, Kehrl J., Altan-Bonnet G. & Altan-Bonnet N. 2020. β-Coronaviruses Use Lysosomes for Egress Instead of the Biosynthetic Secretory Pathway. *Cell* 183: 1520-1535.e14.

González M.A., Pérez-Guaita D., Correa-Royero J., Zapata B., Agudelo L., Mesa-Arango A. & Betancur-Galvis L. 2010. Synthesis and biological evaluation of dehydroabietic acid derivatives. *European Journal of Medicinal Chemistry* 45: 811–816.

Granato D., Reshamwala D., Korpinen R., Azevedo L., Vieira do Carmo M.A., Cruz T.M., Marques M.B., Wen M., Zhang L., Marjomäki V. & Kilpeläinen P. 2022. From the forest to the plate – Hemicelluloses, galactoglucomannan, glucuronoxylan, and phenolic-rich extracts from unconventional sources as functional food ingredients. *Food Chemistry* 381: 132284.

Grass G., Rensing C. & Solioz M. 2011. Metallic Copper as an Antimicrobial Surface. *Applied and Environmental Microbiology* 77: 1541–1547.

Grassi D., Draijer R., Schalkwijk C., Desideri G., D'Angeli A., Francavilla S., Mulder T. & Ferri C. 2016. Black Tea Increases Circulating Endothelial Progenitor Cells and Improves Flow Mediated Dilatation Counteracting Deleterious Effects from a Fat Load in Hypertensive Patients: A Randomized Controlled Study. *Nutrients* 8: 727.

Greatorex J.S., Digard P., Curran M.D., Moynihan R., Wensley H., Wreghitt T., Varsani H., Garcia F., Enstone J. & Nguyen-Van-Tam J.S. 2011. Survival of Influenza A(H1N1) on Materials Found in Households: Implications for Infection Control. *PLoS ONE* 6: e27932.

Guettler K. 2011. How Does Rosin Affect Sound? *String Research Journal* 2: 37–48.

Gulati A., Pomeranz C., Qamar Z., Thomas S., Frisch D., George G., Summer R., DeSimone J. & Sundaram B. 2020. A Comprehensive Review of

Manifestations of Novel Coronaviruses in the Context of Deadly COVID-19 Global Pandemic. *The American Journal of the Medical Sciences* 360: 5–34.
Guo M., Tao W., Flavell R.A. & Zhu S. 2021. Potential intestinal infection and faecal–oral transmission of SARS-CoV-2. *Nature Reviews. Gastroenterology & Hepatology* 18: 269–283.
Hagemeijer M.C., Monastyrska I., Griffith J., Sluijs P. van der, Voortman J., Bergen en Henegouwen P.M. van, Vonk A.M., Rottier P.J.M., Reggiori F. & Haan C.A.M. de. 2014. Membrane rearrangements mediated by coronavirus nonstructural proteins 3 and 4. *Virology* 458: 125–135.
Haldar J., An D., Álvarez de Cienfuegos L., Chen J. & Klibanov A.M. 2006. Polymeric coatings that inactivate both influenza virus and pathogenic bacteria. *Proceedings of the National Academy of Sciences* 103: 17667–17671.
Hall C.B., Douglas R.G. Jr. & Geiman J.M. 1980. Possible Transmission by Fomites of Respiratory Syncytial Virus. *The Journal of Infectious Diseases* 141: 98–102.
Hasan J., Xu Y., Yarlagadda T., Schuetz M., Spann K. & Yarlagadda P.K. 2020. Antiviral and Antibacterial Nanostructured Surfaces with Excellent Mechanical Properties for Hospital Applications. *ACS biomaterials science & engineering* 6: 3608–3618.
Hayawi K., Shahriar S., Serhani M.A., Alashwal H. & Masud M.M. 2021. Vaccine versus Variants (3Vs): Are the COVID-19 Vaccines Effective against the Variants? A Systematic Review. *Vaccines* 9: 1305.
Höfer R. 2015a. Chapter 3B - The Pine Biorefinery Platform Chemicals Value Chain. In: Pandey A., Höfer R., Taherzadeh M., Nampoothiri K.M. & Larroche C. (eds.), *Industrial Biorefineries & White Biotechnology*, Elsevier, Amsterdam, pp. 127–155.
Höfer R. 2015b. Chapter 3B - The Pine Biorefinery Platform Chemicals Value Chain. In: Pandey A., Höfer R., Taherzadeh M., Nampoothiri K.M. & Larroche C. (eds.), *Industrial Biorefineries & White Biotechnology*, Elsevier, Amsterdam, pp. 127–155.
Hoffmann M., Kleine-Weber H., Schroeder S., Krüger N., Herrler T., Erichsen S., Schiergens T.S., Herrler G., Wu N.-H., Nitsche A., Müller M.A., Drosten C. & Pöhlmann S. 2020. SARS-CoV-2 Cell Entry Depends on ACE2 and TMPRSS2 and Is Blocked by a Clinically Proven Protease Inhibitor. *Cell* 181: 271-280.e8.
Hogle J.M., Chow M. & Filman D.J. 1985. Three-Dimensional Structure of Poliovirus at 2.9 Å Resolution. *Science* 229: 1358–1365.
Hulswit R.J.G., Lang Y., Bakkers M.J.G., Li W., Li Z., Schouten A., Ophorst B., Kuppeveld F.J.M. van, Boons G.-J., Bosch B.-J., Huizinga E.G. & Groot R.J. de. 2019. Human coronaviruses OC43 and HKU1 bind to 9-O-acetylated sialic acids via a conserved receptor-binding site in spike protein domain A. *Proceedings of the National Academy of Sciences* 116: 2681–2690.
Hussein R.A., El-Anssary A.A., Hussein R.A. & El-Anssary A.A. 2018. Plants Secondary Metabolites: The Key Drivers of the Pharmacological Actions of Medicinal Plants. In: *Herbal Medicine*, IntechOpen.

Inoue Y., Tanaka N., Tanaka Y., Inoue S., Morita K., Zhuang M., Hattori T. & Sugamura K. 2007. Clathrin-Dependent Entry of Severe Acute Respiratory Syndrome Coronavirus into Target Cells Expressing ACE2 with the Cytoplasmic Tail Deleted. *Journal of Virology* 81: 8722–8729.

ISO 21702:2019. 2020. ISO 21702:2019. *ISO*.

Jackson C.B., Farzan M., Chen B. & Choe H. 2022. Mechanisms of SARS-CoV-2 entry into cells. *Nature Reviews Molecular Cell Biology* 23: 3–20.

Jacobs S.E., Lamson D.M., St. George K. & Walsh T.J. 2013. Human Rhinoviruses. *Clinical Microbiology Reviews* 26: 135–162.

Jokinen J.J. & Sipponen A. 2016. Refined Spruce Resin to Treat Chronic Wounds: Rebirth of an Old Folkloristic Therapy. *Advances in Wound Care* 5: 198–207.

Kadir R. & Hassan B. 2020. Toxicity and repellent effects of wood extractives of five Malaysian wood species on Asian subterranean termite Coptotermes gestroi Wasmann. *European Journal of Wood and Wood Products* 78: 1249–1262.

Kamitani W., Narayanan K., Huang C., Lokugamage K., Ikegami T., Ito N., Kubo H. & Makino S. 2006. Severe acute respiratory syndrome coronavirus nsp1 protein suppresses host gene expression by promoting host mRNA degradation. *Proceedings of the National Academy of Sciences of the United States of America* 103: 12885–12890.

Kanerva M., Puolakka A., Takala T.M., Elert A.M., Mylläri V., Jönkkäri I., Sarlin E., Seitsonen J., Ruokolainen J., Saris P. & Vuorinen J. 2019. Antibacterial polymer fibres by rosin compounding and melt-spinning. *Materials Today Communications* 20: 100527.

Kaur N., Singh R., Dar Z., Bijarnia R.K., Dhingra N. & Kaur T. 2021. Genetic comparison among various coronavirus strains for the identification of potential vaccine targets of SARS-CoV2. *Infection, Genetics and Evolution* 89: 104490.

Khan A.G., Pickl-Herk A., Gajdzik L., Marlovits T.C., Fuchs R. & Blaas D. 2010. Human rhinovirus 14 enters rhabdomyosarcoma cells expressing icam-1 by a clathrin-, caveolin-, and flotillin-independent pathway. *Journal of Virology* 84: 3984–3992.

Kiltie A.E. & Ryan A.J. 1997. SYBR Green I staining of pulsed field agarose gels is a sensitive and inexpensive way of quantitating DNA double-strand breaks in mammalian cells. *Nucleic Acids Research* 25: 2945–2946.

Kim C. & Bergelson J.M. 2012. Echovirus 7 entry into polarized intestinal epithelial cells requires clathrin and Rab7. *mBio* 3: e00304-11.

Kim S.J., Si J., Lee J.E. & Ko G. 2012. Temperature and Humidity Influences on Inactivation Kinetics of Enteric Viruses on Surfaces. *Environmental Science & Technology* 46: 13303–13310.

Kirsanov K.I., Lesovaya E.A., Yakubovskaya M.G. & Belitsky G.A. 2010. SYBR Gold and SYBR Green II are not mutagenic in the Ames test. *Mutation Research* 699: 1–4.

Kramer A., Schwebke I. & Kampf G. 2006. How long do nosocomial pathogens persist on inanimate surfaces? A systematic review. *BMC infectious diseases* 6: 130.
Kugler S., Ossowicz P., Malarczyk-Matusiak K. & Wierzbicka E. 2019. Advances in Rosin-Based Chemicals: The Latest Recipes, Applications and Future Trends. *Molecules* 24: 1651.
Kumar S. & Pandey A.K. 2013. Chemistry and Biological Activities of Flavonoids: An Overview. *The Scientific World Journal* 2013: 162750.
Kumar S., Singh R., Kumari N., Karmakar S., Behera M., Siddiqui A.J., Rajput V.D., Minkina T., Bauddh K. & Kumar N. 2021. Current understanding of the influence of environmental factors on SARS-CoV-2 transmission, persistence, and infectivity. *Environmental Science and Pollution Research International* 28: 6267–6288.
Laajala M. & Marjomäki V. 2019. A Common Receptor Found for Echoviruses. *Trends in Microbiology* 27: 475–477.
Lai J.K.F., Sam I.-C. & Chan Y.F. 2016. The Autophagic Machinery in Enterovirus Infection. *Viruses* 8: 32.
Laireiter M., Schnabel T., Köck A. & Stalzer P. 2013. Active anti-microbial effects of larch and pine wood on four bacterial strains :: BioResources.
Law K.-Y. 2014. Definitions for Hydrophilicity, Hydrophobicity, and Superhydrophobicity: Getting the Basics Right. *The Journal of Physical Chemistry Letters* 5: 686–688.
Layas K.I., Chatterjee P.K. & Pannala A.S. 2022. Protective Effects of Resveratrol Encapsulated In Liposomes or PLA Nanoparticles against Oxidative Stress in NRK-52E Cells. *Nanoparticle* 3: 1–0.
Lee K.Y. 2016. Enterovirus 71 infection and neurological complications. *Korean Journal of Pediatrics* 59: 395–401.
Leung N.H.L. 2021. Transmissibility and transmission of respiratory viruses. *Nature Reviews. Microbiology* 19: 528–545.
Li W., Moore M.J., Vasilieva N., Sui J., Wong S.K., Berne M.A., Somasundaran M., Sullivan J.L., Luzuriaga K., Greenough T.C., Choe H. & Farzan M. 2003. Angiotensin-converting enzyme 2 is a functional receptor for the SARS coronavirus. *Nature* 426: 450–454.
Li R., Narita R., Nishimura H., Marumoto S., Yamamoto S.P., Ouda R., Yatagai M., Fujita T. & Watanabe T. 2018. Antiviral Activity of Phenolic Derivatives in Pyroligneous Acid from Hardwood, Softwood, and Bamboo. *ACS Sustainable Chemistry & Engineering* 6: 119–126.
Li M. & Xu Z. 2008. Quercetin in a lotus leaves extract may be responsible for antibacterial activity. *Archives of Pharmacal Research* 31: 640–644.
Lin Q., Lim J.Y.C., Xue K., Yew P.Y.M., Owh C., Chee P.L. & Loh X.J. 2020. Sanitizing agents for virus inactivation and disinfection. *View (Beijing, China)* 1: e16.
Liu D.X., Liang J.Q. & Fung T.S. 2021. Human Coronavirus-229E, -OC43, -NL63, and -HKU1 (Coronaviridae). *Encyclopedia of Virology*: 428–440.

Liu L., Ma H., Yang N., Tang Y., Guo J., Tao W. & Duan J. 2010. A Series of Natural Flavonoids as Thrombin Inhibitors: Structure-activity relationships. *Thrombosis Research* 126: e365–e378.

Lopresti A.L., Smith S.J., Malvi H. & Kodgule R. 2019. An investigation into the stress-relieving and pharmacological actions of an ashwagandha (Withania somnifera) extract. *Medicine* 98: e17186.

Lu S., Ye Q., Singh D., Cao Y., Diedrich J.K., Yates J.R., Villa E., Cleveland D.W. & Corbett K.D. 2021. The SARS-CoV-2 nucleocapsid phosphoprotein forms mutually exclusive condensates with RNA and the membrane-associated M protein. *Nature Communications* 12: 502.

Lu R., Zhao X., Li J., Niu P., Yang B., Wu H., Wang W., Song H., Huang B., Zhu N., Bi Y., Ma X., Zhan F., Wang L., Hu T., Zhou H., Hu Z., Zhou W., Zhao L., Chen J., Meng Y., Wang J., Lin Y., Yuan J., Xie Z., Ma J., Liu W.J., Wang D., Xu W., Holmes E.C., Gao G.F., Wu G., Chen W., Shi W. & Tan W. 2020. Genomic characterisation and epidemiology of 2019 novel coronavirus: implications for virus origins and receptor binding. *The Lancet* 395: 565–574.

Mahanta U., Khandelwal M. & Deshpande A.S. 2021. Antimicrobial surfaces: a review of synthetic approaches, applicability and outlook. *Journal of Materials Science* 56: 17915–17941.

Mahmood A., Eqan M., Pervez S., Alghamdi H.A., Tabinda A.B., Yasar A., Brindhadevi K. & Pugazhendhi A. 2020. COVID-19 and frequent use of hand sanitizers; human health and environmental hazards by exposure pathways. *Science of The Total Environment* 742: 140561.

Makarov V.A., Braun H., Richter M., Riabova O.B., Kirchmair J., Kazakova E.S., Seidel N., Wutzler P. & Schmidtke M. 2015. Pyrazolopyrimidines: Potent Inhibitors Targeting the Capsid of Rhino- and Enteroviruses. *ChemMedChem* 10: 1629–1634.

Malin J.J., Suárez I., Priesner V., Fätkenheuer G. & Rybniker J. 2020. Remdesivir against COVID-19 and Other Viral Diseases. *Clinical Microbiology Reviews* 34: e00162-20.

Marjomäki V., Pietiäinen V., Matilainen H., Upla P., Ivaska J., Nissinen L., Reunanen H., Huttunen P., Hyypiä T. & Heino J. 2002. Internalization of Echovirus 1 in Caveolae. *Journal of Virology* 76: 1856–1865.

Martikainen M., Salorinne K., Lahtinen T., Malola S., Permi P., Häkkinen H. & Marjomäki V. 2015. Hydrophobic pocket targeting probes for enteroviruses. *Nanoscale* 7: 17457–17467.

Masters P.S. 2006. The Molecular Biology of Coronaviruses. In: *Advances in Virus Research*, Academic Press, pp. 193–292.

Mastromarino P., Capobianco D., Cannata F., Nardis C., Mattia E., De Leo A., Restignoli R., Francioso A. & Mosca L. 2015. Resveratrol inhibits rhinovirus replication and expression of inflammatory mediators in nasal epithelia. *Antiviral Research* 123: 15–21.

Matz J. 2013. Vapendavir significantly improves upper respiratory symptoms of naturally acquired rhinovirus infection in asthmatic adults: Results of a phase 2 clinical trial. *European Respiratory Journal* 42.

Mbithi J.N., Springthorpe V.S. & Sattar S.A. 1991. Effect of relative humidity and air temperature on survival of hepatitis A virus on environmental surfaces. *Applied and Environmental Microbiology* 57: 1394–1399.
McCormack S., Ramjee G., Kamali A., Rees H., Crook A.M., Gafos M., Jentsch U., Pool R., Chisembele M., Kapiga S., Mutemwa R., Vallely A., Palanee T., Sookrajh Y., Lacey C.J., Darbyshire J., Grosskurth H., Profy A., Nunn A., Hayes R. & Weber J. 2010. PRO2000 vaginal gel for prevention of HIV-1 infection (Microbicides Development Programme 301): a phase 3, randomised, double-blind, parallel-group trial. *Lancet* 376: 1329–1337.
Milewska A., Nowak P., Owczarek K., Szczepanski A., Zarebski M., Hoang A., Berniak K., Wojarski J., Zeglen S., Baster Z., Rajfur Z. & Pyrc K. 2018. Entry of Human Coronavirus NL63 into the Cell. *Journal of Virology* 92: e01933-17.
Morawska L. & Cao J. 2020. Airborne transmission of SARS-CoV-2: The world should face the reality. *Environment International* 139: 105730.
Muckelbauer J.K., Kremer M., Minor I., Diana G., Dutko F.J., Groarke J., Pevear D.C. & Rossmann M.G. 1995. The structure of coxsackievirus B3 at 3.5 å resolution. *Structure* 3: 653–667.
Munir M.T., Pailhories H., Eveillard M., Aviat F., Lepelletier D., Belloncle C. & Federighi M. 2019. Antimicrobial Characteristics of Untreated Wood: Towards a Hygienic Environment. *Health* 11: 152–170.
Myllynen M., Kazmertsuk A. & Marjomäki V. 2016. A Novel Open and Infectious Form of Echovirus 1. *Journal of Virology* 90: 6759–6770.
Nawrot-Chorabik K., Sułkowska M. & Gumulak N. 2022. Secondary Metabolites Produced by Trees and Fungi: Achievements So Far and Challenges Remaining. *Forests* 13: 1338.
Nekoua M.P., Alidjinou E.K. & Hober D. 2022. Persistent coxsackievirus B infection and pathogenesis of type 1 diabetes mellitus. *Nature Reviews Endocrinology* 18: 503–516.
Neuman B.W., Kiss G., Kunding A.H., Bhella D., Baksh M.F., Connelly S., Droese B., Klaus J.P., Makino S., Sawicki S.G., Siddell S.G., Stamou D.G., Wilson I.A., Kuhn P. & Buchmeier M.J. 2011. A structural analysis of M protein in coronavirus assembly and morphology. *Journal of Structural Biology* 174: 11–22.
Nhuchhen D., Basu P. & Acharya B. 2014. A Comprehensive Review on Biomass Torrefaction. *International Journal of Renewable Energy & Biofuels*: 1–56.
Nikonov O.S., Chernykh E.S., Garber M.B. & Nikonova E.Yu. 2017. Enteroviruses: Classification, diseases they cause, and approaches to development of antiviral drugs. *Biochemistry. Biokhimiia* 82: 1615–1631.
Nomura R., Kiyota A., Suzaki E., Kataoka K., Ohe Y., Miyamoto K., Senda T. & Fujimoto T. 2004. Human Coronavirus 229E Binds to CD13 in Rafts and Enters the Cell through Caveolae. *Journal of Virology* 78: 8701–8708.
Novak J.E. & Kirkegaard K. 1991. Improved method for detecting poliovirus negative strands used to demonstrate specificity of positive-strand

encapsidation and the ratio of positive to negative strands in infected cells. *Journal of Virology* 65: 3384–3387.
Noyce J.O., Michels H. & Keevil C.W. 2007. Inactivation of Influenza A Virus on Copper versus Stainless Steel Surfaces. *Applied and Environmental Microbiology* 73: 2748–2750.
Oberste M.S., Moore D., Anderson B., Pallansch M.A., Pevear D.C. & Collett M.S. 2009. In Vitro Antiviral Activity of V-073 against Polioviruses. *Antimicrobial Agents and Chemotherapy* 53: 4501–4503.
Oswin H.P., Haddrell A.E., Otero-Fernandez M., Mann J.F.S., Cogan T.A., Hilditch T.G., Tian J., Hardy D.A., Hill D.J., Finn A., Davidson A.D. & Reid J.P. 2022. The dynamics of SARS-CoV-2 infectivity with changes in aerosol microenvironment. *Proceedings of the National Academy of Sciences of the United States of America* 119: e2200109119.
Owczarek K., Szczepanski A., Milewska A., Baster Z., Rajfur Z., Sarna M. & Pyrc K. 2018. Early events during human coronavirus OC43 entry to the cell. *Scientific Reports* 8: 7124.
Owen L., Shivkumar M., Cross R.B.M. & Laird K. 2021. Porous surfaces: stability and recovery of coronaviruses. *Interface Focus* 12: 20210039.
Palmenberg A.C. 1982. In vitro synthesis and assembly of picornaviral capsid intermediate structures. *Journal of Virology* 44: 900–906.
Pandey A., Bani S., Dutt P., Kumar Satti N., Avtar Suri K. & Nabi Qazi G. 2018. Multifunctional neuroprotective effect of Withanone, a compound from Withania somnifera roots in alleviating cognitive dysfunction. *Cytokine* 102: 211–221.
Paul C.W. 2002. Chapter 15 - Hot melt adhesives. In: Dillard D.A., Pocius A.V. & Chaudhury M. (eds.), *Adhesion Science and Engineering*, Elsevier Science B.V., Amsterdam, pp. 711–757.
Peñalva R., Morales J., González-Navarro C.J., Larrañeta E., Quincoces G., Peñuelas I. & Irache J.M. 2018. Increased Oral Bioavailability of Resveratrol by Its Encapsulation in Casein Nanoparticles. *International Journal of Molecular Sciences* 19: 2816.
Pizzato M., Baraldi C., Boscato Sopetto G., Finozzi D., Gentile C., Gentile M.D., Marconi R., Paladino D., Raoss A., Riedmiller I., Ur Rehman H., Santini A., Succetti V. & Volpini L. 2022. SARS-CoV-2 and the Host Cell: A Tale of Interactions. *Frontiers in Virology* 1.
Plötze M. & Niemz P. 2011. Porosity and pore size distribution of different wood types as determined by mercury intrusion porosimetry. *European Journal of Wood and Wood Products* 69: 649–657.
Prasad S., Potdar V., Cherian S., Abraham P. & Basu A. 2020. Transmission electron microscopy imaging of SARS-CoV-2. *The Indian Journal of Medical Research* 151: 241–243.
Rabenau H.F., Cinatl J., Morgenstern B., Bauer G., Preiser W. & Doerr H.W. 2005. Stability and inactivation of SARS coronavirus. *Medical Microbiology and Immunology* 194: 1–6.

Rai N.K., Ashok A. & Akondi B.R. 2020. Consequences of chemical impact of disinfectants: safe preventive measures against COVID-19. *Critical Reviews in Toxicology* 50: 513–520.

Raj V.S., Mou H., Smits S.L., Dekkers D.H.W., Müller M.A., Dijkman R., Muth D., Demmers J.A.A., Zaki A., Fouchier R.A.M., Thiel V., Drosten C., Rottier P.J.M., Osterhaus A.D.M.E., Bosch B.J. & Haagmans B.L. 2013. Dipeptidyl peptidase 4 is a functional receptor for the emerging human coronavirus-EMC. *Nature* 495: 251–254.

Riddell S., Goldie S., Hill A., Eagles D. & Drew T.W. 2020a. The effect of temperature on persistence of SARS-CoV-2 on common surfaces. *Virology Journal* 17: 145.

Riddell S., Goldie S., Hill A., Eagles D. & Drew T.W. 2020b. The effect of temperature on persistence of SARS-CoV-2 on common surfaces. *Virology Journal* 17: 145.

Rodrigues T., Reker D., Schneider P. & Schneider G. 2016. Counting on natural products for drug design. *Nature Chemistry* 8: 531–541.

Romano J.D. & Tatonetti N.P. 2019. Informatics and Computational Methods in Natural Product Drug Discovery: A Review and Perspectives. *Frontiers in Genetics* 10: 368.

Rossmann M.G., Arnold E., Erickson J.W., Frankenberger E.A., Griffith J.P., Hecht H.-J., Johnson J.E., Kamer G., Luo M., Mosser A.G., Rueckert R.R., Sherry B. & Vriend G. 1985. Structure of a human common cold virus and functional relationship to other picornaviruses. *Nature* 317: 145–153.

Rossmann M.G., He Y. & Kuhn R.J. 2002. Picornavirus–receptor interactions. *Trends in Microbiology* 10: 324–331.

Ruokolainen V., Domanska A., Laajala M., Pelliccia M., Butcher S.J. & Marjomäki V. 2019. Extracellular Albumin and Endosomal Ions Prime Enterovirus Particles for Uncoating That Can Be Prevented by Fatty Acid Saturation. *Journal of Virology* 93: e00599-19.

Ruokolainen V., Laajala M. & Marjomäki V. 2020. Real-time Fluorescence Measurement of Enterovirus Uncoating. 10: e3582.

Sattar S.A., Lloyd-Evans N., Springthorpe V.S. & Nair R.C. 1986. Institutional outbreaks of rotavirus diarrhoea: potential role of fomites and environmental surfaces as vehicles for virus transmission. *Epidemiology & Infection* 96: 277–289.

Schaar H.M. van der, Dorobantu C.M., Albulescu L., Strating J.R.P.M. & Kuppeveld F.J.M. van. 2016. Fat(al) attraction: Picornaviruses Usurp Lipid Transfer at Membrane Contact Sites to Create Replication Organelles. *Trends in Microbiology* 24: 535–546.

Schirtzinger E.E., Kim Y. & Davis A.S. 2022. Improving human coronavirus OC43 (HCoV-OC43) research comparability in studies using HCoV-OC43 as a surrogate for SARS-CoV-2. *Journal of Virological Methods* 299: 114317.

Shulla A., Heald-Sargent T., Subramanya G., Zhao J., Perlman S. & Gallagher T. 2011. A Transmembrane Serine Protease Is Linked to the Severe Acute Respiratory Syndrome Coronavirus Receptor and Activates Virus Entry. *Journal of Virology* 85: 873–882.

Simmons G., Gosalia D.N., Rennekamp A.J., Reeves J.D., Diamond S.L. & Bates P. 2005. Inhibitors of cathepsin L prevent severe acute respiratory syndrome coronavirus entry. *Proceedings of the National Academy of Sciences of the United States of America* 102: 11876–11881.

Simons-Linares C.R., Imam Z. & Chahal P. 2021. Viral-Attributed Acute Pancreatitis: A Systematic Review. *Digestive Diseases and Sciences* 66: 2162–2172.

Singla R.K., Dubey A.K., Garg A., Sharma R.K., Fiorino M., Ameen S.M., Haddad M.A. & Al-Hiary M. 2019. Natural Polyphenols: Chemical Classification, Definition of Classes, Subcategories, and Structures. *Journal of AOAC International* 102: 1397–1400.

Sipponen A. & Laitinen K. 2011a. Antimicrobial properties of natural coniferous rosin in the European Pharmacopoeia challenge test. *APMIS* 119: 720–724.

Sipponen A. & Laitinen K. 2011b. Antimicrobial properties of natural coniferous rosin in the European Pharmacopoeia challenge test. *APMIS: acta pathologica, microbiologica, et immunologica Scandinavica* 119: 720–724.

Sittikul P., Sriburin P., Rattanamahaphoom J., Nuprasert W., Thammasonthijarern N., Thaipadungpanit J., Hattasingh W., Kosoltanapiwat N., Puthavathana P. & Chatchen S. 2023. Stability and infectivity of enteroviruses on dry surfaces: Potential for indirect transmission control. *Biosafety and Health* 5: 339–345.

Sizun J., Yu M.W.N. & Talbot P.J. 2000. Survival of human coronaviruses 229E and OC43 in suspension and after drying onsurfaces: a possible source ofhospital-acquired infections. *Journal of Hospital Infection* 46: 55–60.

Smyth M., Pettitt T., Symonds A. & Martin J. 2003. Identification of the pocket factors in a picornavirus. *Archives of Virology* 148: 1225–1233.

Snijder E.J., Decroly E. & Ziebuhr J. 2016. The Nonstructural Proteins Directing Coronavirus RNA Synthesis and Processing. *Advances in Virus Research* 96: 59–126.

Söderberg T.A., Gref R., Holm S., Elmros T. & Hallmans G. 1990. Antibacterial activity of rosin and resin acids in vitro. *Scandinavian Journal of Plastic and Reconstructive Surgery and Hand Surgery* 24: 199–205.

Song Y., Yao H., Wu N., Xu J., Zhang Z., Peng C., Li S., Kong W., Chen Y., Zhu M., Wang J., Shi D., Zhao C., Lu X., Echavarría Galindo M. & Li S. 2023. In situ architecture and membrane fusion of SARS-CoV-2 Delta variant. *Proceedings of the National Academy of Sciences* 120: e2213332120.

Stertz S., Reichelt M., Spiegel M., Kuri T., Martínez-Sobrido L., García-Sastre A., Weber F. & Kochs G. 2007. The intracellular sites of early replication and budding of SARS-coronavirus. *Virology* 361: 304–315.

Sumantran V.N., Boddul S., Koppikar S.J., Dalvi M., Wele A., Gaire V. & Wagh U.V. 2007. Differential growth inhibitory effects of W. somnifera root and E. officinalis fruits on CHO cells. *Phytotherapy Research* 21: 496–499.

Suprewicz Ł., Swoger M., Gupta S., Piktel E., Byfield F.J., Iwamoto D.V., Germann D., Reszeć J., Marcińczyk N., Carroll R.J., Lenart M., Pyrc K., Janmey P., Schwarz J.M., Bucki R. & Patteson A. 2021. Extracellular

vimentin as a target against SARS-CoV-2 host cell invasion. : 2021.01.08.425793.
Taylor M.W. 2014. What Is a Virus? *Viruses and Man: A History of Interactions*: 23–40.
Terio V., Lorusso P., Castrica M., Pandiscia A., Miraglia D., Balzaretti C.M., Tantillo G. & Decaro N. 2021. Survival of a SARS-CoV-2 Surrogate on Flow-Pack Polyethylene and Polystyrene Food Trays at Refrigeration and Room Temperature Conditions. *Applied Sciences* 11: 3977.
Teterina N.L., Pinto Y., Weaver J.D., Jensen K.S. & Ehrenfeld E. 2011. Analysis of Poliovirus Protein 3A Interactions with Viral and Cellular Proteins in Infected Cells ▿ . *Journal of Virology* 85: 4284–4296.
Thiel V., Ivanov K.A., Putics Á., Hertzig T., Schelle B., Bayer S., Weißbrich B., Snijder E.J., Rabenau H., Doerr H.W., Gorbalenya A.E. & Ziebuhr J. 2003. Mechanisms and enzymes involved in SARS coronavirus genome expression. *Journal of General Virology* 84: 2305–2315.
Tiwari A., Patnayak D.P., Chander Y., Parsad M. & Goyal S.M. 2006. Survival of Two Avian Respiratory Viruses on Porous and Nonporous Surfaces. *Avian Diseases* 50: 284–287.
Tuladhar E., Koning M.C. de, Fundeanu I., Beumer R. & Duizer E. 2012. Different Virucidal Activities of Hyperbranched Quaternary Ammonium Coatings on Poliovirus and Influenza Virus. *Applied and Environmental Microbiology* 78: 2456–2458.
Tuthill T.J., Bubeck D., Rowlands D.J. & Hogle J.M. 2006. Characterization of early steps in the poliovirus infection process: receptor-decorated liposomes induce conversion of the virus to membrane-anchored entry-intermediate particles. *Journal of Virology* 80: 172–180.
Ueda K., Kawabata R., Irie T., Nakai Y., Tohya Y. & Sakaguchi T. 2013. Inactivation of Pathogenic Viruses by Plant-Derived Tannins: Strong Effects of Extracts from Persimmon (Diospyros kaki) on a Broad Range of Viruses. *PLOS ONE* 8: e55343.
Veeresham C. 2012. Natural products derived from plants as a source of drugs. *Journal of Advanced Pharmaceutical Technology & Research* 3: 200–201.
Verlinden Y., Cuconati A., Wimmer E. & Rombaut B. 2000. Cell-free synthesis of poliovirus: 14S subunits are the key intermediates in the encapsidation of poliovirus RNA. *Journal of General Virology* 81: 2751–2754.
V'kovski P., Kratzel A., Steiner S., Stalder H. & Thiel V. 2021. Coronavirus biology and replication: implications for SARS-CoV-2. *Nature Reviews Microbiology* 19: 155–170.
Vlasak R., Luytjes W., Spaan W. & Palese P. 1988. Human and bovine coronaviruses recognize sialic acid-containing receptors similar to those of influenza C viruses. *Proceedings of the National Academy of Sciences of the United States of America* 85: 4526–4529.
Vuorinen T., Vainionpää R., Heino J. & Hyypiä T. 1999. Enterovirus receptors and virus replication in human leukocytes. *Journal of General Virology* 80: 921–927.

Walls A.C., Tortorici M.A., Snijder J., Xiong X., Bosch B.-J., Rey F.A. & Veesler D. 2017. Tectonic conformational changes of a coronavirus spike glycoprotein promote membrane fusion. *Proceedings of the National Academy of Sciences of the United States of America* 114: 11157–11162.

Wang K., Chen W., Zhang Z., Deng Y., Lian J.-Q., Du P., Wei D., Zhang Y., Sun X.-X., Gong L., Yang X., He L., Zhang L., Yang Z., Geng J.-J., Chen R., Zhang H., Wang B., Zhu Y.-M., Nan G., Jiang J.-L., Li L., Wu J., Lin P., Huang W., Xie L., Zheng Z.-H., Zhang K., Miao J.-L., Cui H.-Y., Huang M., Zhang J., Fu L., Yang X.-M., Zhao Z., Sun S., Gu H., Wang Z., Wang C.-F., Lu Y., Liu Y.-Y., Wang Q.-Y., Bian H., Zhu P. & Chen Z.-N. 2020. CD147-spike protein is a novel route for SARS-CoV-2 infection to host cells. *Signal Transduction and Targeted Therapy* 5: 1–10.

Wang Y.-Q., Li Q.-S., Zheng X.-Q., Lu J.-L. & Liang Y.-R. 2021a. Antiviral Effects of Green Tea EGCG and Its Potential Application against COVID-19. *Molecules* 26: 3962.

Wang C.C., Prather K.A., Sznitman J., Jimenez J.L., Lakdawala S.S., Tufekci Z. & Marr L.C. 2021b. Airborne transmission of respiratory viruses. *Science* 373: eabd9149.

Wang H., Yang P., Liu K., Guo F., Zhang Y., Zhang G. & Jiang C. 2008. SARS coronavirus entry into host cells through a novel clathrin- and caveolae-independent endocytic pathway. *Cell Research* 18: 290–301.

Warnes S.L., Little Z.R. & Keevil C.W. 2015. Human Coronavirus 229E Remains Infectious on Common Touch Surface Materials. *mBio* 6: 10.1128/mbio.01697-15.

Watanabe M., Ohnishi T., Arai S., Kawakami T., Hayashi K., Ohya K., Hirose S., Yoshinari T., Taharaguchi S., Mekata H., Taniguchi T., Ikarashi Y., Honma M., Goda Y. & Hara-Kudo Y. 2022. Survival of SARS-CoV-2 and bovine coronavirus on common surfaces of living environments. *Scientific Reports* 12: 10624.

Watts S., Ramstedt M. & Salentinig S. 2021. Ethanol Inactivation of Enveloped Viruses: Structural and Surface Chemistry Insights into Phi6. *The Journal of Physical Chemistry Letters* 12: 9557–9563.

Wells A.I. & Coyne C.B. 2019. Enteroviruses: A Gut-Wrenching Game of Entry, Detection, and Evasion. *Viruses* 11: 460.

White J.M. & Whittaker G.R. 2016. Fusion of Enveloped Viruses in Endosomes. *Traffic (Copenhagen, Denmark)* 17: 593–614.

WHO. 2020. Advice for the public on COVID-19 – World Health Organization.

WHO Coronavirus (COVID-19) Dashboard.

Wolff G., Limpens R.W.A.L., Zevenhoven-Dobbe J.C., Laugks U., Zheng S., Jong A.W.M. de, Koning R.I., Agard D.A., Grünewald K., Koster A.J., Snijder E.J. & Bárcena M. 2020. A molecular pore spans the double membrane of the coronavirus replication organelle. *Science (New York, N.y.)* 369: 1395–1398.

Woo P.C.Y., Groot R.J. de, Haagmans B., Lau S.K.P., Neuman B.W., Perlman S., Sola I., Hoek L. van der, Wong A.C.P. & Yeh S.-H. 2023. ICTV Virus Taxonomy Profile: Coronaviridae 2023. *The Journal of General Virology* 104.

Wrapp D., Wang N., Corbett K.S., Goldsmith J.A., Hsieh C.-L., Abiona O., Graham B.S. & McLellan J.S. 2020. Cryo-EM structure of the 2019-nCoV spike in the prefusion conformation. *Science (New York, N.y.)* 367: 1260–1263.

Yamauchi Y. & Greber U.F. 2016. Principles of Virus Uncoating: Cues and the Snooker Ball. *Traffic (Copenhagen, Denmark)* 17: 569.

Yang G.Y., Liao J., Kim K., Yurkow E.J. & Yang C.S. 1998. Inhibition of growth and induction of apoptosis in human cancer cell lines by tea polyphenols. *Carcinogenesis* 19: 611–616.

Yeager C.L., Ashmun R.A., Williams R.K., Cardellichio C.B., Shapiro L.H., Look A.T. & Holmes K.V. 1992. Human aminopeptidase N is a receptor for human coronavirus 229E. *Nature* 357: 420–422.

Yin-Murphy M. & Almond J.W. 1996. Picornaviruses. In: Baron S. (ed.), *Medical Microbiology*, University of Texas Medical Branch at Galveston, Galveston (TX).

Zacheo A., Hodek J., Witt D., Mangiatordi G.F., Ong Q.K., Kocabiyik O., Depalo N., Fanizza E., Laquintana V., Denora N., Migoni D., Barski P., Stellacci F., Weber J. & Krol S. 2020. Multi-sulfonated ligands on gold nanoparticles as virucidal antiviral for Dengue virus. *Scientific Reports* 10: 9052.

Zhang S.-F., Tuo J.-L., Huang X.-B., Zhu X., Zhang D.-M., Zhou K., Yuan L., Luo H.-J., Zheng B.-J., Yuen K.-Y., Li M.-F., Cao K.-Y. & Xu L. 2018. Epidemiology characteristics of human coronaviruses in patients with respiratory infection symptoms and phylogenetic analysis of HCoV-OC43 during 2010-2015 in Guangzhou. *PloS One* 13: e0191789.

Zhuang H., Kim Y.-S., Koehler R.C. & Doré S. 2003. Potential Mechanism by Which Resveratrol, a Red Wine Constituent, Protects Neurons. *Annals of the New York Academy of Sciences* 993: 276–286.

ORIGINAL PAPERS

I

TREE SPECIES-DEPENDENT INACTIVATION OF CORONAVIRUSES AND ENTEROVIRUSES ON SOLID WOOD SURFACES

by

Shroff S., Peramäki A., Väisänen A., Pasanen P., Grönlund K., Nissinen V., Jänis J., Haapala A. & Marjomäki V. 2023

Submitted manuscript.

Tree species-dependent inactivation of coronaviruses and enteroviruses on solid wood surfaces

Sailee Shroff[a], Anni Perämaki[a], Antti Väisänen[b], Pertti Pasanen[b], Krista Grönlund[c], Ville Nissinen[c], Janne Jänis[c], Antti Haapala[c,d,†], Varpu Marjomäki[a*†]

[a] Department of Biological and Environmental Sciences and Nanoscience Center, University of Jyväskylä, Jyväskylä, Finland.
[b] Department of Environmental and Biological Sciences, University of Eastern Finland, Kuopio, 70210, Finland.
[c] Department of Chemistry, Sustainable Technologies, University of Eastern Finland, 80100 Joensuu, Finland.
[d] FSCN Research Centre, Mid Sweden University, SE-85170 Sundsvall, Sweden.

†Shared last authors

*Corresponding author
Varpu Marjomäki, Professor in Cell and Molecular Biology, Vice Head
University of Jyväskylä,
Department of Biological and Environmental Sciences/Nanoscience Centre
Survontie 9C,
40500 Jyväskylä, Finland.
+358 405634422
varpu.s.marjomaki@jyu.fi
https://www.jyu.fi/vmarjomaki

Abstract:

The ongoing challenge of viral transmission, exemplified by the Covid pandemic and recurrent viral outbreaks, necessitates the exploration of sustainable antiviral solutions. This study investigates the under-explored antiviral potential of wooden surfaces. We evaluated the antiviral efficacy of various wood types, including coniferous and deciduous trees against enveloped coronaviruses and non-enveloped enteroviruses like coxsackie virus A9. Our findings revealed excellent antiviral activity manifesting already within 10 to 15 minutes in Scots pine and Norway spruce, particularly against enveloped viruses. In contrast, other hardwoods displayed varied efficacy, with oak showing effectiveness against enterovirus. This antiviral activity was consistently observed across a spectrum of humidity levels (20 to 90 RH%), while the antiviral efficacy manifested itself more rapidly at 37 °C v/s 21 °C. Key to our findings is the chemical composition of these woods. Resin acids and terpenes were prevalent in pine and spruce, correlating with their antiviral performance, while oak's high phenolic content mirrored its efficacy against enterovirus. The pine surface absorbed a higher fraction of the corona virus in contrast to oak, whereas enteroviruses were not absorbed on those surfaces. This study highlights the role of bioactive chemicals in the antiviral action of wood and opens new avenues for employing wood surfaces as a natural, sustainable barrier against viral transmissions.

Key words: antiviral, coronavirus, enterovirus, persistence, solid surface, wood.

1. Introduction

Since prehistoric times, wood has played an essential role in tools, utilities and built environment. The 20th century witnessed excessive exploitation of wood that together with rapid industrial advancements provided several alternatives like plastics and metals in interior surfacing and utilities in our built environment. Recent trends, underlined by sustainability concerns and appreciation for wood's unique aesthetic and haptic properties are reclaiming the use of wood in many daily uses [1,2].

Parallel to these material trends, the 21st century is marked by emerging health challenges, notably viral outbreaks such as SARS and COVID-19. Transmission mechanisms for these viruses include not only direct human-to-human contact but also interactions with contaminated surfaces [3–5]. Viruses do not replicate outside their host cells; however, they are able to persist for a long period of time on different surfaces as fomites [6]. While enveloped viruses, such as coronaviruses, exhibit quite short surface persistence up to 5 days, non-enveloped viruses on the other hand, shielded by robust protein capsids, can endure for weeks, often resisting standard disinfection techniques. This is due to the presence of a strong protein capsid which is difficult to break down with disinfectants [7,8]. While disinfectants remain the primary strategy for neutralizing surface pathogens, their efficacy is limited and their continuous use poses environmental, health, and material degradation concerns [9,10].

The intersection of these trends points to a need for research into antiviral surfaces and this has sparked a new interest amongst scientists to reduce the circulating viral load. Wood holds promise as a material capable of mitigating the spread of pathogens due to its intricate composition and architecture. Currently, the few commercially available antiviral surfaces and disinfectants present the only way to reduce the number of pathogens on solid surfaces. Disinfectants usually exhibit limited efficacy, prolonged use raises health concerns for the user, they have adverse environmental impact, carry the potential for pathogen resistance and destroy the natural microbiota as well [10]. Additionally, repeated use of disinfectants reduces the longevity of the surface, for example, disinfectants are known to harden plastic and crack rubber [9].

Historical practices have showcased wood’s inherent antimicrobial properties, evidenced in traditional methods like the use of wooden boards in cheese and wine production [11]. The underlying antimicrobial mechanisms are believed to arise from wood’s hygroscopic nature, which promotes rapid drying, and the antimicrobial compounds it naturally contains [12,13]. However, the interplay of various factors, such as wood type, surface condition, and ambient conditions, necessitates more comprehensive research [14].

While the antibacterial and antifungal properties of wood have been documented across cultures and time periods, the investigation into its antiviral potential has remained relatively unexplored until recent years. In one study, Greatorex and colleagues showed a reduction of more than seven logs of Influenza A viral titer on pine surface after 24 h [15].

In another study by Chin and colleagues at the beginning of the COVID-19 pandemic suggested that SARS-CoV-2 viral titer could be reduced by four logs post 24 h treatment on a wood surface [16]. To the best of our knowledge, there is no literature that demonstrates the persistence of enveloped and non-enveloped viruses on different wood species and after short contact times. Also, the effect of environmental factors like temperature and relative humidity (RH) or modification of wood surface properties on the persistence of viruses on wood has not been comprehensively tested.

This work aimed to bridge the knowledge gap by investigating the antiviral properties of wood surfaces, emphasizing both enveloped and non-enveloped viruses. Through rigorous analysis, we explored the impact of different wood species, treatments, and environmental conditions on viral persistence. Our findings offer insights into the intricate relationship between the organic chemical compounds of wood and their potential to mitigate viral loads.

2. Materials and Methods

2.1 Cells, viruses, and surfaces

We used two cell lines, MRC-5 and A549 cells, which were obtained from the American Type Culture Collection (Manassas, VA, USA). MRC-5 cells are fibroblast-like cells derived from normal lung tissue obtained from a 14-week-old male foetus. While A549 cells are adenocarcinoma human alveolar basal epithelial cells. MRC-5 cells were cultured in Minimum Essential Medium (MEM), while A549 cells were cultured in Dulbecco's Modified Eagle Medium (DMEM). Both culture media were supplemented with 10% Foetal Bovine Serum (FBS), 1% penicillin-streptomycin, and 1% GlutaMAX, all from Gibco (Paisley, UK). The cultures were maintained in a humidified incubator with 5% CO_2 at 37 °C.

Beta Coronavirus 1 (OC43 strain; ATCC®VR-1558™)(Manassas, VA, USA) was propagated following the protocol by Dent and Neuman (2015) with minor modification while coxsackie virus A9 (CVA9; Griggs strain; ATCC) was produced and purified as described previously by Myllynen et al (2016) [17].

Six different varieties of wood species were used in this study: Scots pine (*Pinus sylvestris*), silver birch (*Betula pendula*), grey alder (*Alnus incana*), eucalyptus (*Eucalyptus globulus*), pedunculate oak (*Quercus robur*) and Norway spruce (*Picea abies*). In addition, different coarseness of pine (coarseness: 80, 120, 320, 1000 and planned grit sanded surfaces), wood-plastic composite (about 50% wood flour, 50% polypropylene) and two differently thermo-treated spruce (*Picea abies*) and pine samples (ThermoWood® S and D modified timber, see e.g., Cai et al. 2019) were also tested. Industrial grade polyethylene (PE) was used as a plastic control sample. The wood materials were sterilized by γ-radiation and the plastic with 70% ethanol.

2.2 Surface persistence studies

For the persistence studies, test samples (wood and plastic surfaces) were placed in 12-well plates. A 5 µl droplet of the virus (corresponding to 8×10^4 PFU) was inoculated onto the centre of each sample's surface. These plates were then transferred to a custom-built humidity chamber (Kenttäviiva Ltd, Finland) for specified time intervals. The chamber's temperature and relative humidity were adjusted as needed for the experiments (e.g., 21/37 ℃ and 20/40/60% RH). To achieve higher RH conditions (>90% RH), 6 mL of ddH2O was added to each 12-well plate, which was then sealed with parafilm during incubation. After the specified time points, the samples were gently flushed with media and rocked for 1 minute to release the virus particles into the medium. The flushed media was collected into Eppendorf tubes placed on ice and further diluted 100 times with media. A 2% MEM solution was used as the flushing media for coronaviruses, while a 1% DMEM solution was used for enteroviruses.

2.3 Cytopathic effect (CPE)

To determine the infectivity of the flushed viruses, we employed the Cytopathic Effect (CPE) assay. For coronaviruses, MRC-5 cells were cultured for 24 hours at 37 °C in 96-well flat-bottomed microtiter plates (Sarstedt, Numbrecht, Germany) at a density of 15,000 cells/well in 100 µl of 10% MEM. Meanwhile, for enteroviruses, A549 cells were cultured under similar conditions with 10% DMEM at a density of 12,000 cells/well.

Following the surface persistence studies, the flushed media from the surfaces and virus control was added to the cultured cells. The plates were then incubated for five days at 34 °C for coronaviruses and two days at 37 °C for enteroviruses, or until the cytopathic effect was visible. Once the cytopathic effect was observed, the cells were washed twice with PBS and then stained for 10 minutes using a CPE dye solution (comprising 0.03% crystal violet, 2% ethanol, and 36.5% formaldehyde). Post this, excess stain was removed with two washes of ddH20. Stained cells were lysed using a CPE lysis buffer (0.8979 g of sodium citrate and 1N HCl in 47.5% ethanol). The absorbance from the plates was subsequently read at 570 nm using the VICTORTM X4 multilabel reader from PerkinElmer (Turku, Finland).

2.4 Statistical analysis

The results from the CPE assay were plotted as a column graph of the cell viability with standard error means using GraphPad Prism 9 (GraphPad Software, San Diego, CA, USA). The CPE results were normalized against the cell control. The statistical significance was calculated using the one-way analysis of variance (ANOVA), followed by the Bonferroni test (* $p < 0.05$, ** $p < 0.01$, *** $p < 0.001$ and **** $p < 0.0001$).

2.5 Direct flushing

To assess potential differential absorption of HCoV-OC43 and CVA9 within different wood surfaces, a direct flushing experiment was devised. A 5 µl droplet containing HCoV-OC43 (8×10^4 PFU) and CVA9 (1×10^5 PFU) was applied to the surfaces of pine and oak, followed by a 15-minute incubation at room temperature under high RH conditions (>90% RH). Subsequently, the surfaces bearing HCoV-OC43 and CVA9 were flushed with 2% MEM and 1% DMEM, respectively. The quantification of viral RNA in the flush samples was performed using RT-PCR and qPCR methods.

2.6 RT-PCR and qPCR

The protocol for the cDNA synthesis using RT-PCR and amplification using qPCR was performed as described previously by Turkki et al (2019) [18]. The reverse primer specific to HCoV-OC43 was 5'-AATGTAAAGATGRCCGCGTATT, and the corresponding forward primer was 5'-TGTTAGGCCRATAATTGAGGAC (Merck). For enterovirus, the reverse primer was 5'-GAAACACGGACACCCAAAGTA and forward primer was 5'-CGGCCCCTGAATGCGGCTAA. qPCR was used for determining relative amounts of viral RNA or virus infection between samples in two ways. To evaluate effects on virus infection, samples were taken from 3 day cultivation from MRC-5 cells after the flushed samples were applied on cells. In contrast, in evaluating the relative amount of viruses that were absorbed on the surfaces, the qPCR was performed directly from the flushed samples, without cultivation on cells.

2.7 Immunolabeling and confocal microscopy

Confocal microscopy was employed to examine various stages of the coronavirus infection cycle. In this study, two separate experiments were conducted: one with a total infection time of 2 hours, and the other with a total infection time of 15 hours. At first, a 5 µl droplet of purified HCoV-OC43 virus (2×10^6 PFU) was applied to the Pine and PE surfaces and incubated for 1 hour at room temperature with approximately 92% RH. After incubation, the viruses were flushed from the surfaces and added into two 96-well plates containing sub-confluent MRC-5 cells at a multiplicity of infection (MOI) of 100. The virus in the 96-well plates were allowed to settle on the host cell surface for 1 hour at room temperature. Following this the plates were transferred to 34 °C for another 1 hour. At the end of this incubation period, the cells were gently flushed with PBS to remove any unbound virus. Cells in the plate one were fixed with 4% paraformaldehyde and permeabilized with 0.2% Triton X-100 for 5 minutes, as this was the end of the 2 hour infection time. In the other plate, PBS was replaced with 2% MEM, and the infection continued for the remaining 13 hours at 34 °C. At the end of the 15 hour incubation period, the cells were similarly fixed and permeabilized as mentioned above to proceed for immunolabeling.

The cells were labelled with primary antibodies against the coronavirus spike protein and the cellular tubulin (#sc-58886, Santa Cruz Biotechnology) for 1 hour at room temperature. The S-protein antibody was generously provided by Moona Huttunen and Ilkka Julkunen (University of Turku). For secondary labelling, Alexa Fluor 555 goat polyclonal IgG against rabbit (catalog no. A-21429; Thermo Fisher Scientific) and Alexa Fluor 488 goat polyclonal IgG against mouse (catalog no. A-21121; Thermo Fisher Scientific) antibodies were used. Secondary antibodies were added to the cells for 50 minutes and incubated under dark conditions. Following the secondary antibody labelling, three cycles of PBS washes were given to remove any unbound secondary antibodies. The second PBS wash contained 4',6-diamidino-2-phenylindole (DAPI) (Invitrogen/Molecular Probes, ref. D3571) at a dilution of 1:40000 to stain the cellular nuclei. Imaging was conducted using a Nikon A1R confocal microscope equipped with a 40× objective and 1.25 Numerical Aperture (NA). Three lasers were employed: a 405 nm diode laser, a 488 nm multiline argon laser, and a 561 nm sapphire laser. Montages of the images were generated using Fiji2 software (ImageJ).

2.8 Volatile organic compounds from wood specimen

In order to study easily evaporated chemical components from wood specimen that can interact with virus deposits on the surface, (total) volatile organic compounds ((T)VOCs) emitted by wood specimens (25×25×10 mm in dimensions) at fixed 25 °C and 40 °C temperatures were collected in two consecutive tests using Tenax® TA adsorbent tubes (Markes International Inc., Sacramento, CA) containing 200 mg of sorbent (Figure S1A). The first test employed untreated, dry wood specimens. The specimens were dampened before the second test by submerging them in water for one hour and sealing them in airtight zip bags for 24 hours. The specimens were left to sit for two hours under normal laboratory conditions before the second set of VOC sampling after the 24 hours of moisture absorption to get rid of excess surface moisture. Hence a total of four samples were collected from each wood species. Sample collection adopts features from the Finnish Building Information Foundation's (2023) method to evaluate and classify chemical emissions from building materials and the ISO 16000-6:2021 standard (International Organization for Standardization 2021) for active VOC sampling.

VOC emission sampling was preceded by placing the wood specimens on tinfoil plates inside the chambers (V = 114 mL) of a Micro-Chamber/Thermal Extractor M-CTE250 apparatus (Markes International Inc.) equilibrating to the target sampling temperature over 5 minutes. The VOC samples were drawn from the chambers' dedicated sampling outlets, while nitrogen served as the inert carrier gas at a 75 mL/min flow rate. Sampling lasted for 10 minutes at 25°C, and for 4 minutes at 40 °C to prevent adsorbent tube saturation.

The samples were analyzed using a thermal desorption-gas chromatography-mass spectrometry (TD-GC-MS) system consisting of a TD100 thermal desorber (Markes International Inc.) (Figure S1B), a 7890A gas chromatograph (Agilent Technologies Inc.,

Santa Clara, CA) equipped with an HP-5 ms UI column with 60 m length, 0.25 mm inner diameter and 0.25 μm film thickness (Agilent Technologies Inc.), and a 5975C mass spectrometer (Agilent Technologies Inc.) running on scan mode. VOC species were identified by their retention times and ion fingerprints using the MSD ChemStation software (Agilent Technologies Inc.) and NIST20 MS-library (National Institute of Standards and Technology, Gaithersburg, MD). A four-point calibration curve was constructed using HC 48 component 40,353-U standard solution samples (Supelco Inc., Bellefonte, PA). The individual compound concentrations were calculated as toluene equivalents, according to the ISO 16000-6:2021 standard. The results were background-corrected using blank tinfoil plate samples collected concurrently with the wood specimen VOC samples.

2.9 Chemical fingerprinting of semivolatile chemicals from wood specimen

To further characterize and classify the wood specimen chemical composition, the most abundant semivolatile organic compounds (SVOCs) were determined using thermal desorption connected directly to the high-resolution mass spectrometer. Experiments were performed on a Bruker timsTOF quadrupole time-of-flight (Q-TOF) instrument (Bruker Daltonics GmbH, Bremen, Germany), equipped with a direct insertion probe (DIP) fitted into an atmospheric-pressure chemical ionization (APCI) source (Figure S2A). The DIP device allows direct analysis of semivolatile (polar and nonpolar) compounds without the need for sample preparation, which well complements the conventional VOC analysis using TD-GC-MS.

In this work, a small amount of wood for each species (~1.5 mg) was placed inside a tip of a pre-combusted quartz capillary, sealed with a thin layer of clean quartz filter (Figure S2B). The capillary was placed inside the DIP-APCI source and vaporizer temperature was then ramped from 100 to 450 °C with 50 °C steps. After each step, the temperature was held at the target temperature for 1.5 minute before the next increment. The total heating time was therefore ~11.5 minute (Figure S3A). Three different temperature regimes can be distinguished; at 100-150 °C residual moisture and most VOC compounds are liberated (*drying phase*), at 200-300 °C SVOC compounds (e.g., small oxygenates, fatty/resin acids, and phenolic compounds and their derivatives) desorb (*desorption phase*), while at >300 °C, decomposition of hemicellulose, cellulose and lignin occurs (*pyrolysis phase*), which liberates a complex mixture of high-mass oxygenates and aromatic/polyaromatic hydrocarbons (HCs). The liberated compounds are then ionized in the APCI source, and their accurate masses are determined by the Q-TOF analyzer (Figure S3B, lower panel).

APCI source was operated in the negative-ion mode to obtain optimal response for oxygenated compounds. The instrument was externally mass calibrated prior to the experiments with sodium perfluoroheptanoic acid clusters within the mass (m/z) range of 50-1000. The mass spectra were further internally re-calibrated using a custom-made reference mass list (wood extractives and typical mild pyrolysis components). Following

the re-calibration, extracted ion chromatograms (all ions) of the selected time regions of the *desorption phase* at 200, 250, and 300 °C were obtained, and elemental formulae for the compounds were obtained using the following parameters; elemental formula: $^{12}C_{0\text{-}100}{}^{1}H_{0\text{-}500}{}^{16}O_{0\text{-}20}$; H/C ratio = 0-3; mSigma score ≤ 1000; relative abundance ≥ 0.01%; mass error ≤ 15 ppm; both odd and even electron ions allowed.

The instrument was operated, and the data acquired using Bruker qtofControl 2.1 software and the data post-processing was accomplished by Bruker DataAnalysis 5.2 software. The van Krevelen (VK) diagrams (i.e., a plot of atomic H/C to O/C ratio for each detected compound) was made using Ceres View. The compound classifications were based on the criteria proposed elsewhere (Wu et al. 2004). Some compounds were further identified by using the CompoundCrawler database search engine.

3. Results

3.1 Persistence of human coronavirus on different wood species

We used the CPE assay to determine the persistence of HCoV-OC43 on various wood species. The tested wood species included Scots pine, silver birch, grey alder, eucalyptus, pedunculate oak, and Norway spruce. We examined both shorter (1 – 15 min) and longer (1 – 4 h) incubation times of the virus with the wood surface. The results obtained from the CPE assay highlighted significant differences in the persistence of HCoV-OC43 on different wood surfaces especially in the shorter time intervals.

Notably, on the pine surface, the viral infectivity started to reduce as early as after 5 minutes of incubation on the surface (Figure 1A), while on the spruce surface, the infectivity declined drastically starting after 10 minutes. In case of birch and alder surfaces, virus infectivity decreased within the tested shorter incubation times but did not reach as high effectivity as pine and spruce. Strikingly, eucalyptus and oak surfaces could not reduce the infectivity of the HCoV-OC43 virus within the shorter incubation times.

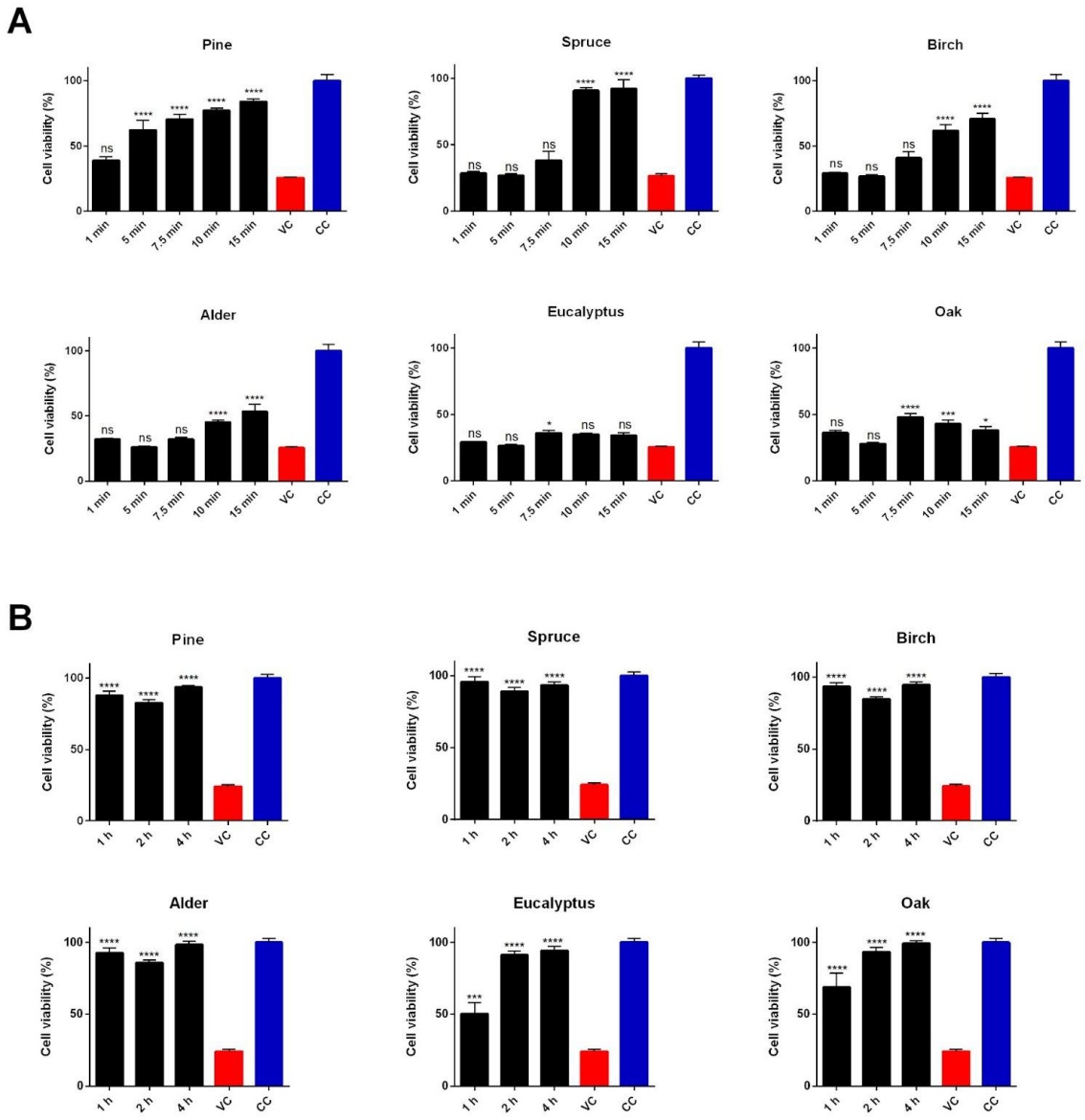

Figure 1. Infectivity of HCoV-OC43 recovered from six different wood species after (A) shorter incubation times (1 – 15 min) and (B) longer incubation times (1 – 4 h). The results have been normalized against the cell control (CC) which was set to 100% cell viability. Virus without any surface treatment was used as a virus control (VC). All the results are presented as an average + standard errors of the mean (SEM). The statistically significant differences between the test samples and VC are indicated with asterisks: * $p < 0.05$, *** $p < 0.001$, **** $p < 0.0001$, ns is not significant (analyzed with one-way ANOVA with Bonferroni test).

When we extended the incubation times of the virus on the surface to 1 hour, pine, spruce, birch and alder exhibited full reduction of infectivity, while eucalyptus and oak exhibited full activity only after 2 hours (Figure 1B). These results indicated that eucalyptus and oak were not as expeditious as other wood species in inactivating HCoV-OC43 on its surface and they could be potential fomites to transmit coronaviruses during the first few hours.

3.2 Effect of relative humidity and temperature on persistence on HCoV-OC43 on different wood species

Initial assessments on wood surfaces were conducted under conditions of elevated humidity (exceeding 90% RH) at room temperature (Figure 1A and B). Recognizing that real-world conditions vary considerably, it was imperative to examine how fluctuations in temperature and humidity might influence our observations. To this end, experiments were orchestrated across two distinct temperatures, 21 °C (reflective of Nordic indoor environments) and 37 °C (reminiscent of tropical climates). Furthermore, we selected three RH levels: 20%, 40%, and 60%, thereby encompassing a spectrum ranging from 20% to 90%, which aligns with the range frequently encountered both indoors and outdoors, irrespective of seasonal variations.

Comparative analyses between the two temperature settings revealed an intriguing pattern: viral infectivity was markedly reduced at 37 °C relative to 21 °C (Figures 2 & 3). Eucalyptus wood offered a striking illustration of this trend. Here, the virus was entirely inactivated post one hour of exposure at 37 °C. However, the viral entities persisted and remained infectious under similar conditions at 21 °C. Similarly, the silver birch surface demonstrated total viral inactivation within a mere 15 minutes at 37 °C, a stark contrast to its behaviour at 21 °C. This thermal effect aligns with extant literature. For instance, Wang et al. (2020) delineated how reduced temperatures, coupled with heightened humidity, often prolong the survivability of coronaviruses on surfaces.

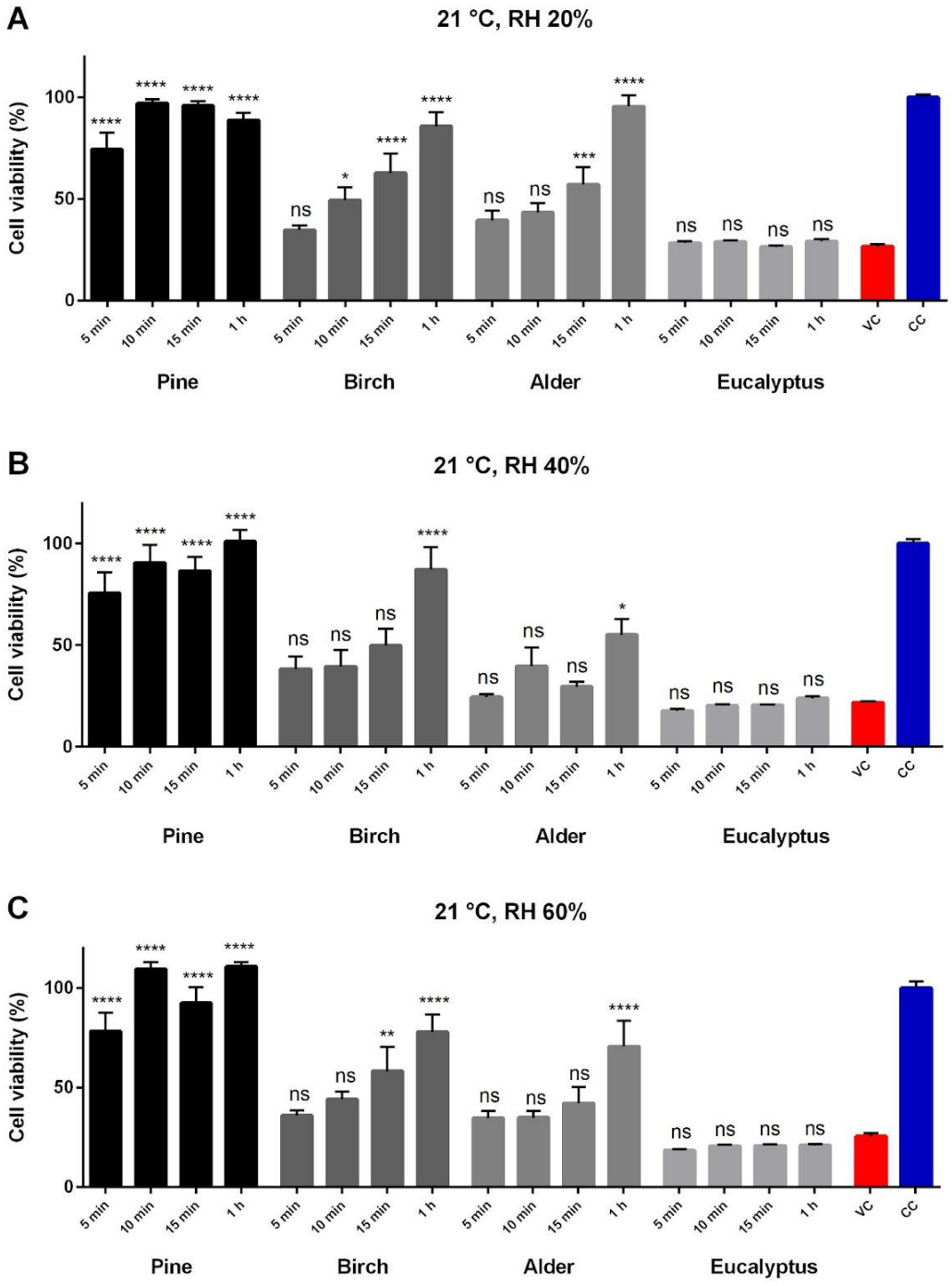

Figure 2: Infectivity of HCoV-OC43 recovered from pine, birch, alder and eucalyptus surfaces after incubating for various durations (5 minutes, 10 minutes, 15 minutes and 1 hour) at 21 °C under different RHs: (A) 20% (B) 40% and (C) 60%. The results have been normalized against the cell control (CC) which was set to 100% cell viability. Virus (VC) without any surface treatment was used as a positive control. All the results are presented as an average + standard errors of the mean (SEM). The statistically significant differences between the test samples and VC are indicated with asterisks: * $p < 0.05$, ** $p < 0.01$, **** $p < 0.0001$, ns is not significant (analyzed with one-way ANOVA with Bonferroni test).

In contrast to the influence of temperature, there appears to be no direct linear relationship between different humidity levels and the loss of virus infectivity. At 21°C, variations in humidity, from low to high, appeared inconsequential in terms of influencing virus

infectivity. However, at higher temperatures, extreme RHs, such as 20% and 90%, supported the virus's persistence for a longer duration compared to 40%. A salient observation emerged when assessing virus behaviour on alder wood at 37 °C. While at both 20% and 90% RH, the virus was rendered non-infectious after a 15-minute exposure (as seen in Figure 3A and 3C), a swifter inactivation occurred at 40% humidity, where the virus lost its infectivity in under 10 minutes (Figure 3B). These results suggest that RH plays a minor role at 21 °C but its impact becomes accentuated at heightened temperatures.

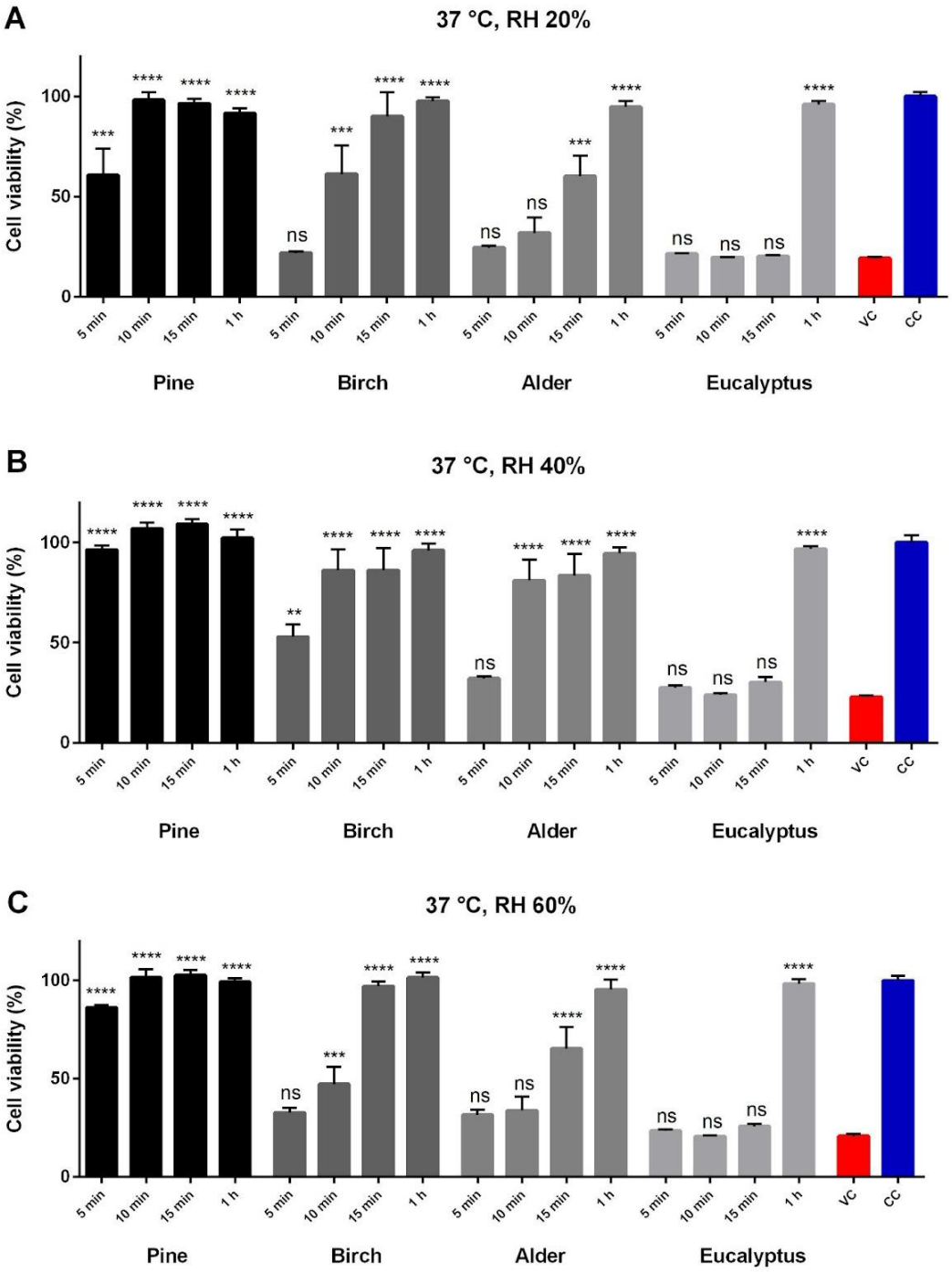

Figure 3: Infectivity of HCoV-OC43 recovered from pine, birch, alder and eucalyptus surfaces after incubating for various durations (5 minutes, 10 minutes, 15 minutes and 1 hour) at 37 °C under different RHs: (A) 20% (B) 40% and (C) 60%. The results have been normalized against the cell control (CC) which was set to 100% cell viability. Virus (VC) without any surface treatment was used as a positive control. All the results are presented as an average + standard errors of the mean (SEM). The statistically significant differences between the test samples and VC are indicated with asterisks: ** $p < 0.01$, *** $p < 0.001$, **** $p < 0.0001$, ns is not significant (analyzed with one-way ANOVA with Bonferroni test).

3.3 Delayed inactivation of non-enveloped viruses on different wood surfaces

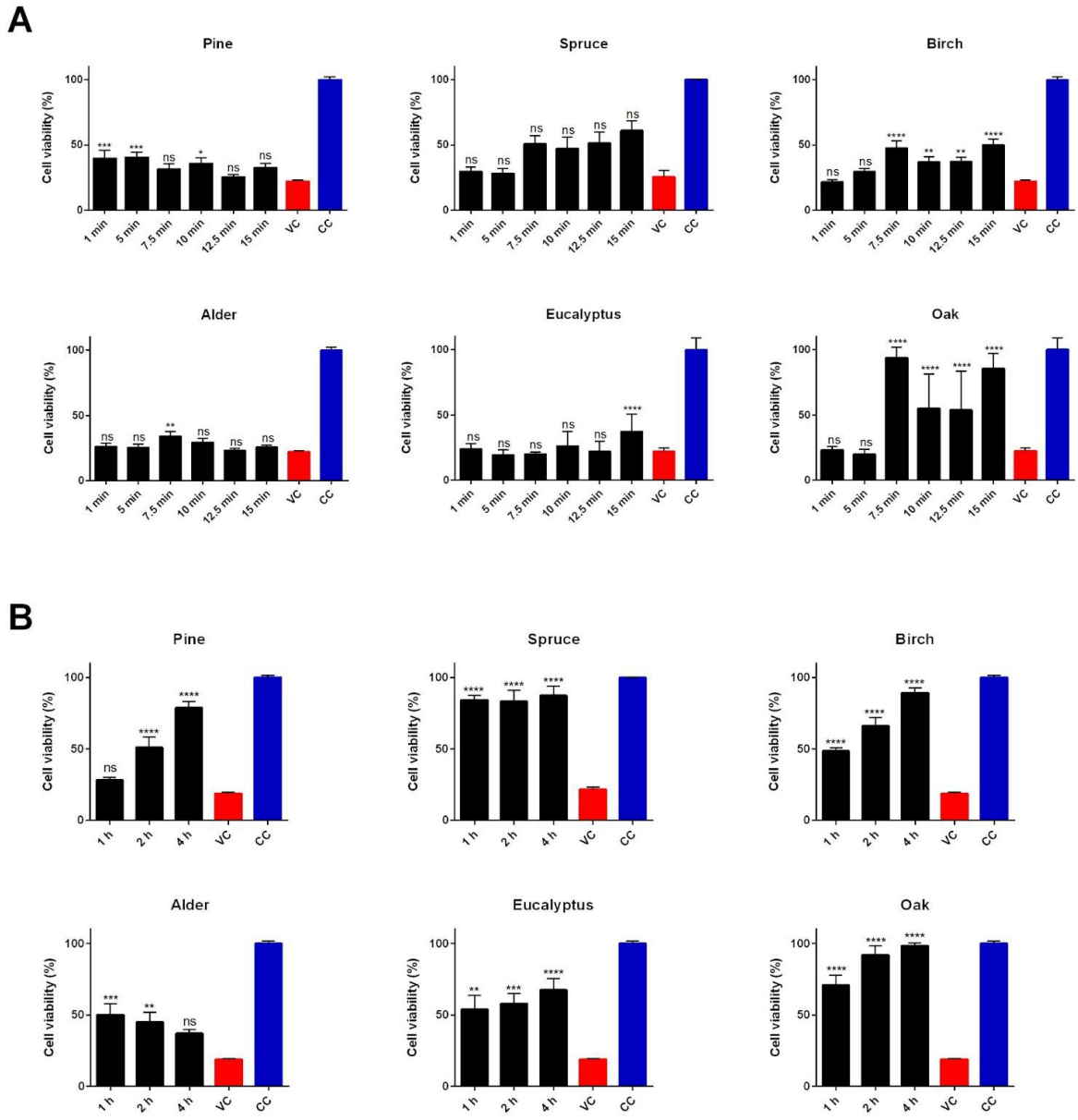

Figure 4: Infectivity of CVA9 recovered from six different wood species after (A) shorter incubation times (1 – 15 min) and (B) longer incubation times (1 – 4 h). The results have been normalized against the cell control (CC) which was set to 100% cell viability. Virus (VC) without any surface treatment was used as a positive control. All the results are presented as an average + standard errors of the mean (SEM). The statistically significant differences between the test samples and VC are indicated with asterisks: * $p < 0.05$,

** $p < 0.01$, *** $p < 0.001$, **** $p < 0.0001$, ns is not significant (analyzed with one-way ANOVA with Bonferroni test).

In addition to the enveloped viruses, it was equally important to also test more stable non-enveloped viruses like Coxsackievirus A9 (CVA9) on the same surfaces. The persistence of CVA9 was tested in two separate experiments, one was for a shorter time ranging from 1 to 15 minutes and the other was for longer period ranging from 1 to 4 hours (Figure 4A and 4B). The results with the shorter time of incubation on the surface showed no significant loss of infectivity on any of the tested wood surfaces except for oak, which showed loss in viral infectivity already starting at 7.5 minutes (Figure 4A). The results with the longer time of incubation on the surface showed varying results for the different wood species (Figure 4B). The virus on the spruce surface showed a complete loss of infectivity after 1 h of incubation, while pine, birch and eucalyptus showed a good loss of infectivity only after 4 h. Alder showed negligible effect even after long incubation periods. These results demonstrate that specific wood species can affect the persistence of non-enveloped viruses on its surface, but these species are interestingly different from those affecting the enveloped coronaviruses. Oak wood showed the fastest inactivation capability followed by pine, birch and eucalyptus, while some surfaces like alder showed no antiviral effect.

3.4 Coronaviruses and enteroviruses differ in their absorption to wood surfaces

In order to decipher the mechanism by which the wood surface demonstrate the antiviral effect, the RNA of the viruses flushed from the wood surface was quantified using qPCR. In addition to pine, oak was chosen as these surfaces had such differing abilities to inactivate coronaviruses and enteroviruses. The viral RNA flushed from the surfaces after a 15 min incubation was first converted to a more stable form of cDNA and then the cDNA was amplified using qPCR. The results from the qPCR revealed that both pine and oak absorbed coronaviruses on the surfaces as their relative amount was clearly lower than the amount of input virus, respectively (Figure 5). A difference of 2.5 and 1.1 logs corresponds to a 99.68% and 92.37% reduction in viral RNA on the pine and oak surfaces, respectively, compared to the input virus. Interestingly, enteroviruses showed no difference between the pine and oak surfaces and showed that the virus load was totally flushed away from the surface after 15 min incubation. This is interesting, as oak showed great efficacy against enteroviruses already after 15 min (Figure 4A). These results indicate that pine wood absorbs more coronaviruses but not non-enveloped enteroviruses.

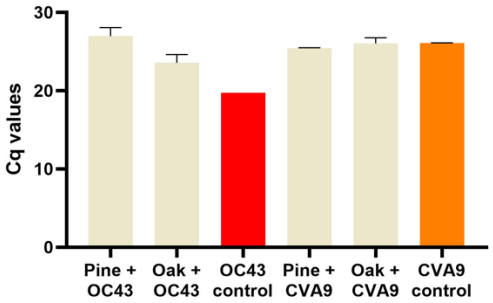

Figure 5: Detection of viral RNA after flushing directly from the (A) pine and (B) Oak surface. HCoV-O43 and CVA9 was incubated on the different wood surfaces for 15 min after which the viral RNA in the flush was quantified using RT-PCR and qPCR techniques. In the virus control (VC) sample, the virus has not been incubated on any surface and the input virus has directly been quantified using PCR. All the results are presented as an average + standard errors of the mean (SEM).

3.5 Coronaviruses flushed from the pine surface lose their ability to initiate infection

We tested the infection potential from samples flushed from the pine surface after 1 h treatment by confocal microscopy. In order to follow the infection cycle of coronaviruses inside MRC-5 cells, the spike protein of the virion was labelled and imaged. Two time points were followed in cells: the virus was allowed to proceed with infection up to 2 hours while in the other case it was allowed to proceed for 15 hours. A virus without surface treatment and viruses flushed from the PE surface were used as control for comparison. The results from the confocal images after 2 h of infection showed bright red spots within the cellular boundaries in case of the virus control and viruses flushed from the PE surface, indicating that virus attachment and internalization was initiated in these two cases (Figure 6A). In the case of the viruses flushed from the pine surface, no such observation was made. Further, after 15 hour incubation inside cells, the viruses flushed from the pine surface did not show cells full of newly synthetised spike proteins like the other samples. This confirmed that the viruses flushed from the pine surface had lost their infection potential (Figure 6B).

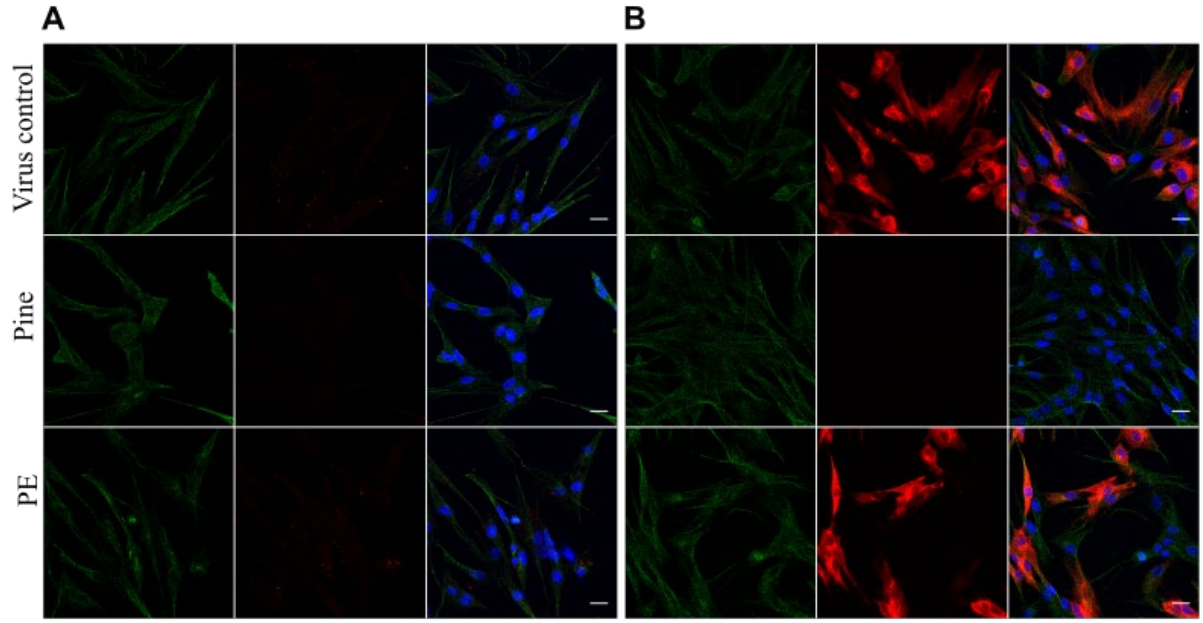

Figure 6. Confocal images of MRC-5 cells infected with HCoV-OC43 flushed from pine and PE surfaces. Time when images were acquired is A) 2 h and B) 15 h post infection. The presence of viral spike protein is visible in red, nucleus in blue and cytoskeletal tubulin in green colour. Scale bar - 30 μm.

3.6 Wood species have significantly different organic chemical compositions

Wood samples exhibited notable variations in the emission of total volatile organic compounds (TVOCs). To investigate the dissimilarities in chemical composition, particularly regarding easily evaporable substances, emissions were collected and analyzed from both dry and wetted wood specimens. The findings revealed a distinct correlation between the emitted chemical compounds at temperatures of 25 °C and 40 °C and the samples' ability to deactivate viruses. Of the species assessed, Scots pine stood out by registering the highest cumulative emission rate, accompanied by an expansive range of identified chemical entities across both dry and wetted samples (see Figure 7A and 7B). Similarly, silver birch and spruce posted elevated emission figures, predominantly evident in the wetted samples (as depicted in Figure 7B). Contrarily, the alder, eucalyptus, and oak samples marked significantly subdued emission figures across the board.

Dry wood samples predominantly emitted aldehydes, alcohols, organic acids, and terpenes, although the overall number of components and their volume were relatively low. Conversely, wetted wood specimens consistently showcased more diverse and abundant chemical emissions, with the test temperature also exerting a notable influence. The identified components were very similar to those found in dry wood, including terpenes (in pine), aldehydes, alcohols, organic acids, as well as some cyclic hydrocarbons and ketones.

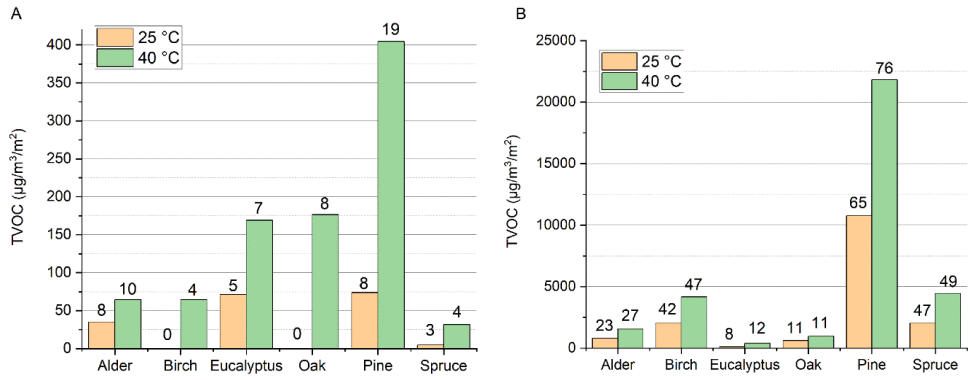

Figure 7: Total volatile organic compound (TVOC) emissions for A) dry wood specimen and B) wetted wood specimen, both averages of two samples analysed. The bars reflect the total emission from wood in 25 °C and 40 °C conditions while the numbers on top of the bar indicate how many chemical components were identified from each specimen. More detailed results on 20 most abundant chemicals and total emissions from specimens are provided in supplementary Tables S1 and S2.

Chemical fingerprinting of SVOC compounds by DIP-APCI-QTOF mass spectrometry revealed considerable differences between wood species studied. The temperature region of 200-300 °C (*desorption* phase) was selected for a more detailed analysis because most SVOC compounds are liberated at these temperatures. Thus, DIP-APCI-QTOF MS is complementary to the TD-GC-MS analysis. Figure 8 represents the van Krevelen diagrams for the compounds detected upon thermal desorption of pine, birch, oak, and eucalyptus samples at 200 °C (2.8-3.0 minutes), 250 °C (4.3-4.5 minutes), and 300 °C (5.8-6.0 minutes) (for spruce and alder, see Figure S4).

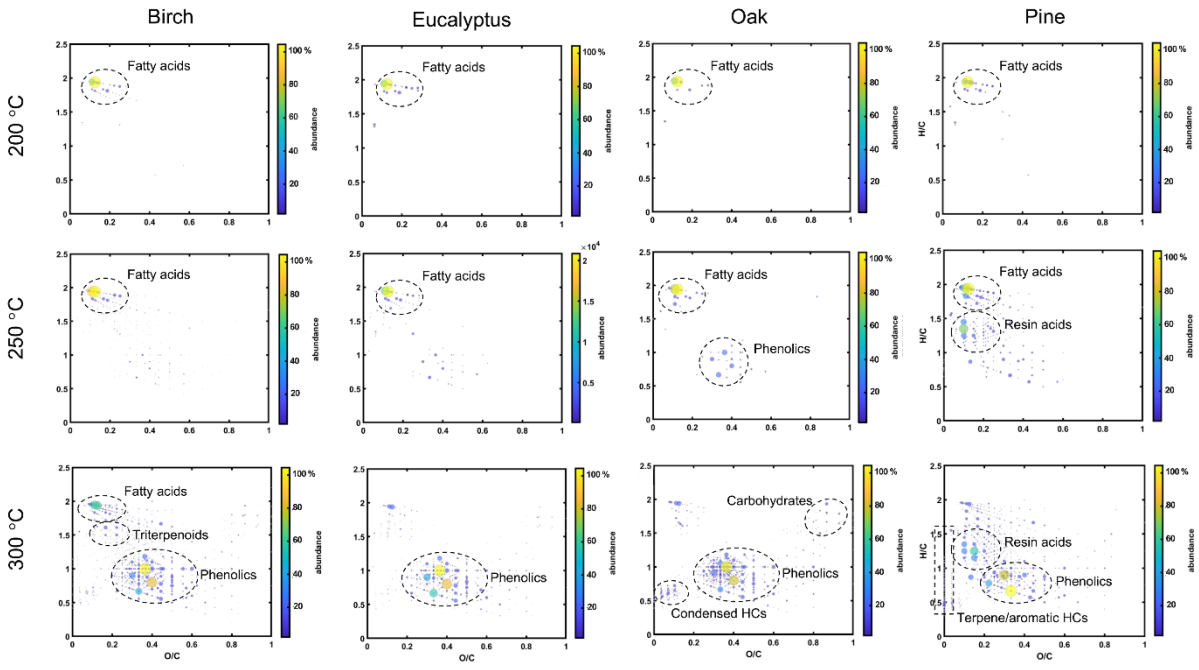

Figure 8: Van Krevelen diagrams for the semivolatile organic compound (SVOCs) from model species of wood analyzed by DIP-APCI-QTOF system. Here pine and birch represent cases of excellent-to-good antiviral activity, whereas oak and eucalyptus represent cases of low-to-none in terms of antivirality. Similar

summary of detected component groups for alder and spruce can be found in supplementary Figure S4. Key differences arise from presence of resin components in pine and rather abundant presence of phenolic compounds in both pine and birch in comparison to other tree species.

The main compounds desorbed at 200 °C were saturated and non-saturated fatty acids, showing no marked differences between the wood species. In contrast, at 250 °C pine wood showed desorption of compounds at H/C ≈ 0.1-0.3 and O/C ≈ 1-1.5, representing different resin acids and other diterpenoids. At 250 °C, the other three wood species showed very little difference to those observed at 200 °C. The biggest differences were observed at 300 °C, where pine wood liberates a mixture of phenolic acids and aldehydes (e.g., cinnamate and coniferyl aldehyde), stilbenes and flavonoids (e.g., flavan-3-ol), and a number of resin acids. In contrast to the other wood species, pine also showed desorption of different terpene hydrocarbons, observed at O/C = 0 and H/C ≈ 0.2-0.8. All hardwood species also liberated phenolic extractives at 300 °C, and oak wood also showed some condensed hydrocarbon (HC) species as well as a small number of hemicellulose-derived monosaccharides. In addition, birch wood showed presence of triterpenoids and hydroxy/epoxy fatty acids. Spruce showed rather similar characteristics to that of pine, although considerably less resin acids were observed, and alder was very similar to the other hardwood species (Figure S4).

3.7 Modification to natural wood can significantly alter virus persistence

Wood materials used in household and commercial settings are modified physically and/or chemically to increase their shelf life and protect them from the adverse impacts of weathering, pests, and biological degradation. To examine whether modifications like reducing the coarseness, combining with plastic or thermal treatments would retain its antiviral efficacy against viruses, we tested the persistence of HCoV-OC43 on these modified wood surfaces. The first tests were made with a wood-plastic composite and as a control we used PE plastic for comparison. The HCoV-OC43 virus was added to the two surfaces and incubated for up to an hour, after which the infectivity of the viruses flushed from these surfaces from each timepoint was evaluated using the CPE assay. As per the CPE assay results, the viral infectivity remained unchanged even after one hour of incubation on both these surfaces (Figure 9A and Figure 9B). These results indicate that due to the presence of plastic in the wood composite, the wood composite surface acted just like the polyethylene plastic and completely lost its ability to inactivate viruses on its surface.

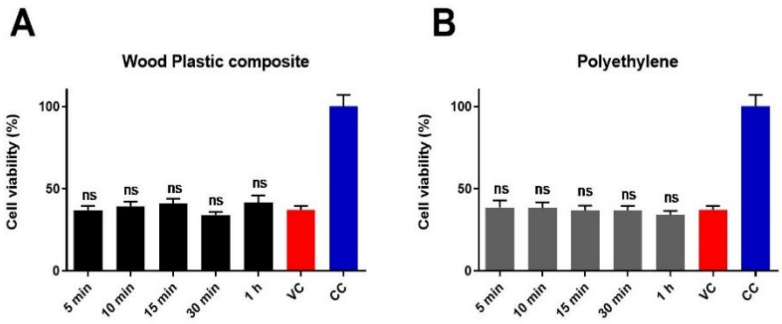

Figure 9. Infectivity of HCoV-OC43 recovered from (A) wood plastic composite and (B) PE plastic determined using CPE assay. Wood composite is about 50% wood and 50% plastic, PE is used as a control plastic sample. The non-infected cell controls have been set as 100% cell viability. Results are presented as an average of four sample replicates, each including three technical replicates on MRC-5 cells. Statistical significance of the samples against virus control are shown above the bars (ns means no statistical significance).

The effect of different coarseness levels (Pine 80, 120, 320, 1000 and planed) on the persistence of HCoV-OC43 was also tested similarly. The CPE assay demonstrated that there were no differences in how the viral infectivity declined on the differently polished surfaces compared to the unpolished surface (Figure 1 and Figure S5). For all the polished pine wood surfaces, the infectivity of the virus was lost closer to the 15 minute time point. These results suggest that surface coarseness did not play a major role in altering the persistence of HCoV-OC43 on pine wood surface.

In the third type of wood modifications, we tested two types of thermally treated ThermoWood® (Thermo-S and Thermo-D) pine and spruce surfaces. Thermo-S referring to indoor use product class where the dimensional stability was improved with milder temperatures (190 °C), and outdoor uses targeting Thermo-D (D stands for durability) applying a higher temperature regime (212 °C). Viruses were incubated on various surfaces for durations of 5, 10, and 15 minutes, and their infectivity was assessed using the CPE assay. For Thermo-S and Thermo-D pine surfaces, complete viral inactivation occurred within 15 minutes (Figure S6A), similar to untreated pine (Figure 1A). However, Thermo-S and Thermo-D treated spruce showed different outcomes. While untreated spruce inactivated the virus within 10 minutes, Thermo-S required 15 minutes, and Thermo-D preserved viral infectivity throughout the incubation (Figure S6B). This implies that the thermal treatment effects vary across wood species, with Thermo-D treated spruce potentially aiding in virus transmission. Thermo-D treatment on spruce surface allows the viruses to persist on its surface and can be a potential fomite surface for virus transmission.

DIP-APCI-QTOF MS analysis was conducted on thermally treated wood. The van Krevelen diagrams for SVOC compounds from Thermo-D and Thermo-S treated pine and spruce are shown in Figure S7. The results indicate that there were no marked differences between pine and either thermally treated samples. Both, Thermo-S and Thermo-D samples liberated slightly higher amounts of resins at 250 and 300 °C and lower amount of phenolics at 300 °C, as compared to the untreated wood. In contrast,

different results were observed with the spruce samples. Thermo-S sample did not have marked differences to that of the untreated spruce, but Thermo-D treated spruce liberated much higher content of resin acids and phenolics as well as some carbohydrates (mono- and disaccharides), suggesting that more severe lignin and hemicellulose degradation occurs upon thermal treatment at 212 °C.

4. Discussion

While the antibacterial activity of wood has been extensively studied, there are only few antiviral studies on wood materials, and especially the differences between wood species are largely unknown. Also studies in which wood surface topography or chemical modification would have been assessed as factors to contribute to antivirality are scarce. We show here that native wood materials are in general very good in their antiviral efficacy. Many wood species that are commonly used in indoor and outdoor housing, such as pine, spruce, and birch, killed coronavirus infectivity within a 15 minute time frame. However, species like oak, eucalyptus and alder showed much lower efficacy. Notably, enveloped, and non-enveloped viruses responded differently to these surfaces.

Our CPE assay results showed that pine and spruce are the most challenging surfaces for coronaviruses to stay infectious. The infectivity was already destroyed after 5-10 minutes compared to alder, oak, and eucalyptus, in which viruses stayed infectious during the shortest incubation times at room temperature. It is challenging to compare these results to previous studies since only a few studies have been done with wood surfaces, and, in previous studies, wood species were not described in detail. Chin et al. (2020) reported that after two days, no infective SARS-CoV-2 was detected on the treated wood surface in their experiments (room temperature, RH 65%) while Duan et al. (2003) reported that SARS-CoV stayed infectious for 4-5 days at room temperature on wood board [16,19].

In our studies, we simulated standardized test conditions by incubating the virus on the surface at room temperature and over 90% RH. Additionally, it was important to note that indoor humidity levels can vary significantly, especially in Nordic countries. Wintertime conditions may see indoor humidity drop to very low levels, even below 20%, while summertime conditions typically range between 50% and 70%. In southern European countries, where temperatures can soar up to 40 °C during the summer, the environmental factors are distinctly different. To account for this variability, we conducted experiments incubating viruses on four different wood species under three different RH conditions (20%, 40%, and 60%) at two different temperatures (21 °C and 37 °C)

We observed, expectedly, that the virus persists less at higher temperatures. This has been shown by several other studies [6,19–21]. We expected that humidity conditions could affect the results. Humidity conditions can, for example, influence the water absorption properties of wood, which could further affect the virus's survival on the wood surface. However, it was surprising to find out that humidity played such a small role in the tested time frame. Our studies found that the relationship between RH and infectivity reduction was not so clear at room temperature. However, at 37 °C, we observed that moderate RH

conditions destroy viral infectivity most efficiently. Thus, the relationship between RH and viral infectivity seems to be not linear, but U-shaped, as reported earlier by Casanova et al. (2010) [22]. They also suggested that the relationship between temperature and RH is different depending on temperature conditions.

It is known that the porosity of wood and pore diameters vary among species. This might affect the faster drying of viruses on the wood surface. For example, the total porosity of birch is determined to be 60.5%, and pine is 69.7%, whereas the total porosity of oak is only 53.8% [23]. When comparing these porosities to our coronavirus persistence results, it seems that the higher the porosity, the more quickly coronavirus infectivity got destroyed on the surface. We also tested the wood composite and found that virus persistence was very similar to plastic. These results match well with previous studies showing that viruses stay viable longer on nonporous materials than on porous materials [24–27]. One of the explanations for faster inactivation could be the drying of the viruses. Cox (1993) reported over decades ago that dehydration causes damage to the bilayer membrane of viruses and leads to other violating structural changes such as Maillard reactions of proteins and oxidation of lipids [28]. The envelope proteins are needed in cell penetration, and thus the damage to the viral envelope makes them inactive. Porous materials draw moisture away from absorbed viruses more efficiently, whereas, on non-porous surfaces, a moist microenvironment might enable prolonged virus survival. Chatterjee et al. (2021) reported that the bulk liquid in the respiratory droplets evaporate in minutes on both porous and non-porous surfaces [29]. They pointed out that the critical factor is a microscopic thin residual liquid film that enables the virus to survive despite the drying of bulk droplets. Porous materials absorb these thin films more efficiently because of the material's fibres and pores, and thus viruses are inactivated faster. However, more specific studies supporting these physiochemical hypotheses are needed.

Our qPCR flushing experiment results indicated that wood could also retain more viral RNA than plastic. Viral particles may be physically trapped on the wood surface, which could also explain why the viral infection potential was weaker in virus samples incubated on the porous wood surfaces. The viruses might stay infectious on the surface but were stuck or absorbed inside the wood surface and did not get released to the flushing medium. This way, the number of infective viruses added to the cells was smaller and thus not so infectious for the cells in the CPE experiments. Interestingly, however, we observed that pine could not absorb enteroviruses and flushed viruses in a similar manner from pine and for the hardwood oak, which showed high antiviral efficacy despite of low absorbance. Furthermore, the porosity is not that different between species, e.g., pine vs oak, that it would explain all loss of infectivity also in the case of coronaviruses. Therefore, the results clearly pointed to other mechanisms, i.e., antiviral compounds in the wood species themselves.

The chemical composition of wood typically includes around 40-45% cellulose, 20-25% hemicellulose, and 20-30% lignin. The rest (around 5%) of wood composition is known as extractives. Extractives are organic compounds such as resins, flavonoids, terpenoids,

essential oils, sterols, alkaloids, fatty alcohols, phenolics (such as tannins), and gums which can be extracted from the wood using polar or non-polar solvents [30]. While cellulose does not show any antimicrobial properties [31], hemicellulose has demonstrated indirect antimicrobial activity [32], and lignans and extractives have repeatedly demonstrated very good antimicrobial effects [12,33]. These extractives are known to play a major role in many functional aspects of the plant cells and improve wood's natural resistance against decay organisms [34]. There are some studies about the antiviral properties of extractives in the literature. For example, some diterpenoids extracted from pine are studied to inhibit viral RNA expression of influenza virus A [35]. Tannins extracted from spruce and pine are also proven to have antiviral efficacy against non-enveloped coxsackievirus A9, as we found recently [36].

We conducted analysis on volatile organic components from six wood species under both dry and wet conditions at two distinct temperature settings. Notably, the species with the highest antiviral activity, namely pine, spruce, and birch, also exhibited the most significant chemical emissions in terms of both variety and volume. While certain abundant chemicals were identified, the contribution of individual components to antiviral activity remains unspecified. Distinctly, pine and spruce contained natural resin acids and displayed a higher count of phenolic compounds and hydrocarbons compared to the other species.

Chemical analysis of spruce and Scots pine within the temperature range of 150 to 300 °C revealed an increasing presence of resin acids and phenolic compounds, characteristics of coniferous species (Figure S8). Previous studies have suggested the antiviral efficacy of lignin constituents, possibly through reactive oxygen species generated from lignin phenol oxidation [37]. Confirming prior research by Willför et al. (2003ab) and Esteves et al. (2013), our findings indicated that pine emitted more resin acids, phenolic components, and certain hydrocarbons than spruce [38–40]. However, a variation was observed in the retention of some resins at higher temperatures. The prominence of phenolic compounds likely originates from lignin breakdown.

Furthermore, in thermally modified wood samples, the emergence of carbohydrates suggests the decomposition of hemicelluloses into sugar monomers [41]. Despite a decrease in the absolute volume of chemicals in thermally modified samples, their composition exhibited greater diversity. It appears that pine retains a higher count of antiviral resin and phenol components than spruce, potentially explaining their varied antiviral performance. The elevated presence of hemicellulose monomers in thermally modified spruce and its subsequent reduced antiviral activity might be associated with carbohydrate chain cleavage, a concept discussed by Li et al. (2021) [42]. However, the interplay between carbohydrates and viruses warrants further investigation. Our upcoming research will assess virus viability in response to specific pure substances at defined concentrations on surfaces. Current findings, although informative, do not sufficiently pinpoint which components, lost during thermal modification, impact antiviral efficiency. The DIP-APCI-QTOF analysis (see Figure 8) demonstrates that diverse non-structural components

vaporize at varying temperatures across different wood species. Such compositional alterations can be meticulously traced, as recently shown by Castillia et al. (2020) [43].

Wood materials encountered in daily environments are often subjected to various chemical or mechanical treatments. Consequently, it is imperative to investigate the influence of these treatments on the antiviral properties of wood. Heat treatments, known to alter the physical characteristics of wood[44], for example, can affect the wood's ability to absorb moisture. Our investigation of two thermally treated wood samples, pine and spruce, revealed that pine retains its antiviral efficacy post-thermal treatment. However, in the case of spruce, increased thermal treatment was observed to diminish its antiviral efficacy, though the specific chemical mechanisms underlying this reduction remain to be clarified.

Altogether, our results reveal remarkable differences in the antiviral efficacy between wood species and between coronaviruses and enteroviruses. It is evident that while porosity and absorption disparities of a material contribute to its antiviral efficacy, it is primarily the chemical composition of the wood surfaces that governs the antiviral functionality. Future research will focus on identifying the most effective antiviral compounds present in wood and understanding how they interact with viruses. This could lead to innovative developments in antiviral materials inspired by these natural properties. Meanwhile, our findings also illuminate the practical utility of untreated wood surfaces as a natural, effective barrier against viral transmissions, opening avenues for their application in public health strategies.

5. Acknowledgements

We thank Dr. Christopher Rüger from the University of Rostock for the use of Ceres Viewer program. The mass spectrometry facility is supported by Biocenter Finland (FINStruct) and Biocenter Kuopio. Funding for the study was obtained by AH from Academy of Finland (grants no. 329884 and 335524) and by VM from Jane and Aatos Erkko Foundation and from Academy of Finland (grant no 342251).

Author contribution

S.S., A.P., A.V., P.P., K.G., V.N., and J.J. performed the experimental studies and carried out the formal analysis. S.S., A.P., A.H., and V.M. wrote the original draft. S.S., K.G., V.N., J.J., and A.H. contributed to the artwork. A.H. and V.M. conceptualized the original idea, designed and supervised the study, raised the funding, and reviewed and edited the final draft.

Competing interest

The authors report that there are no competing interests to declare.

References

1. Dukarska, D. & Mirski, R. Wood-Based Materials in Building. *Materials* **16**, 2987 (2023).
2. Marschallek, B. E., Löw, A. & Jacobsen, T. You can touch this! Brain correlates of aesthetic processing of active fingertip exploration of material surfaces. *Neuropsychologia* **182**, 108520 (2023).
3. Barker, J., Stevens, D. & Bloomfield, S. F. Spread and prevention of some common viral infections in community facilities and domestic homes. *Journal of Applied Microbiology* **91**, 7–21 (2001).
4. Hota, B. Contamination, disinfection, and cross-colonization: are hospital surfaces reservoirs for nosocomial infection? *Clin Infect Dis* **39**, 1182–1189 (2004).
5. Zhang, J., Wang, S. & Xue, Y. Fecal specimen diagnosis 2019 novel coronavirus-infected pneumonia. *J Med Virol* **92**, 680–682 (2020).
6. Firquet, S. *et al.* Survival of Enveloped and Non-Enveloped Viruses on Inanimate Surfaces. *Microbes Environ* **30**, 140–144 (2015).
7. Wood, A. & Payne, D. The action of three antiseptics/disinfectants against enveloped and non-enveloped viruses. *J Hosp Infect* **38**, 283–295 (1998).
8. Imai, K. *et al.* Disinfection efficacy and mechanism of olanexidine gluconate against norovirus. *American Journal of Infection Control* **50**, 764–771 (2022).
9. Curran, E. T., Wilkinson, M. & Bradley, T. Chemical disinfectants: Controversies regarding their use in low risk healthcare environments (part 1). *J Infect Prev* **20**, 76–82 (2019).
10. Dewey, H. M., Jones, J. M., Keating, M. R. & Budhathoki-Uprety, J. Increased Use of Disinfectants During the COVID-19 Pandemic and Its Potential Impacts on Health and Safety. *ACS Chem. Health Saf.* **29**, 27–38 (2022).
11. Aviat, F. *et al.* Microbial Safety of Wood in Contact with Food: A Review. *Comprehensive Reviews in Food Science and Food Safety* **15**, 491–505 (2016).
12. Laireiter, M., Schnabel, T., Köck, A. & Stalzer, P. Active anti-microbial effects of larch and pine wood on four bacterial strains :: BioResources. https://bioresources.cnr.ncsu.edu/ (2013).
13. Pailhoriès, H. *et al.* Oak in Hospitals, the Worst Enemy of Staphylococcus aureus? *Infection Control & Hospital Epidemiology* **38**, 382–384 (2017).
14. Carpentier, B. Sanitary quality of meat chopping board surfaces: a bibliographical study. *Food Microbiology* **14**, 31–37 (1997).
15. Greatorex, J. S. *et al.* Survival of Influenza A(H1N1) on Materials Found in Households: Implications for Infection Control. *PLoS One* **6**, e27932 (2011).
16. Chin, A. W. H. *et al.* Stability of SARS-CoV-2 in different environmental conditions. *The Lancet Microbe* **1**, e10 (2020).
17. Myllynen, M., Kazmertsuk, A. & Marjomäki, V. A Novel Open and Infectious Form of Echovirus 1. *J Virol* **90**, 6759–6770 (2016).
18. Turkki, P. *et al.* Slow Infection due to Lowering the Amount of Intact versus Empty Particles Is a Characteristic Feature of Coxsackievirus B5 Dictated by the Structural Proteins. *Journal of Virology* **93**, 10.1128/jvi.01130-19 (2019).
19. Duan, S.-M. *et al.* Stability of SARS Coronavirus in Human Specimens and Environment and Its Sensitivity to Heating and UV Irradiation. *BES* **16**, 246–255 (2003).
20. Rabenau, H. F. *et al.* Stability and inactivation of SARS coronavirus. *Med Microbiol Immunol* **194**, 1–6 (2005).

21. van Doremalen, N., Bushmaker, T. & Munster, V. J. Stability of Middle East respiratory syndrome coronavirus (MERS-CoV) under different environmental conditions. *Euro Surveill* **18**, 20590 (2013).
22. Casanova, L. M., Jeon, S., Rutala, W. A., Weber, D. J. & Sobsey, M. D. Effects of Air Temperature and Relative Humidity on Coronavirus Survival on Surfaces. *Appl Environ Microbiol* **76**, 2712–2717 (2010).
23. Plötze, M. & Niemz, P. Porosity and pore size distribution of different wood types as determined by mercury intrusion porosimetry. *Eur. J. Wood Prod.* **69**, 649–657 (2011).
24. Kampf, G., Todt, D., Pfaender, S. & Steinmann, E. Persistence of coronaviruses on inanimate surfaces and their inactivation with biocidal agents. *J Hosp Infect* **104**, 246–251 (2020).
25. Riddell, S., Goldie, S., Hill, A., Eagles, D. & Drew, T. W. The effect of temperature on persistence of SARS-CoV-2 on common surfaces. *Virology Journal* **17**, 145 (2020).
26. van Doremalen, N. *et al.* Aerosol and Surface Stability of SARS-CoV-2 as Compared with SARS-CoV-1. *New England Journal of Medicine* **382**, 1564–1567 (2020).
27. Liu, D. X., Liang, J. Q. & Fung, T. S. Human Coronavirus-229E, -OC43, -NL63, and -HKU1 (Coronaviridae). *Encyclopedia of Virology* 428–440 (2021) doi:10.1016/B978-0-12-809633-8.21501-X.
28. Cox, C. S. Roles of water molecules in bacteria and viruses. *Origins Life Evol Biosphere* **23**, 29–36 (1993).
29. Chatterjee, S., Murallidharan, J. S., Agrawal, A. & Bhardwaj, R. Why coronavirus survives longer on impermeable than porous surfaces. *Phys Fluids (1994)* **33**, 021701 (2021).
30. Nascimento, M. S. *et al.* Phenolic Extractives and Natural Resistance of Wood. in *Biodegradation - Life of Science* (IntechOpen, 2013). doi:10.5772/56358.
31. Orlando, I. *et al.* Chemical Modification of Bacterial Cellulose for the Development of an Antibacterial Wound Dressing. *Frontiers in Bioengineering and Biotechnology* **8**, (2020).
32. Bouaziz, F., Koubaa, M., Ellouz Ghorbel, R. & Ellouz Chaabouni, S. Biological properties of water-soluble polysaccharides and hemicelluloses from almond gum. *Int J Biol Macromol* **95**, 667–674 (2017).
33. Dong, X. *et al.* Antimicrobial and antioxidant activities of lignin from residue of corn stover to ethanol production. *Industrial Crops and Products* **34**, 1629–1634 (2011).
34. Schultz, T. P. & Nicholas, D. D. Naturally durable heartwood: evidence for a proposed dual defensive function of the extractives. *Phytochemistry* **54**, 47–52 (2000).
35. Ha, T. K. Q. *et al.* Antiviral Activities of Compounds Isolated from Pinus densiflora (Pine Tree) against the Influenza A Virus. *Biomolecules* **10**, 711 (2020).
36. Granato, D. *et al.* From the forest to the plate – Hemicelluloses, galactoglucomannan, glucuronoxylan, and phenolic-rich extracts from unconventional sources as functional food ingredients. *Food Chemistry* **381**, 132284 (2022).
37. Boarino, A. *et al.* Lignin: A Sustainable Antiviral Coating Material. *ACS Sustainable Chem. Eng.* **10**, 14001–14010 (2022).

38. Willför, S., Hemming, J., Reunanen, M. & Holmbom, B. Phenolic and Lipophilic Extractives in Scots Pine Knots and Stemwood. **57**, 359–372 (2003).
39. Willför, S., Hemming, J., Reunanen, M., Eckerman, C. & Holmbom, B. Lignans and Lipophilic Extractives in Norway Spruce Knots and Stemwood. **57**, 27–36 (2003).
40. Esteves, B., Velez Marques, A., Domingos, I. & Pereira, H. Chemical changes of heat treated pine and eucalypt wood monitored by FTIR. *Maderas. Ciencia y tecnología* **15**, 245–258 (2013).
41. Čabalová, I., Zachar, M., Kačík, F. & Tribulová, T. Impact of thermal loading on selected chemical and morphological properties of spruce ThermoWood :: BioResources. https://bioresources.cnr.ncsu.edu/ (2019).
42. Li, R. *et al.* Conversion of Beech Wood into Antiviral Lignin–Carbohydrate Complexes by Microwave Acidolysis. *ACS Sustainable Chem. Eng.* **9**, 9248–9256 (2021).
43. Castilla, C., Rüger, C. P., Lavanant, H. & Afonso, C. Ion mobility mass spectrometry of in situ generated biomass pyrolysis products. *Journal of Analytical and Applied Pyrolysis* **156**, 105164 (2021).
44. Vainio-Kaila, T., Kyyhkynen, A., Rautkari, L. & Siitonen, A. Antibacterial Effects of Extracts of Pinus sylvestris and Picea abies against Staphylococcus aureus, Enterococcus faecalis, Escherichia coli, and Streptococcus pneumoniae. *BioResources* **10**, 7763–7771 (2015).

Supplementary materials

Chemical analyses – TVOC measurements using TD-GC-MS system

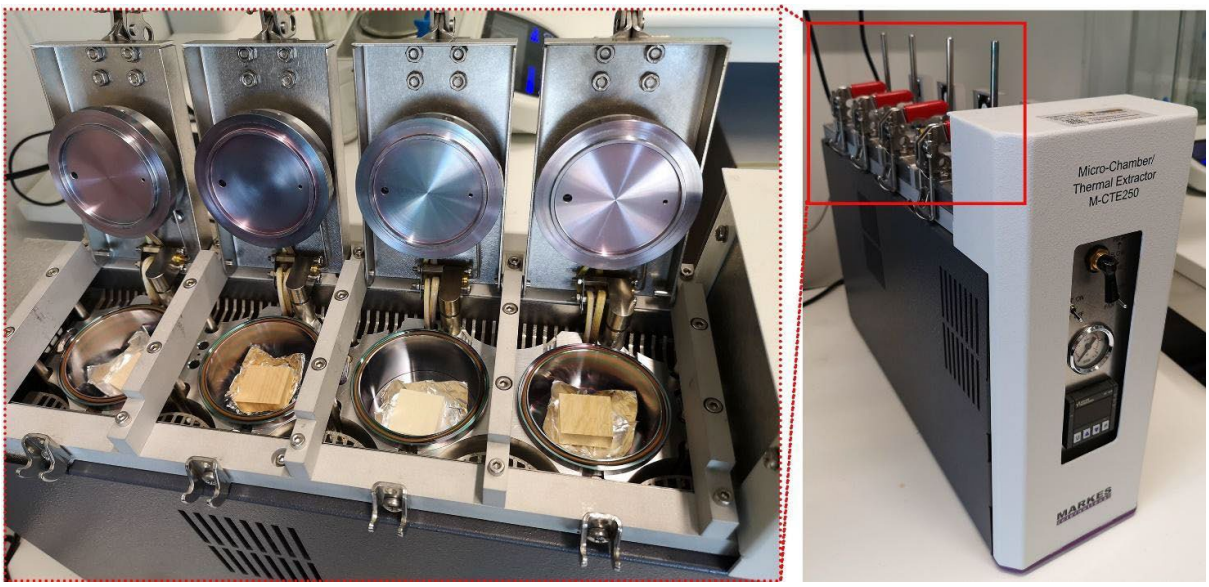

Figure S1. Measurement setup for TVOC emissions from wood specimen at 25 and 40 °C placing the wood specimens on tinfoil plates inside the chambers of a Micro-Chamber/Thermal Extractor M-CTE250 apparatus (Markes International Inc.), equilibrating to the target sampling temperature and drawing emitted VOCs via the chambers' dedicated sampling outlets.

Table S1. Total volatile organic compounds (TVOC) emissions (top 20 selected components and total number of identified emitted chemicals) from dry (moisture content ca. 8%) wood specimens in 25 °C and 40 °C incubation.

Chemical compounds emitted	Alder		Birch		Eucalyptus		Oak		Pine		Spruce	
	25 ℃	40 ℃	25 ℃	40 ℃	25 ℃	40 ℃	25 ℃	40 ℃	25 ℃	40 ℃	25 ℃	40 ℃
1-Nonene	2.1	2.6	-	-	-	-	-	-	-	-	-	-
3-Carene	-	-	-	-	-	-	-	-	-	35.3	-	-
3-Ethylpyrazoline	-	-	-	-	-	-	-	-	-	15.9	-	10.4
Acetic acid	3.8	2.6	-	47.8	30.2	44.0	-	79.8	9.7	41.2	0.5	5.5
Alpha-pinene	-	-	-	-	-	-	-	-	21.1	73.9	-	-
Benzaldehyde	-	-	-	-	-	-	-	-	-	28.5	-	-
Benzoic acid	-	1.5	-	-	-	-	-	15.9	-	9.1	-	-
Butenone	-	-	-	-	-	-	-	-	10.7	11.1	-	-
Decalactone	-	-	-	-	-	-	-	23.2	-	-	-	-
Decanal	9.7	33.1	-	5.0	22.4	42.1	-	16.7	8.5	61.9	4.0	6.8
Decanoic acid	-	-	-	-	-	-	-	33.2	-	-	-	-
Ethylhexanol	3.1	-	-	-	-	-	-	-	-	10.1	-	-
Hexanal	1.8	2.7	-	-	-	-	-	-	6.7	22.8	-	-
Linalool	3.1	3.5	-	7.7	-	-	-	-	-	-	-	-
Menthofuran	-	-	-	-	-	15.0	-	-	3.3	14.7	-	-
Nonanal	7.5	12.2	-	4.0	10.7	11.5	-	7.7	9.4	47.3	0.3	9.1
Nonene	-	-	-	-	-	15.0	-	-	-	11.5	-	-
Octanal	4.1	6.4	-	-	4.8	30.5	-	-	4.3	21.5	-	-
Hexenyl acetate	-	-	-	-	3.1	10.9	-	-	-	-	-	-
TVOC ($\mu g/m^3/m^2$)	35.2	64.5	0.0	64.5	71.3	168.9	0.0	176.5	73.7	404.9	4.8	31.8
No. of components	8	10	0.0	4	5.0	7	0.0	8	8.0	19	3.0	4

Table S2. Total volatile organic compounds (TVOC) emissions (top 20 selected components and total number of identified emitted chemicals) from briefly wetted wood specimens in 25 °C and 40 °C incubation.

Chemical compounds emitted	Alder		Birch		Eucalyptus		Oak		Pine		Spruce	
	25 °C	40 °C	25 °C	40 °C	25 °C	40 °C	25 °C	40 °C	25 °C	40 °C	25 °C	40 °C
3-Carene	-	-	-	-	-	-	-	-	934	1838	-	-
Acetic acid	66	134	271	292	40	141	446	542	-	-	207	326
Alpha-pinene	-	-	-	-	-	-	-	-	1645	3573	290	692
Alpha-terpeniol	-	-	-	-	-	-	-	-	-	-	134	321
Butanol	-	-	27	64	-	-	-	-	-	314	-	-
Decanal	14	22	-	-	18	56	9	51	-	-	-	52
Heptanal	12	20	39	83	-	-	-	-	160	283	-	72
Heptanone	-	-	33	66	-	-	-	-	107	203	-	-
Heptenone	-	-	22	50	-	-	-	-	-	-	-	-
Hexanal	437	829	656	1429	5	19	72	144	3318	7343	414	1055
Hexanoic acid	-	-	-	72	-	-	-	-	106	400	88	-
Limonene	-	-	-	-	-	-	-	-	-	-	139	279
Nonanal	15	22	24	61	10	38	9	43	120	283	-	-
Octanal	-	-	30	59	-	12	9	15	389	396	-	-
Octenal	17	28	26	72	-	-	-	-	220	314	32	58
Pentanal	51	90	81	146	-	-	5	11	758	1478	92	209
Pentanol	47	91	-	-	-	-	5	11	1045	2309	106	293
Pentenol	-	-	286	759	-	-	-	-	-	-	-	-
Pentylfuran	-	-	33	-	-	-	-	-	129	-	-	-
Styrene	42	67	68	124	-	-	35	60	-	-	-	-
TVOC ($\mu g/m^3/m^2$)	808	1566	2041	4179	97	398	615	979	10782	21816	2051	4442
No. of components	23	27	42	47	8	12	11	11	65	76	47	49

Chemical analyses – SVOC measurements using DIP-APCI-QTOF setup

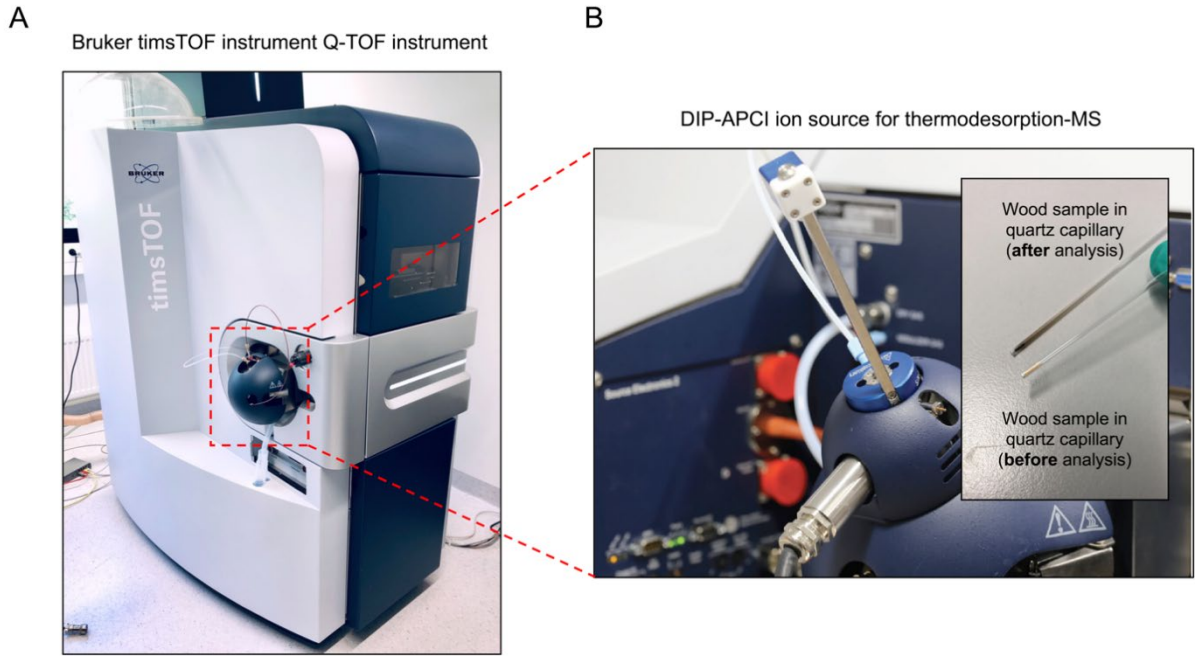

Figure S2. A) Measurement setup for DIP-APCI-QTOF chemical analysis for wood specimen and B) the outlook of wood sample in sample capillary before and after analysis (specimens were charred after measurements at 450 °C but the analyses consider only the desorption phase (see also Fig. S2).

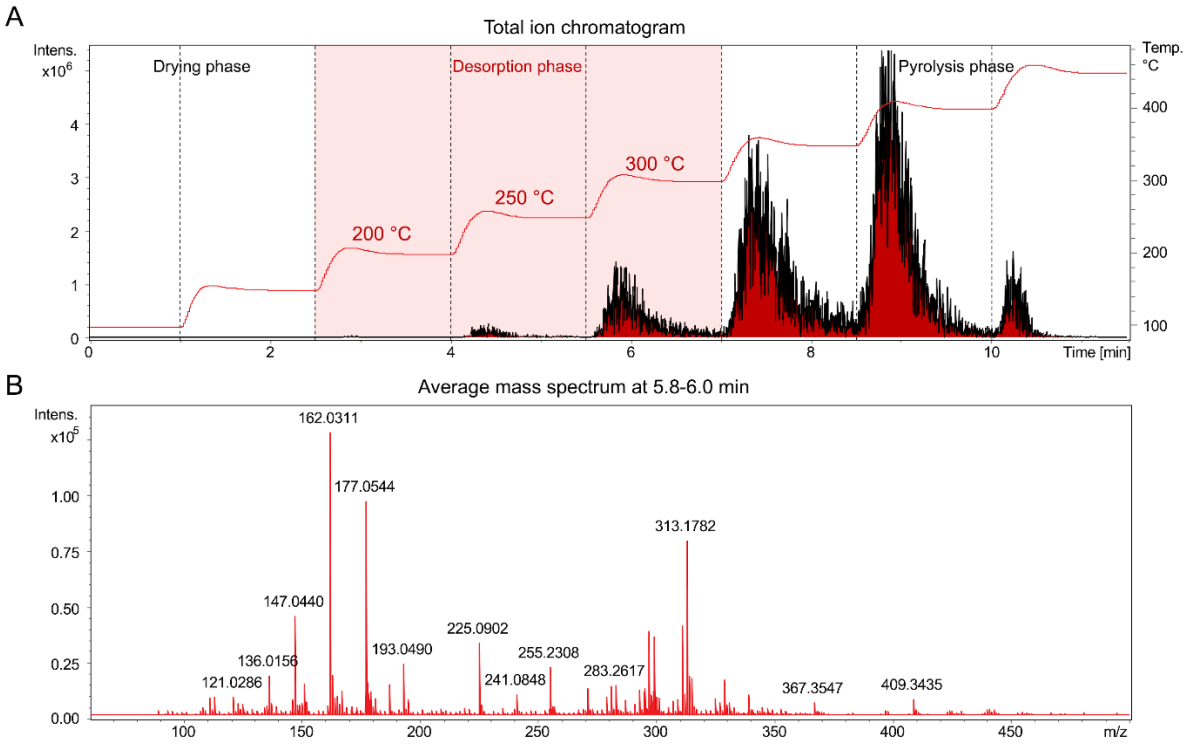

Figure S3. A) Selection of tested temperature gradient with DIP-APCI-QTOF MS and the summed abundance of detected chemical compounds in the desorption range. Chemicals observed at higher temperatures (pyrolysis phase) contain a significant number of thermal decomposition products that no longer represent the properties of native wood. Similarly, chemicals detected at below 200 °C (drying phase) were considered to have no impact on antiviral activity due to their immensely low abundance. B) Total ion chromatogram of a sample showing typical mass spectra detected while heating the sample from 250 to 300 °C which was used to identify compounds and classify them via Van Krevelen diagrams (color-coded for relative intensity) with the criteria stated in the manuscript.

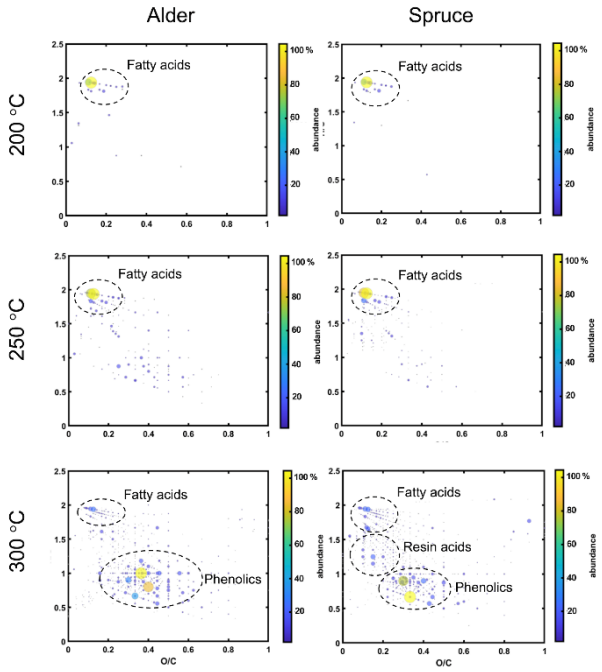

Figure S4. Van Krevelen diagrams for spruce and alder samples. The components of spruce were more numerous and closer to the (coniferous) pine wood than other tested species, including some amount of resin compounds detected at 300 °C. The components identified from alder were not significantly different from other deciduous trees like oak and eucalyptus and there were hardly any resin acid group chemicals present.

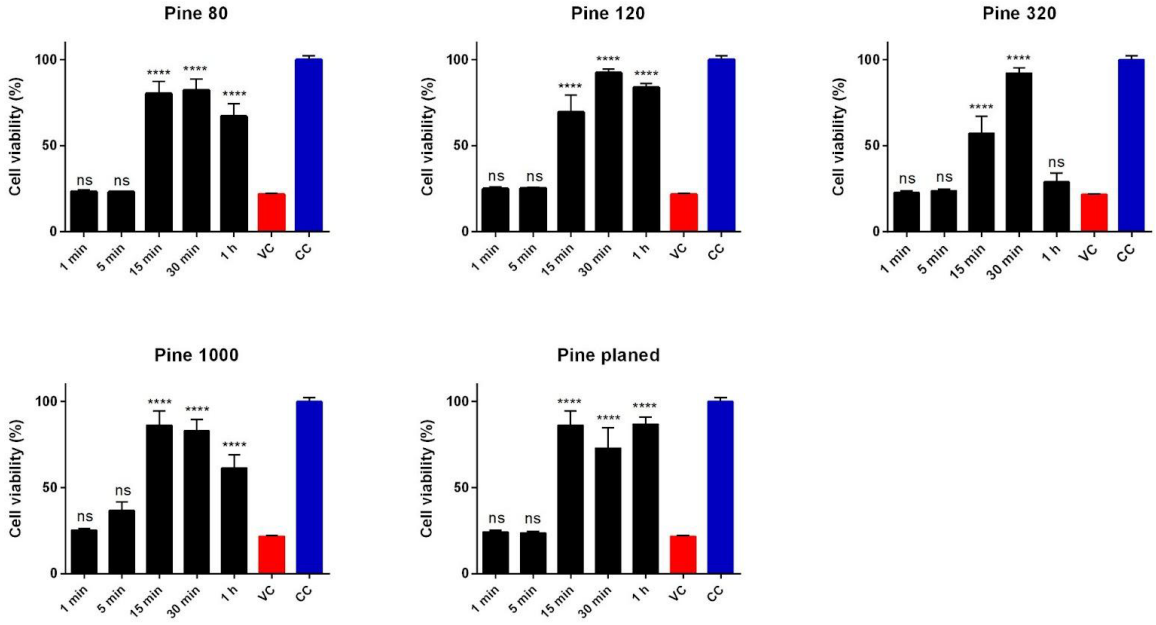

Figure S5 Infectivity of HCoV-OC43 virus recovered from different coarseness of pine (A) Pine 80, (B) Pine 120, (C) Pine 320, (D) Pine 1000 and (E) Pine planed determined using the CPE assay. The graphs have been normalized against the cell control. All the results are presented as an average of three biological replicates. Each replicate included three technical repeats on the cells. Statistical significances of the samples against virus control are shown as stars above the bars (****$p < 0.0001$ and ns means no statistical significance).

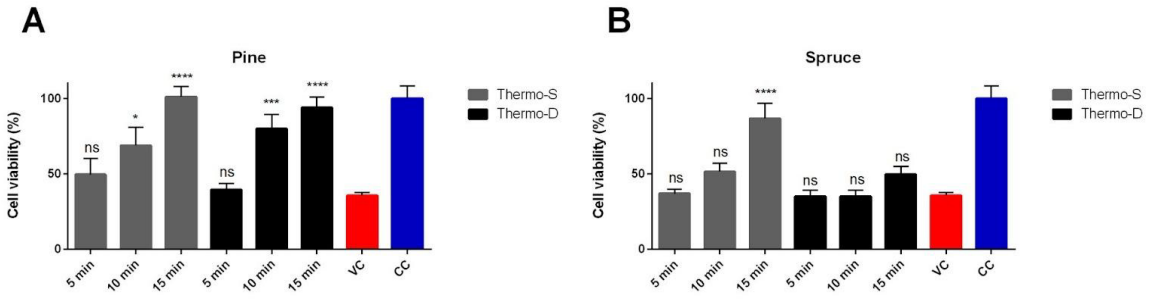

Figure S6. Infectivity of HCoV-OC43 recovered from (A) thermo-treated pine and (B) thermo-treated spruce wood samples determined using CPE assay. Thermal modifications are classified in two: Thermo-S and Thermo-D. The non-infected cell controls have been set as 100% in cell viability. Results are presented as an average of four sample replicates, each including three technical replicates on MRC-5 cells. Statistical significances of the samples against virus control are shown as stars above the bars (* $p < 0.05$, ***$p < 0.001$, ****$p < 0.0001$, and ns means no statistical significance).

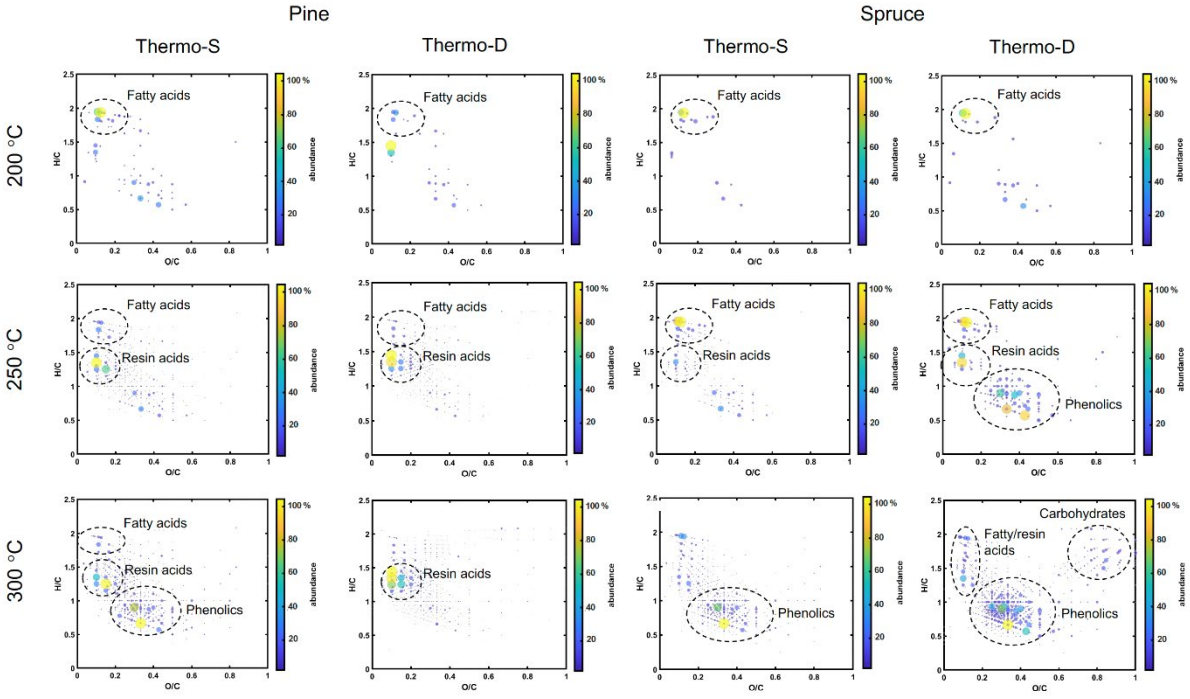

Figure S7. Van Krevelen diagrams for the compounds detected from the Thermo-S and Thermo-D treated pine and spruce samples at 200, 350, and 300 °C. Reported abundance does not directly correspond to the quantified volumes of chemical constituents. When comparing the resin, phenol and fatty acid contents of untreated spruce to Thermo-S and -D treated ones we see 2-3 times smaller quantities of chemicals emitted.

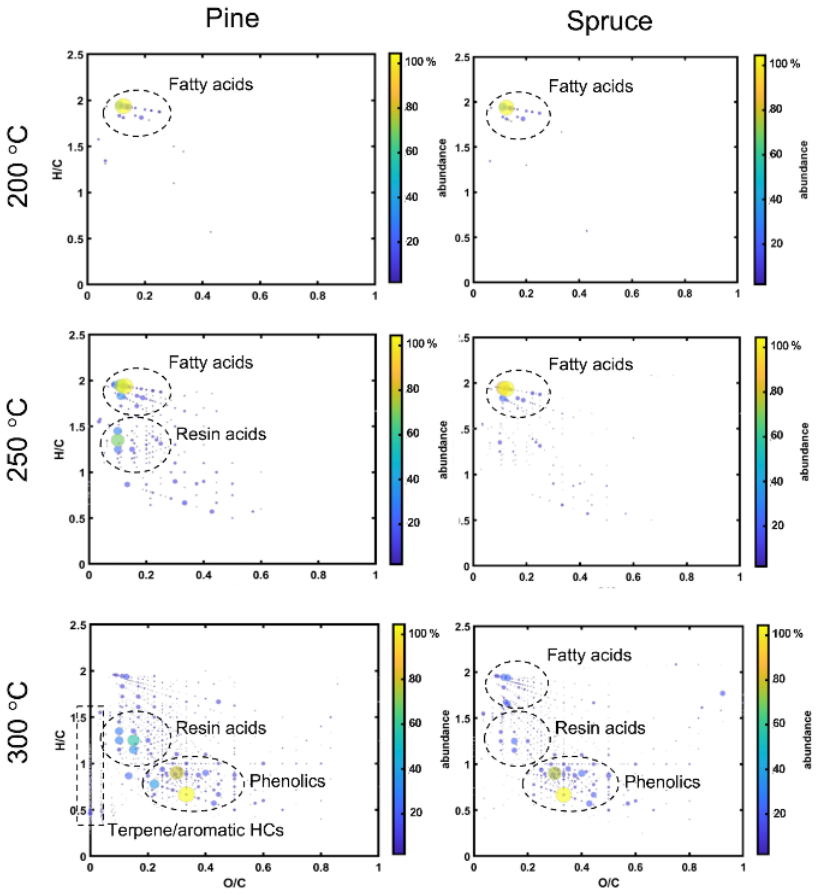

Figure S8: Van Krevelen diagrams for the semivolatile organic compound (SVOCs) from native pine and spruce analyzed by DIP-APCI-QTOF MS. Key differences arise from the presence of resin components and various aromatic hydrocarbons in pine, while smaller volume of resins arises in spruce only when measured at 300 °C. There is a rather abundant presence of phenolic compounds in both species, but their presence is more intense in pine.

II

ANTIVIRAL ACTION OF A FUNCTIONALIZED PLASTIC SURFACE AGAINST HUMAN CORONAVIRUSES

by

Shroff S., Haapakoski M., Tapio K., Laajala M., Leppänen M., Plavec Z., Haapala A., Butcher S.J., Ihalainen J.A., Toppari J.J., & Marjomäki V. 2024

Microbiology Spectrum, e03008-23.

https://doi.org/10.1128/spectrum.03008-23

AMERICAN SOCIETY FOR MICROBIOLOGY | Microbiology Spectrum

| Open Peer Review | Virology | Research Article

Antiviral action of a functionalized plastic surface against human coronaviruses

Sailee Shroff,[1] Marjo Haapakoski,[1] Kosti Tapio,[2,3] Mira Laajala,[1] Miika Leppänen,[1] Zlatka Plavec,[4,5] Antti Haapala,[6,7] Sarah J. Butcher,[4,5] Janne A. Ihalainen,[1] J. Jussi Toppari,[2] Varpu Marjomäki[1]

AUTHOR AFFILIATIONS See affiliation list on p. 21.

ABSTRACT Viruses may persist on solid surfaces for long periods, which may contribute to indirect transmission. Thus, it is imperative to develop functionalized surfaces that will lower the infectious viral load in everyday life. Here, we have tested a plastic surface functionalized with tall oil rosin against the seasonal human coronavirus OC43 as well as severe acute respiratory syndrome coronavirus 2. All tested non-functionalized plastic surfaces showed virus persistence up to 48 h. In contrast, the functionalized plastic showed good antiviral action already within 15 min of contact and excellent efficacy after 30 min over 90% humidity. Excellent antiviral effects were also observed at lower humidities of 20% and 40%. Despite the hydrophilic nature of the functionalized plastic, viruses did not adhere strongly to it. According to helium ion microscopy, viruses appeared flatter on the rosin-functionalized surface, but after flushing away from the rosin-functionalized surface, they showed no apparent structural changes when imaged by transmission electron microscopy of cryogenic or negatively stained specimens or by atomic force microscopy. Flushed viruses were able to bind to their host cell surface and enter endosomes, suggesting that the fusion with the endosomal membrane was halted. The eluted rosin from the functionalized surface demonstrated its ability to inactivate viruses, indicating that the antiviral efficacy relied on the active leaching of the antiviral substances, which acted on the viruses coming into contact. The rosin-functionalized plastic thus serves as a promising candidate as an antiviral surface for enveloped viruses.

IMPORTANCE During seasonal and viral outbreaks, the implementation of antiviral plastics can serve as a proactive strategy to limit the spread of viruses from contaminated surfaces, complementing existing hygiene practices. In this study, we show the efficacy of a rosin-functionalized plastic surface that kills the viral infectivity of human coronaviruses within 15 min of contact time, irrespective of the humidity levels. In contrast, non-functionalized plastic surfaces retain viral infectivity for an extended period of up to 48 h. The transient attachment on the surface or the leached active components do not cause major structural changes in the virus or prevent receptor binding; instead, they effectively block viral infection at the endosomal stage.

KEYWORDS antiviral surface, virus persistence, human coronavirus, plastic, tall oil rosin

During the past few decades, the threat of infectious diseases has been on the rise. A recent example is the COVID-19 pandemic, which was caused by the severe acute respiratory syndrome coronavirus 2 (SARS-CoV-2) causing high mortality (1). Development of strategies to combat the transmission of these contagious pathogens is currently a global priority. During the COVID-19 pandemic, preventive strategies like the use of face masks, travel restrictions, surface disinfection, hand sanitization, and mass vaccination were used (2). Vaccines reduced morbidity and mortality to a large extent but did not help eliminate the virus. Thus, to complement these strategies, we

Editor JJ Miranda, Barnard College, Columbia University, New York, New York, USA

Address correspondence to Varpu Marjomäki, varpu.s.marjomaki@jyu.fi.

The authors declare no conflict of interest.

See the funding table on p. 22.

Received 4 August 2023
Accepted 16 December 2023
Published 16 January 2024

need novel antiviral surfaces that lower the virus load directly on contaminated surfaces, decreasing the probability of virus transmission.

Respiratory viruses, like coronaviruses, are transmitted mainly through large droplets and small aerosols from infected people when they breathe, cough, sneeze, and converse. Every cough or sneeze produces about 3,000 or 40,000 droplets, respectively, with an average viral load of 7×10^6 copies/mL, subject to the size of the droplet, severity of infection, and type of respiratory activity (3). Smaller aerosols can stay in the air for a longer duration and actively transmit the virus, while larger droplets quickly settle on inanimate objects and contaminate the surface (3). Contaminated fomite surfaces can be classified into two categories, i.e., porous and non-porous surfaces. Studies have suggested that viruses stay infectious on porous surfaces only from minutes to hours due to the capillary action of the pores and faster evaporation rate from the surface (4). On the other hand, viruses may stay active on non-porous surfaces for days to several weeks (5–7).

To reduce the viral load on non-porous surfaces like plastic, several disinfectants or surfactants, such as quaternary ammonium, sodium hypochlorite, and hydrogen peroxides, are used (8). However, due to the health hazards associated with the regular use of strong disinfectants, laborious repetitive cleaning, crazing in plastics, and a direct, negative impact on biodiversity, we need safer and more sustainable options (9, 10). Some strategies have been developed in the past to design self-cleaning plastics with anti-microbial properties (11). However, these methods can be expensive and toxic to humans and the environment (12). An alternate approach is to explore natural organic products as potential antivirals.

Coniferous tree-derived resin and rosin compounds have been explored for their therapeutic potential in the past (13). Rosins come from tall oil, which is a side stream product obtained by a process called kraft pulping of coniferous tree barks (14). Tall oil contains a mixture of 5%–50% fatty acids, 15%–55% resin acids, and 5%–35% unsaponifiable and neutral materials. Rosin components have demonstrated excellent anti-inflammatory, antitumor, antifungal, and antibacterial activities (15–19). The antiviral nature of rosin and its components has also been recognized, for example, against influenza, respiratory syncytial virus, SARS-CoV-2, and herpes simplex virus (20–22). Despite the widespread use of rosin compounds in various industrial applications, such as adhesives, rubbers, paints, coatings, soaps, detergents, paper cutting, varnishes, and emulsions, their potential as antiviral agents in applications has been relatively overlooked (14).

In our study, we show that a plastic surface functionalized with tall-oil rosin effectively inactivates the seasonal human coronavirus OC43 (HCoV-OC43) and the more virulent SARS-CoV-2. Through molecular virology assays and different imaging modalities, we demonstrate that the rosin-functionalized plastic leads to efficient loss of virus infectivity by actively releasing rosin.

MATERIALS AND METHODS

Cells

Human lung fibroblast (MRC-5) cells and green monkey kidney epithelial (Vero E6) cells were both obtained from the American type of culture collection (ATCC, Manassa, VA, USA). Both cell lines were propagated in Eagle's Minimum Essential Medium (MEM) (Gibco, Paisley, UK) supplemented with 10% fetal bovine serum (Gibco, Paisley, UK), 1% L-GlutaMAX (Gibco, Paisley, UK), 1% antibiotics (penicillin/streptomycin) (Gibco, Paisley, UK) and stored in a humidified 5% CO_2 incubator at 37°C.

Viruses

Severe acute respiratory syndrome coronavirus 2 used in our experiments was kindly provided by the University of Helsinki. The SARS-CoV-2 virus (SARS-CoV-2/Finland/1/2020) was an isolate from the first COVID-19 patient in Finland (GenBank:

MT020781.2) (23). HCoV-OC43 (ATCC VR1558) was obtained from the American Type Culture Collection (Manassa, VA, USA). The virus was cultured in MRC-5 cells containing 2% MEM with a multiplicity of infection (MOI) of 2. The inoculum was replaced after 2 h of infection with fresh 2% MEM. The supernatant containing the cultured crude virus was collected 2 days post-infection (p.i.). The cell debris was pelleted using a swing-out rotor at 2,700 × *g* for 3 min at room temperature (RT) (Heraeus Megafuge 1.0 R, Germany). The supernatant was flash frozen and stored as a crude working stock at −80°C.

Purification of HCoV-OC43 virus

The purification protocol for the HCoV-OC43 virus was adapted and modified from Dent et al. (24). A subconfluent layer of MRC-5 cells cultivated in a 175 cm^3 flask was infected with HCoV-OC43 (ATCC) at an MOI of 3 for 72 h, after which the supernatant was collected and the cell debris was pelleted by centrifugation at 10,000 × *g* at 4°C for 20 min. The virus in the supernatant was precipitated using 10%, wt/vol polyethylene glycol 6000 and 2.2% of NaCl (25). The solution was stirred for 30 min at 4°C, after which the precipitate was centrifuged at 10,000 × *g* at 4°C, for 30 min. The pellet was dissolved in 3 mL HEPES saline buffer [1 mM HEPES pH 6.7, 0.9% NaCl (wt/vol)] and stored on ice. The solution containing the virus appeared viscous in consistency. The virus was concentrated by pelleting through a stepwise sucrose gradient (10%–20%–30%) at 100,000 × *g* at 4 °C for 2 h. The gradient was prepared by adding 3 mL of 30% sucrose to the bottom, followed by the same amount of 20% and then 10% on the top. The pellet was dissolved in 100 µL of cold HEPES saline buffer and stored at −80 °C. The infectivity of the virus batch was calculated using the end-point titration method (26).

Plastic samples

We used two types of plastic surfaces for our study: low-density polyethylene (standard LDPE) and PREXELENT, generously provided by Premix Ltd. The plastic surfaces were dimensioned as 1 cm^2. PREXELENT is a functional plastic that is prepared by incorporating 10 wt% of rosin extracted from coniferous trees into standard LDPE (patent WO2018229190A1). Throughout our article, we will refer to PREXELENT as rosin-functionalized plastic and in the figure sets as rosin. Standard LDPE was chosen as a control to compare the results of the rosin-functionalized plastic. "Conifer pitch," which is the active ingredient inside the rosin-functionalized plastic, was also provided in powder form by Premix Ltd. Additionally, a variety of industrial grade plastic varieties like acrylonitrile butadiene styrene (ABS), polyamide (PA6), polycarbonate (PC), polypropylene (PP), and polymethyl methacrylate (PMMA) were obtained via Aikolon Ltd. Prior to the experiments, all samples were sterilized with 70% ethanol for 30 s.

Infectivity of HCoV-OC43 studied on different surfaces using a cytopathic effect inhibition assay and RT-qPCR

The persistence of HCoV-OC43 and the antiviral effect of the rosin-functionalized plastic against HCoV-OC43 were studied using the cytopathic effect (CPE) inhibition assay, modified from Schmidtke et al. (27). The experiments were conducted following the international standard ISO 21702, which is a test method to determine the antiviral activity on plastic surfaces, with slight modifications. Ethanol-sterilized plastic samples were added to a 12-well plate with relative humidity (RH) of ~92%, maintained using 6 mL of ddH_2O. The RH maintained inside the plate assembly was measured with a commercial RuuviTag wireless sensor (Ruuvi Ltd, Finland). MRC-5 cells were seeded at a density of 15,000 cells/well in a 96-well flat-bottomed microtiter plate (Sarstedt, Numbrecht, Germany) and allowed to grow overnight (O/N) in an incubator at 37°C, with 5% CO_2. On the following day, a droplet of 5 µL of HCoV-OC43 virus (1.60×10^4–10^5 PFU) was loaded onto the different plastic surfaces and incubated for different time points (24, 48, and 72 h) at RT and ~92% RH inside the 12-well plates. We used several controls in the experiment (i) an equivalent amount of virus without any surface treatment was used as a positive control. (ii) MRC-5 cells without any virus infection were used as a negative

control (or mock infection). (iii) Additionally, a sample control without the addition of the virus was used to test the cytotoxicity of the surfaces on MRC-5 cells. A glass coverslip was gently placed on the virus-loaded surfaces to ensure maximum contact of the virus with the surface. At the end of each incubation time point, the surface was rinsed with 995 µL of 2% MEM, followed by gentle rocking of the 12-well plate for 1 min to facilitate the detachment of the virus from the surface. The medium containing the flushed virus was added to the cultured MRC-5 cells (MOI: 0.01–0.1) in a 96-well plate. The cells were incubated for 5 days in a humidified 5% CO_2 incubator at 34°C until the cytopathic effect (rounding and detachment of cells) was seen. After the development of the cytopathic effect, the cells were washed twice with phosphate buffer saline (PBS), after which they were stained with a CPE stain (containing 0.03% crystal violet, 2% ethanol, and 3.5% formaldehyde in ddH_2O) for 12–15 min. Next, the cells were washed twice with ddH_2O to get rid of excess stain, and finally, the cells were lysed for 5 min to elute the stain out of healthy cells with the help of CPE lysis buffer (0.03 M sodium citrate and 1 N HCl in 47.5% ethanol). Thereafter, the viable cells were quantified by measuring the absorbance of the stain in the 96-well plate at 570 nm (Victor X4 2030 Multilabel Reader, PerkinElmer). The amount of infectious viral RNA in the sample was also quantified using RT-qPCR from the cell culture supernatant collected 3 days p.i. The protocol for RT-PCR and qPCR has been elaborately described in "Quantification of HCoV-OC43 viral RNA directly flushed from the surfaces using RT-qPCR" section.

The effect of humidity on the antiviral function of the rosin-functionalized plastic was studied similarly as above, with the exception that the incubation of the virus-loaded surface was done inside a custom-made chamber fitted in a laminar in the BSL2 facility, capable of accurate measurements of temperature and relative humidity (Kenttäviiva Ltd, Finland). In addition, the coverslip was not used on the surface in order to allow various humidities to act on the surface and on the viruses. During the experiment, the RH was controlled to either 20% or 40% and the incubation times were shorter (5, 15, 30, and 60 min) compared to those tested earlier.

Persistence of SARS-CoV-2 measured using RT-qPCR

The persistence studies of SARS-CoV-2 on the standard LDPE and rosin-functionalized plastic were carried out in a Biosafety level-3 unit. Vero E6 cells were grown in a 96-well flat-bottomed microtiter plate, with each well containing 50,000 cells. The cell cultures were maintained for 24 h at 37°C in an environment with 5% CO_2. On the following day, a 5 µL droplet (5×10^3 PFU) of the SARS-CoV-2 was added on top of both the surfaces and incubated for different time points (5 min, 30 min, 1 h, 2 h, and 4 h) at RT and ~92% RH. At the end of each time point, the surface containing the virus was flushed with 2% MEM and gently mixed for 1 min to detach any virus from the surface. The flushed virus was then added to the Vero E6 cells at an MOI of 0.005. The cells were then placed in a humidified incubator with 5% CO_2 at a temperature of 34°C for a 3-day incubation period. After 3 days post-infection, the supernatant was collected and the viral RNA was extracted.

The RNA from the supernatant was extracted using the Chemagic viral DNA/RNA kit (Perkin Elmer) and the Chemagic 360 instrument. For the RNA extraction, a master mix containing Poly (A) RNA, Proteinase K, and Lysis buffer 1 was mixed in the proportion mentioned inside the kit by the manufacturer. The samples were initially diluted 10 times in ddH_2O. The diluted samples and the master mix were added into deep-well Chemagic plates. In a different low-well plate, 15 µL of magnetic beads was pipetted, and in a deep-well Chemagic plate, 80 µL of elution buffer was added. The RNA was extracted using the Chemagic 360 machine as per the manufacturer's instructions. The extracted RNA was stored at −80°C. After the RNA isolation, a TaqMan-based real time RT-PCR assay was used to transcribe the viral RNA, amplify it, and detect the SARS-CoV-2 genes using the SARS-CoV-2 RT-qPCR reagent kit (Perkin Elmer, Turku, Finland).

In order to compare the relative amounts of viral RNA (number of infective viruses) present in the culture supernatant after 3 days of cultivation in cells, we used the Cq

values obtained from the qPCR experiment. Cq values obtained from the qPCR reaction of the virus flushed from the standard LDPE and rosin-functionalized plastic surfaces were placed into the following self-derived equation to obtain the difference in the RNA amount, ΔRNA:

$$\Delta RNA = 0.9646e^{0.6948 \cdot \Delta Cq}$$

where ΔCq is the Cq value difference between the mean of the rosin-functionalized plastic surface to the mean of the standard LDPE surface. A log value of ΔCq was then calculated to describe the difference in virus amounts.

Statistical analysis

The results from the CPE assays were plotted as a column graph of cell viability, and the statistical analysis was performed using GraphPad Prism software 6 (GraphPad Software, San Diego, CA, USA). The CPE results were normalized against the mock infection and are presented as mean + standard error of the mean (SEM). The statistical significance was calculated by performing a one-way analysis of variance (ANOVA) of all test samples against the virus control followed by the Bonferroni tests (*P < 0.05, **P < 0.01, ***P < 0.001, and ****P < 0.0001).

Quantification of HCoV-OC43 viral RNA directly flushed from the surfaces using RT-qPCR

A droplet of 5 µL of HCoV-OC43 (1.60×10^5 PFU) was loaded onto the standard LDPE and rosin-functionalized surface and incubated for different time points (1, 5, 15, and 30 min and 1, 2, and 4 h) at RT, ~92% RH inside 12-well plates. A similar amount of virus without any surface treatment was used as a positive control. At the end of each time point, the virus on the surface was rinsed with 995 µL of culture media (2% MEM) and gently agitated for 1 min to facilitate the detachment of the virus from the surface. RT-qPCR was then used to measure the amount of viral RNA in the flushed samples. Processing of the flushed samples to measure the viral RNA was done through the following steps: (i) the samples were diluted five times with RNase-free water (J71768, Thermo Fisher Scientific, Geel, Belgium) and heat treated for 5 min at 75°C to release the RNA from the viruses. (ii) Reverse transcription (RT′) was carried out to make cDNA from the viral RNA using 20U M-MLV reverse transcriptase enzyme (Promega, WI, USA), RT-buffer (Promega, WI, USA), RNase-free water (J71768, Thermo Fisher Scientific), 4U RNAsin ribonuclease inhibitor (Promega, WI, USA), 0.5 mM dNTPs (Promega, WI, USA), and 1.2 µM reverse primer (5′-AATGTAAAGATGRCCGCGTATT) (Merck, Darmstadt, Germany). The RT′ reaction was carried out for 1 h at 42°C, and then the RT′ enzyme was inactivated at 70°C for 10 min. (iii) Finally, the cDNA was amplified using qPCR. A master mix containing SYBR Green Supermix (BioRad), 600 nM forward (5′-TGTTAGGCCRATAATTGAGGAC) (Merck, Darmstadt, Germany) and reverse primers (5′-AATGTAAAGATGRCCGCGTATT) (Merck, Darmstadt, Germany) and the RNase-free water was prepared as per the manufacturer's protocol. cDNA template (5 µL) from the RT′ reaction was added to the prepared master mix and run through the Touch Thermal Cycler (BioRad C100, BioRad, Helsinki, Finland). The amplification steps were as follows: 10 min at 95°C, 40 cycles of 15 s at 95°C and 1 min at 50°C, 5 s at 72°C, 1 min at 95°C, followed by cooling at 12°C for 10 min.

Transmission electron microscopy

Purified HCoV-OC43 (10 µL of 1.09×10^8 PFU) was added on the sterilized standard LDPE and rosin-functionalized plastic and incubated for 1 h at RT with ~92% RH. Post-incubation, 10 µL of PBS was added to the surface and the droplet was gently mixed. A virus control of the same amount without any surface treatment was also prepared. Formvar-coated copper grids were glow discharged (EMS/SC7620 mini-sputter coater), and negative staining was done as previously described (28). Briefly, 5 µL of virus (control,

standard LDPE, and rosin-functionalized plastic) was added onto the copper grids for 30 s and blotted with Whatman paper (Whatman 3 MM). The samples were negatively stained using 1% (wt/vol) phosphotungstic acid for 10 s and blotted. The samples were dried O/N before imaging in a JEOL JEM-1400 transmission electron microscope (JEOL, Tokyo, Japan) equipped with a LaB_6 filament. The images were captured using a bottom-mounted Quemesa 4,008 × 2,664-pixel CCD camera.

Atomic force microscopy

A volume of 10 µL of purified HCoV-OC43 virus (1.09×10^7 PFU) was deposited on the standard LDPE and rosin-functionalized plastic surfaces and incubated for 1 h at RT with a RH of ~92%. Post-incubation, 10 µL of 2.5% glutaraldehyde (GA) was added to fix the virus and maintain the morphology. Post-fixation, the droplet containing the virus was transferred onto the silicon surface that was pretreated with air (oxygen/nitrogen) plasma (Electron Microscopy Sciences, Hatfield, PA, USA) and 0.01% poly-l-lysine for 15 min to enhance the attachment of the viruses to the surface. Virus without any surface treatment was used as a control and was added directly onto poly-l-lysine-coated silicon chips for atomic force microscopy (AFM) measurements. Bruker Dimension Icon atomic force microscope (Bruker Corporation, Billerica, MA, USA) and Scanasyst fluid tips (nominal radius 20 nm) were used during the liquid AFM measurements. Peak force quantitative nanomechanical mapping mode was used in all the measurements. Imaging was done in PBS (scan size of 5 µm, scan rate varying between 0.332 and 0.939 Hz, and peak force amplitude between 100 and 200 nm). The peak force setpoint was kept below 1 nN and the scan rate, peak force, and peak force amplitude were adjusted to minimize the forces between the tip and the virus to obtain the best image quality. Bruker analysis software 1.9 version was used to plot and analyze the data. In addition, the data were plotted and tested for statistical significance in Origin Pro 2022. Viruses that appeared in large clusters were excluded from the measurements.

Helium ion microscopy

A 5 µL droplet of HCoV-OC43 virus (5.45×10^6 PFU) was loaded onto the standard LDPE and rosin-functionalized plastic surfaces on ice and fixed in 2 mL of 2.5% GA + 0.1 M sodium cacodylate (NaCaC) solution for 30 min. After three washes with 0.1 M NaCaC solution, 3 min each, the surfaces were stained for 30 min with 1% OsO_4 prepared in 0.1 M NaCaC. After two washes with 0.1 M NaCaC solution, the surfaces were subjected to increasing ethanol series (50%, 70%, 96%, and 99%) and dried using a critical point dryer (Leica Microsystems EM CPD300). The samples were stored in a vacuum chamber until they were taken for helium ion microscopy (HIM) (Zeiss Orion Nanofab) imaging, where the acceleration voltage of 30 kV and an aperture of 10 mm were used. Spot size 6 was used, giving an ion current of 0.2 pA. It was possible to image the plastic samples without a flood gun, but on the rosin-functionalized plastic, the charge compensation was used with line averaging. Imaging was done from an 85° tilted angle. The aspect ratio of the particles was calculated by measuring their maximum height and the width of the single particles from the images.

Hydrophobicity measurements

A water droplet of 40 µL was added on top of the standard LDPE and rosin-functionalized plastic. Images of the droplet were taken from the side and top angle using a smartphone camera (Xiaomi MI 8). The contact angle was measured from the base of the surface using Inkscape drawing software (Inkscape Project 2020).

Cryo-electron microscopy

Purified HCoV-OC43 virus (5 µL, 5.45×10^7 PFU) was added to the surfaces and incubated for 1 h at RT with ~92% RH. Post-incubation, 5 µL of HEPES saline was added to the surface and the droplet was gently mixed. A virus control without any surface treatment

and with the same amount was also prepared. A total of 10 µL of the virus collected from the surface was exposed to ultraviolet (UV)-C irradiation at 100 mJ cm^{-2} using a UVP crosslinker CL-1000 (Analytik Jena, Jena, Germany) at A_{254} nm for inactivation before plunge freezing (29). The virus samples were loaded on a glow-discharged Quantifoil electron microscopy grid with 2 nm carbon film R1.2/1.3, mesh 300 and incubated for 1 min before plunging at 22°C, 85% humidity, and 1.5 s blotting time with the Leica EM GP plunger. Cryo-electron microscopy (CryoEM) data were collected using a FEI Talos Arctica field emission transmission electron microscope (TEM), equipped with a Falcon III direct electron detector at the Instruct-FI Centre's CryoEM Core Facility. Data were collected in counting mode at 150,000× nominal magnification at a 0.97 Å/pixel sampling rate using a total dose of 30 e^{-} $Å^{-2}$. Movies were motion corrected using Relion's motion correction (30–36) implemented in Scipion 3.0.12 (37, 38) and the contrast transfer function was estimated using ctffind4 (39–41). Images were further adjusted in Corel Draw 2023 to improve the contrast of viral features.

Sedimentation assay

Genome release from the virus capsid was studied using ultracentrifugation. For this experiment, 5 µL of the purified HCoV-OC43 virus (2×10^6 PFU) was added to the surface with a glass coverslip and incubated for 1 h at RT with ~92% RH. Post-incubation, the samples were flushed with 2% MEM and collected into polyallomer centrifuge tubes (Beckman, Palo Alto, CA, USA). The flushed content was ultracentrifuged (A-95 rotor, 20 psig, 30 min) using the Beckman Coulter Airfuge centrifuge (Brea, CA, USA). A virus of the same amount, without any pretreatment on the surface, was used as an experimental control. Post-centrifugation, the supernatant was collected in a separate tube, and the pellet was redissolved in 2% MEM. The RNA from both the pellet and supernatant was isolated using the QIAamp Viral RNA Mini kit (Qiagen, Hilden, Germany, ref. 52906). The isolated RNA was converted into cDNA and amplified using RT-PCR and qPCR as described above. The cDNA was diluted 100 times before performing the qPCR.

Binding assay

MRC-5 cells were cultured in a 6-well plate with a flat glass bottom (Fisher Scientific) at a density of 350,000 cells/well and incubated O/N at 37°C. On the subsequent day, 10 µL of the purified HCoV-OC43 virus (1.89×10^7 PFU) was added to the surface with a glass coverslip and incubated for 1 h at RT with ~92% RH. Post-incubation, the samples were flushed with 2% MEM and the flushed virus was added to the MRC-5 cells on ice for 1 h while rocking. After three washes with 0.5% BSA/PBS, 5 min each, the 6-well plate was subjected to three cycles of freeze-thaw by alternating between −80°C and RT to detach the cells from the bottom of the plate. The viral RNA from the virus bound to cells was isolated using the QIAamp Viral RNA Mini kit (Qiagen, Hilden, Germany, ref. 52906). The isolated RNA was converted into cDNA and amplified using RT-PCR and qPCR as described above. The cDNA was diluted 1,000 times before performing the qPCR.

Immunofluorescence and confocal microscopy

Confocal microscopy was applied to study the different stages of the virus infection cycle. Purified HCoV-OC43 virus (5 µL, 2×10^6 PFU) was added to the surfaces and incubated for 1 h at RT with ~92% RH. Viruses flushed from the surfaces were added onto cells (MOI: 100) into 96-well plates and kept at RT for 1 h, followed by 1 h at 34°C. Infection was allowed to proceed for 1 or 15 h at 34°C and then the cells were fixed with 4% paraformaldehyde in PBS. Cells were permeabilized with 0.2% Triton X-100 for 5 min, followed by antibody labeling with affinity-purified rabbit monoclonal antiserum against the S protein (1:16 diluted), mouse monoclonal antisera against human beta-tubulin (#sc-58886, Santa Cruz Biotechnology) or J2 (Scicons, Hungary) against the dsRNA. The secondary antibodies used were Alexa Fluor 555 goat polyclonal IgG against rabbit (catalog no. A-21429; Thermo Fisher Scientific) and Alexa Fluor 488 goat polyclonal IgG

against mouse (catalog no. A-21121; Thermo Fisher Scientific). The second PBS wash was supplemented with 4′,6-diamidino-2-phenylindole (DAPI) (Invitrogen/Molecular Probes, ref. D3571) (1:40,000) in PBS to stain the cellular nucleus. All antibody dilutions were made in 3% BSA in PBS. The cells were imaged using a Nikon A1R confocal microscope. Images were taken with a 40× objective and numerical aperture of 1.25. Three lasers were used: a 405 nm diode laser, a 488 nm multiline argon laser, and a 561 nm sapphire laser. The virus spike protein and dsRNA channels were adjusted with the cell control, such that the cell control had a very low signal. Several images were taken using the automation option in the software to accumulate at least 700 cells per case. The montages from the images were made with Fiji2 (ImageJ). Cell profiler 4.2.1 was used to quantify the amount of infection in the wells. The nuclei were selected as primary objects, and the infected cells were then identified as secondary objects if they were present around the previously identified primary object (nuclei). The primary objects were identified using the Otsu thresholding method. Once the primary and secondary objects were classified, the software automatically calculated the area and the intensity of the secondary objects, which were then exported as an Excel data sheet. At this point, manual thresholding was done to differentiate infected cells from non-infected cells having some background signal. The data were subsequently plotted as a column graph and represented as infection (%).

UV-vis spectroscopy

To measure the rosin content secreted to the flush medium, rosin-functionalized plastic was flushed with ddH_2O for 1 h and O/N using gentle rocking. As a reference of the patented compound embedded inside the rosin-functionalized plastic, Premix Ltd. provided us with a powdered sample of elemental conifer pitch (secreted and cured oleoresin mixture) that was dissolved in 94%, vol/vol of ethanol and 10-fold serial dilutions were made to obtain a final concentration of 0.0001%, wt/vol of conifer pitch. The UV-vis spectra of the flushed material without any further dilution were measured with LAMBDA 850 UV-Vis spectrometer (Perkin Elmer Life Sciences) and Quartz cuvettes (Hellma) with optical pathlength of 1 cm. The measured raw spectra were background corrected with the measured spectrum of EtOH using Origin 2022 software.

RESULTS

Virus persistence and antiviral studies

Rapid loss of coronavirus infectivity on rosin-functionalized plastic compared to other plastic surfaces

The persistence of HCoV-OC43 on different plastic surfaces was evaluated at multiple time points using a CPE inhibition assay. The results showed a similar trend of virus persistence on all the plastic surfaces for the first 24 h (Fig. 1A). Highly infectious viruses were recovered from all the surfaces at 24 h. At 48 h, the amount of virus infectivity recovered from the ABS, PA6, and PC surfaces was not statistically different from the virus control; however, there were statistical differences in the virus infectivity recovered from the PMMA, PP, and LDPE surfaces. This suggests that there was some loss of virus infectivity on these surfaces. Almost full loss of infectivity of HCoV-OC43 from all the above-mentioned surfaces was seen at 72 h. To ensure that the results from the persistence of the virus come solely from the virus infectivity and not from any toxicity associated with the different plastic surfaces, we measured their cytotoxicity as well. Cytotoxicity was measured by flushing the surface with media and adding it to the cells. The results showed that none of the plastic surfaces were cytotoxic (data not shown). These findings revealed the actual extent of HCoV-OC43 persistence on various plastic surfaces.

As mentioned in the Materials and Methods section, rosin-functionalized plastic was prepared by incorporating tall-oil rosin into standard LDPE plastic through a patented

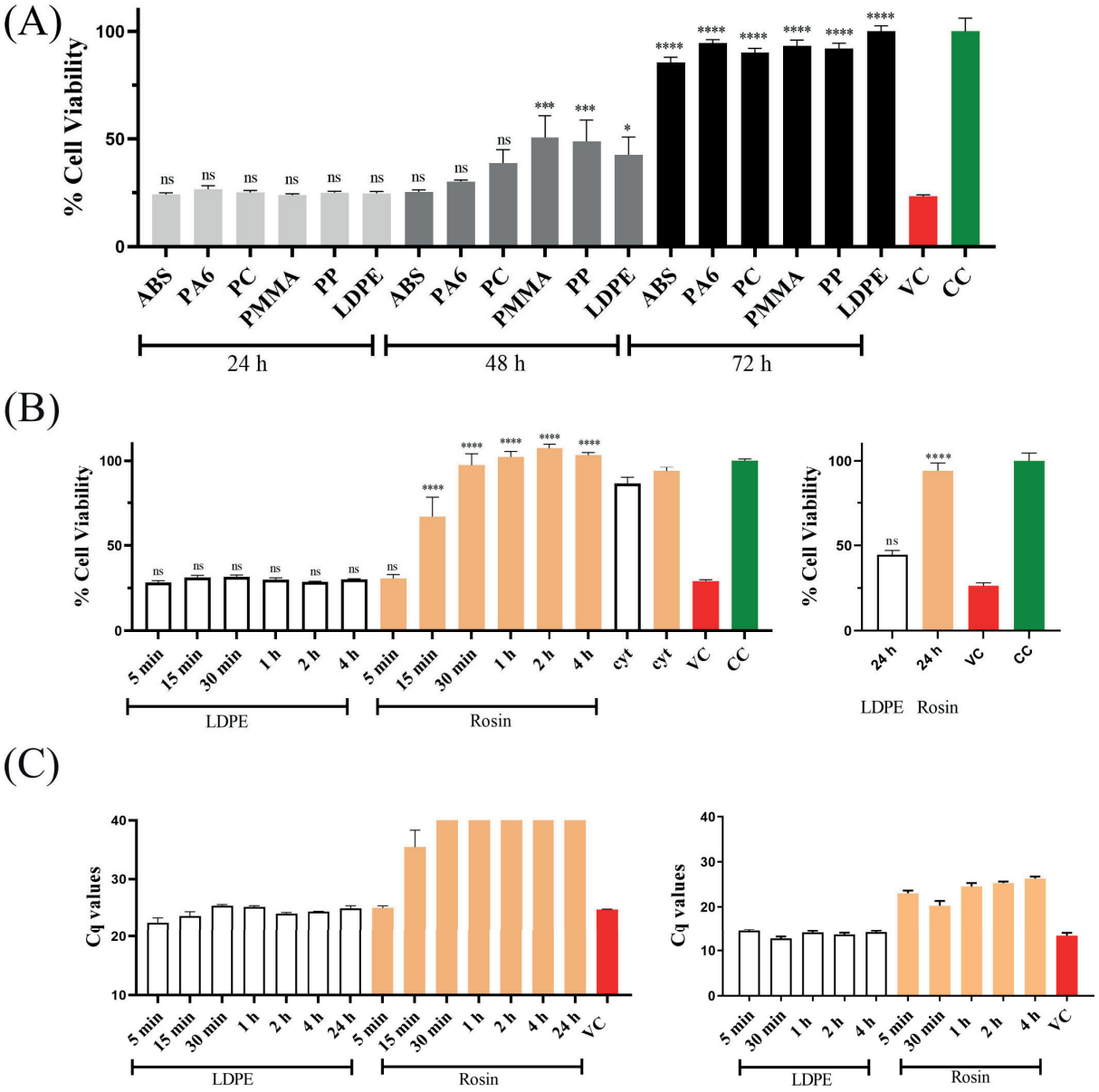

FIG 1 Persistence of HCoV-OC43 on (A) different plastic surfaces measured up to 72 h. Virus titer on various plastic surfaces—1.6×10^4 PFU. (B) Standard LDPE and rosin-functionalized plastic measured up to 24 h of contact time with the surface. Virus titer on standard LDPE and rosin-functionalized plastic surface—1.6×10^5 PFU. In both (A) and (B), a CPE assay was conducted to assess cell viability post-infection, and the treated samples and virus control were normalized against the cell control. The experiments were replicated three times, with each condition having three technical replicates. (C) Infectivity of HCoV-OC43 and SARS-CoV-2 on standard LDPE and rosin-functionalized plastic, measured up to 24 and 4 h of contact time, respectively, using RT-qPCR (see Materials and Methods). The qPCR experiment was conducted twice, each with three technical replicates. For all panels (A through C), the results are presented as average values + SEM. Statistical analysis employed one-way ANOVA, followed by the Bonferroni test (*$P < 0.05$, ***$P < 0.001$, and ****$P < 0.0001$). ns, not significant; VC, virus control; CC, cell control; and cyt, cytotoxicity.

technology (Patent no. WO2018229190A1). Industrial grade standard LDPE was selected as one of the controls in all our experiments to enable comparison of the results with those obtained using the rosin-functionalized plastic. The persistence of the HCoV-OC43

virus on the rosin-functionalized plastic was also tested at different time points. From the CPE assay result (Fig. 1B), there was a gradual loss of virus infectivity starting at 15 min and a complete loss of infectivity at 30 mins. Even with an extended incubation of 24 h on the surface, the antiviral effect of the rosin-functionalized plastic surface against HCoV-OC43 was sustained. In contrast, the virus on the standard LDPE surface remained infectious until the maximum time point tested (24 h). The cytotoxicity results of the standard LDPE and rosin-functionalized plastic indicated that they were both non-toxic toward MRC-5 cells (Fig. 1B).

To compare the relative amount of infectious viral RNA recovered from the standard LDPE and rosin-functionalized plastic surfaces for HCoV-OC43 and SARS-CoV-2, we collected the supernatant from virus-infected cells after 3 days p.i. and performed qPCR analysis, as shown in Fig. 1C. The results were presented as bar graphs of the quantification cycle (Cq) values. Cq values are inversely related to the amount of RNA in the sample, meaning higher Cq values correspond to lower detected viral RNA levels. For both HCoV-OC43 and SARS-CoV-2, the Cq values of the virus samples flushed from the standard LDPE surface were quite similar to the virus control. This indicated that highly infectious virus was recovered from the standard LDPE surface at all time points. In the case of HCoV-OC43, low Cq values were reported for the virus sample recovered from the rosin-functionalized plastic surface after 5 min of incubation. Beyond this initial period, Cq values from virus samples were much higher after 15 min and undetectable after 30 min and later, indicating a rapid decline in viral titers on the rosin-functionalized plastic surface. A similar pattern was observed for SARS-CoV-2, except the virus was inactivated even earlier, within 5 min on this surface.

Using the Cq values, we calculated the logarithmic reduction in virus infectivity on the rosin-functionalized plastic surface compared to standard LDPE. For HCoV-OC43, there was a 3.54 logarithmic reduction of infective viruses after just 15 min of contact with the rosin-functionalized plastic surface. Since Cq values were undetectable for subsequent time points, we considered the upper limit of detection for the qPCR machine (Cq value of 40) and estimated a reduction of more than 4 logs. For SARS-CoV-2, there was a 2.59 logarithmic reduction within 5 min of contact with the rosin-functionalized surface. Thereafter (up to 4 h), infectivity continued to decrease, reaching a reduction of 3.67 logs.

Humidity does not affect the antiviral efficacy of rosin-functionalized plastic

The previous assays to determine the antiviral activity of the rosin-functionalized plastic surface were performed at exceedingly high RH (over 90%), as per the ISO standards. However, we were also interested to know if lower humidity would have any effect on the antiviral activity of the surfaces containing rosin compounds. For this, the virus persistence at lower RHs (20% and 40%) was studied. The results depict no major difference in the infectivity of the viruses recovered from the standard LDPE surface compared to the virus control at 20% or 40% RH (Fig. 2A and B). However, there was a difference in the persistence of HCoV-OC43 on the rosin-functionalized plastic at lower humidity (20% and 40%) compared to higher humidity (over 90%). At the lower humidities, the virus lost its infectivity already at 15 min of contact time (Fig. 2A and B) with the rosin-functionalized plastic, whereas at higher humidity, the virus was completely inactivated only after 15 min (Fig. 1B). Altogether, these results indicate that at higher humidity, the virus can persist for a longer period, delaying its inactivation on the rosin-functionalized plastic.

Antiviral mechanism of action and virus morphology studies

Viruses do not bind strongly on the rosin-functionalized plastic surface

One of the plausible explanations for the loss of virus infectivity could be the strong interaction/binding between the rosin-functionalized plastic and the virus. To study this, an experiment was designed to recover the virus from the surface by gentle flushing and then quantifying the relative amounts of viral RNA in the flushed media using qPCR. The

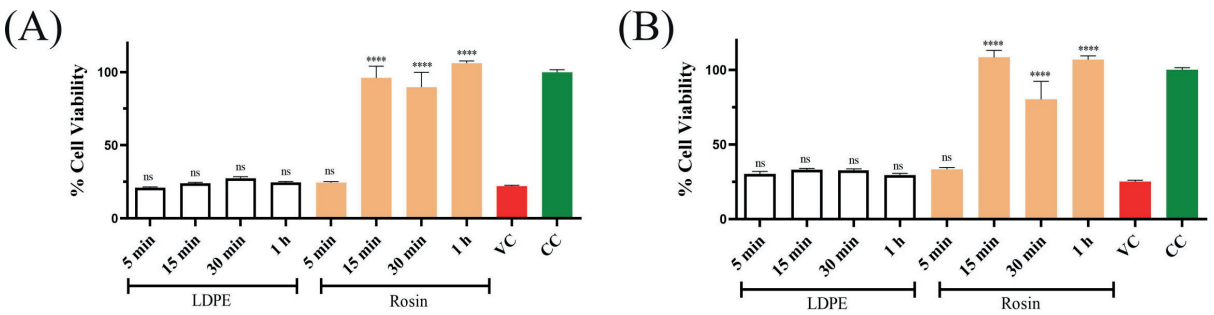

FIG 2 The impact of lower humidity (A) 20% and (B) 40% on the antiviral activity of the rosin-functionalized plastic surface against HCoV-OC43. The experiments were conducted three times, with each condition including three technical replicates. The CPE results are presented as average values + standard error of the mean. Statistical analysis utilized one-way ANOVA, followed by the Bonferroni test (****$P < 0.0001$). ns, not significant; VC, virus control; and CC, cell control.

results showed that the media flushed from the standard LDPE and rosin-functionalized plastic contained a similar amount of viral RNA. This amount was also comparable to the virus control, which was not added on any surface (Fig. 3). This result indicated that the virus did not strongly adhere to either of the surfaces and the reason for the loss of infectivity on the rosin-functionalized plastic was not surface binding.

AFM and TEM studies show no apparent changes in the coronavirus structure

Another reason for the loss of virus infectivity could be that the rosin from the functionalized plastic might have caused some structural changes to the virus. TEM and AFM were used to study these changes. Negatively stained images of the viruses collected from the standard LDPE and the rosin-functionalized plastic appeared similar to that of the control viruses (Fig. 4A). Viruses appeared mostly spherical to elliptical in shape with finger-like projections (spikes) originating from its envelope. In addition, the center of the virus appeared darkly stained. The mean diameter of the viruses was calculated to be an average of 110 nm.

For AFM studies, the flushed viruses were transferred onto a silicon surface to ease imaging while using the tapping mode in liquid. Viruses flushed from the surfaces were found to bind very quickly to the silicon surface because of poly-l-lysine, which makes the surface hydrophilic. AFM studies showed that the virus was spherical to

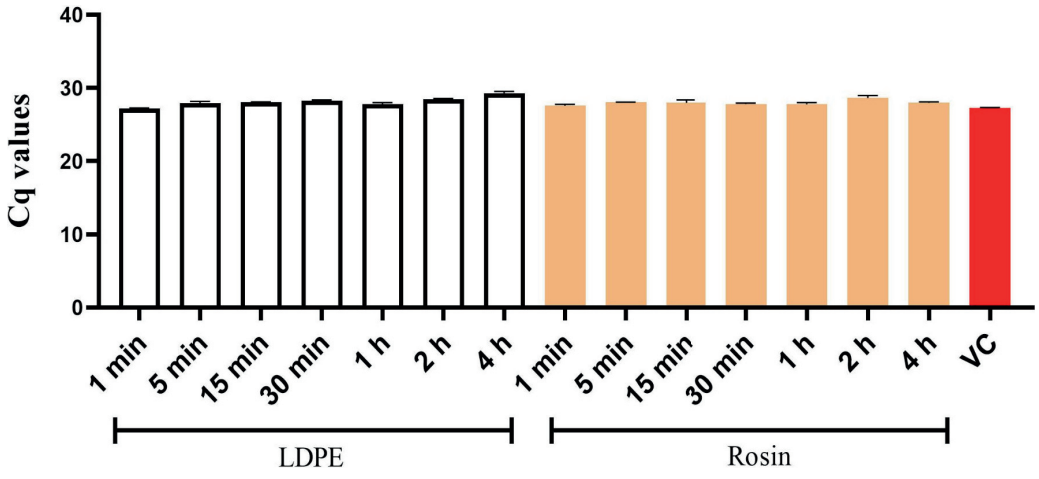

FIG 3 Detection of HCoV-OC43 viral RNA using qPCR from samples flushed from standard LDPE and rosin-functionalized plastic, measured at various contact time points. The experiments were conducted twice, including three technical replicates. VC, virus control.

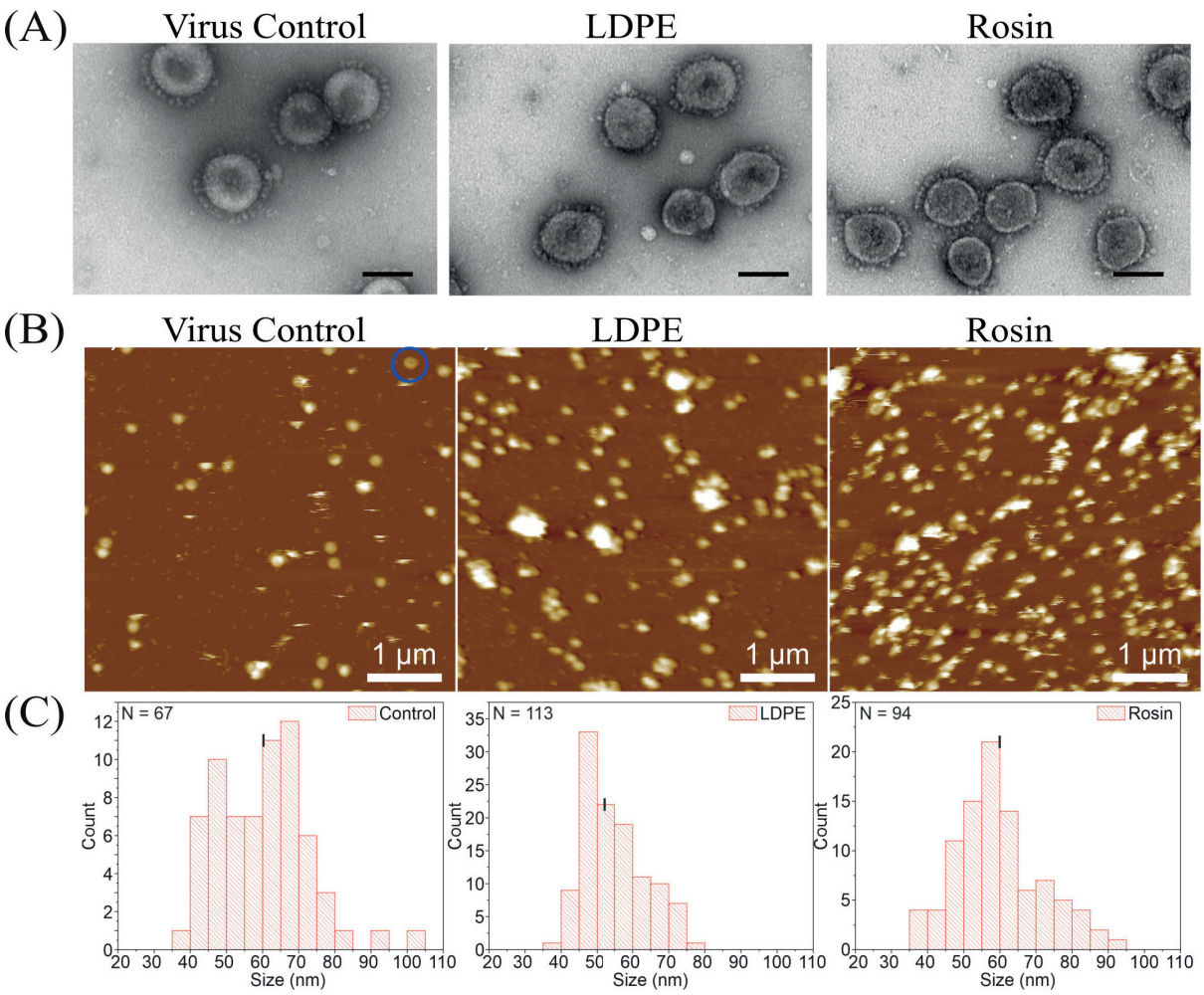

FIG 4 Studying the impact of rosin-functionalized plastic and standard LDPE on the structure of HCoV-OC43 using (A) TEM and (B) AFM in liquid. The scale bar corresponds to 100 nm and 1 µm in the TEM and AFM images, respectively. In panel B, the blue circle highlights a doughnut-shaped virus. (C) The histogram derived from the AFM images illustrates the average size distribution of the height of individual viruses after being flushed from their respective surfaces. The average mean heights for the control virus, viruses flushed from standard LDPE, and rosin-functionalized plastic were 60.1 ± 1.6, 54.7 ± 0.8, and 59.9 ± 1.3 nm, respectively.

ellipsoidal, which was consistent with the TEM results. Also, most of these viruses seemed to be present as single particles (Fig. 4B). Sometimes a doughnut-shaped virus was also observed, and an example of one is highlighted in a blue circle in the control virus image (Fig. 4B). A histogram (Fig. 4C) depicting the height distribution of single viruses flushed from the standard LDPE, rosin-functionalized plastic, and control virus was plotted. The black lines (in the histogram) depict the mean value of the height of the virus, which were calculated as 60.1 ± 1.6, 54.7 ± 0.8, and 59.9 ± 1.3 nm for the control, standard LDPE, and rosin-functionalized plastic samples, respectively. The size distribution of the viruses was wider in the case of control and rosin-functionalized plastic compared to the standard LDPE sample, but the mean sizes remained similar for all samples. Overall, no major changes in the virus structure were observed after being recovered from either the standard LDPE or rosin-functionalized plastic.

Coronaviruses appear flatter on rosin-functionalized plastic compared to that on standard LDPE

Until this stage, structural studies focused on the viruses that were flushed from the surfaces. However, it was equally important to observe the virus in its native form while it was still present on those surfaces. To accomplish this, HIM was employed, which allows for the visualization of material topology without the need for additional metal coating. As seen in Fig. 5A (i) and (ii), the standard LDPE and rosin-functionalized plastic are densely populated with about 70 nm sized virus particles. The density of the virus particles between the surfaces was quite similar, but, on the rosin-functionalized plastic, the viruses appeared to be flatter compared to those on the standard LDPE surface. To quantify this, width-to-height aspect ratios were measured from the HIM images (data not shown). Ratio of the virus on the rosin-functionalized plastic result was 2.5 ± 0.5 (S.D.) and on the standard LDPE surface was 1.6 ± 0.3(S.D.). These results demonstrated that adding the virus on top of the rosin-functionalized plastic resulted in significantly flatter virus particles. Images of the plain LDPE and rosin-functionalized plastic surfaces were taken as controls to show that the bumps seen on the surfaces were contours of the viruses and not of any surface artifacts/irregularities (data not shown).

It was important to understand whether the flattening out of the viruses on the functionalized surface was due to the hydrophilic/hydrophobic nature of the surface. For this, we took images of a droplet of water on the standard LDPE and rosin-functionalized plastic and measured the contact angle of the droplet on the surface using the Inkscape software (Fig. 5B). The contact angle measured for the standard LDPE surface was 95° and for rosin-functionalized plastic was 55°. These results suggested that the rosin-functionalized plastic is more hydrophilic than the standard LDPE surface and gives support to the reasoning for flattening of the viruses on the functionalized surface.

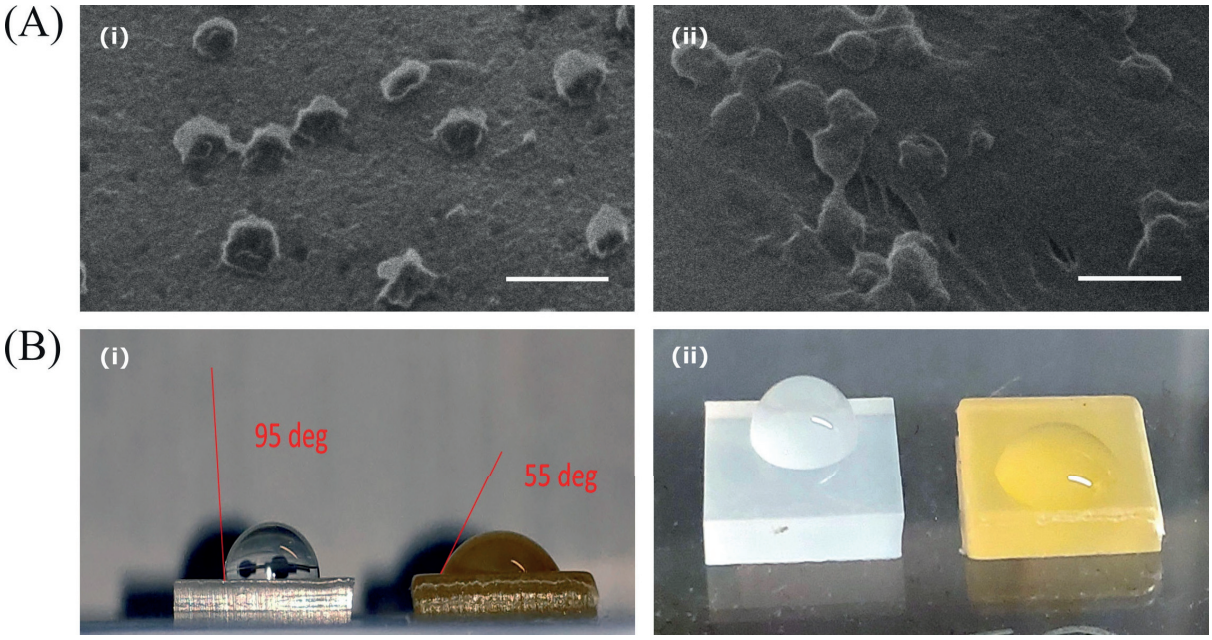

FIG 5 (A) HIM images of HCoV-OC43 on (i) standard LDPE and (ii) rosin-functionalized plastic. The viruses underwent a 1-h treatment on these surfaces before imaging with the HIM. Scale bar: 200 nm. (B) Camera-captured images of a water droplet on the surfaces of standard LDPE (left) and rosin-functionalized plastic (right) to measure the droplet contact angle. (i) Side view and (ii) top view.

HCoV-OC43 flushed from the rosin-functionalized plastic retains its spikes and genome

High-resolution cryoEM was also used to examine the ultrastructure of HCoV-OC43 post-treatment on the standard LDPE and rosin-functionalized plastic surfaces. The virus flushed from both these surfaces looked structurally similar to the virus control (Fig. 6A). It retained its spikes on the surface, primarily in the prefusion state, and the nucleocapsid inside the virion was clearly visible containing the genome inside the viral envelope. Sedimentation assay was also performed to detect the presence of the genome using ultracentrifugation. The viral RNA in the pellet was quantified using qPCR. The qPCR results (Fig. 6B) showed that the amount of viral RNA recovered from the viruses flushed from the standard LDPE (Cq 21.04) and rosin-functionalized plastic (Cq 22.75) was comparable to the virus control (Cq 20.96), suggesting that the genome of the virus flushed from these surfaces was present inside the envelope. The sedimentation assay results confirmed the presence of genome inside virions, a representative of which can be seen by cryoEM.

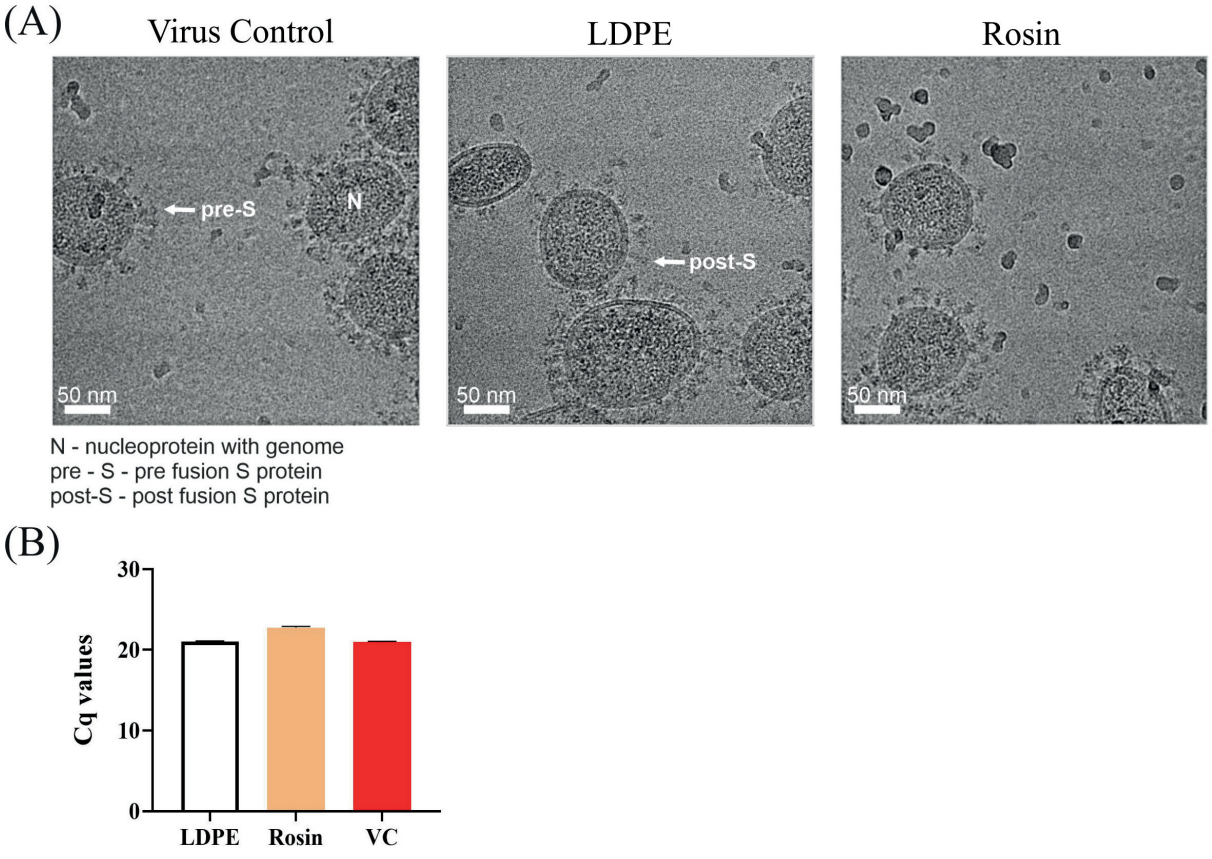

FIG 6 Investigation of HCoV-OC43 viral genome release through (A) CryoEM and (B) qPCR. (A) Representative CryoEM micrographs of virus control and from viruses flushed from LPDE and rosin-functionalized plastic. The arrows indicate a prefusion conformation spike, while "N" indicates the nucleocapsid containing the genome. Over 700 images (each with two to three viruses) were examined and analyzed to study the viruses flushed from the rosin-functionalized plastic surface. (B) Viruses flushed from both the surfaces and control viruses were all sedimented by airfuge, and the amount of pelleted RNA was measured using qPCR.

The active component inside the functionalized surface leaches out of the surface and contributes toward the antiviral activity

Absorption spectroscopy was performed to the flushed material in comparison to the reference compound (kindly provided by Premix Ltd) to study if the material leaches significant amounts of rosin from the surface. We measured the absorption spectra of three samples, 1 h flush from the rosin-functionalized plastic, O/N flush from the rosin-functionalized plastic, and the reference compound (0.0001, wt/vol conifer pitch). The 1 h and O/N-flushed samples had RNase-free water as a solvent, and the reference compound was dissolved in 94%, vol/vol ethanol. The data in the graph in Fig. 7A have been plotted after normalizing the O/N-flushed sample with the 1 h sample. The O/N and 1-h-flushed samples show remarkably similar spectra, but they deviated slightly from the absorption spectrum of the reference sample. The reference sample shows hardly any absorption near 300 nm unlike the flushed samples with a broad absorption band at about 310 nm. The flushed samples have two absorption bands at 245 and 220 nm, like the reference sample with maxima near 240 and 216 nm. The small difference to the reference sample is likely due to some additives/fillers that the company uses to embed the rosin inside the plastic surface. Another explanation is that the molecules behave differently in different solvents due to the difference in solubility, and thus, they absorb differently due to different extinction coefficients.

To confirm that the active ingredient from the functionalized surface is responsible for the antiviral activity, we evaluated the 1 h flushed media against the HCoV-OC43 virus. From the CPE results (Fig. 7B), we could see that the flush was able to effectively rescue the cells from the virus infection. Both these results suggest that the antiviral activity of the functionalized surface comes from the leaching of the active ingredient to the surface and a direct interaction with the virus.

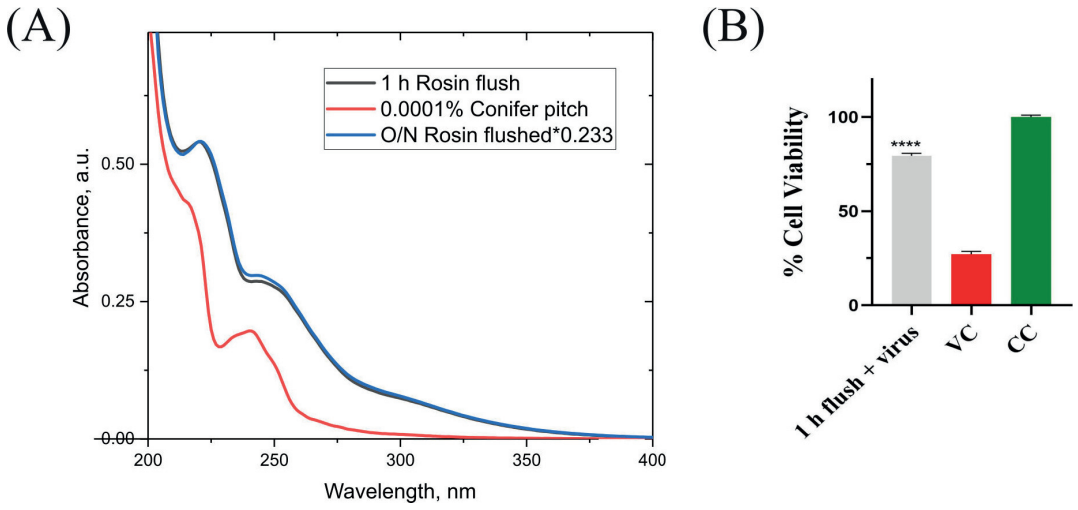

FIG 7 The active component inside the functionalized surface leaches out into the media and can be detected using UV-vis spectroscopy and can inhibit the HCoV-OC43 virus infection. (A) The spectrum of the O/N rosin-functionalized plastic flushed sample (blue line) was normalized with the 1 h rosin-functionalized plastic flushed sample (black line). The reference spectrum of 0.0001% wt/vol conifer pitch in EtOH sample is shown in red. (B) Evaluation of the antiviral activity of 1 h flushed media against HCoV-OC43. The experiment was done once with three technical repeats. Results are plotted as average values + SEM. Statistical analysis employed one-way ANOVA, followed by the Bonferroni test (****$P < 0.0001$). VC, virus control and CC, cell control.

Effects on the HCoV-OC43 infection cycle

Viruses flushed from the rosin-functionalized plastic can enter cells, but the infection does not proceed beyond the endosomal stage

As there were only minor changes in the virus structure despite a complete loss of infection, we wanted to study if the virions were able to still bind to their receptors and enter cells. To study this, an *in vitro* binding assay was performed. The results from the qPCR-based binding assay (Fig. 8A) demonstrated that the viruses flushed from the standard LDPE and rosin-functionalized plastic surfaces were able to bind to its host cells similarly to the control virus, suggesting that the spikes in the coronavirus surface were intact to promote binding to its host cell receptors. We further confirmed the virus binding and internalization using confocal microscopy. The viruses flushed from the standard LDPE and rosin-functionalized plastic surfaces were added onto MRC-5 cells and allowed to bind for a certain amount of time before they were fixed and immunolabeled for imaging. Normal binding to the host cells was followed by internalization over a period of 2 h (Fig. 8B). The internalized virus appeared to be lining the cellular boundaries as well as accumulating in small vesicles close to the plasma membrane. There was no apparent difference observed between the viruses flushed from the surface samples and the virus control. These results support the previous TEM, cryoEM, and sedimentation assay results that the viruses were intact, could promote receptor binding through the presence of prefusion state spikes on the viral surface, and enter cells (Fig. 4A, 6A, and B).

To study the fate of the bound virus, in another experiment, the virus was allowed to internalize for 15 h inside the cells after 1 h of binding at RT. Post 15 h, the cells were similarly fixed, permeabilized, and labeled. From Fig. 9A we can see that the virus control and the virus flushed from the standard LDPE surface produced a high amount of S-protein, indicating that the translation of proteins occurred normally inside these cells. In contrast, the virus flushed from the rosin-functionalized plastic remained accumulated inside the vesicles (endosomes).

The percentage of infection in the standard LDPE-treated and rosin-functionalized plastic-treated viruses was normalized against the virus control. There were no apparent differences in the infectivity between the cells infected with the standard LDPE-treated surface and the virus control, as also seen with the CPE assay previously (Fig. 1B). However, the viruses treated on the rosin-functionalized surface were incapable of infecting the MRC-5 cells (Fig. 9B). Furthermore, we saw that the virus accumulated inside the vesicles did not proceed with replication, as no signal for dsRNA (green) was detected (Fig. 9C). These results indicated that the virus flushed from the rosin-functionalized plastic successfully binds onto the host cell, internalizes inside vesicles, but due to interactions with rosin compounds becomes incapable of proceeding with protein translation and viral replication.

DISCUSSION

Respiratory viruses can spread through direct and indirect transmission routes. While various strategies are in place to limit direct transmission, such as travel restrictions, usage of face masks, and routine sanitization practices, there are fewer options available to address the indirect route of transmission through fomite surfaces. Repeated surface disinfection and the use of biocidal agents are commonly employed measures. The indirect route of virus transmission depends on several factors, most notably, the ability of the virus to remain active on the surface of a material. It is thus important to prepare for future outbreaks by designing antiviral surfaces that would effectively reduce the spread in the community. Functionalizing surfaces with biologically derived materials from nature to reduce indirect transmission is still relatively uncommon. However, due to their natural origin, such materials hold great promise as sustainable alternatives for microbial inactivation.

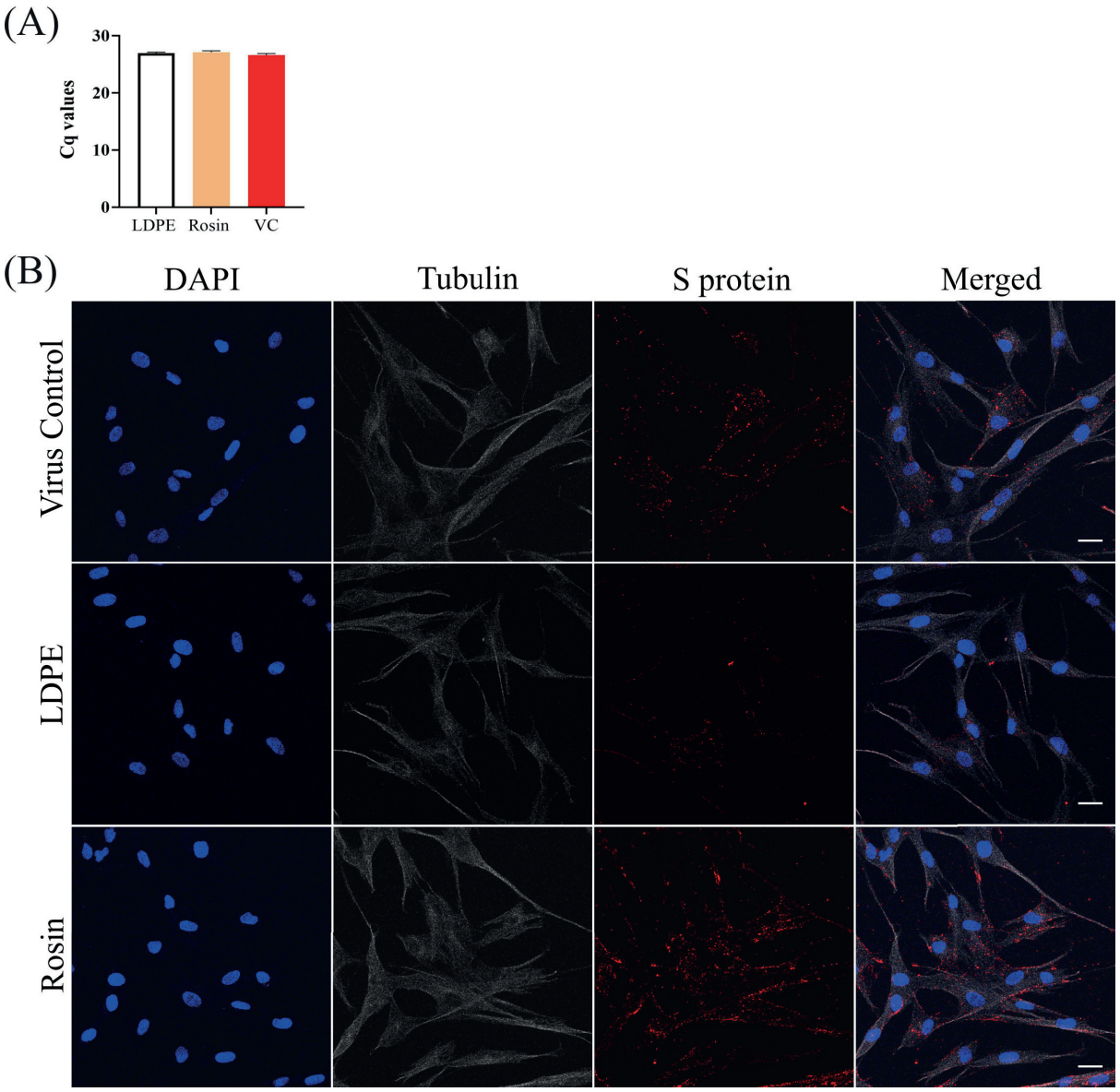

FIG 8 HCoV-OC43 virus binding onto its host cell receptors studied using (A) binding assay. The virus binding to host cell receptors was examined by facilitating synchronized virus binding onto the host cells, followed by recovery of the bound virus using RNA extraction, RT-PCR, and qPCR techniques. The experiment was performed three times with three technical replicates. VC, virus control. (B) Confocal microscopy. The viruses flushed from the surfaces were allowed to bind to MRC-5 cells for 1 h at RT and then internalize for another hour at 34°C. The virus-infected cells were fixed, permeabilized, and labeled with affinity-purified monoclonal rabbit anti-OC43-S protein, followed by a secondary goat anti-rabbit antibody (Alexa 555). The nucleus was stained blue with DAPI, and the cytoskeleton tubulin (gray) was labeled with a J2 primary antibody and goat anti-mouse secondary antibody (Alexa 488). Scale bar: 30 µm.

When studying antiviral surfaces, it is essential to first have a detailed understanding of the persistence of the virus on different fomite surfaces. Among the different known fomite surfaces, plastic demands particular attention. Although plastic is susceptible to degradation by disinfectants and UV-C, different grades of plastic have widespread use in household, commercial, and industrial settings. In the past, several studies have demonstrated good persistence of different human coronavirus species on plastic

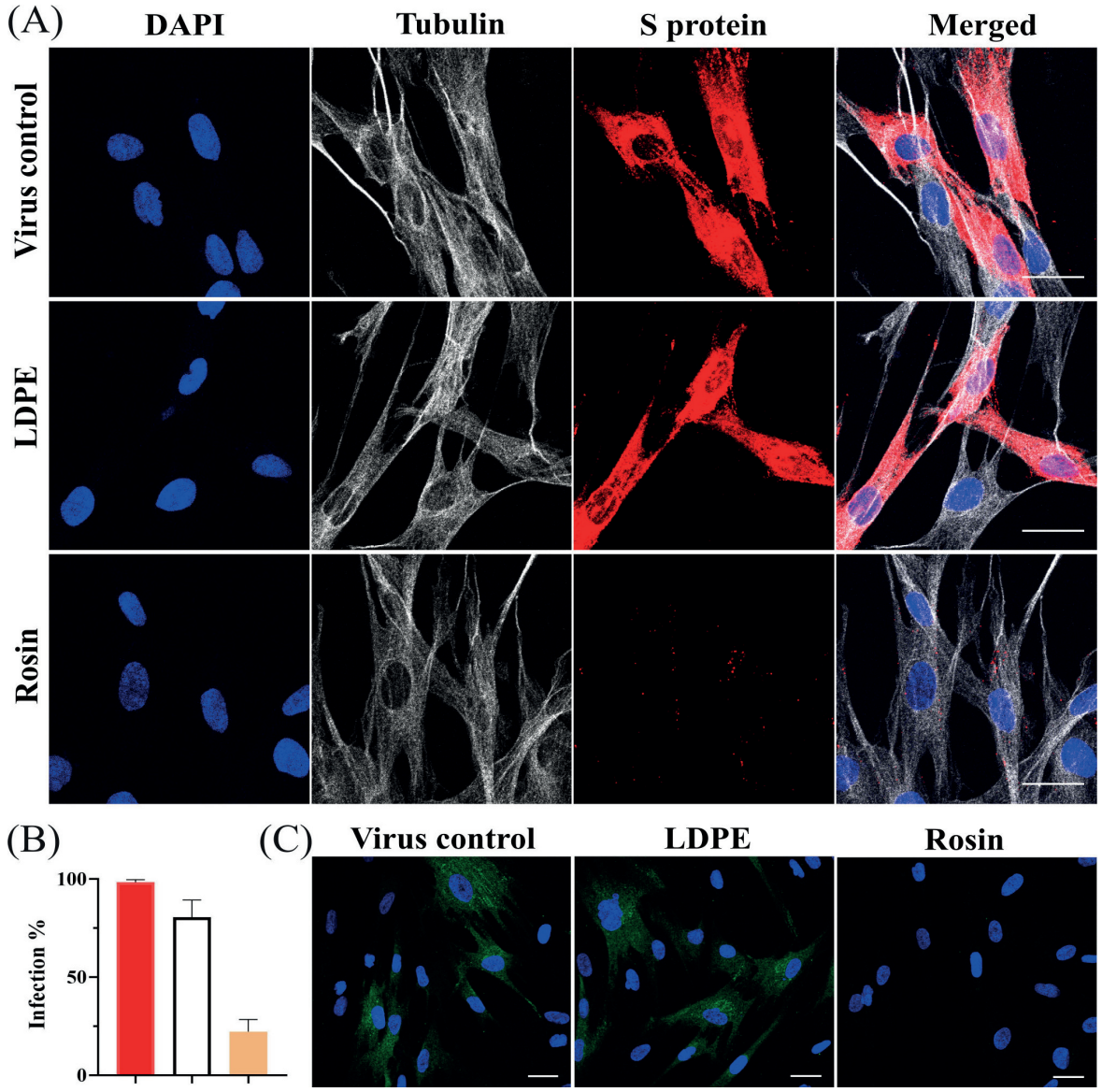

FIG 9 (A) Confocal microscopy images illustrating the entrapment of the virus within vesicles 15 h after infection, following flushing from the rosin-functionalized surface. Viruses from both surfaces and the control virus were allowed to infect cells for 15 h, followed by fixing, permeabilizing, and immuno-labeling with antibodies. The S protein of the virus is labeled in red, the cell nucleus in blue, and the cell cytoskeleton tubulin in gray. (B) Percentage of virus-infected cells calculated from confocal images using Cell Profiler. (C) Detection of dsRNA in HCoV-OC43-infected MRC-5 cells 15 h p.i. The nuclei are shown in blue and the dsRNA in green. dsRNA is present in the virus control and the viruses flushed from the standard LDPE surface; however, the viruses flushed from the rosin-functionalized plastic do not show any dsRNA. Scale bar: 30 µm.

surfaces. For instance, Warnes and colleagues reported infective HCoV-229E on PTFE and polyvinyl chloride plastic surface for 5 days at 21°C and RH of 40%–50% (42). Independent studies by Duan et al. (43) and Rabenau et al. (44) reported the persistence of SARS-CoV (strain P9 and FFM1) on plastic at RT for up to 4 and 6 days, respectively (43, 44). Rabenau and colleagues reported further that the HCoV-229E could persist on plastic only for 24 h at RT. These variations in coronavirus persistence can be attributed to the interplay of multiple factors such as environmental conditions (temperature,

relative humidity, wind speed, etc.), type and surface topology of the plastic, virus type and concentration, and mode of deposition used in the experiments (11). While some publications do not specify the type of plastic being used in the study and generalize it as just "plastic," the type of polymers may affect the surface properties, such as hydrophobicity/hydrophilicity, which could also affect the persistence. While we lack standardized methods and conditions for testing, all the previous studies suggest that non-functionalized plastic retains the infectivity of coronaviruses well.

We focused here to explore the antiviral properties of a plastic surface functionalized with rosin (resin acid mixture) against human coronaviruses. HCoV-OC43 was chosen as a model for the study due to its structural and genetic similarity to the more virulent SARS-CoV-2 (45), allowing for work in a BSL-2 laboratory, although we also verified the results with SARS-CoV-2 as well. All the non-functionalized surfaces sustained high virus infectivity for the first 48 h, which was expected in the light of the previous studies (42–44). However, strikingly, the rosin-functionalized plastic exhibited remarkable antiviral efficacy against both the seasonal coronavirus and SARS-CoV-2 already within 15 min of contact time. Previously, several efforts have been made to add antiviral properties to surfaces, e.g., through functionalization with biocidal compounds (46), antiviral polymers (47, 48), metallic and nanoparticle coatings (49), and surface texturing (46, 50). In a study performed by Zhou and colleagues (50), an antiviral plastic surface designed by nanopatterning and coating of silver nanoparticles showed antiviral effect against SARS-CoV-2 after 1 h of contact time. In another recent study by Butot and colleagues (51), the antiviral activity of quaternary ammonium compounds (QACs) and copper-coated polyethylene terephthalate surface against HCoV-229E and SARS-CoV-2 was shown. Both surfaces were able to reduce viral titers, but the QAC-coated surface did not work after one round of washing. Here, we present a more sustainable solution using rosin-functionalized plastic. This surface showed an excellent 3–4 log reduction of SARS-CoV-2 and low toxicity against cells.

The survival time of the virus on a surface is influenced by various factors, among which RH plays a crucial role (11). RH can vary significantly across different seasons and indoor environments, impacting virus persistence. Previous studies have reported diverse patterns of virus persistence under different conditions of RH. For instance, Biryukov and colleagues (52) observed a linear decrease in SARS-CoV-2 persistence on an ABS plastic surface with increasing RH. In contrast, Morris and colleagues (53) found that the SARS-CoV-2 persisted for a longer period at extreme humidities, indicating a U-shaped relation with RH. However, we observed little effect of RH on the antiviral efficacy of the rosin-functionalized surface. The virus was inactivated at an earlier time point at lower humidities of 20% and 40% compared to higher humidity levels of 92%. However, rosin-functionalized plastic showed excellent inactivation within the first 30 min of contact with the functionalized surface in all tested humidities.

To gain a better understanding of the antiviral mechanism of the rosin-functionalized plastic, our study employed advanced imaging techniques such as AFM, TEM, HIM, and cryoEM to investigate the status and morphology of the flushed viruses. Interestingly, our investigations did not reveal any apparent structural changes in the virus, which could explain the observed loss of infectivity. This suggested that the rosin-functionalized surface had minimal impact on the size, shape, and physical dimensions of individual virus particles. Additionally, we investigated the structure of the virus on rosin-functionalized plastic using HIM. Notably, we observed distinct differences between the virus on the functionalized and the non-functionalized surfaces. On the functionalized surface, the viruses appear flatter in shape. This observation could be explained by the contact angle measurements, which suggested that the functionalized plastic was more hydrophilic (contact angle: 55°) compared to the non-functionalized one (contact angle: 95°). The hydrophilic nature of the functionalized plastic caused the droplets containing the virus to spread out, resulting in the flattening of the viruses. Despite this flattening, flushed viruses from rosin-functionalized surface did not appear different from the

viruses flushed from the non-functionalized plastic, suggesting that the hydrophilicity may play a minor role in killing the virus infectivity.

It is known that viruses tend to persist for longer periods on hydrophobic surfaces as opposed to hydrophilic surfaces (4). This behavior has been explained by Paton and colleagues (54), who proposed that on hydrophobic surfaces, droplets dry in a beaded shape, creating a higher volume-to-surface ratio. This drying process brings the virus particles, organic material, and salts in proximity, offering a protective environment against desiccation. Owen and colleagues (55) suggest further that faster desiccation from hydrophilic surfaces can potentially alter the pH and salt concentration inside the droplet, thereby affecting the stability of the lipids in the viral envelope. However, the hydrophilicity of the rosin-functionalized surface does not solely explain the observed antiviral effect. Namely, the quantification of viral RNA using qPCR demonstrated that the virus added to the surface was easily flushed off into the surrounding media, indicating a weak and temporary interaction between the virus and the hydrophilic surface.

Our imaging results as well as the fact that even short periods of encounter with the functionalized surface caused a strong antiviral effect, both pointed out to the direction that active rosin leaching out from the surface could be the cause of action. Indeed, we could demonstrate through absorption spectroscopy that the active ingredient inside the functionalized plastic leached out into the flush medium. Importantly, the leached flush was independently capable of causing the antiviral effect. Thus, it is likely that the leached rosin components contribute to most of the antiviral effect.

Previously, in addition to SARS-CoV-2, other enveloped viruses such as influenza A virus and respiratory syncytial virus have been shown to be affected by products derived from tall oil. However, non-enveloped viruses like encephalomyocarditis virus (EMCV) were not affected (20). Bell and colleagues, therefore, proposed that the lack of efficacy against non-enveloped viruses suggests the involvement of the lipids in the viral envelope by inhibiting the fusion between the viral envelope and host cell membranes. As bacteria also have membranes, it is no wonder that resin could have effects also on bacterial survival. Indeed, Sipponen and colleagues (56) showed the effect of Norway spruce-derived resin salves on bacterial membranes. The interaction of the resin salve caused the thickening of the bacterial membrane in *Staphylococcus aureus*. They additionally reported changes in the branching of the fatty acids and an altered membrane potential. Another study by Jokinen and Siponen (57) also demonstrated the antibacterial activity of refined spruce resin in treating chronic wounds. Tall oil rosin is a mixture of eight closely related resin acids, of which abietic acid and dehydroabietic acid have been more heavily studied for their antimicrobial properties. In a study by Agudelo-Gomez and colleagues (21), they not only showed antiherpetic activity (HHV-1 and HHV-2) of commercial abietic acid and dehydroabietic acid but also developed their analogs that displayed enhanced antiviral activity. Another study by Fonseca and colleagues (58) demonstrated the antiviral activity of dehydroabietic acid and their analogs against varicella-zoster virus and cytomegalovirus. We have preliminary results showing excellent antiviral efficacy of the rosin-functionalized plastic against the African Swine Fever Virus (J. D. Hemmink, S. Shroff, N. Chege, M. Haapakoski, L. K. Dixon, and V. Marjomäki, unpublished results). As this virus is known to be very difficult to decontaminate, these results suggest that rosin-functionalized plastic may also serve as an antiviral surface for more stable viruses and a larger variety of enveloped viruses. Furthermore, rosin chemicals are biobased, easy to apply to conventional polymer matrices, available in bulk, and very affordable, especially in comparison to several proposed nanomaterial applications. So, the industrial applications of this approach have promise in locations where surface contact plays a role in the transfer of pathogens like public spaces, hospitals, shops, transport, etc.

Using confocal microscopy, we show that, despite the 1 h encounter on the rosin surface with HCoV-OC43 and the resulting total block in infectivity, the viruses were successful in binding to MRC-5 cells. This indicates that the leached rosin components were not altering the functionality of the spike proteins to promote receptor binding.

This is in line with our cryoEM evaluation of the flushed viruses, which showed intact spikes that were mostly in the prefusion stage. As the binding to receptors was not inhibited, the virions were able to proceed and enter cytoplasmic vesicles. However, importantly, post entry, the viruses were stuck inside vesicles and did not proceed with replication and translation in the cytoplasm, which was demonstrated by confocal labeling of replication intermediates. It thus seems obvious that the block in infectivity was in the endosomal membrane fusion step that occurs between the viral envelope and the endosomal membrane. The two major sites on the virus surface involved in membrane fusion are the S2 subunit of the viral spike protein and the viral lipid-rich envelope (59). The S2 subunit has two heptad repeats HR1 and HR2 that form a six-helix bundle, which are responsible for membrane fusion and genome release. In addition to a possible direct effect on spike proteins and their processing, the viral membrane is likely to be affected due to interactions between the envelope lipids and the bioactive rosin components. This study was not able to pinpoint the mechanism of action by the leaching rosin; however, it did confirm its effective response in inactivating viruses on treated surfaces. It will be remarkably interesting to study and identify in the future what exact steps in the fusion process are affected by the rosin components.

Through this study, we demonstrate that the plastic surface functionalized with rosin effectively compromises the infectivity of coronaviruses. Importantly, the rosin-functionalized surface leaches enough rosin components to kill the fusion capability of coronaviruses when they have been in contact with the surface even for a relatively brief time. Due to the conserved nature of membrane fusion of enveloped viruses from different virus families, this rosin-functionalized plastic might serve as a broadly acting antiviral solution for a larger variety of viruses. Altogether, we propose that the rosin-functionalized plastic is a promising candidate as an antiviral surface for enveloped viruses.

ACKNOWLEDGMENTS

We would like to thank Premix company for the plastic material for the study. A special acknowledgment to Petri Papponen from the University of Jyväskylä for his technical expertise in sample preparation and imaging with the HIM and TEM. We are grateful to Prof. Tarja Sironen (University of Helsinki) for letting us use the BSL-3 facility in Helsinki for testing our samples with SARS-CoV-2. We thank Moona Huttunen and Ilkka Julkunen from the University of Turku for providing the N-protein and S-protein antibodies against HCoV-OC43 for the confocal studies. We would like to thank Pasi Laurinmäki, Aušra Domanska, and Behnam Lak from the Biocenter Finland HiLIFE cryoEM Unit at the University of Helsinki within the Instruct-FI Centre for their assistance with CryoEM imaging and acknowledge the Instruct-ERIC (PID:23122; VID:39418) for providing the funding for the same.

This work was supported by a grant from Business Finland (4445/31/2021) to V.M., Academy of Finland grants to S.J.B. (336471 and 315950), the Sigrid Juselius Foundation (95-7202-38 to S.J.B.), and the Jane and Aatos Erkko Foundation (to S.J.B., V.M., and J.J.T.).

AUTHOR AFFILIATIONS

[1]Department of Biological and Environmental Sciences, Nanoscience Center, University of Jyväskylä, Jyväskylä, Finland
[2]Department of Physics, Nanoscience Center, University of Jyväskylä, Jyväskylä, Finland
[3]Department of Neuroscience and Biomedical Engineering, Aalto University, Espoo, Finland
[4]Molecular and Integrative Bioscience Research Programme, Faculty of Biological and Environmental Sciences, University of Helsinki, Helsinki, Finland
[5]Institute of Biotechnology, Helsinki Institute of Life Sciences, University of Helsinki, Helsinki, Finland
[6]Sustainable Technologies group, Department of Chemistry, University of Eastern Finland, Joensuu, Finland

[7]FSCN Research Centre, Mid Sweden University, Sundsvall, Sweden

AUTHOR ORCIDs

Sarah J. Butcher http://orcid.org/0000-0001-7060-5871
Varpu Marjomäki http://orcid.org/0000-0002-4592-5926

FUNDING

Funder	Grant(s)	Author(s)
Business Finland	4445/31/2021	Varpu Marjomäki
Academy of Finland (AKA)	336471, 315950	Sarah J. Butcher
Sigrid Juséliuksen Säätiö (Sigrid Jusélius Stiftelse)	95-7202-38	Sarah J. Butcher
Jane ja Aatos Erkon Säätiö (J&AE)		Sarah J. Butcher J. Jussi Toppari Varpu Marjomäki

AUTHOR CONTRIBUTIONS

Sailee Shroff, Conceptualization, Data curation, Formal analysis, Investigation, Methodology, Writing – original draft | Marjo Haapakoski, Investigation, Writing – review and editing | Kosti Tapio, Conceptualization, Data curation, Formal analysis, Investigation, Methodology, Writing – original draft, Writing – review and editing | Mira Laajala, Investigation | Miika Leppänen, Conceptualization, Data curation, Formal analysis, Investigation, Methodology, Writing – original draft | Zlatka Plavec, Conceptualization, Data curation, Formal analysis, Investigation, Methodology, Writing – review and editing | Antti Haapala, Writing – original draft, Writing – review and editing | Sarah J. Butcher, Formal analysis, Writing – review and editing | Janne A. Ihalainen, Data curation, Formal analysis, Investigation, Methodology, Writing – review and editing | J. Jussi Toppari, Conceptualization, Methodology, Writing – review and editing | Varpu Marjomäki, Conceptualization, Formal analysis, Funding acquisition, Methodology, Supervision, Writing – review and editing

ADDITIONAL FILES

The following material is available online.

Open Peer Review

PEER REVIEW HISTORY (review-history.pdf). An accounting of the reviewer comments and feedback.

REFERENCES

1. Zhu Z, Lian X, Su X, Wu W, Marraro GA, Zeng Y. 2020. From SARS and MERS to COVID-19: a brief summary and comparison of severe acute respiratory infections caused by three highly pathogenic human coronaviruses. Respir Res 21:224. https://doi.org/10.1186/s12931-020-01479-w
2. Krittanawong C, Maitra N, Kumar A, Hahn J, Wang Z, Carrasco D, Zhang HJ, Sun T, Jneid H, Virani SS. 2022. COVID-19 and preventive strategy. Am J Cardiovasc Dis 12:153–169.
3. Tang S, Mao Y, Jones RM, Tan Q, Ji JS, Li N, Shen J, Lv Y, Pan L, Ding P, Wang X, Wang Y, MacIntyre CR, Shi X. 2020. Aerosol transmission of SARS-CoV-2? evidence, prevention and control. Environ Int 144:106039. https://doi.org/10.1016/j.envint.2020.106039
4. Chatterjee S, Murallidharan JS, Agrawal A, Bhardwaj R. 2021. Why coronavirus survives longer on impermeable than porous surfaces. Phys Fluids33:021701. https://doi.org/10.1063/5.0037924
5. Riddell S, Goldie S, Hill A, Eagles D, Drew TW. 2020. The effect of temperature on persistence of SARS-CoV-2 on common surfaces. Virol J 17:145. https://doi.org/10.1186/s12985-020-01418-7
6. Kampf G, Todt D, Pfaender S, Steinmann E. 2020. Persistence of coronaviruses on inanimate surfaces and their inactivation with biocidal agents. J Hosp Infect 104:246–251. https://doi.org/10.1016/j.jhin.2020.01.022
7. Carraturo F, Del Giudice C, Morelli M, Cerullo V, Libralato G, Galdiero E, Guida M. 2020. Persistence of SARS-CoV-2 in the environment and COVID-19 transmission risk from environmental matrices and surfaces. Environ Pollut 265:115010. https://doi.org/10.1016/j.envpol.2020.115010
8. Lin Q, Lim JYC, Xue K, Yew PYM, Owh C, Chee PL, Loh XJ. 2020. Sanitizing agents for virus inactivation and disinfection. VIEW (Beijing) 1:e16. https://doi.org/10.1002/viw2.16

9. Nabi G, Wang Y, Hao Y, Khan S, Wu Y, Li D. 2020. Massive use of disinfectants against COVID-19 poses potential risks to urban wildlife. Environ Res 188:109916. https://doi.org/10.1016/j.envres.2020.109916
10. Dewey HM, Jones JM, Keating MR, Budhathoki-Uprety J. 2022. Increased use of disinfectants during the COVID-19 pandemic and its potential impacts on health and safety. ACS Chem Health Saf 29:27–38. https://doi.org/10.1021/acs.chas.1c00026
11. Mouritz AP, Galos J, Linklater DP, Ladani RB, Kandare E, Crawford RJ, Ivanova EP. 2021. Towards antiviral polymer composites to combat COVID-19 transmission. Nano Sel 2:2061–2071. https://doi.org/10.1002/nano.202100078
12. Kumah EA, Fopa RD, Harati S, Boadu P, Zohoori FV, Pak T. 2023. Human and environmental impacts of nanoparticles: a scoping review of the current literature. BMC Public Health 23:1059. https://doi.org/10.1186/s12889-023-15958-4
13. Kugler S, Ossowicz P, Malarczyk-Matusiak K, Wierzbicka E. 2019. Advances in rosin-based chemicals: the latest recipes, applications and future trends. Mol 24:1651. https://doi.org/10.3390/molecules24091651
14. Höfer R. 2015. Chapter 3B - the pine biorefinery platform chemicals value chain, p 127–155. In Pandey A, Höfer R, Taherzadeh M, Nampoothiri KM, Larroche C (ed), Industrial Biorefineries & White Biotechnology. Elsevier, Amsterdam.
15. Kopper BJ, Illman BL, Kersten PJ, Klepzig KD, Raffa KF. 2005. Effects of diterpene acids on components of a conifer bark beetle–fungal interaction: tolerance by ips pini and sensitivity by its associate ophiostoma ips. Environ Entomol 34:486–493. https://doi.org/10.1603/0046-225X-34.2.486
16. Sipponen A, Laitinen K. 2011. Antimicrobial properties of natural coniferous rosin in the European pharmacopoeia challenge test. APMIS 119:720–724. https://doi.org/10.1111/j.1600-0463.2011.02791.x
17. Xing Y, Zhang W, Song J, Zhang Y, Jiang X, Wang R. 2013. Anticancer effects of a novel class rosin-derivatives with different mechanisms. Bioorg Med Chem Lett 23:3868–3872. https://doi.org/10.1016/j.bmcl.2013.04.069
18. Neto Í, Faustino C, Rijo P. 2015. Antimicrobial abietane diterpenoids against resistant bacteria and biofilms. In The battle against microbial pathogens: Basic science, technological advances and educational programs
19. Thummuri D, Guntuku L, Challa VS, Ramavat RN, Naidu VGM. 2018. Abietic acid attenuates RANKL induced osteoclastogenesis and inflammation associated osteolysis by inhibiting the NF-KB and MAPK signaling. J Cell Physiol 234:443–453. https://doi.org/10.1002/jcp.26575
20. Bell SH, Fairley DJ, Kettunen H, Vuorenmaa J, Orte J, Bamford CGG, McGrath JW. 2021. Rosin soap exhibits virucidal activity. Microbiol Spectr 9:e0109121. https://doi.org/10.1128/spectrum.01091-21
21. Agudelo Gómez L, Betancur L, González-Cardenete M. 2012. Anti HHV-1 and HHV-2 activity *in vitro* of abietic and dehydroabietic acid derivatives. Pharmacol online 1:36.
22. Gigante B, Santos C, Silva AM, Curto MJM, Nascimento MSJ, Pinto E, Pedro M, Cerqueira F, Pinto MM, Duarte MP, Laires A, Rueff J, Gonçalves J, Pegado MI, Valdeira ML. 2003. Catechols from abietic acid: synthesis and evaluation as bioactive compounds. Bioorg Med Chem 11:1631–1638. https://doi.org/10.1016/s0968-0896(03)00063-4
23. Haveri A, Smura T, Kuivanen S, Österlund P, Hepojoki J, Ikonen N, Pitkäpaasi M, Blomqvist S, Rönkkö E, Kantele A, Strandin T, Kallio-Kokko H, Mannonen L, Lappalainen M, Broas M, Jiang M, Siira L, Salminen M, Puumalainen T, Sane J, Melin M, Vapalahti O, Savolainen-Kopra C. 2020. Serological and molecular findings during SARS-CoV-2 infection: the first case study in Finland, January to February 2020. Euro Surveill 25:2000266. https://doi.org/10.2807/1560-7917.ES.2020.25.11.2000266
24. Dent S, Neuman BW. 2014. Purification of coronavirus virions for cryo-EM and proteomic analysis. Coronavir 1282:99–108. https://doi.org/10.1007/978-1-4939-2438-7
25. Yamamoto KR, Alberts BM, Benzinger R, Lawhorne L, Treiber G. 1970. Rapid bacteriophage sedimentation in the presence of polyethylene glycol and its application to large-scale virus purification. Virol 40:734–744. https://doi.org/10.1016/0042-6822(70)90218-7
26. Reed LJ, Muench H. 1938. A simple method of estimating fifty per cent endpoints12. Am J Epidemiol 27:493–497. https://doi.org/10.1093/oxfordjournals.aje.a118408
27. Schmidtke M, Schnittler U, Jahn B, Dahse H-M, Stelzner A. 2001. A rapid assay for evaluation of antiviral activity against coxsackie virus B3, influenza virus A, and herpes simplex virus type 1. J Virol Methods 95:133–143. https://doi.org/10.1016/s0166-0934(01)00305-6
28. Reshamwala D, Shroff S, Sheik Amamuddy O, Laquintana V, Denora N, Zacheo A, Lampinen V, Hytonen VP, Tastan Bishop Ö, Krol S, Marjomäki V. 2021. Polyphenols epigallocatechin gallate and resveratrol, and polyphenol-functionalized nanoparticles prevent enterovirus infection through clustering and stabilization of the viruses. Pharma 13:1182. https://doi.org/10.3390/pharmaceutics13081182
29. Plavec Z, Domanska A, Liu X, Laine P, Paulin L, Varjosalo M, Auvinen P, Wolf SG, Anastasina M, Butcher SJ. 2022. SARS-CoV-2 production, purification methods and UV inactivation for proteomics and structural studies. Virus 14:1989. https://doi.org/10.3390/v14091989
30. Zivanov J, Nakane T, Scheres SHW. 2019. A bayesian approach to beam-induced motion correction in cryo-EM single-particle analysis. IUCrJ 6:5–17. https://doi.org/10.1107/S205225251801463X
31. Kimanius D, Dong L, Sharov G, Nakane T, Scheres SHW. 2021. New tools for automated Cryo-EM single-particle analysis in RELION-4.0. Biochem J 478:4169–4185. https://doi.org/10.1042/BCJ20210708
32. Scheres SHW. 2012. RELION: implementation of a bayesian approach to cryo-EM structure determination. J Struct Biol 180:519–530. https://doi.org/10.1016/j.jsb.2012.09.006
33. Scheres SHW. 2023. A bayesian view on cryo-EM structure determination - PMC. Retrieved 7 Jul 2023. https://doi.org/10.1016/j.jmb.2011.11.010
34. Kimanius D, Forsberg BO, Scheres SH, Lindahl E. 2016. Accelerated cryo-EM structure determination with parallelisation using GPUs in RELION-2. eLife 5:e18722. https://doi.org/10.7554/eLife.18722
35. Zivanov J, Nakane T, Forsberg BO, Kimanius D, Hagen WJ, Lindahl E, Scheres SH. 2023. New tools for automated high-resolution cryo-EM structure determination in RELION-3. eLife 7. Retrieved 7 Jul 2023. https://doi.org/10.7554/eLife.42166
36. Scheres SHW. 2014. Beam-induced motion correction for sub-megadalton cryo-EM particles. Elife 3:e03665. Retrieved Jul 2023. https://doi.org/10.7554/eLife.03665
37. Sorzano CO, de la Rosa Trevín JM, Otón J, Vega JJ, Cuenca J, Zaldívar-Peraza A, Gómez-Blanco J, Vargas J, Quintana A, Marabini R, Carazo JM. 2013. Semiautomatic, high-throughput, high-resolution protocol for three-dimensional reconstruction of single particles in electron microscopy. Methods Mol Biol Clifton NJ 950:171–193.
38. de la Rosa-Trevín JM, Quintana A, Del Cano L, Zaldívar A, Foche I, Gutiérrez J, Gómez-Blanco J, Burguet-Castell J, Cuenca-Alba J, Abrishami V, Vargas J, Otón J, Sharov G, Vilas JL, Navas J, Conesa P, Kazemi M, Marabini R, Sorzano COS, Carazo JM. 2016. Scipion: a software framework toward integration, reproducibility and validation in 3D electron microscopy. J Struct Biol 195:93–99. https://doi.org/10.1016/j.jsb.2016.04.010
39. Grant T, Rohou A, Grigorieff N. 2018. cisTEM, user-friendly software for single-particle image processing. eLife 7:e35383. https://doi.org/10.7554/eLife.35383
40. Rohou A, Grigorieff N. 2015. CTFFIND4: fast and accurate defocus estimation from electron micrographs. J Struct Biol 192:216–221. https://doi.org/10.1016/j.jsb.2015.08.008
41. Mindell JA, Grigorieff N. 2003. Accurate determination of local defocus and specimen tilt in electron microscopy. J Struct Biol 142:334–347. https://doi.org/10.1016/s1047-8477(03)00069-8
42. Warnes SL, Little ZR, Keevil CW. 2015. Human coronavirus 229E remains infectious on common touch surface materials. mBio 6:e01697-15. https://doi.org/10.1128/mBio.01697-15
43. Duan SM, Zhao XS, Wen RF, Huang JJ, Pi GH, Zhang SX, Han J, Bi SL, Ruan L, Dong XP, SARS Research Team. 2003. Stability of SARS coronavirus in human specimens and environment and its sensitivity to heating and UV irradiation. Biomed Environ Sci 16:246–255.
44. Rabenau HF, Cinatl J, Morgenstern B, Bauer G, Preiser W, Doerr HW. 2005. Stability and inactivation of SARS coronavirus. Med Microbiol Immunol 194:1–6. https://doi.org/10.1007/s00430-004-0219-0
45. Schirtzinger EE, Kim Y, Davis AS. 2022. Improving human coronavirus OC43 (HcoV-OC43) research comparability in studies using HCoV-OC43 as a surrogate for SARS-CoV-2. J Virol Methods 299:114317. https://doi.org/10.1016/j.jviromet.2021.114317

46. Linklater DP, Mah SWL, Tzanov V, Baulin V, Borg NA, Moad G, Simons R, O'Connor AJ, Ivanova EP. 2023. Current perspectives on the development of virucidal nano surfaces. Curr Opi Col & Inter Sci 67:101720. https://doi.org/10.1016/j.cocis.2023.101720
47. Haldar J, An D, Alvarez de Cienfuegos L, Chen J, Klibanov AM. 2006. Polymeric coatings that inactivate both influenza virus and pathogenic bacteria. Proc Natl Acad Sci U S A 103:17667–17671. https://doi.org/10.1073/pnas.0608803103
48. Ai H, Wang F, Xia Y, Chen X, Lei C. 2012. Antioxidant, antifungal and antiviral activities of chitosan from the larvae of housefly. Food Chem 132:493–498. https://doi.org/10.1016/j.foodchem.2011.11.033
49. Han J, Chen L, Duan SM, Yang QX, Yang M, Gao C, Zhang BY, He H, Dong XP. 2005. Efficient and quick inactivation of SARS coronavirus and other microbes exposed to the surfaces of some metal catalysts. Biomed Environ Sci 18:176–180.
50. Zhou Y, Fletcher NF, Zhang N, Hassan J, Gilchrist MD. 2021. Enhancement of antiviral effect of plastic film against SARS-CoV-2: combining nanomaterials and nanopatterns with scalability for mass manufacturing. Nano Lett 21:10149–10156. https://doi.org/10.1021/acs.nanolett.1c02266
51. Butot S, Baert L, Zuber S. 2021. Assessment of antiviral coatings for high-touch surfaces by using human coronaviruses HCoV-229E and SARS-CoV-2. Appl Environ Microbiol 87:e0109821. https://doi.org/10.1128/AEM.01098-21
52. Biryukov J, Boydston JA, Dunning RA, Yeager JJ, Wood S, Reese AL, Ferris A, Miller D, Weaver W, Zeitouni NE, Phillips A, Freeburger D, Hooper I, Ratnesar-Shumate S, Yolitz J, Krause M, Williams G, Dawson DG, Herzog A, Dabisch P, Wahl V, Hevey MC, Altamura LA, Frieman MB. 2020. Increasing temperature and relative humidity accelerates inactivation of SARS-CoV-2 on surfaces. mSphere 5:e00441-20. https://doi.org/10.1128/mSphere.00441-20
53. Morris DH, Yinda KC, Gamble A, Rossine FW, Huang Q, Bushmaker T, Fischer RJ, Matson MJ, van Doremalen N, Vikesland PJ, Marr LC, Munster VJ, Lloyd-Smith JO. 2020. Mechanistic theory predicts the effects of temperature and humidity on inactivation of SARS-CoV-2 and other enveloped viruses. bioRxiv:2020.10.16.341883. https://doi.org/10.1101/2020.10.16.341883
54. Paton S, Spencer A, Garratt I, Thompson KA, Dinesh I, Aranega-Bou P, Stevenson D, Clark S, Dunning J, Bennett A, Pottage T. 2021. Persistence of severe acute respiratory syndrome coronavirus 2 (SARS-CoV-2) virus and viral RNA in relation to surface type and contamination concentration. Appl Environ Microbiol 87:e0052621. https://doi.org/10.1128/AEM.00526-21
55. Owen L, Shivkumar M, Cross RBM, Laird K. 2022. Porous surfaces: stability and recovery of coronaviruses. Inter Focu 12:20210039. https://doi.org/10.1098/rsfs.2021.0039
56. Sipponen A, Peltola R, Jokinen JJ, Laitinen K, Lohi J, Rautio M, Mannisto M, Sipponen P, Lounatmaa K. 2009. Effects of Norway spruce (*Picea abies*) resin on cell wall and cell membrane of *Staphylococcus aureus*. Ultrastruct Pathol 33:128–135. https://doi.org/10.1080/-01913120902889138
57. Jokinen JJ, Sipponen A. 2016. Refined spruce resin to treat chronic wounds: rebirth of an old folkloristic therapy. Adv Wound Care (New Rochelle) 5:198–207. https://doi.org/10.1089/wound.2013.0492
58. Fonseca T, Gigante B, Marques MM, Gilchrist TL, De Clercq E. 2004. Synthesis and antiviral evaluation of benzimidazoles, quinoxalines and indoles from dehydroabietic acid. Bioorg Med Chem 12:103–112. https://doi.org/10.1016/j.bmc.2003.10.013
59. Jackson CB, Farzan M, Chen B, Choe H. 2022. Mechanisms of SARS-CoV-2 entry into cells. Nat Rev Mol Cell Biol 23:3–20. https://doi.org/10.1038/s41580-021-00418-x

III

POLYPHENOLS EPIGALLOCATECHIN GALLATE AND RESVERATROL, AND POLYPHENOL-FUNCTIONALIZED NANOPARTICLES PREVENT ENTEROVIRUS INFECTION THROUGH CLUSTERING AND STABILIZATION OF THE VIRUSES

by

Reshamwala D., Shroff S., Sheik Amamuddy O., Laquintana V., Denora N., Zacheo A., Lampinen V., Hytonen V.P., Tastan Bishop Ö., Krol S. & Marjomäki V. 2021

Pharmaceutics 13: 1182.

https://doi.org/10.3390/pharmaceutics13081182

pharmaceutics

MDPI

Article

Polyphenols Epigallocatechin Gallate and Resveratrol, and Polyphenol-Functionalized Nanoparticles Prevent Enterovirus Infection through Clustering and Stabilization of the Viruses

Dhanik Reshamwala [1,†], Sailee Shroff [1,†], Olivier Sheik Amamuddy [2], Valentino Laquintana [3], Nunzio Denora [3], Antonella Zacheo [4], Vili Lampinen [5], Vesa P. Hytonen [5,6], Özlem Tastan Bishop [2], Silke Krol [7,‡] and Varpu Marjomäki [1,*,‡]

1 Department of Biological and Environmental Science/Nanoscience Center, University of Jyväskylä, 40014 Jyväskylä, Finland; dhanik.d.reshamwala@jyu.fi (D.R.); sailee.s.shroff@jyu.fi (S.S.)
2 Research Unit in Bioinformatics (RUBi), Department of Biochemistry and Microbiology, Rhodes University, Makhanda 6140, South Africa; oliserand@gmail.com (O.S.A.); o.tastanbishop@ru.ac.za (Ö.T.B.)
3 Department of Pharmacy–Pharmaceutical Sciences, University of Bari "Aldo Morro", 70125 Bari, Italy; valentino.laquintana@uniba.it (V.L.); nunzio.denora@uniba.it (N.D.)
4 Laboratory for Nanotechnology, IRCCS Istituto Tumori "Giovanni Paolo II", 70124 Bari, Italy; antonellazacheo@gmail.com
5 Faculty of Medicine and Health Technology, Tampere University, 33520 Tampere, Finland; vili.lampinen@tuni.fi (V.L.); vesa.hytonen@tuni.fi (V.P.H.)
6 Fimlab Laboratories, 33520 Tampere, Finland
7 Laboratory for Personalized Medicine, National Institute of Gastroenterology, "S. de Bellis" Research Hospital, 70013 Castellana Grotte, Italy; silke.krol@aol.com
* Correspondence: varpu.s.marjomaki@jyu.fi; Tel.: +358-405634422
† These authors contributed equally to this work.
‡ These authors contributed equally to this work.

Abstract: To efficiently lower virus infectivity and combat virus epidemics or pandemics, it is important to discover broadly acting antivirals. Here, we investigated two naturally occurring polyphenols, Epigallocatechin gallate (EGCG) and Resveratrol (RES), and polyphenol-functionalized nanoparticles for their antiviral efficacy. Concentrations in the low micromolar range permanently inhibited the infectivity of high doses of enteroviruses (10^7 PFU/mL). Sucrose gradient separation of radiolabeled viruses, dynamic light scattering, transmission electron microscopic imaging and an in-house developed real-time fluorescence assay revealed that polyphenols prevented infection mainly through clustering of the virions into very stable assemblies. Clustering and stabilization were not compromised even in dilute virus solutions or after diluting the polyphenols-clustered virions by 50-fold. In addition, the polyphenols lowered virus binding on cells. In silico docking experiments of these molecules against 2- and 3-fold symmetry axes of the capsid, using an algorithm developed for this study, discovered five binding sites for polyphenols, out of which three were novel binding sites. Our results altogether suggest that polyphenols exert their antiviral effect through binding to multiple sites on the virion surface, leading to aggregation of the virions and preventing RNA release and reducing cell surface binding.

Keywords: polyphenols; functionalized gold nanoparticles; antiviral efficacy; enteroviruses; stabilization

Citation: Reshamwala, D.; Shroff, S.; Sheik Amamuddy, O.; Laquintana, V.; Denora, N.; Zacheo, A.; Lampinen, V.; Hytonen, V.P.; Tastan Bishop, Ö.; Krol, S.; et al. Polyphenols Epigallocatechin Gallate and Resveratrol, and Polyphenol-Functionalized Nanoparticles Prevent Enterovirus Infection through Clustering and Stabilization of the Viruses. *Pharmaceutics* **2021**, *13*, 1182. https://doi.org/10.3390/pharmaceutics13081182

Academic Editor: Hyun-ouk Kim

Received: 29 June 2021
Accepted: 28 July 2021
Published: 31 July 2021

1. Introduction

The gold standard in viral disease management is prevention, which is vaccination. Pandemics with new viruses remind us that the development and approval of vaccines takes time. Moreover, vaccines are not 100% efficient, and especially elderly people and immunocompromised individuals may not generate sufficient protection against infectious

agents. Therefore, powerful broadly acting antivirals with a more general inhibitory mechanism of action are required.

Non-enveloped enteroviruses are very stable and stay infective on surfaces and in the environment for long periods. Their entry is mostly via the gastro-intestinal tract, but also through the upper respiratory system. They cause a high number of acute infections such as flu, aseptic meningitis and myocarditis, but also contribute to chronic diseases such as dilated cardiomyopathy, asthma or type I diabetes [1]. For enteroviruses, no approved antivirals exist, and there are vaccines available only against poliovirus and EV71 [1]. Therefore, it is necessary to reduce the viral load on the surfaces and in the environment and prevent infection in the primary infection sites. An optimal solution to tackle virus infection would be a drug that directly kills virus infectivity and additionally prevents the virus from entering cells.

Nature provides a large variety of potential antimicrobials and antivirals. Those may be of endophyte origin, secreted by the symbiotic fungi or bacteria living in plants [2]. One example is Resveratrol (3,5,4′-trihydroxy-trans-stilbene), which is a polyphenol, non-flavonoid compound and is produced by plants in response to cellular damage or pathogen attacks [3]. Resveratrol (RES) is found in strongly pigmented vegetables and fruits such as the skin of grapes, blueberries and peanuts, and it has strong bioactive potential [3–5]. Like RES, flavonoids are polyphenols found as secondary metabolites in vegetables, fruits, nuts, red wine and tea. They share great similarity in structure to RES and great promise to be used as antivirals [6–8].

In the present study, EGCG and RES were tested for their antiviral efficacy, and the mechanisms of action was elucidated against the stable non-enveloped enterovirus B group viruses. While RES is considered completely non-toxic [9], high amounts of free EGCG show in vitro hepatotoxic effects, and in particular in cases in vivo [10,11]. Therefore, here, free polyphenols as well as polyphenols functionalized onto gold nanoparticles (AuNPs) were studied for their antiviral efficiency, as binding polyphenols to AuNPs can reduce toxicity. The effect of reduced toxicity by nanoparticle binding has been shown previously for molecules with a known hepatotoxic profile [12]. AuNPs were synthesized by green chemistry using the polyphenols as redox agents to further reduce the toxic components in the preparations. AuNPs synthesized using green chemistry have been previously reported to act as antivirals [13].

In this work, we show that both RES and EGCG have a direct and long-lived antiviral effect through binding to multiple sites on the virus particles, preventing the virus from opening, reducing the binding to the cell surface and inducing clustering of the virions.

2. Materials and Methods

2.1. Cells

Human alveolar basal epithelial adenocarcinoma (A549) cells and Green Monkey Kidney (GMK) cells were obtained from American type culture collection (ATCC, Manassas, VA, USA). The A549 and GMK cell lines were propagated in Dulbecco's Modified Eagle Medium (DMEM) (Gibco, Paisley, UK) and Eagle's Minimum Essential Medium (MEM) (Gibco, Paisley, UK) respectively, supplemented with 10% Fetal Bovine Serum (FBS, Gibco, Paisley, UK), 1% L-GlutaMAX (Gibco, Paisley, UK) and 1% antibiotics (penicillin/streptomycin) (Gibco, Paisley, UK) in a humidified 5% CO_2 incubator at 37 °C.

2.2. Viruses

Coxsackievirus B3 (CVB3; Nancy strain), Coxsackie virus B1 (CVB1, CONN 5 strain) and Coxsackievirus A9 strain (CVA9; Griggs strain), obtained from ATCC, were produced and purified as described before [14–16], with the only exception of adding 0.1% (*v*/*v*) TWEEN® 80 (Sigma-Aldrich, Steinheim, Germany) during the freeze–thaw cycle.

2.3. Polyphenols

Epigallocatechin gallate (EGCG) and Resveratrol (RES) were purchased from Sigma-Aldrich (Munich, Germany). EGCG was dissolved in water and Resveratrol in 0.02 M NaOH. Stock concentrations of EGCG and RES were 6.5 mM (3 mg/mL) and 8.8 mM (2 mg/mL) respectively, and were stored at −20 °C.

2.4. Nanoparticle Preparations

The green chemistry approach using the polyphenolic compounds as redox agents was chosen to reduce the number of potentially toxic molecules present on the surface of the gold nanoparticles (AuNPs). These polyphenols are supposed to form a stable and stabilizing layer on the AuNPs, as it was observed for citrate AuNPs shown by Mandal et al. [17]. For the preparation of RES-coated gold nanoparticles (RES-AuNPs), we used a modified protocol by Sanna et al. [18]. In brief, 20.8 mg of $HAuCl_4 \cdot 3\ H_2O$ (Sigma-Aldrich, Milan Italy) was dissolved in 12 mL of bi-distilled water on ice. Next, an ice-cold light-yellow solution of 3.0 mg of RES in 1.5 mL of 0.02 M NaOH solution was quickly added under vortexing. Under continuous vortexing, the temperature of the solution was slowly raised to room temperature (RT). Immediately after RES addition, the solution became brownish, after 10 min reddish, and after vortexing at 500 rpm for 1 h, the color turned into wine red. Unbound RES was removed by a series of washing (first wash: 0.02 M NaOH; second wash: H_2O) and centrifugation steps (2 × 14,000 rpm, 20 min at 4 °C to remove NaOH; 1 × 12,000 rpm, 20 min at 4 °C to remove H_2O), and the pellet was finally resuspended in water. The centrifugation was carried out by a Microfuge 40R with a Fiberlite F21-48 x2 Fixed Angle Rotor, 45°, R_{max} 97 mm (ThermoFisher, Rome, Italy). The final gold concentration was 5.3 mg/mL, as determined by ICP-MS. The concentration of RES in the stock solution was calculated (Supplementary Material) to be 34.4 µM.

For the preparation of EGCG-AuNPs, 5.9 mg of EGCG was dissolved in 15 mL of bi-distilled water and cooled on ice. An ice-cold solution of 12.9 mg of $HAuCl_4 \cdot 3\ H_2O$ in 2 mL of H_2O was added quickly and mixed by shaking on ice for another 10 min. After the color changed from bright yellow to red within 1 min, the temperature of the solution was slowly increased to RT for 2 h under continuous vortexing at 500 rpm. The excess EGCG was removed by a series of washing and centrifugation steps (2× centrifugation at 14,000 rpm for 20 min at 4 °C addition of ddH_2O, 1× centrifugation at 12,000 rpm for 20 min at 4 °C). The deep red pellet was resuspended in water. The final gold concentration was 1.64 mg/mL, as determined by ICP-MS. The concentration of EGCG in the stock solution was calculated (Supplementary Material) to be 5.61 µM.

Quantitative Analysis of EGCG and RES Bound to the AuNP Surface

The amount of EGCG and RES present on the surface of the gold nanoparticles was estimated indirectly by the substitution with L-cysteine. The thiol group of the cysteine binds stronger to the gold than the aromatic ring system of polyphenols, and therefore will replace it. The colorimetric method finally determines the remaining free thiol groups of the L-cysteine, assuming a complete substitution of the polyphenols by cysteine [19]. The residual-free thiol groups of L-cysteine in solution after polyphenol exchange on the nanoparticle surface were quantified photometrically using Ellman's reagent (5,5′-dithiobis (2-nitrobenzoic acid)). The amount of polyphenols was then calculated considering a 1:1 ratio of replacement (1 cysteine replaces 1 polyphenol).

For its determination, a fresh stock solution of 1 mg of cysteine in 1 mL of 0.5 M phosphate buffer, pH 8.0, was diluted to a final concentration in L-cysteine of 102 mM. 100 µL of this solution was mixed with different volumes of EGCG-AuNPs or RES-AuNPs stock solution (ranging from 10 to 100 µL) and 0.5 M phosphate buffer solution at pH 8.0 to reach a final solution volume of 500 µL. This was mixed with 500 mL of Ellman's reagent solution (3 mg dissolved in 10 mL of 0.5 M phosphate buffer, pH 8.0). The resulting mixture was incubated in the dark and at room temperature for 2 h. After this time, the samples were centrifuged at 13,000 rpm for 5 min (Mikro 22 R, Hettich Zentrifugen, Germany) and

100 µL of each sample was transferred into a microplate reader (PerkinElmer VICTOR X3 Multilabel) to measure absorbance at 450 nm. The amount of thiol groups was estimated from a standard curve of L-cysteine.

2.5. Dynamic Light Scattering Measurements

For dynamic light scattering (DLS) measurements, CVA9 virus samples were diluted in PBS from a stock solution (5×10^{10} PFU/mL) to 2×10^{9}, 2×10^{8}, 5×10^{7} and 2×10^{7} PFU/mL. EGCG was added to each of these dilutions such that its final concentration was 6.5 µM. Experimental virus controls with the same dilutions but without the EGCG were also prepared. Both the control virus and EGCG-treated virus were incubated for 1 h at 37 °C. Post-incubation, the virus/virus cluster size distribution was measured by DLS at 25 °C with the Zetasizer Nano ZS instrument (Malvern Instruments, Malvern, UK). The attenuator was set by the system according to scattering intensity of the sample and set measurement position at 3 mm. As controls, we measured both EGCG and PBS buffer alone. As expected, no particles were observed in the controls.

2.6. Antiviral Activity Assay

The antiviral activity of the polyphenols against species B enteroviruses was determined using a cytopathic effect (CPE) inhibition assay, modified from Schmidtke et al. [20]. Briefly, A549 cells were cultured for 24 h at 37 °C in 96-well flat-bottomed microtiter plate (Sarstedt, Numbrecht, Germany) at a density of 12,000 cells/well in 100 µL of DMEM supplemented with 10% FBS, 1% GlutaMAX and 1% penicillin/streptomycin antibiotics. The following day, each of the viruses (2×10^{7} PFU/mL for CVB3 and CVB1 and 2×10^{8} PFU/mL for CVA9) were pre-incubated with the compounds for 1 h at 37 °C. The virus–compound mixture was further diluted 10 times with DMEM to obtain a final MOI of 10 for CVB3 and CVB1 and 100 for CVA9. This mix was then added to cells for 24 h in a humidified 5% CO_2 incubator at 37 °C. A virus without the compound was used as a positive control and a mock infection without the virus and compound as a negative control for the experiments. The development of a cytopathic effect (CPE) was monitored using light microscopy. The next day, the cells were fixed and stained for 10 min with CPE dye (0.03% crystal violet, 2% ethanol and 36.5% formaldehyde) after washing twice with PBS. After two washes with water, the stained viable cells were lysed using a lysis buffer (0.8979 g of sodium citrate and 1N HCl in 47.5% ethanol) to elute the crystal violet. Then, the absorbance was measured spectrophotometrically at 570 nm using the VICTOR^{TM} X4 multilabel reader (PerkinElmer, Turku, Finland). This assay was performed twice independently for each of the virus–compound concentrations.

2.7. Cytotixicity Assay

Cytotoxicity studies were performed using the CPE inhibition assay by adding the compounds (without any virus) to A549 cells. Mock infection was used as a negative control. This assay was performed twice independently.

2.8. Time of Addition Studies

Time of addition studies were performed using the CPE inhibition assay. Briefly, A549 cells were cultured for 24 h in 96-well flat-bottomed microtiter plate at a density of 12,000 cells/well in 100 µL of DMEM supplemented with 10% FBS, 1% GlutaMAX and 1% penicillin/streptomycin antibiotics. On the subsequent day, cells were infected with CVB3 (MOI 10) for 1 h at 37 °C. Afterwards, excess virus was removed by repeated washing. Then, fresh media (supplemented with 10% FBS, 1% GlutaMAX and 1% penicillin/streptomycin) containing EGCG (65 µM) and RES (880 µM) were added, and cells were incubated for 24 h. Virus control (without the compounds), compound control (without virus) and mock infection were used as controls for the studies. This assay was performed twice independently for each of the virus–compound concentrations, with 5 technical replicates in each experiment.

2.9. Radioactive Labeling of CVA9

The radioactive virus was produced in confluent monolayers of GMK cells, which were washed and incubated with PBS for 15 min at 37 °C and infected with CVA9 (Griggs strain; ATCC) diluted in low-methionine-cysteine medium (MP Biomedicals, Illkrich, France) supplemented with 1% FBS and 1% Glutamax. After 3 h of infection, 40 µCi/mL of radioactive [^{35}S] methionine/cysteine (PerkinElmer, Boston, MA, USA) diluted in low-methionine-cysteine medium supplemented with 1% FBS was added to the cells, and virus replication was allowed to proceed for 24 h at 37 °C. After three freeze–thaw cycles, the supernatant was cleared by pelleting at 2500× *g* for 10 min. TWEEN® 80 (0.1% *v/v*) was added to the pellet and incubated on ice for 30 min. Post-incubation, centrifugation was performed for 10 min with 4000× *g* at 4 °C. The collected supernatant was added on a 2 mL sucrose cushion (40%). The cushions were ultracentrifuged with an SW-41 rotor at 151,263× *g* for 2.5 h (4 °C). All the liquid up until the cushion and first 500 µL fraction from the top were discarded, and the next 3 × 500 µL fractions were collected, which were pelleted with a 70Ti rotor at 90,140× *g* for 2 h at 4 °C. The concentrated virus was then layered on top of the 10 mL sucrose gradient (5–20%) and ultracentrifuged with a SW-41 rotor at 151,263× *g* for 2 h (4 °C). Fractions (500 µL) were collected from the top to the bottom of the cushion and small samples from each fraction were mixed with a scintillation cocktail UltimaGold™ (PerkinElmer, Waltham, MA, USA) for counting the radioactivity (counts per minute) using a Tri-Carb® 2910TR liquid scintillation analyzer (PerkinElmer, Downers Grove, IL, USA). The 160S-containing fractions were pooled and used for the experiments (7000 CPM/µL; 1.4 × 10^9 PFU/mL).

2.10. Gradient Assay

Metabolically labeled CVA9 (70,000 CPM corresponding to 1.4 × 10^8 PFU/mL) was pre-treated with EGCG (6.5 µM) and RES (1.8 mM) for 1 h at 37 °C. A virus control (without the compounds but the same treatment) and fresh virus (without the polyphenols and without treatment) were used as positive controls for the assay. The test and control samples were further diluted 10 times using a buffer, PBS-$MgCl_2$ (PBS containing 2 mM $MgCl_2$). The samples were then layered over 10 mL sucrose (5–20%) gradients and ultracentrifuged with a SW-41 rotor at 151,263× *g* (average g value) for 2 h (4 °C) using the SW-41 rotor. Gradients were fractionated from top to bottom (500 µL fractions) and mixed with a scintillation cocktail for counting the radioactivity using a PerkinElmer Tri-Carb® 2910TR liquid scintillation analyzer.

2.11. Real-Time Fluorescence Uncoating Assay

The real-time fluorescence uncoating assay has been previously described for measuring uncoating of enteroviruses at 37 °C [16,21]. The assay is based on the fluorescence emitted by SYBR Green II (SGII) when bound to viral genomic RNA. The experiment was carried out in a 96-well plate with a total reaction volume of 100 µL. Each well contained 0.5 µg of Coxsackievirus B3, 10× SGII (Life Technologies, Eugene, OR, USA) diluted in double-distilled water (ddH_2O), polyphenol-functionalized nanoparticles EGCG-AuNPs (Au concentration 16.4 µg/mL, ligand concentration 5.61 × 10^{-2} µM) and RES-AuNPs (Au concentration 53 µg/mL, ligand concentration 3.44 × 10^{-1} µM) in storage buffer PBS-$MgCl_2$ and opening buffer (20 mM NaCl, 6 mM KH_2PO_4, 12 mM K_2HPO_4 and 0.01% faf-BSA). We had two experimental controls: one was a virus in the storage buffer and the other contained a virus in the opening buffer. The samples were prepared on ice to prevent any effect of temperature on uncoating. Additionally, we had controls to exclude fluorescence quenching/enhancement from other molecules in the reaction mix. RNAse at a final concentration of 10 µg/mL was used to distinguish between the fluorescence originating from porous intermediate virions (allowing entry of SGII inside) and the RNA in solution. The fluorescence was recorded every 15 min for an hour at 37 °C using the PerkinElmer Multilabel Reader Victor X4 installed with a F485 lamp filter, F535 emission filter and a counting time of 1 s.

2.12. Particle Stability Thermal Release Assay (PaSTRy)

The PaSTRy assay was performed as described before [22]. The experiment was carried out in thin-walled PCR plates (Agilent, Amstelveen, Netherlands). A reaction mixture containing 0.5 µg of Coxsackievirus B3 and EGCG (65 µM) in storage buffer or opening buffer was preincubated for 1 h at 37 °C and 5% CO_2. Post-incubation, 10× SGII (Invitrogen) in ddH_2O was added to the reaction mix, and a final volume of 50 µL was aliquoted into the thin-walled PCR plates. The thermal cycler (BioRad C100, Helsinki, Finland) recorded the fluorescence in quadruple from 20 to 90 °C with 0.5 °C intervals. The fluorescence data output was extracted from the BioRad CFX manager (2.1 software, accessed on 10 October 2020) and processed in Microsoft Excel (2016). The melt curve was obtained by plotting the relative fluorescence units (RFU) values versus temperature. The melting temperature (Tm) was determined from the melt peak, which was plotted using the derivative of the RFU as a function of temperature (d(RFU)/dT).

2.13. Transmission Electron Microscopy

A reaction mixture containing the CVA9 (1.6×10^{10} PFU/mL), polyphenols (EGCG, 650 µM; RES, 880 µM), polyphenol-functionalized nanoparticles EGCG-AuNPs (Au concentration 164 µg/mL, ligand concentration 5.61×10^{-1} µM) and RES-AuNPs (Au concentration 530 µg/mL, ligand concentration 3.44 µM) in buffer (PBS-$MgCl_2$) was incubated for 1 h at 37 °C and 5% CO_2. During the incubation, the Formvar-coated copper grids were glow-discharged using the EMS/SC7620 Mini sputter coater (Electron Microscopy Sciences, Hatfield, PA, USA). Post-incubation, 5 µL of the reaction mixture was pipetted on the glow-discharged grids for 20 s and then blotted away using Whatman paper. To negatively stain the sample, 5 µL of 1% (*w*/*v*) Phosphotungstic acid (PTA in water, pH adjusted to neutrality) (Sigma-Aldrich, Shinagawa-ku, Japan) or 2% (*w*/*v*) Uranyl acetate (Electron Microscopy Sciences, Hatfield, PA, USA) was pipetted on grids and incubated for 30 s, and blotted away using Whatman paper. The samples were visualized in a JEOL JEM-1400 transmission electron microscope (JEOl, Tokyo, Japan). The diameter of functionalized gold nanoparticles from the images taken using the TEM was measured by automated counting using the BioImageXD software (www.bioimagexd.net, accessed on 16 January 2021).

2.14. Radioactive Binding Assay

A549 cells were cultured for 24 h in 96-well flat-bottomed microtiter plates at a density of 12,000 cells/well in 100 µL of DMEM supplemented with 10% FBS, 1% GlutaMAX and 1% penicillin/streptomycin antibiotics. On day 2, ^{35}SMet/Cys-CVA9 (28,000 CPM corresponding to 1.38×10^8 PFU/mL) was pre-treated with the polyphenols and polyphenol-functionalized nanoparticles EGCG (65 µM), RES (880 µM), EGCG-AuNPs (Au concentration 16.4 µg/mL, ligand concentration 5.61×10^{-2} µM) and RES-AuNPs (Au concentration 53 µg/mL, ligand concentration 3.44×10^{-1} µM) in buffer (PBS-$MgCl_2$), and incubated at 37 °C for 1 h. Virus control without the compound was also prepared and incubated. Post-incubation, the sample tubes were placed on ice and 1% DMEM was added to make the final volume reach 100 µL. Following this, the samples with DMEM were added to the cells. Then, the 96-well plate was kept on ice while rocking for 1 h to ensure uniform binding of the virus on the cell surface. Next, the media was aspirated from each well and three washes with ice-cold PBS were performed to remove any unbound virus from the cell surface. To detach the cells, 150 µL of 1% Triton was added to the wells and incubated for 30 min. The entire liquid was transferred to a tube containing 4 mL of scintillation cocktail UltimaGold™ and measured using the Tri-Carb® 2910TR liquid scintillation analyzer.

2.15. Dilution and Temperature Assays

Dilution and temperature assays were performed using the CPE inhibition assay. For the dilution assay, CVB3 (4.4×10^8 PFU/mL), polyphenol-functionalized nanoparticles EGCG-AuNPs (Au concentration 164 µg/mL, ligand concentration 5.61×10^{-1} µM) and RES-AuNPs (Au concentration 530 µg/mL, ligand concentration 3.44 µM) in buffer (PBS-

$MgCl_2$) were incubated at 37 °C for 1 h. An experimental virus control (without the compounds) and fresh virus control (without the compounds and without any incubation) were used as two controls for the assay. Post-incubation, each of the test samples and the experimental virus control were divided equally into two tubes, one was diluted 50 times using a buffer (PBS-$MgCl_2$) and the other part was stored at −20 °C (as an undiluted sample). The diluted samples were incubated over 72 h at 37 °C, such that equal fractions from them were collected at regular time-intervals (1, 6, 24, 48 and 72 h) and stored at −20 °C. At the end of 72 h, all the diluted and undiluted samples were further diluted with DMEM and added onto the cells, to obtain a final MOI of 15. On the subsequent day, the plates were stained for CPE as explained before.

When testing the effect of temperatures, two approaches were used. One with longer and the other with shorter times of incubation. For testing the longer periods of incubation, CVB3 (4.4×10^8 PFU/mL) was pre-treated with EGCG (650 μM), RES (880 μM), EGCG-AuNPs (Au concentration 164 μg/mL, ligand concentration 5.61×10^{-1} μM) and RES-AuNPs (Au concentration 530 μg/mL, ligand concentration 3.44 μM) in buffer (PBS-$MgCl_2$) at RT (21 °C), 8 and 37 °C for 72 h. An experimental virus control (without the compounds) and fresh virus control (without the compounds and without any incubation) were used as two controls for the assay. Test samples and the experimental virus control were collected after incubating at the above-mentioned temperatures for 6, 24, 48 and 72 h and stored at −20 °C. After 72 h, all the samples were further diluted with DMEM and added to the cells, to obtain a final MOI of 15. On the subsequent day, the plates were stained for CPE, as explained before. In case of shorter incubation times, CVA9 (2×10^7 PFU/mL) was pre-treated with EGCG (6.5 μM) at 21 or 37 °C for 1 min, 5 min and 1 h and then added to the cells.

2.16. Blind Docking of Polyphenolic Compounds against CVA9 and CVB3

2.16.1. The Experimental Design

For the in silico docking experiment, the polyphenols Epigallocatechin gallate (EGCG) and Resveratrol (RES) were to be blindly docked over large external surfaces of the viral capsids of CVA9 and CVB3. Due to the overly large surfaces to be scanned, the capsids were segmented into relatively large grid boxes centered around their fold axes (2, 3 and 5) of rotational symmetry. This strategy was used in order to obtain overlapping segments spanning as much of the viral capsid surfaces as possible.

2.16.2. Ligand Preparation

The molecular structures of the polyphenolic compounds, Epigallocatechin gallate (Drug Bank ID: DB03823) and Resveratrol (Drug Bank ID: DB02709), were reconstituted and protonated from their SMILE strings using the RDKit library. The MGLTools software [23] was then used to assign Gasteiger partial charges and merge non-polar hydrogen atoms.

2.16.3. Capsid Preparation

Full capsids for the CVA9 Griggs strain (PDB ID: 1D4M) [24] and CVB3 Nancy strain (PDB ID: 6GZV) [25] were reconstituted from their first biological assemblies using the PyMOL software. While the CVA9 capsid was already protonated, the PDB2PQR tool was used to protonate the CVB3 capsid to pH 7. However, as this altered the chain labels and segment identifiers, an in-house Python script (capsidockprep.py) was designed to restore these labels. In order to screen the maximum outer surface area from the capsid, the grid box center was placed at each individual capsid fold axis of rotational symmetry, with the box y-z plane being perpendicular to the axis of rotation and partially embedded within the capsid. In order to do so, centroids (x, y and z coordinates measured in angstroms) for each of the fold axes were selected, before shifting the box along the *x*-axis by 10 Å to the right. Internally, before shifting, the capsid centroid is centered at the origin (0, 0, 0) prior to rotating the capsid centroid position vector to be along the *x*-axis. For simplicity, the PDB2PQR tool is wrapped within an in-house Python script to enable protonation when

the "ph" parameter is set. Similar to AutoDock Vina, a grid interval size of 0.375 Å is used. The "gridsize" parameter is specified in grid points. The grid parameters for all of the fold axes are provided in Table 1. The AutoDock Vina plugin from PyMOL was used to visualize the effects of shifting and grid sizing.

Table 1. Parameters for grid placement along the fold capsid fold axes.

Strain	Fold Axis	Centroid (Å)	Grid Size (in Grid Points)	Shift along x Axis (Å)
CVA9	2	−75.446, 105.465, −13.389	40 × 100 × 100	10
	3	−103.647, 73.405, 5.830	40 × 120 × 120	10
	5	−44.878, 108.985, 50.228	90 × 180 × 180	10
CVB3	2	118.389, 223.579, 288.589	40 × 100 × 100	10
	3	110.197, 256.603, 256.603	40 × 120 × 120	10
	5	183.400, 251.025, 292.820	90 × 180 × 180	10

The preprocessing by the in-house Python script greatly reduced the number of atoms by including protein chains belonging to any atom within the grid box, whilst keeping chain labels and segment IDs. Due to the high number of atoms required to capture the complete protomers in their protonated form for the 5-fold axis (beyond the limit of the PDB format), the experiment was focused around the 2- and 3-fold axes of rotation symmetry. As performed for the ligands, charges were assigned, and non-polar hydrogen atoms were merged using MGLTools.

2.16.4. Capsid Ligand Docking

QuickVina-W [26] was used for docking the polyphenolic compounds, with a grid center of (0, 0, 0) and grid dimensions as defined in Table 1. The runs were performed at an exhaustiveness of 1000 with 24 cores per job, using GNU Parallel [27] at the Centre for High-Performance Computing (CHPC). A maximum of 20 top ligand binding poses were retained in each case run.

2.16.5. Analysis of Docking Results

The Arpeggio tool [28] was then used to estimate the protein–ligand interactions around a subset of the complex trimmed at a maximum radius of 14 Å around the ligand atoms. An in-house Python script (without any external library dependency) was used to extract this subset, retaining the chain label and segment ID. Hydrogen bonding, hydrophobic interactions and the binding energy scores were then used to characterize ligand binding. The distributions of these measurements across the entire docking experiment were arranged according to the strains and the detected binding sites. In order to differentiate the binding sites from existing ones, both the canonical hydrophobic pocket [24] and the VP1-VP3 druggable interprotomer pocket (the Butcher Neyts' pocket) from Abdelnabi and co-workers [25] were carefully mapped on all 3D structures, as their compositions and locations were not identical in each strain. In the case of the hydrophobic pocket, the PyVOL plugin [29] in PyMOL was used, specifying VP1 as the search space and a minimal pocket volume of 400 Å, in addition to the default parameters. The minimum volume had been determined beforehand using the palmitic acid-contacting residues (any protein atom within 4 Å of each ligand atom) from a 3D structure of the CVB3 Woodruff strain (PDB ID: 1COV) [30] to guide the cavity search. In the case of the interprotomer pocket, the PROMALS3D web server [31] was used to align the VP1 sequences and correct for any misaligned residue positions using 3D structural information. The ligand-interacting residues (binding the benzene sulfonamide derivative) from CVB3 (6GZV) identified by PDB were used as a reference in a sequence alignment with the CVA9 (1D4M) strain to obtain homologous positions for the latter [32]. No correction was needed for VP3 residues of the interprotomer surface, as the alignment contained no gaps. Unless specified otherwise, residues have been numbered according to the respective crystal structures.

2.17. Statistical Analysis

Statistical analysis was performed using GraphPad Prism 6 (GraphPad Software, San Diego, CA, USA). Data are presented as mean ± standard error (SEM). The 50% effective concentrations (EC_{50}) and 50% cytotoxic concentrations (CC_{50}) were calculated by regression analysis of the dose–response curves generated from the experimental data using the software. Statistical significance was calculated by performing one-way/two-way ANOVA followed by the Bonferroni test (* $p < 0.05$, ** $p < 0.01$, *** $p < 0.001$ and **** $p < 0.0001$).

3. Results

3.1. Epigallocatechin Gallate and Resveratrol Show Antiviral Activity on Enteroviruses

To evaluate whether selected polyphenolic compounds have antiviral effects on the chosen human enteroviruses (CVB1, CVB3, CVA9), we performed a cytopathic effect (CPE) inhibition assay on A549 cells. A high amount of CVB1 virus (10^7 PFU/mL) was pre-treated with 10-fold serial dilutions of each compound for 1 h at 37 °C before adding to cells. Untreated virus and mock infection were used as positive and negative controls in the assay, respectively. The CPE analysis showed that Epigallocatechin gallate (EGCG) and Resveratrol (RES) as free molecules have a potent inhibitory effect on virus infection (Figure 1A,B). At a concentration of 6.5 µM of EGCG (Figure 1A, left) and 880 µM of RES (Figure 1B, left), CVB1 was efficiently inhibited. A significant toxicity could not be detected for any of the tested concentrations of the compounds (Figure 1A,B, right).

Next, we tested EGCG and RES bound to gold nanoparticles (Figure 1A,B, middle). The functionalized gold with EGCG or RES both showed antiviral activity. Nevertheless, RES-AuNPs were more efficient in inhibiting CVB1 infection than EGCG-AuNPs (RES ligand concentration 3.44×10^{-1} µM versus EGCG ligand concentration 5.61×10^{-1} µM). However, the necessary concentrations of ligand bound to AuNPs needed for virus inactivation were several orders of magnitude lower than the free polyphenols.

TEM images showed that the RES particles were smaller than the EGCG-AuNPs (Figure 1C, left). Automated determination of average core diameter from TEM images using BioImageXD software resulted in 131.5 ± 7.1 and 78.6 ± 2.3 nm for EGCG-AuNP and RES-AuNP, respectively. DLS analysis of the nanoparticles showed similar diameters as the TEM images, indicating that only one layer of polyphenol was attached. The zeta potential of the nanoparticles was −35 and −40 mV for the RES-AuNPs and the EGCG-AuNPs, respectively. The determination of gold content by ICP-MS showed a 3-fold higher concentration of gold for RES-AuNPs as compared to EGCG-AuNPs (Figure 1C).

We calculated the number of polyphenol molecules per AuNPs considering the nanoparticle diameter. Moreover, we assumed from the DLS versus TEM data that we have only one monolayer of molecules, which are oriented parallel to the surface, as observed previously for aromatic ring systems [17], and approximating the area of the polyphenol molecules from their molecule length and width, as measured by the Avogadro software. The calculations resulted in 47,239 EGCG molecules per AuNP and 19,122 RES molecules per AuNP. By considering the concentration of gold determined by ICP-MS and the diameter of the AuNP from TEM, the concentration of ligands was calculated to be 5.61 µM for EGCG and 34.4 µM for RES (see detailed calculations in the Supplementary Materials). The calculated ligand concentrations were confirmed by an indirect quantitative analysis. For this analysis, EGCG and RES ligands present on the AuNP surface were replaced by an exchange with cysteine. The thiol group of cysteine has a stronger, quasi-covalent binding affinity to gold than the polyphenols. After incubation of EGCG-AuNP or RES-AuNP with a solution of cysteine, the remaining free thiol groups were determined photometrically using a colorimetric reaction with Ellman reagent. A 1:1 ratio of cysteine to polyphenol was assumed. The concentration of EGCG and RES determined by the Ellman test was 5.5 ± 0.1 µM for EGCG and 42.9 ± 1.1 µM for RES, respectively. In the following assays, we have used the calculated concentration.

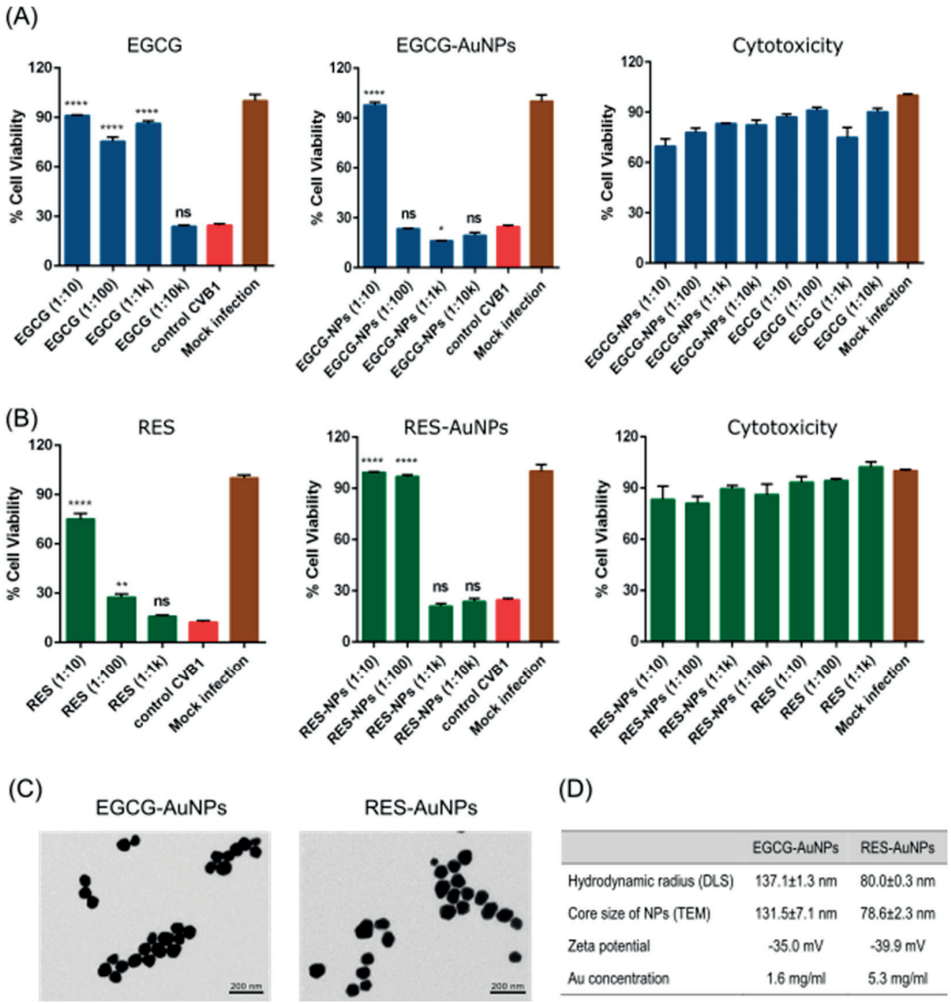

Figure 1. Polyphenols and polyphenol-functionalized nanoparticles block virus infection. (**A**) Epigallocatechin gallate (EGCG) and (**B**) Resveratrol (RES) and polyphenol-functionalized nanoparticles (AuNPs) were screened against CVB1 using the CPE inhibition assay to evaluate infection and cytotoxicity of the polyphenolic compounds. The test samples and the virus control are normalized against the mock infection. N = 3 replicates for each dilution of the samples tested. Average values + standard error of the mean (SEM) are shown. * $p < 0.05$, ** $p < 0.01$and **** $p < 0.0001$ versus the virus control (analyzed using the one-way ANOVA with Bonferroni tests). (**C**) Transmission electron microscopy images of EGCG-AuNPs and RES-AuNPs. (**D**) Physico-chemical characteristics of the polyphenol-functionalized AuNPs. The mean core size of the nanoparticles was calculated using the BioImage XD software by processing TEM images containing 684 (EGGC-AuNPs) and 2411 (RES-AuNPs) nanoparticles, respectively. The results of the TEM and DLS are expressed as average values ± standard error of the mean (SEM). Hydrodynamic size and zeta potential were evaluated from three separate readings using a Malvern Zetasizer. Au concentration was obtained using ICP-MS. Scale bars = 200 nm.

3.1.1. Detailed Antiviral Efficacy Studies

Once the preliminary screening results confirmed the antiviral activity of the polyphenols and the polyphenol-functionalized nanoparticles for CVB1, the antiviral efficacy on different enteroviruses was calculated as 50% effective concentrations (EC_{50}) by regression analysis from their dose–response curves. The antiviral studies were performed using the CPE inhibition assay, where we incubated the compounds with high amounts of CVB3 (2×10^7 PFU/mL) for 1 h at 37 °C. As shown in Figure 2A and Table 2, both polyphenols

and the corresponding nanoparticles protected the A549 cells from CVB3 infection in a dose-dependent manner. The EC_{50} value for EGCG was 3.411 μM, 32 times more effective than RES (107.894 μM). Interestingly, the ligands bound to AuNPs (0.051 μM for EGCG and 0.004 μM for RES) were 67 or 26,974 times more potent than the free polyphenols, respectively. The RES-AuNPs were in this case 13 times more potent than EGCG-AuNPs against CVB3 infection.

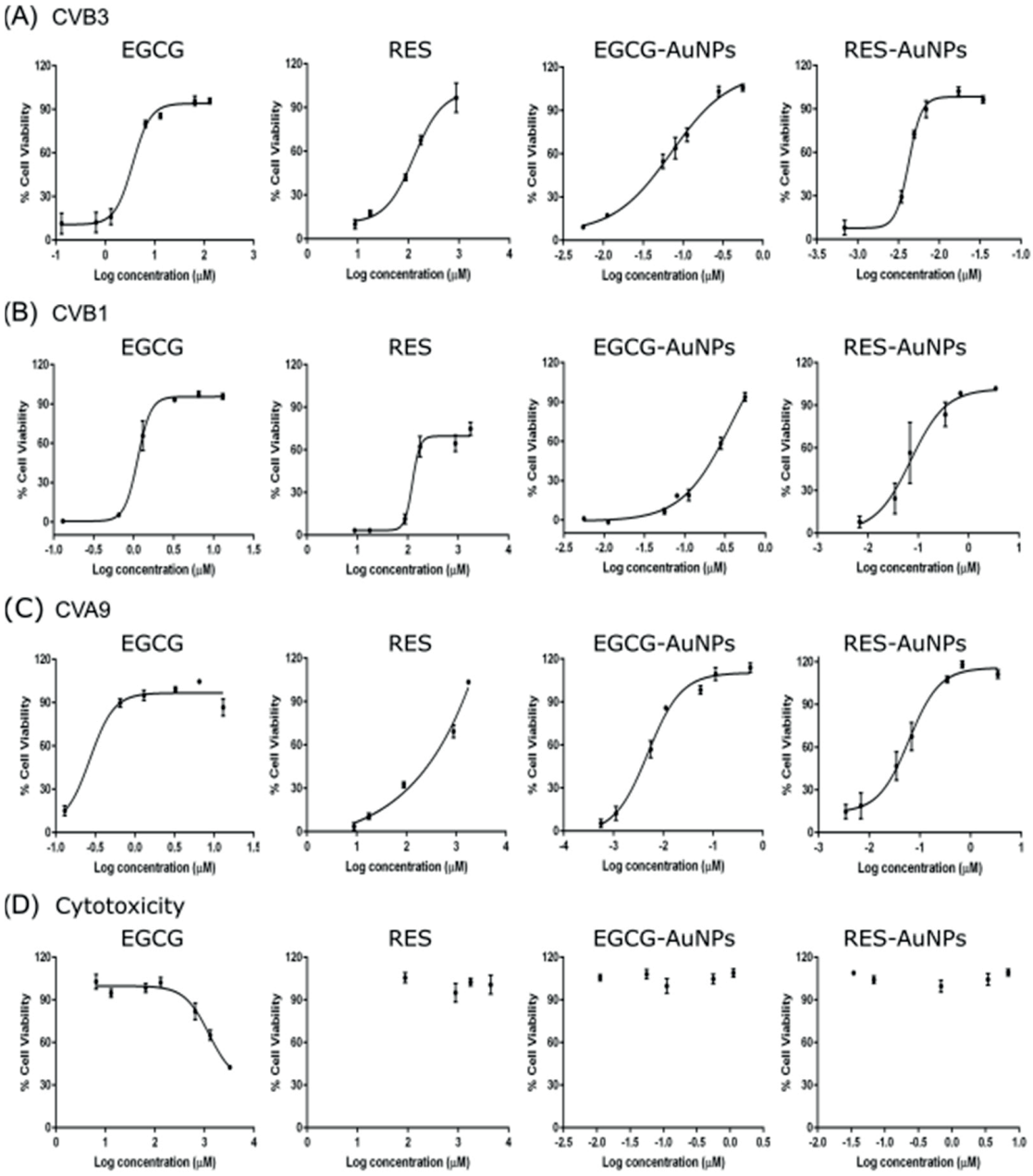

Figure 2. Dose–response curves for studying the antiviral efficacy of Epigallocatechin gallate (EGCG) and Resveratrol (RES) and polyphenol-functionalized nanoparticles (AuNPs), against (**A**) CVB3, (**B**) CVB1 and (**C**) CVA9 and their (**D**) cytotoxicity, using the CPE inhibition assay. Drug concentration of the compounds are shown as Log (10) of μM on the *x*-axis. The results are mean of two independent experiments and are expressed as average values ± standard error of the mean (SEM).

Table 2. Antiviral activity and cytotoxicity of polyphenols and polyphenol-functionalized AuNPs.

Virus	Compounds	EC_{50} (μM)	Fold Improvement	CC_{50} (μM)	SI
CVB3	NP-EGCG	0.051	67	>1.122	>22.000
	EGCG	3.411		2218.196	650.306
	NP-Res	0.004	26,974	>6.880	>1720.000
	Res	107.894		>4400.000	>40.780
CVB1	NP-EGCG	0.237	5	>1.122	>4.734
	EGCG	1.140		2218.196	1945.785
	NP-Res	0.068	2101	>6.880	>101.176
	Res	142.889		>4400.000	>30.793
CVA9	NP-EGCG	0.004	67	>1.122	>280.500
	EGCG	0.266		2218.196	8339.082
	NP-Res	0.039	8471	>6.880	>176.410
	Res	330.369		>4400.000	>13.318

EC_{50}—50% effective concentration, CC_{50}—50% cytotoxic concentration, SI—selectivity index.

We also tested the compounds for inhibition of other enteroviruses, using highly concentrated CVB1 (2×10^7 PFU/mL) and CVA9 (2×10^8 PFU/mL) enteroviruses. Figure 2B,C and Table 2 show that EGCG is 3 and 13 times more effective for CVB1 and CVA9 respectively, than for CVB3. In general, the RES ligand was less effective compared to the EGCG ligand. The results also show that the ligands have better efficacy when functionalized on the gold nanoparticle for RES. Depending on the virus and the ligand, there was a 5- to 26,974-fold improvement in efficacy (Table 2). Usually, the improvement in efficacy was better for RES than for EGCG. This can be due to an increased solubility of RES when bound on nanoparticles.

Since the polyphenols and functionalized AuNPs both exhibited potent antiviral activity, we tested if the inhibitory effect was due to bound ligands and not due to free ligands present in the solution. This was confirmed by pelleting the functionalized AuNPs by ultracentrifugation and testing the pellet for the antiviral activity. The antiviral activity of the NP solution was similar to the activity in the resuspended pellet of AuNPs, confirming that antiviral efficacy was not related to detached ligands (Supplementary Figure S1).

Detailed cytotoxicity studies using the CPE inhibition assay on uninfected cells were repeated under the same conditions as used for the antiviral studies (Figure 2D). Mock infection, having no virus or compounds, was used as a control for the assay. As shown in Figure 2D, none of the compounds reduced the viability of A549 cells at the effective antiviral concentrations, thus verifying the antiviral potential of the compounds. The 50% cytotoxic concentrations (CC_{50}) calculated by regression analysis from the dose–response curves are shown in Table 2. The results showed no toxicity for RES or for both AuNPs, while for EGCG, we detected toxicity at a very high concentration (CC_{50}: 2.218 mM). Thus, the selectivity index (SI) deduced from the ratio of CC_{50}/EC_{50} is incalculable for compounds other than EGCG. For EGCG, the SI values are very high for all tested viruses (Table 2). Based on the high (or incalculable) SI values, it can be said that these compounds effectively protect the A549 cells from the tested enterovirus infections with no toxicity.

3.1.2. EGCG and RES Show Long-Term Antiviral Efficacy at Different Temperatures

To investigate the antiviral efficacy of the polyphenols further, we performed antiviral tests for the functionalized AuNPs at different temperatures and different periods of incubation (Figure 3A). First, the functionalized AuNPs were pre-incubated with the virus at 8, 21 and 37 °C. Untreated viruses in PBS-$MgCl_2$ buffer incubated at the same temperatures were used as an experimental control. Virus infectivity was measured after incubating the polyphenols with viruses for 6, 24, 48 and 72 h using the CPE assay. The results showed that the observed effective concentrations of EGCG-AuNPs (ligand concentration 5.61×10^{-1} μM) and RES-AuNPs (ligand concentration 3.44 μM) inhibited infection at the tested temperatures, at least for the whole period for which the untreated

virus was showing infectivity. Namely, in the control experiment with the untreated virus, it was observed that the virus infectivity was decreasing with time, more quickly at higher temperatures, as expected.

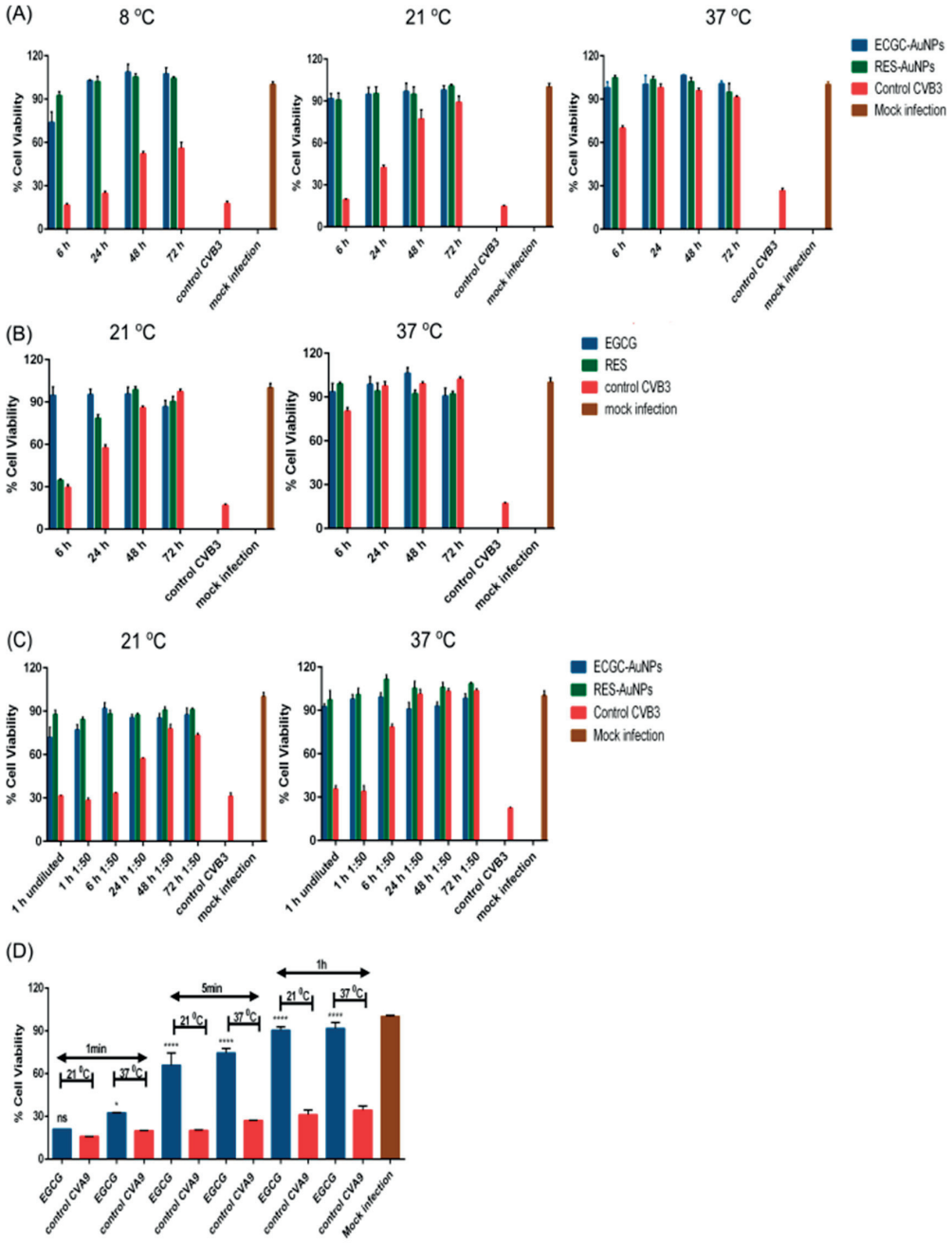

Figure 3. Effect of time and temperature (**A**,**B**,**D**) and dilution (**C**) on antiviral activity of polyphenols and polyphenol-functionalized nanoparticles (AuNPs). (**A**,**B**) EGCG-AuNPs (ligand concentration 5.61×10^{-1} μM), RES-AuNPs (ligand concentration 3.44 μM), EGCG (650 μM) and RES (880 μM) were incubated with CVB3 (4.4×10^{8} PFU/mL) at different temperatures over 72 h. Sample fractions were collected at 6, 24, 48 and 72 h and a CPE was performed from them.

(**C**) The effect of dilution on the antiviral activity of polyphenol-functionalized nanoparticles (AuNPs) after an initial preincubation of 1 h between CVB3 (4.4×10^8 PFU/mL) with EGCG-AuNPs (ligand concentration 5.61×10^{-1} μM) and RES-AuNPs (ligand concentration 3.44 μM). (**D**) EGCG (6.5 μM) and CVA9 (2×10^7 PFU/mL) were incubated at different time intervals (1 min, 5 min and 1 h) and at different temperatures (21 and 37 °C). Results (**A**–**D**) are expressed as the number of viable cells left, detected by crystal violet staining. Every experiment had an experimental virus control that was used to assess the infectivity of the virus at each point and a mock infection showing the status of viable cells. Experiments 3A and 3B were performed twice with $n = 3$, and experiments 3C and 3D were performed once, with $n = 3$ and $n = 2$, respectively. The results are expressed as average values + standard error of the mean (SEM). Experiments 3A, 3B and 3C were analyzed by two-way ANOVA and 3D by one-way ANOVA, followed by the Bonferroni test (* $p < 0.05$, and **** $p < 0.0001$).

The experiments were repeated with the ligands at 21 and 37 °C (Figure 3B). The results were similar to those with AuNPs. Interestingly, RES could not rescue cells from infection before 6 h at 21 °C, but was already quite effective after 24 h. We then tested whether the antiviral efficacy was lost if the solution was diluted after the initial incubation with the virus (Figure 3C). The hypothesis was that strong dilution may disconnect the virus and ligand or ligand-NP and lead to a re-established infectivity. After 1 h of incubation of the virus with functionalized AuNPs at 37 and 21 °C, we diluted the solution 50 times and continued the incubation. Samples were collected from diluted solutions at different time points (1, 6, 24, 48 and 72 h) and tested for infectivity on A549 cells. The CPE analysis of diluted and control virus samples (normalized to contain comparable amounts of virus) showed that the 50-times diluted samples maintained the antiviral activity very well, and similarly to undiluted samples (Figure 3C). Similar results were observed with EGCG and RES without AuNPs even when diluted (data not shown).

We also wanted to understand the effectiveness of polyphenols at shorter incubation time intervals at 21 and 37 °C (Figure 3D). The results showed that already, 1 min of incubation slightly increased the cell viability, as indicated by reduced lytic viral activity. This effect was more apparent at 37 °C. After 5 min of incubation, cell viability increased strongly at both temperatures, and 1 h of incubation already showed full protection. These results thus confirm that the polyphenols show good antiviral efficacy at various temperatures and after a short contact time.

3.2. Mechanism of Action

To understand if the compounds acted as inhibitors for virus attachment or in other steps of infection, we performed a simple time of addition study. In the assay, cells were first infected with CVB3 for 1 h at 37 °C and then the compounds were added, followed by overnight incubation. As shown in Figure 4A, polyphenols did not exhibit any antiviral activity when added 1 h post-infection (p.i.). This excludes antiviral action on intracellular processes.

Three possible mechanisms of pre-entry action were studied: (1) the polyphenols and polyphenol-functionalized nanoparticles stabilize the virus and prevent its opening (and release of genome), (2) the compounds prevent binding of the virions to the cell surface and (3) the capsid is disrupted or damaged by the polyphenols, and thus, the genome is prematurely released from the virions.

A potential increase in capsid stability of the virions was tested in a thermal stability assay, PaSTRy [15,22]. In the assay, gradual heating of the virus up to 90 °C induces the uncoating and release of the viral RNA to the solution, typically between 40 and 50 °C for enteroviruses [22]. Non-fluorescent SGII in the medium intercalates within the double-stranded regions in the viral RNA and emits fluorescence upon binding [33]. Increase in capsid stability would lead to a higher melting temperature, whereas lower melting temperature would suggest destabilization.

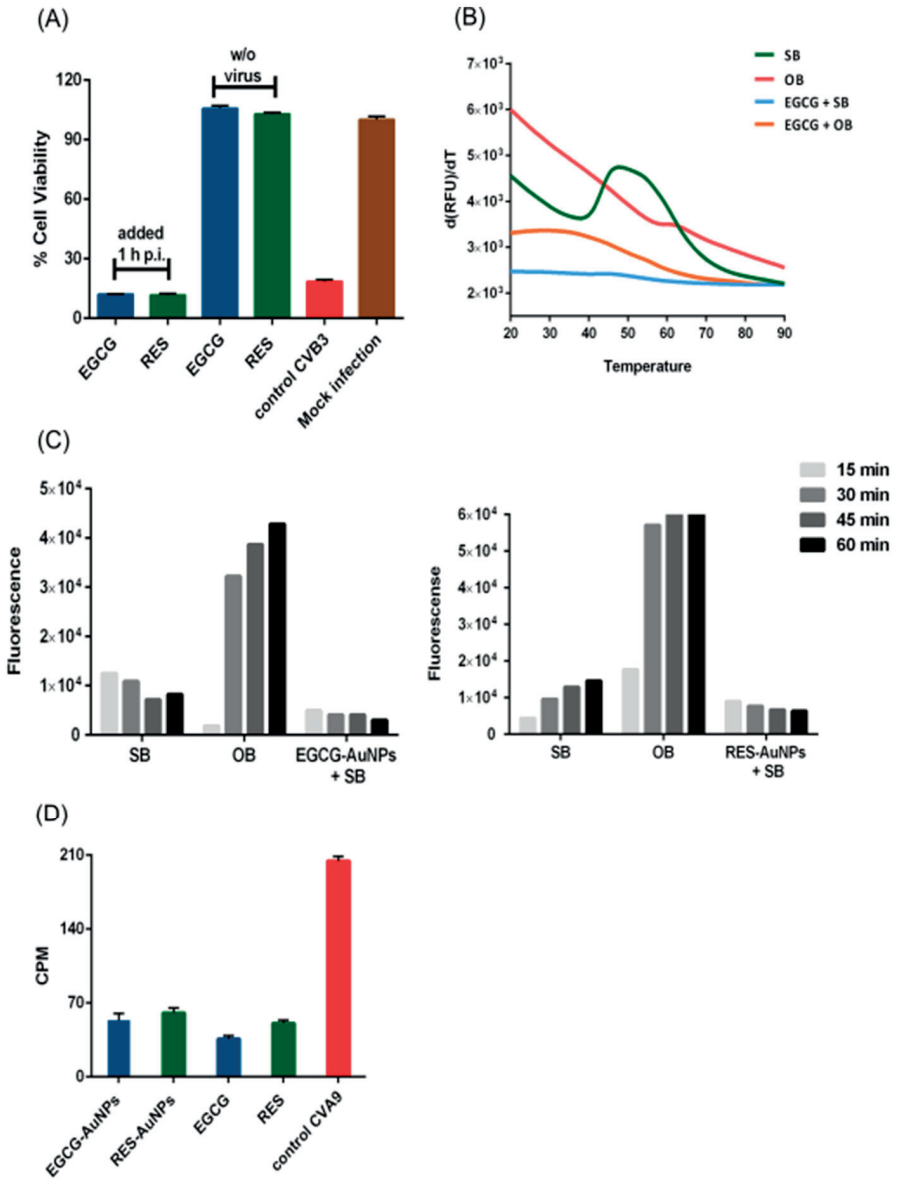

Figure 4. Studies on mechanism of antiviral activity of polyphenols and polyphenol-conjugated nanoparticles (AuNPs). (**A**) Time of addition assay, where the polyphenols EGCG (65 μM) and RES (880 μM) were added to cells 1 h post-infection. The results are the mean of two independent experiments, with $n = 5$. Average values + standard errors of the mean (SEM) are shown. (**B**) The PaSTRy assay measures the thermal stability of CVB3 (0.5 μg) in the presence of the EGCG (65 μM). The tests were performed in the presence of the storage buffer (SB; PBS with 2 mM $MgCl_2$) and opening buffer (OB; 20 mM NaCl, 6 mM KH_2PO_4, 12 mM K_2HPO_4 and 0.01% faf-BSA), depicted as blue and orange color, respectively. This is a representative result from three experiments, with $n = 3$. (**C**) The Uncoating assay shows that EGCG-AuNPs and RES-AuNPs lower the release of the viral RNA from virions and prevent expansion of the virions. The assay is based on real-time fluorescence spectroscopy, which detects high fluorescence of SGII when it is bound to the viral genome, either free RNA released from the virions or virion-bound RNA when SGII can enter an expanded virus.

Here, CVB3 (0.5 µg) was incubated with SB or OB as controls or with SB in the presence of EGCG-AuNPs (ligand concentration 5.61×10^{-2} µM; left graph) or RES-AuNPs (ligand concentration 3.44×10^{-1} µM; right graph). The fluorescence values have been subtracted with the measurement of RNAse in the assay, and the difference between the calculations, which is the net release of RNA, has been plotted in the graphs. Both the graphs are a representative result from three experiments. (**D**) The binding assay measures the binding of metabolically radio-labeled virus onto the cells in the presence of compounds on ice. Control CVA9 is the binding measured from the virus without polyphenols. Average values of radioactivity (CPM, counts per minute) + standard error of the mean (SEM) are shown from one representative experiment that was performed twice with similar results, with $n = 3$.

Untreated CVB3 in a storage buffer (PBS $MgCl_2$) had a transition temperature of 42 °C (Figure 4B), while in an opening buffer, the fluorescence was maximal already without heating [16,21]. The opening buffer promotes virus opening by releasing the pocket factor with a combination of albumin and low sodium/high potassium content. When 0.5 µg of CVB3 was pre-incubated with a concentration of 65 µM EGCG, strikingly, low fluorescence was recorded and no transition could be observed in the tested temperature range, probably because EGCG stabilized the virion and prevents genome release (Figure 4B). If the opening buffer was added to the EGCG-treated virus, the initial fluorescence was higher but still lower than in the absence of EGCG and, again, no significant transition was observed during the heating.

To study the mechanism of this unexpected stabilization in detail, we used our previously developed real-time spectroscopy uncoating assay, which can detect the viral genome at various stages of uncoating in vitro at physiological temperature, 37 °C. This assay relies on the fact that SGII is able to bind to the virus RNA inside the expanded capsid and outside the broken capsid, but the dye is excluded from the intact capsid [16,21]. Thus, this approach enables us to detect the expanded, primed state and the fully opened state of the virus, while the intact virus would show no fluorescence. For this assay, CVB3, polyphenol-functionalized nanoparticles and SGII were mixed in a buffer, and the fluorescence was measured. The control virus in the storage buffer revealed a low background fluorescence that did not change much during the 1 h experiment at 37 °C, suggesting that the virus is relatively stable at 37 °C in this buffer (Figure 4C), as expected from earlier studies [16]. The assay includes a subsequent addition of RNAse to the samples that degrades the released RNA. The RNase molecule is too large (72 kDa) to enter the primed virus particles and digest the viral genome, hence allowing to distinguish fully open capsids from partially damaged ones. SGII is small enough (0.45 kDa) to enter, bind to the genome and emit fluorescence [15]. The values after RNAse addition were subtracted from the fluorescence values without RNAse, thus providing the net RNA released from the viruses in the assay. The presence of EGCG-AuNPs or RES-AuNPs caused an even lower overall fluorescence compared to the control virus sample in this assay, suggesting that the functionalized AuNPs prevented expansion that normally occurs to some extent in the storage buffer at 37 °C. The fluorescence did not change with time, confirming that the functionalized AuNPs prevented opening and RNA release. The results were similar if the free polyphenols were added instead of polyphenol-functionalized AuNPs (data not shown).

To test whether the presence of ligands also prevents binding of the virus to the surface receptors of A549 cells, we performed a binding assay using a metabolically radiolabeled virus. Radioactive ^{35}SMet/Cys-CVA9 was first incubated with the compounds for 1 h, followed by binding them to A549 cells for another 1 h on ice, and continuing by thorough washings. Measurement of the radioactivity from the virus bound to the cell surface in the presence of the compounds revealed that both the ligands and the functionalized nanoparticles drastically reduced binding of the virus to the cell surface (Figure 4D). The results altogether suggest that the EGCG, RES and their functionalized AuNPs interact directly with the capsid, stabilize it strongly and hence prevent the infection by both preventing uncoating and receptor binding.

Polyphenols Cause Clustering and Aggregation of the Enteroviruses

With a sucrose gradient, viruses can be separated into intact, empty and expanded/intermediate particles [15,16]. Such a separation was performed with the radioactive ^{35}SMet/Cys-CVA9, pre-incubated with EGCG or RES for 1 h at 37 °C (Figure 5A). Fresh virus control without the polyphenols and without preliminary incubation at 37 °C showed a typical single peak of intact viruses covering about 4–5 fractions in the bottom part of the gradient. Incubation of the control virus in the storage buffer for 1 h at 37 °C showed no significant difference to the fresh virus. Only a small peak broadening can be observed due to the presence of some expanded virions [15]. Strikingly, when the virus was treated with the polyphenols, there was a complete loss of radioactivity. We assume that the clustering of the virus induced by the polyphenols led to aggregates, which precipitated or adhered to the walls of the tubes. Myllynen et al. [15] observed a similar loss of radioactivity when vulnerable virus preparations were aggregated during fractionation in a $CsCl_2$ gradient.

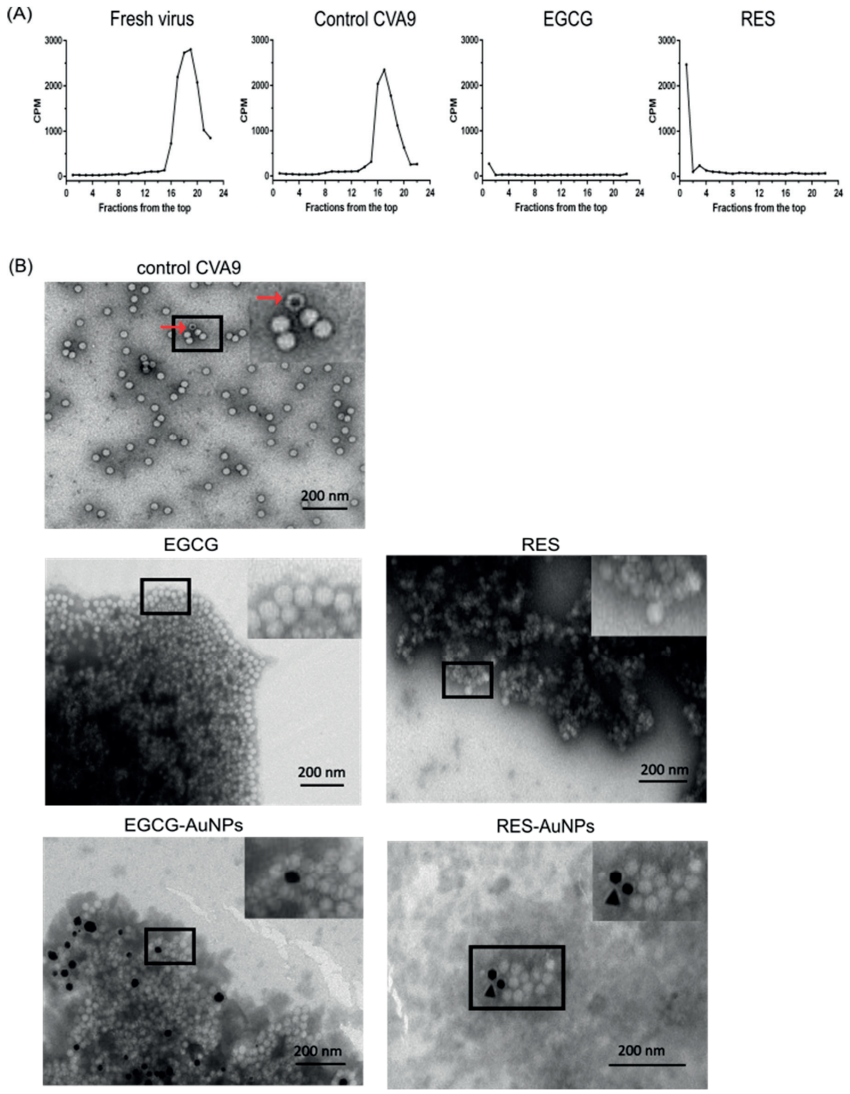

Figure 5. *Cont.*

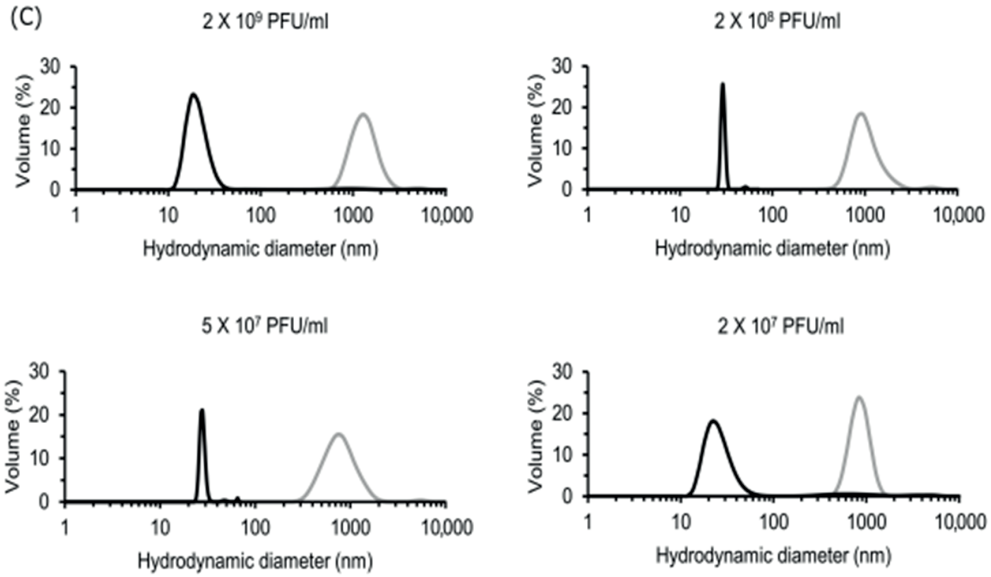

Figure 5. Aggregation/clustering of enteroviruses identified using (**A**) sucrose gradient (5–20%) separation of the metabolically radiolabeled CVA9 after incubation with the polyphenols for 1 h at 37 °C, and (**B**) negatively stained TEM images of CVA9 (1.6×10^{10} PFU/mL) and CVA9 treated with EGCG (650 μM), RES (880 μM), EGCG-AuNPs (ligand concentration 5.61×10^{-1} μM) and RES-AuNPs (ligand concentration 3.44 μM). Scale bar, 200 nm. The viral particles with a dark inner center (marked with a red arrow in the control CVA9 TEM image) can be easily differentiated as empty/broken virus capsids. (**C**) Dynamic light scattering analysis of EGCG (6.5 μM) with different dilutions of CVA9.

To test our hypothesis, we pretreated the virus with polyphenols or polyphenol-functionalized AuNPs for 1 h and then visualized them under the transmission electron microscope. Figure 5B shows negatively stained control viruses and viruses treated with polyphenols and polyphenol-functionalized AuNPs. Control viruses mostly showed single viruses distributed homogenously over the grid. Intact virus particles have the stain around the capsid and have a bright center, whereas those that are expanded, or broken/empty allow the stain to enter the capsid and have a darker appearance or dark center, respectively (some empty virions are indicated in Figure 5B). In the presence of the polyphenols or polyphenol-functionalized AuNPs, virus particles appeared only in large aggregates. Interestingly, the viruses inside the aggregates seemed to be intact, and empty virus particles were rarely seen. However, some uneven coloring of the virions was observed. These results confirmed that, in addition to stabilization of the particles, the polyphenols cause clustering of the viruses.

To observe the clustering of the viruses in a more robust way in solution, we performed DLS after EGCG treatment. We detected the virus in DLS with a hydrodynamic diameter of ~22 nm, which is a little lower than expected for CVA9 (Figure 5C). However, this peak could be detected in a very reproducible manner, and we observed only a few aggregates in the virus samples by DLS. After treating the virus samples with EGCG, the virus-associated peak completely disappeared, and particles were detected only in the size range of 650–1240 nm, further confirming that, indeed, polyphenols cause aggregation of the enteroviruses. The virus was then diluted using 10-fold dilutions while keeping the EGCG concentration constant. The aggregates appeared upon every dilution, indicating that a high concentration of viruses was not a prerequisite for aggregate forming. A similar size distribution was observed in all tested dilutions.

We also studied if the clustering with a lower titer of the virus would still cause a similar drop of infectivity. We did this by drastically reducing the CVB3 concentration to 2×10^5 PFU/mL, which is 100 times less than in the previous experiment (Supplementary Figure S2). Despite the dilution of 100 times, we observed an efficient antiviral effect.

3.3. Discovery of Multiple Ligand Binding Sites on the Surface of CVA9 and CVB3

The docking poses were visualized from the 2-fold (Figure 6) and 3-fold (Figure 7) axes of symmetry, respectively. From the PyVOL calculations, the hydrophobic pockets (HPs) were visibly smaller in CVB3 (subfigures B and D from Figures 1 and 2) compared to CVA9 (subfigures A and C from Figures 6 and 7). More specifically, in CVB3, the buried HP site was found to be composed of VP1 residue positions 93, 95, 190–194, 205–212 and 258–261 (residue numbering according to 6GZV). The analogous pocket in CVA9, however, consisted of residues 95–98, 115, 117, 144, 146, 170, 181, 183, 186–188, 192, 193, 210, 212–216 and 219 in CVA9 (residue numbering according to 1D4M). Abdelnabi and co-workers' work describes the Butcher-Neyts pocket that comprise VP1 residue positions 73, 76, 77, 78, 234 and 236, and VP3 residue positions 234–236 in CVB3 [25]. While CVA9 and CVB3 shared identical residue loci for the VP3 component of the Butcher-Neyts pocket, CVB3 had VP1 mutations M76F and E77T and VP3 mutations D234Q and K236F (using CVA9 as a reference). EGCG was the only compound found to bind the Butcher-Neyts pocket in CVA9, albeit with dissimilar contact residues, consisting of D158, D159, Y160, W162, Q163 and R222 from VP1, and the VP3 residues Q233, D234, N235 and R237 (Figure 7A). In our experimental set-up, the Butcher-Neyts pocket was more completely exposed within the docking grid box covering the 3-fold axis protomers, which explains the absence of bound ligands within the grids designed for the 2-fold axis of symmetry.

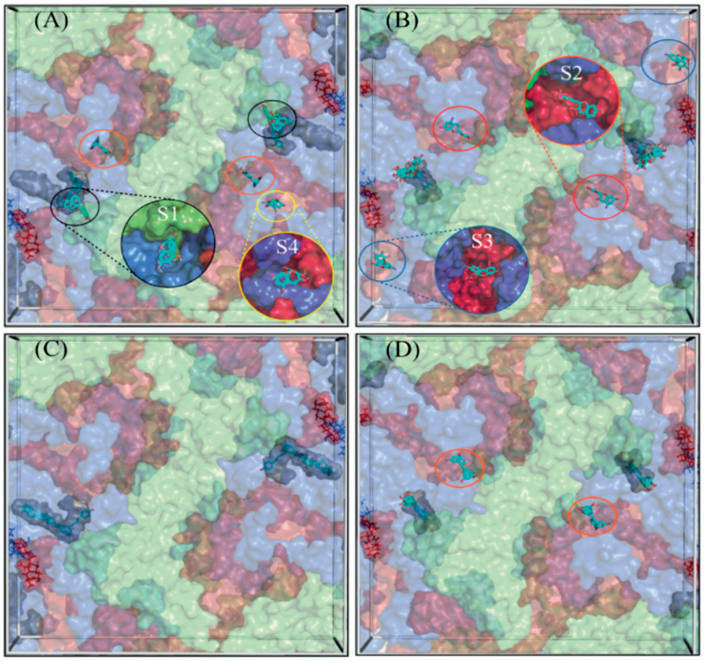

Figure 6. Docking grid boxes centered at the 2-fold axis, for EGCG (top subfigures) and RES (bottom subfigures). CVA9 is on the left (**A**,**C**) while CVB3 is on the right (**B**,**D**). The hydrophobic pocket is represented as a grey surface, while the residues for the Butcher-Neyts pocket are represented as lines. Capsid proteins VP1–VP3 are colored blue, light green and red, respectively. VP4 is not shown. Docked poses are represented as sticks. The binding sites S1, S2 and S3 are colored black, red and blue. Tentative site S4 is in circled in yellow. The additional binding site (S4) was found using EGCG (Figure 1A, circled in yellow) in CVA9 only. There is less statistical support for this site, as only one ligand pose was found in this region. However, with a favorable binding energy (−7 kcal/mol) and an estimated six hydrogen bonds, it cannot be completely ignored. The binding surface for the potential S4 site comprises VP1 residues T274, R275, K276, T280, V281, T282, T283 and V284, and VP3 residues N57, Q59, R86, D92, S93 and V94. As these residues are recorded only from one observation, it is not a consensus for S4.

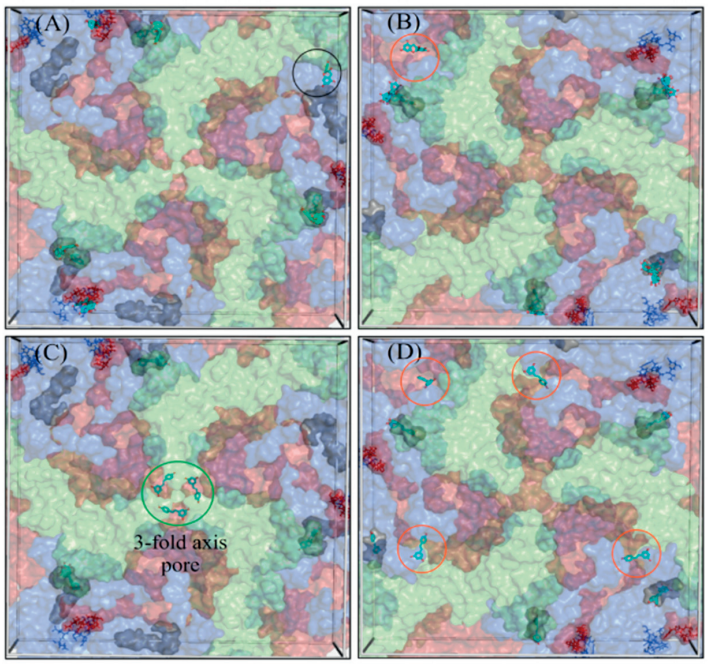

Figure 7. Docking grid boxes centered at the 2-fold axis, for EGCG (top subfigures) and RES (bottom subfigures). CVA9 is on the left (**A**,**C**) while CVB3 is on the right (**B**,**D**). The hydrophobic pocket is represented as a grey surface, while the residues for the Butcher-Neyts pocket are represented as lines. Capsid proteins VP1–VP3 are colored blue, light green and red, respectively. VP4 is not shown. Docked poses are represented as sticks. The binding sites S1, S2 and S3 are colored black, red and blue. Tentative site S4 is in circled in yellow. The additional binding site (S4) was found using EGCG (Figure 1A, circled in yellow) in CVA9 only. There is less statistical support for this site, as only one ligand pose was found in this region. However, with a favorable binding energy (−7 kcal/mol) and an estimated six hydrogen bonds, it cannot be completely ignored. The binding surface for the potential S4 site comprises VP1 residues T274, R275, K276, T280, V281, T282, T283 and V284, and VP3 residues N57, Q59, R86, D92, S93 and V94. As these residues are recorded only from one observation, it is not a consensus for S4.

Four novel binding sites were found, each with the support of more than one ligand pose, and were named S1, S2, S3 and the 3-fold axis pore, based on consensus residues shared across ligand-contacting surfaces. A fifth one—tentatively named S4—had a lower level of support, as it was bound only once. S1 was detected only in CVA9 and comprised the VP1 residues Y208, G209, N211, F262, S263, V264 and D265, and VP2 residues M132, G133, G134, G138, Q139, A140 and F141, from a consensus of all 16 detected ligand poses at that site. S2 was present in both CVA9 and CVB3. In CVA9, S2 comprised VP1 residues F202 and T283, and VP3 residues R86, L87, Q88, P137, G138, A139, Q181, D182, E183, T185, S186, A187, G188 and Y189, and was derived from two poses. In CVB3, S2 is composed of VP1 residue F199 and VP3 residues P86, G140, A186, G187, G188 and F189, obtained from a consensus of residue contacts derived from 12 ligand poses. The 3-fold axis pore was detected in the CVA9 capsid only in the case of RES (Figure 8). Its consensus ligand-contacting surfaces (derived from four poses) are composed of VP2 residues R12, E27, K116, R193 and T194, VP3 residues A124, A126, T127, I158, G159 and L160 and the VP4 residue L68 in CVA9. In the same figure, the three ligand binding sites subtending the 3-fold axis with a similar rotational symmetry provide support for an actual binding site. Upon closer inspection, these sites were found to be connected, as part of a larger cavity. Access to this hollow space in CVA9 is lined with residues such as methionine (VP3), phenylalanine

(VP2) and aspartic acid (VP3). The fact that these all have titratable side chains suggests that pH may play a role in driving the pore dynamics.

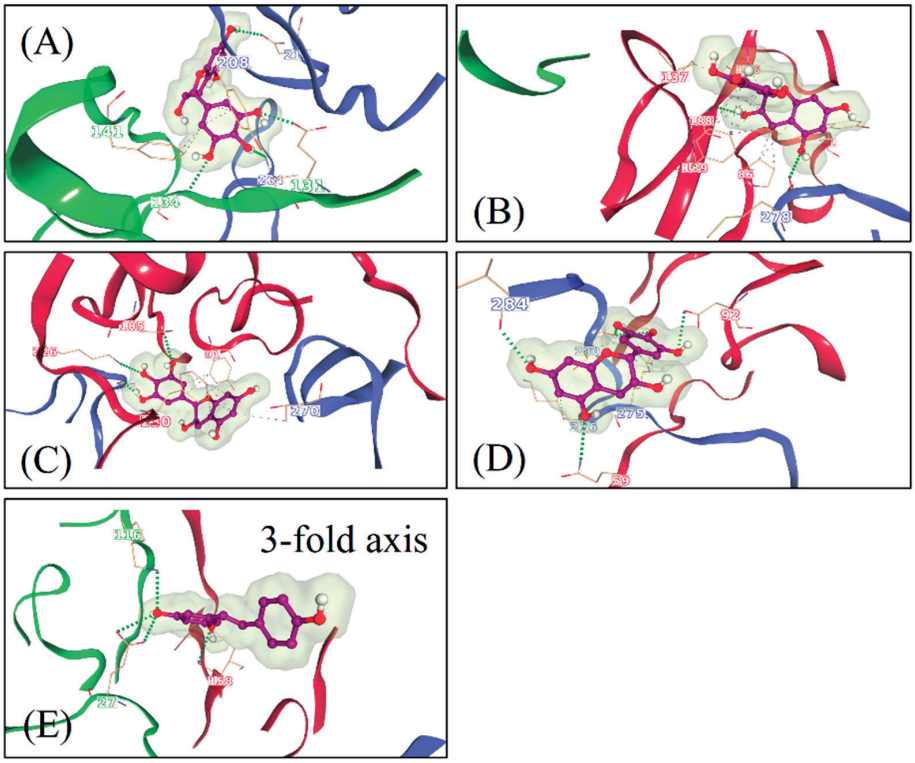

Figure 8. Protein–ligand interactions for example poses obtained at the newly determined binding sites, namely for EGCG at sites (**A**) S1 in CAV9, (**B**) S2 in CBV3, (**C**) S3 in CBV3, (**D**) S4 in CAV9 and (**E**) RES at the 3-fold axis pore in CAV9. Hydrogen bonds and hydrophobic interactions are depicted as dashed green and grey lines, respectively. Interacting residues are labeled, and the capsid proteins VP1–VP3 are colored blue, light green and red, respectively.

For a closer inspection of the non-bonded interactions occurring for RESV and EGCG, single ligand poses docked at each of the newly found sites are depicted in Figure 8. Their favorable binding energy scores and multiplicity of binding locations, combined to the formation of multiple H-bonding interactions, provide good support for the stability of these compounds for each of the Coxsackievirus strains. For instance, using the binding locations described in Figures 6 and 7, EGCG forms four H-bonding interactions involving VP1 and VP2 in CAV9 at S1, two H-bonds at S2 in CBV3 involving VP1 and VP3, three H-bonds at S3 in CBV3 involving VP1 and VP3 and five potential H-bonds at S4 in CAV9. Similarly, RES forms five potential H-bonding interactions with residues from VP2 and VP3 at the 3-fold axis pore in CAV9. While there are many more ligand binding poses from both the strains and binding sites, only one pose is shown per site, as an example.

RES and EGCG Show Differential Binding Patterns for CVA9 and CVB3

RES has fewer H-bond acceptors compared to EGCG, in addition to having a smaller size and larger hydrophobicity, as detailed in the Discussion Section. All docked poses (across ligands and strains) are summarized in Figure 9 in terms of ligand binding energies, their aggregated number of H-bonds and hydrophobic interactions at each of the six sites (S1, S2, S3, 3-fold, Butcher-Neyts pocket and HP). Our results suggest that there are both specific and shared binding sites for EGCG and RES, with strain also playing a role. Ligand binding at the sites S1 and the pore found at the 3-fold axis was only noted in CVA9. The

S1 site was bound by EGCG only with CVA9. In the case of S2, EGCG showed strain bivalence, although the calculated affinity was slightly higher in CVA9. RES also bound to S2, but only in the CVB3 strain. RES displayed slightly higher estimated affinity compared to EGCG for the same site. Binding to the S3 site was achieved only by EGCG in CVB3. Binding at the pore found at the 3-fold axis was only observed in the case of RES, only in CVA9. EGCG was found to be bound to the Butcher-Neyts pocket only in CVA9. HP was bound by both compounds in both strains. The most favorable binding energies were recorded for both EGCG and RES in the HP of CVA9, most likely due to the shape and partial charges present within the deeper hydrophobic tunnel. RES however displayed the highest affinities for the HP, which suggests more favorable binding poses due to the linear ligand shape. Both compounds performed worse in the CVB3 HP compared to CVA9, most likely due to the shallower hydrophobic pocket. The binding energies recorded at sites S1, S2, S3 and 3-fold axes are generally lower than those observed in the HP, most likely due to a decreased exposure to protein surfaces.

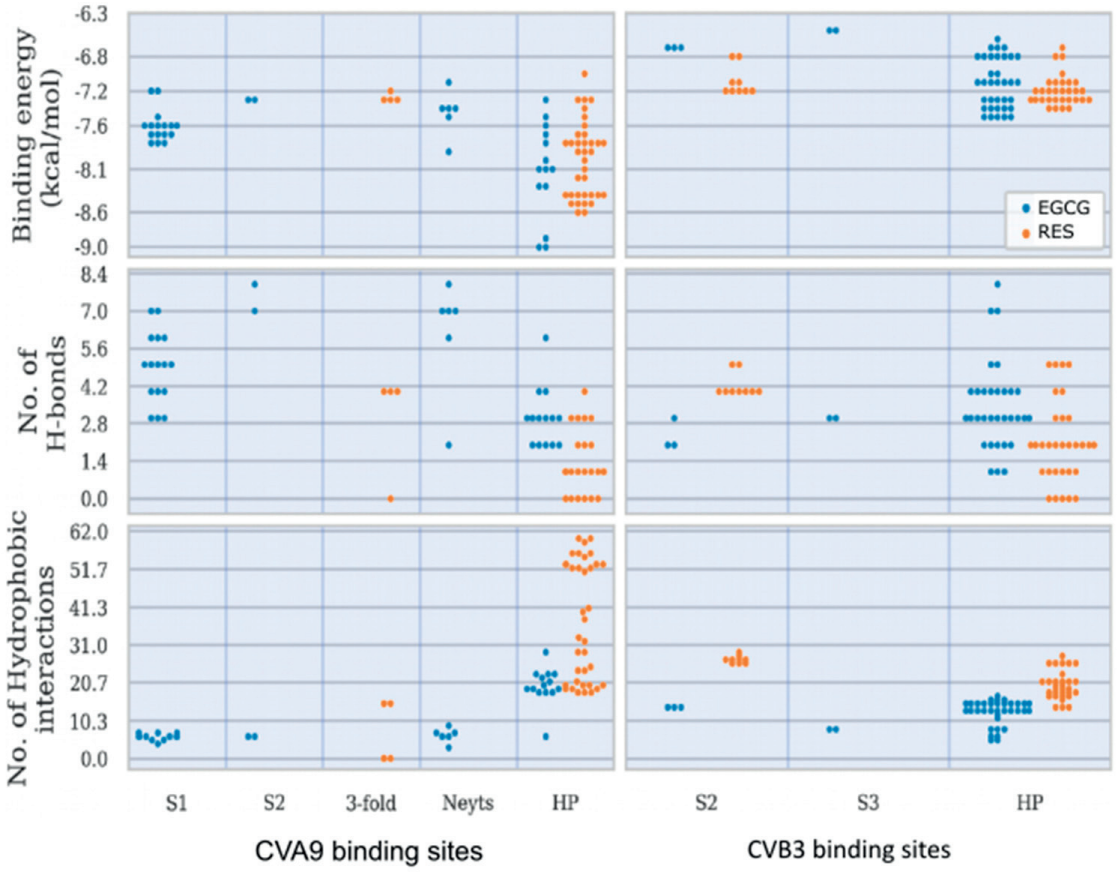

Figure 9. Summary of the binding characteristics of EGCG and RES at each of the six binding sites across CVA9 and CVB3. Each dot is an experimental unit, for which the binding energy, number of H-bonds and number of hydrophobic interactions are shown for CVA9 (left subfigures) and CVB3 (right subfigures). HP—hydrophobic pocket, Neyts—the Butcher-Neyts pocket.

Overall, EGCG bound to more sites in both CVA9 and CVB3. However, RES showed high selectivity for the hydrophobic pocket. The high number of binding sites for both compounds (compounded by the capsid symmetries) may entail a noticeable dysfunction of viral capsid behavior, especially more so in CVA9 due to the comparatively higher

number of sites and the lower binding energies for the HP region. This also explains the difference in inhibition efficacy of EGCG as compared to RES.

4. Discussion

There is a great need for broad-acting non-toxic antivirals that reduce the virus load in the body or on surfaces. Present and future pandemics as well as the yearly occurring epidemics cause high economic costs due to hospitalizations and absence from workplaces and from schools. Enteroviruses still lack a clinically accepted antiviral for treatment or disinfection of hands and surfaces. Therefore, we studied two polyphenols, EGCG from green tea and RES from red grapes and other fruits, as soluble polyphenols and polyphenol-functionalized gold nanoparticles and explored the mechanism of action for the molecules on three very stable, non-enveloped enteroviruses (CVA9, CVB1 and CVB3).

Our results showed that EGCG and RES have strong antiviral efficacy against the three enterovirus serotypes. Antiviral efficacy in general was already known for the two polyphenols before [34], but not for enteroviruses. The EC_{50} values were in the range of 0.266–3.411 μM for EGCG and 107.894–330.369 μM for RES, thus suggesting a good efficacy already at low concentrations. The CC_{50} showed no cytotoxicity. The polyphenols bound to the AuNPs showed EC_{50} values in the range of 0.004–0.237 μM for EGCG and 0.004–0.068 μM for RES.

Most antivirals target cellular replication steps of the viruses, such as promoting apoptosis and via inhibiting Nf-kB or MAPK pathways and replication [5,35,36]. Most studies on the polyphenols as antivirals for enteroviruses focus on EV71 and observe antiviral action past entry and during replication of the viruses. Our results reveal that both EGCG and Resveratrol act as entry and attachment inhibitors by binding to enterovirus surfaces. This was confirmed by the time of addition CPE assay when polyphenols pre-incubated with viruses showed inhibition, while drugs added after entry to cells had no effect. In silico docking data further showed that these polyphenols could bind to multiple areas on the virion surface. Other drugs binding directly to enterovirus capsids, such as pleconaril, target the hydrophobic pocket that is normally housed by an aliphatic lipid such as palmitic or oleic acid [37,38]. The hydrophobic pocket has been associated with capsid stability and suggested to release its lipid upon viral RNA release [39]. We have recently shown that albumin treatment of enteroviruses Echovirus 1 and CVA9 do expand the virion, which is typically an event associated with emptying of the pocket. However, we showed that treatment with albumin, which may steal fatty acids from the virion, does not yet lead to virus uncoating but rather virus priming to an intermediary form, leading to virus RNA release only upon further cues, such as changes in concentration of key ions [16,21]. Here, we have studied three viruses, two of which show similarly spacious pockets, whereas the CVB3 Nancy strain has a collapsed pocket that cannot house large molecules. Consequently, CVA9 showed the highest estimated binding energies for both drugs in the HP. In addition, simulations showed that the HP is the preferable docking site for the drugs with the 73% of the docking poses associated with it.

A novel algorithm that was developed for this study to reveal the docking of the molecules on enterovirus surfaces considered larger areas around the 2- and 3-fold symmetry axis. Remarkably, the docking poses for the polyphenols, RES and EGCG on the viral capsids suggested the existence of multiple binding sites, as seen from the 2-fold (Figure 6) and 3-fold (Figure 7) axes of symmetry, respectively. It seemed that the binding locations were influenced by both the physico-chemical characteristics of the polyphenols, the geometric landscapes and partial charge distributions present within the capsid assemblies for each strain. While both compounds are polyphenolic, Resveratrol is classified by PubChem as smaller and more hydrophobic (2 heterocycles, an XLogP3 value of 3.1 and 3 H-bond acceptors) than EGCG (4 heterocycles, an XLogP3 value of 1.2 and 11 H-bond acceptors) [40], which we believe to be a main factor influencing the distribution of the ligand binding sites. The fact that the HPs detected in CVA9 are much deeper than those of CVB3 may explain the better fit of the smaller Resveratrol further inside the capsid

compared to EGCG. Altogether, three new sites were found, in addition to the known HP and the recently discovered pocket that we call the Butcher-Neyts pocket [25].

Our results suggest that there are both specific and shared binding sites for EGCG and RES, with the strain also playing a role. HP showed good binding by both viruses and both drugs, suggesting that it is the main attraction on the virion surface. Instead, S1 was only detected with EGCG in CVA9, while EGCG bound S2 in both CVA9 and CVB3. Resveratrol bound to S2 only in CVB3 but to the 3-fold axis only in CVA9, further suggesting that the structural differences of the drugs as well as of the virions dictate the docking to the virions.

The predicted binding energies were lower in the newly found docking sites in comparison to the canonical HP, probably due to its deep invagination and charges present in the pocket. In silico-determined binding energies only provide a general estimation of the affinity of ligand binding and are generally useful for doing preliminary ranking of docked ligands. However, the frequency of binding to a site can additionally assist in the evaluation of lower-scoring poses. Out of the 159 docking poses, the HP ranked first with 73% of poses assigned to it, followed by S1 (10%), S2 (9%), the Butcher-Neyts pocket (4%), the pore at the 3-fold axis (3%) and the S3 site (1%). As the Neyts pocket has already been independently proven experimentally, there are valid reasons to believe that S1, S2 and the 3-fold pore are actual novel binding sites, based on the closeness in percentage clustering, a partial overlap in the range of binding energies and the number of H-bonding interactions. There is less support for the S3 site and S4, even though both may occur.

It is no wonder that the multiple ligand binding sites on the capsid led to a strong antiviral effect directly on the virion. Our studies on the molecular mechanisms of the action showed that stabilization rather than premature RNA release occurred for enteroviruses. This was shown by several methods: (1) thermal assay, (2) our previously developed real-time uncoating assay, (3) radioactive gradient assay and (4) TEM. Stabilization and prevention of virus uncoating was evident even at higher temperatures. Our results also showed that ligand binding was accompanied by strong clustering of the virions in addition to prevention of virion uncoating in the clusters.

The fact that EGCG is a bigger molecule with more hydroxy groups can be the reason why, in comparison to RES, it is more efficient in inhibiting the enteroviruses. The number of hydroxy groups has been addressed before for the difference in antiviral action of the polyphenols, apigenin and luteolin [36]. Interestingly, Resveratrol being a nearly flat molecule (Supplementary Figure S3) is more closely attached to the surface of a gold nanoparticle. Previous experiments indicate that aromatic rings are oriented parallel to the gold surface [17]. EGCG has a nearly planar aromatic ring system with one ring perpendicular to the base (Supplementary Figure S3).

This indicates that partial immersion of the EGCG is possible and can be responsible for the increase in stability and the subsequent virus aggregation. On the other hand, the three-dimensional structure of the free EGCG molecule can cross-link several viruses by immersing into their binding pockets and inducing cross-linking of two viruses, explaining why the free EGCG is more efficient than the RES molecule. RES is six times more concentrated when bound to AuNPs as compared to EGCG. Moreover, the molecules are presented on smaller nanoparticles that have a strong surface curvature. Even if we assume that RES only penetrates slightly into the pockets because it is nearly parallel to the surface, the sheer number of interactions between virus and RES and the RES presentation by the more curved surface of nanoparticles can work as a cross-linker between multiple binding pockets on several viruses. This could explain why RES bound to nanoparticles is more efficient than the free molecule.

Another interesting fact that we observed in our infection experiments was that RES was slower to inhibit virus infection. After 6 h, its antiviral efficacy was still moderate, whereas after 24 h and later, it had reached full efficiency, while EGCG was very efficient already at earlier time points. This may be directly because RES has fewer docking sites on the virion surface. However, it may also be because it has less hydroxylic groups on its structure, leading to lower binding affinity.

Altogether, the two studied polyphenols showed great antiviral efficacy for all three studied enteroviruses. The discovered mechanism of action is that the polyphenols immerse in several binding sites on the virion surface, resulting in stabilization of the virions against opening, even in harsh conditions. In addition, formation of large clusters was observed, which might be another efficient way to lower the incidence of virions entering cells. Clustering and the resulting precipitation of the virus–polyphenol or polyphenol–AuNP clusters indicate a potential use for safe water clearing applications and for decontamination of surfaces. Future studies will focus on clarifying if the clustered viruses will be prevented from penetrating the mucus layer or be used as vaccines. Previous studies have also demonstrated the therapeutic potential of polyphenols such as EGCG and Curcumin, for treating protein aggregation diseases associated with peripheral neuropathy [41]. The mechanism by which EGCG works, to prevent the disease progression in case of amyloid fibril formation, is by stabilizing the protein after binding to it and forming soluble nontoxic aggregates [42,43]. EGCG interacts with amyloid-forming proteins through hydrophobic interactions or H-bonds, forming stable oligomers [44]. Similar interactions between the virus capsid and polyphenols have been described in our computational studies. Whether the mechanism behind virus stability/loss of infectivity and prevention of formation of amyloid aggregates reported previously is the same remains to be shown.

In general, it can be concluded that especially the AuNP-bound polyphenols might have interesting potential in future applications for (i) antiviral surface coatings, which can already reduce the viral load before it is transferred to the body surface and unintentionally up-taken, and (ii) as oral antivirals. The oral administration of the polyphenol-coated nanoparticles is especially interesting as the nanoparticle and the bound polyphenol are localized in the primary infection site for enteroviruses, in the gut, before they likely pass through the intestinal cell layer and hence can significantly reduce the viral load of the intestine. The systemic toxicity of these nanoparticles will be determined in future animal experiments. It requires consideration as the polyphenol-AuNPs due to their size and nearly neutral surface charge have optimal properties to penetrate the mucus layer of the intestinal tract [45,46].

5. Conclusions

Based on our findings, EGCG and RES effectively inhibit enterovirus infection, even after short encounters with the viruses and at various temperatures. Interestingly, the studied polyphenols have better efficacy when functionalized on gold nanoparticles, particularly for RES. The efficacy of the compounds was not compromised even when diluted 50 times. Mechanistic studies revealed that the polyphenols and polyphenol-functionalized AuNPs (i) cause clustering and stabilization of the virions, (ii) prevent the release of viral RNA and (iii) prevent the virus from binding to the cell surface. In silico docking experiments of these molecules against 2- and 3-fold symmetry axes of the capsid identified three novel binding sites in addition to the canonical hydrophobic pocket, and the Butcher-Neyts pocket. The presence of several binding sites for the polyphenols explains the strong increase in the stability. The strong clustering and inactivation of the virions may turn out to be helpful for future applications, for example, vaccination.

Supplementary Materials: The following are available online at https://www.mdpi.com/article/10.3390/pharmaceutics13081182/s1, Figure S1: Testing whether the antiviral efficacy was solely dependent on the ligand bound to the nanoparticles or from the unbound ligands possibly present in the nanoparticle preparation, Figure S2: Testing the antiviral efficacy of EGCG using lower viral titer of CVB3 (2×10^5 PFU/mL), Figure S3: 3D structure of (A) EGCG and (B) RES, Supplementary Calculations 1: calculation of number of ligands per nanoparticles, Supplementary Calculations 2: calculation of ligand concentration in AuNP stock solution. Supplementary Table S1: Parameters for the calculation of the number of ligands per AuNP, Supplementary Table S2: Parameters for the calculation of the ligand concentration bound to the AuNP in the stock solution.

Author Contributions: D.R., S.S., S.K. and V.M. conceptualized the study; D.R., S.S., O.S.A., V.L. (Valentino Laquintana), N.D., V.L. (Vili Lampinen), A.Z. and V.P.H. performed the investigations; V.M. acquired funding; S.K. and V.M. were the project administrators; O.S.A. and Ö.T.B. performed the programming; D.R., S.S., O.S.A., S.K. and V.M. wrote the manuscript; Ö.T.B., V.P.H., S.K. and V.M. reviewed and edited the manuscript. All authors have read and agreed to the published version of the manuscript.

Funding: This work was supported by the Jane and Aatos Erkko foundation (V.M.).

Institutional Review Board Statement: Not applicable.

Informed Consent Statement: Not applicable.

Data Availability Statement: Not applicable.

Acknowledgments: We would like to thank Amirbabak Sioofy-Khojine from Tampere University for helping with regression curves and EC_{50} and CC_{50} calculations.

Conflicts of Interest: The authors declare no conflict of interest.

References

1. Stone, V.M.; Hankaniemi, M.M.; Laitinen, O.H.; Sioofy-Khojine, A.B.; Lin, A.; Lozano, I.M.D.; Mazur, M.A.; Marjomäki, V.; Loré, K.; Hyöty, H.; et al. A hexavalent Coxsackievirus B vaccine is highly immunogenic and has a strong protective capacity in mice and nonhuman primates. *Sci. Adv.* **2020**, *6*, eaaz2433. [CrossRef] [PubMed]
2. Linnakoski, R.; Reshamwala, D.; Veteli, P.; Cortina-Escribano, M.; Vanhanen, H.; Marjomäki, V. Antiviral Agents From Fungi: Diversity, Mechanisms and Potential Applications. *Front. Microbiol.* **2018**, *9*, 2325. [CrossRef] [PubMed]
3. Filardo, S.; Di Pietro, M.; Mastromarino, P.; Sessa, R. Therapeutic potential of resveratrol against emerging respiratory viral infections. *Pharmacol. Ther.* **2020**, *214*, 107613. [CrossRef] [PubMed]
4. Vestergaard, M.; Ingmer, H. Antibacterial and antifungal properties of resveratrol. *Int. J. Antimicrob. Agents* **2019**, *53*, 716–723. [CrossRef] [PubMed]
5. Zhang, L.; Li, Y.; Gu, Z.; Wang, Y.; Shi, M.; Ji, Y.; Sun, J.; Xu, X.; Zhang, L.; Jiang, J.; et al. Resveratrol Inhibits Enterovirus 71 Replication and Pro-Inflammatory Cytokine Secretion in Rhabdosarcoma Cells through Blocking IKKs/NF-κB Signaling Pathway. *PLoS ONE* **2015**, *10*, e0116879.
6. Williamson, M.; McCormick, T.G.; Nance, C.L.; Shearer, W. Epigallocatechin gallate, the main polyphenol in green tea, binds to the T-cell receptor, CD4: Potential for HIV-1 therapy. *J. Allergy Clin. Immunol.* **2006**, *118*, 1369–1374. [CrossRef]
7. Kawai, K.; Tsuno, N.H.; Kitayama, J.; Okaji, Y.; Yazawa, K.; Asakage, M.; Hori, N.; Watanabe, T.; Takahashi, K.; Nagawa, H. Epigallocatechin gallate, the main component of tea polyphenol, binds to CD4 and interferes with gp120 binding. *J. Allergy Clin. Immunol.* **2003**, *112*, 951–957. [CrossRef]
8. Kim, M.; Kim, S.-Y.; Lee, H.W.; Shin, J.S.; Kim, P.; Jung, Y.-S.; Jeong, H.-S.; Hyun, J.-K.; Lee, C.-K. Inhibition of influenza virus internalization by (−)-epigallocatechin-3-gallate. *Antivir. Res.* **2013**, *100*, 460–472. [CrossRef]
9. Cottart, C.-H.; Nivet-Antoine, V.; Laguillier-Morizot, C.; Beaudeux, J.-L. Resveratrol bioavailability and toxicity in humans. *Mol. Nutr. Food Res.* **2009**, *54*, 7–16. [CrossRef]
10. Kučera, O.; Mezera, V.; Moravcova, A.; Endlicher, R.; Lotková, H.; Drahota, Z.; Červinková, Z. In VitroToxicity of Epigallocatechin Gallate in Rat Liver Mitochondria and Hepatocytes. *Oxidative Med. Cell. Longev.* **2015**, *2015*, 476180. [CrossRef]
11. Isbrucker, R.; Edwards, J.; Wolz, E.; Davidovich, A.; Bausch, J. Safety studies on epigallocatechin gallate (EGCG) preparations. Part 2: Dermal, acute and short-term toxicity studies. *Food Chem. Toxicol.* **2006**, *44*, 636–650. [CrossRef]
12. Yang, F.; Medik, Y.; Li, L.; Tian, X.; Fu, D.; Brouwer, K.L.R.; Wagner, K.; Sun, B.; Sendi, H.; Mi, Y.; et al. Nanoparticle Drug Delivery Can Reduce the Hepatotoxicity of Therapeutic Cargo. *Small* **2020**, *16*, e1906360. [CrossRef] [PubMed]
13. Meléndez-Villanueva, M.A.; Morán-Santibañez, K.; Sanmiguel, J.J.M.; Rangel-López, R.; Garza-Navarro, M.A.; Rodríguez-Padilla, C.; Zarate-Triviño, D.G.; Trejo-Ávila, L.M. Virucidal Activity of Gold Nanoparticles Synthesized by Green Chemistry Using Garlic Extract. *Viruses* **2019**, *11*, 1111. [CrossRef] [PubMed]
14. Huttunen, M.; Waris, M.; Kajander, R.; Hyypiä, T.; Marjomäki, V. Coxsackievirus A9 Infects Cells via Nonacidic Multivesicular Bodies. *J. Virol.* **2014**, *88*, 5138–5151. [CrossRef]
15. Myllynen, M.; Kazmertsuk, A.; Marjomäki, V. A Novel Open and Infectious Form of Echovirus 1. *J. Virol.* **2016**, *90*, 6759–6770. [CrossRef]
16. Ruokolainen, V.; Domanska, A.; Laajala, M.; Pelliccia, M.; Butcher, S.J.; Marjomäki, V. Extracellular Albumin and Endosomal Ions Prime Enterovirus Particles for Uncoating That Can Be Prevented by Fatty Acid Saturation. *J. Virol.* **2019**, *93*, 599. [CrossRef]
17. Mandal, S.; Bonifacio, A.; Zanuttin, F.; Sergo, V.; Krol, S. Synthesis and multidisciplinary characterization of polyelectrolyte multilayer-coated nanogold with improved stability toward aggregation. *Colloid Polym. Sci.* **2011**, *289*, 269–280. [CrossRef]
18. Sechi, M.; Sanna, V.; Pala, N.; Manconi, P.; Mariani, A.; Dedola, S.; Rassu, M.; Crosio, C.; Iaccarino, C.; Dessi, G. Single-step green synthesis and characterization of gold-conjugated polyphenol nanoparticles with antioxidant and biological activities. *Int. J. Nanomed.* **2014**, *9*, 4935–4951. [CrossRef] [PubMed]

19. Perrone, M.; Lopalco, A.; Lopedota, A.; Cutrignelli, A.; Laquintana, V.; Douglas, J.; Franco, M.; Liberati, E.; Russo, V.; Tongiani, S.; et al. Preactivated thiolated glycogen as mucoadhesive polymer for drug delivery. *Eur. J. Pharm. Biopharm.* **2017**, *119*, 161–169. [CrossRef]
20. Schmidtke, M.; Schnittler, U.; Jahn, B.; Dahse, H.-M.; Stelzner, A. A rapid assay for evaluation of antiviral activity against coxsackie virus B3, influenza virus A, and herpes simplex virus type 1. *J. Virol. Methods* **2001**, *95*, 133–143. [CrossRef]
21. Ruokolainen, V.; Laajala, M.; Marjomäki, V. Real-time Fluorescence Measurement of Enterovirus Uncoating. *Bio-Protocol* **2020**, *10*, e3582. [CrossRef]
22. Martikainen, M.; Salorinne, K.; Lahtinen, T.; Malola, S.; Permi, P.; Häkkinen, H.; Marjomäki, V. Hydrophobic pocket targeting probes for enteroviruses. *Nanoscale* **2015**, *7*, 17457–17467. [CrossRef]
23. Morris, G.M.; Huey, R.; Lindstrom, W.; Sanner, M.F.; Belew, R.K.; Goodsell, D.S.; Olson, A.J. AutoDock4 and AutoDockTools4: Automated docking with selective receptor flexibility. *J. Comput. Chem.* **2009**, *30*, 2785–2791. [CrossRef]
24. Hendry, E.; Hatanaka, H.; Fry, E.; Smyth, M.; Tate, J.; Stanway, G.; Santti, J.; Maaronen, M.; Hyypiä, T.; Stuart, D. The crystal structure of coxsackievirus A9: New insights into the uncoating mechanisms of enteroviruses. *Structure* **1999**, *7*, 1527–1538. [CrossRef]
25. Abdelnabi, R.; Geraets, J.A.; Ma, Y.; Mirabelli, C.; Flatt, J.W.; Domanska, A.; Delang, L.; Jochmans, D.; Kumar, T.A.; Jayaprakash, V.; et al. A novel druggable interprotomer pocket in the capsid of rhino- and enteroviruses. *PLoS Biol.* **2019**, *17*, e3000281. [CrossRef]
26. Hassan, N.M.; Alhossary, A.A.; Mu, Y.; Kwoh, C. Protein-Ligand Blind Docking using QuickVina-W with Inter-Process Spatio-Temporal Integration. *Sci. Rep.* **2017**, *7*, 15451. [CrossRef] [PubMed]
27. Tange, O. GNU Parallel: The Command-Line Power Tool. *Login* **2011**, *36*, 42–47.
28. Jubb, H.; Higueruelo, A.; Ochoa-Montaño, B.; Pitt, W.; Ascher, D.B.; Blundell, T.L. Arpeggio: A Web Server for Calculating and Visualising Interatomic Interactions in Protein Structures. *J. Mol. Biol.* **2017**, *429*, 365–371. [CrossRef] [PubMed]
29. Smith, R.H.B.; Dar, A.C.; Schlessinger, A. PyVOL: A PyMOL Plugin for Visualization, Comparison, and Volume Calculation of Drug-Binding Sites. *Biorxiv* **2019**, 816702. [CrossRef]
30. Muckelbauer, J.K.; Kremer, M.; Minor, I.; Tong, L.; Zlotnick, A.; Johnson, J.E.; Rossmann, M.G. Structure determination of coxsackievirus B3 to 3.5 Å resolution. *Acta Crystallogr. Sect. D Biol. Crystallogr.* **1995**, *51*, 871–887. [CrossRef]
31. Pei, J.; Kim, B.-H.; Grishin, N.V. PROMALS3D: A tool for multiple protein sequence and structure alignments. *Nucleic Acids Res.* **2008**, *36*, 2295–2300. [CrossRef]
32. Waterhouse, A.M.; Procter, J.; Martin, D.; Clamp, M.; Barton, G.J. Jalview Version 2–a multiple sequence alignment editor and analysis workbench. *Bioinformatics* **2009**, *25*, 1189–1191. [CrossRef]
33. Saarnio, V.K.; Salorinne, K.; Ruokolainen, V.P.; Nilsson, J.R.; Tero, T.-R.; Oikarinen, S.; Wilhelmsson, L.M.; Lahtinen, T.M.; Marjomäki, V.S. Development of functionalized SYBR green II related cyanine dyes for viral RNA detection. *Dye. Pigment.* **2020**, *177*, 108282. [CrossRef]
34. Orhan, D.D.; Özçelik, B.; Özgen, S.; Ergun, F. Antibacterial, antifungal, and antiviral activities of some flavonoids. *Microbiol. Res.* **2010**, *165*, 496–504. [CrossRef] [PubMed]
35. Du, N.; Li, X.; Bao, W.; Wang, B.; Xu, G.; Wang, F. Resveratrol-loaded nanoparticles inhibit enterovirus 71 replication through the oxidative stress-mediated ERS/autophagy pathway. *Int. J. Mol. Med.* **2019**, *44*, 737–749. [CrossRef] [PubMed]
36. Lv, X.; Qiu, M.; Chen, D.; Zheng, N.; Jin, Y.; Wu, Z. Apigenin inhibits enterovirus 71 replication through suppressing viral IRES activity and modulating cellular JNK pathway. *Antivir. Res.* **2014**, *109*, 30–41. [CrossRef]
37. Pevear, D.C.; Tull, T.M.; Seipel, M.E.; Groarke, J.M. Activity of Pleconaril against Enteroviruses. *Antimicrob. Agents Chemother.* **1999**, *43*, 2109–2115. [CrossRef]
38. Smyth, M.S.; Martin, J.H. Picornavirus Uncoating. *Mol. Pathol. MP* **2002**, *55*, 214–219. [CrossRef]
39. Smyth, M.; Pettitt, T.; Symonds, A.; Martin, J. Identification of the pocket factors in a picornavirus. *Arch. Virol.* **2003**, *148*, 1225–1233. [CrossRef] [PubMed]
40. Kim, S.; Chen, J.; Cheng, T.; Gindulyte, A.; He, J.; He, S.; Li, Q.; Shoemaker, B.A.; Thiessen, P.A.; Yu, B.; et al. PubChem 2019 update: Improved access to chemical data. *Nucleic Acids Res.* **2019**, *47*, D1102–D1109. [CrossRef]
41. Ferreira, N.; Saraiva, M.J.; Almeida, M. Natural polyphenols inhibit different steps of the process of transthyretin (TTR) amyloid fibril formation. *FEBS Lett.* **2011**, *585*, 2424–2430. [CrossRef] [PubMed]
42. Ferreira, N.; Cardoso, I.; Domingues, M.R.; Vitorino, R.; Bastos, M.; Bai, G.; Saraiva, M.J.; Almeida, M. Binding of epigallocatechin-3-gallate to transthyretin modulates its amyloidogenicity. *FEBS Lett.* **2009**, *583*, 3569–3576. [CrossRef]
43. Ferreira, N.; Saraiva, M.J.; Almeida, M.R. Epigallocatechin-3-Gallate as a Potential Therapeutic Drug for TTR-Related Amyloidosis: "In Vivo" Evidence from FAP Mice Models. *PLoS ONE* **2012**, *7*, e29933. [CrossRef] [PubMed]
44. del Amo, J.M.L.; Fink, U.; Dasari, M.; Grelle, G.; Wanker, E.E.; Bieschke, J.; Reif, B. Structural Properties of EGCG-Induced, Nontoxic Alzheimer's Disease Aβ Oligomers. *J. Mol. Biol.* **2012**, *421*, 517–524. [CrossRef]
45. Pearson, J.P.; Chater, P.I.; Wilcox, M.D. The properties of the mucus barrier, a unique gel–how can nanoparticles cross it? *Ther. Deliv.* **2016**, *7*, 229–244. [CrossRef] [PubMed]
46. de Sousa, I.P.; Steiner, C.; Schmutzler, M.; Wilcox, M.D.; Veldhuis, G.J.; Pearson, J.P.; Huck, C.; Salvenmoser, W.; Bernkop-Schnürch, A. Mucus permeating carriers: Formulation and characterization of highly densely charged nanoparticles. *Eur. J. Pharm. Biopharm.* **2015**, *97*, 273–279. [CrossRef]

pharmaceutics

MDPI

Supplementary Materials: Polyphenols Epigallocatechin Gallate and Resveratrol, and Polyphenol-Functionalized Nanoparticles Prevent Enterovirus Infection through Clustering and Stabilization of the Viruses

Dhanik Reshamwala, Sailee Shroff, Olivier Sheik Amamuddy, Valentino Laquintana, Nunzio Denora, Antonella Zacheo [4], Vili Lampinen, Vesa P. Hytonen, Özlem Tastan Bishop, Silke Krol and Varpu Marjomäki

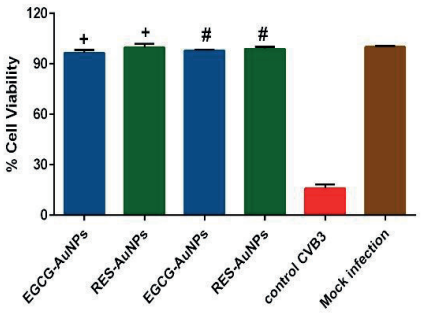

Supplementary figure 1. Testing whether the antiviral efficacy was solely dependent on the ligand bound to the nanoparticles or also from the unbound ligands possibly present in the nanoparticle preparation. In the experiment, AuNP conjugates were ultracentrifuged (10 Psi which corresponds to roughly 50 000 x g, for 30 min) and the pellet was resuspended in ddH2O which was then tested against CVB3 (2 X 10^7 PFU/mL).
+ NPs tested before ultracentrifugation
# NPs tested after ultracentrifugation

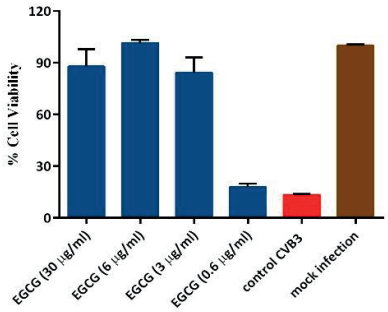

Supplementary figure 2. Testing the antiviral efficacy of EGCG using low viral titer of CVB3 (2 X 10^5 PFU/mL).

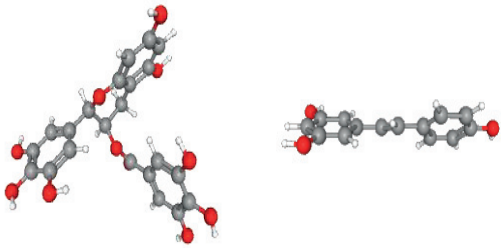

Supplementary figure 3. 3D structure of A) EGCG[1]and B) RES[1].

Supplementary calculation 1: Calculation of number of ligands per nanoparticles.

From the TEM images we assume that the AuNP are spherical. Using the average diameter from the TEM analysis the surface area of the sphere can be calculated by

$$A_{uNP}=4*\pi*r^2=2*\pi*d^2$$

It is assumed that the 2 aromatic rings (fig. S 3) are oriented parallel to the gold nanoparticle surface (fig. S 3) as we have observed for other aromatic rings in previous experiments [2]. The length and width of the ligand contact area was determined by means of the Avogadro software[1]. The contact area is that of an ellipsoid, hence the area of the ligand is

$$A_{ligand} =\pi*a*b$$

Assuming now the tightest possible ligand packing on the nanoparticle surface, the number N of polyphenols per surface is

$$N= A_{AuNP}/A_{ligand}$$

Supplementary Table 1. Parameters for the calculation of the number of ligands per AuNP

	D* [nm]	A_{AuNP} [nm²]	Ligand a/b# [nm]	A_{ligand} [nm²]	N(ligand/AuNP)
EGCG	131.5 ± 7.1	108 650	0.64/1.14	2.3	47,239
RES	78.6± 2.3	38 817	0.54 /1.2	2.03	19,122

* determined by TEM

calculated by Avogadro software [1]

Supplementary calculation 2: Calculation of ligand concentration in AuNP stock solution

For the calculation of the ligand concentration bound to AuNP in the stock solution, we calculate first the number of AuNP. For this we calculate first the volume of the spherical AuNP using the radius r, determined in TEM analysis (r=D/2).

$$V_{AuNP}=4/3*\pi*r^3$$

With the nanoparticle volume V_{AuNP} and the density of gold, δ_{Au} we calculated the mass of a single AuNP, m_{AuNP}. The gold content of the stock solution, m_{Au} was measured by ICP-MS. This allows us to calculate the number of AuNP, N_{AuNP} in stock solution by

$$N_{AuNP}= m_{Au}/ m_{AuNP}$$

The calculation reported in table S1 gives us the number of ligand per AuNP, N_{ligand} which allows us to calculate the total number of ligands in the stock solution of gold nanoparticles per L. The concentration of bound ligand to the nanoparticles is calculated by

$$c_{ligand} = N_{ligand} / N_A$$

N_A is the constant of Avogardo ($6.02214086 \times 10^{23}$ mol^{-1}); N_{ligand} is the number of ligand per L.

Supplementary Table 2. Parameters for the calculation of the ligand concentration bound to the AuNP in the stock solution.

	D ^ [nm]	V_{AuNP} [nm^3]	V_{NP} [cm^3]	δ_{Au} [g/cm^3]	m_{AuNP} [g]	m_{Au} # [g/L]	N_{AuNP} /L	N_{ligand} /NP	N_{ligand} /L	c_{ligand} [µM]
EGCG	131.5	1,190,627	$1.19 * 10^{-15}$	19.32	$2.30 * 10^{-14}$	1.64	$7.13 * 10^{13}$	47,239	$3.37 * 10^{18}$	5.61
RES	78.6	254,253	$2.54 * 10^{-16}$		$4.91 * 10^{-15}$	5.3	$1.08 * 10^{15}$	19,122	$2.06 * 10^{19}$	34.4

^ determined by TEM

determined by ICP-MS

References

[1] Hanwell, M.D.; Curtis, D.E.; Lonie, D.C.; Vandermeersch, T.; Zurek, E.; Hutchison, G.R. Avogadro: An Advanced Semantic Chemical Editor, Visualization, and Analysis Platform. Journal of Cheminformatics **2012**, *4*, 17.

[2] Mandal, S.; Bonifacio, A.; Zanuttin, F.; Sergo, V.; Krol, S. Synthesis and Multidisciplinary Characterization of Polyelectrolyte Multilayer-Coated Nanogold with Improved Stability Toward Aggregation. Colloid Polym. Sci. **2011**, *289*, 269-280.